UNIVERSITY OF SOUTHAMPTON

FACULTY OF ENGINEERING AND APPLIED SCIENCE
INSTITUTE OF SOUND AND VIBRATION RESEARCH

THE ACTIVE MINIMISATION OF HARMONIC ENCLOSED SOUND FIELDS WITH PARTICULAR APPLICATION TO PROPELLER INDUCED CABIN NOISE

by

Andrew John Bullmore

A thesis submitted for the award of

Doctor of Philosophy

October 1987

ACKNOWLEDGEMENTS

This work has been performed under a research grant awarded by the Department of Trade and Industry and their support is gratefully acknowledged. The assistance of British Aerospace plc is also gratefully acknowledged, particularly for their provision of, and permission to publish, the experimental flight data included in this thesis.

I wish to extend my most sincere gratitude to all those people, too numerous to mention individually, who have so willingly lent me their time, experience and support during the past four years. In particular I would like to thank Dr. S.J. Elliott and Dr. P.A. Nelson for their guidance and enthusiasm as project supervisors, and also Dr. R.J. Pinnington for his helpful comments on the structural response aspects of the work. I would also like to acknowledge the helpful cooperation of Mr. J.F. Evers and Mr. B. Chidley of British Aerospace.

Thanks are also due to Mrs. M. Strickland for her typing of this text.

Lastly, but by no means least, for her patience and understanding over the past four years, and particularly over the last nine months, I would like to thank Sarah.

TABLE OF CONTENTS

UNIVERSITY OF SOUTHAMPTON

ABSTRACT

FACULTY OF ENGINEERING AND APPLIED SCIENCE
INSTITUTE OF SOUND AND VIBRATION RESEARCH

DOCTOR OF PHILOSOPHY

THE ACTIVE MINIMISATION OF HARMONIC ENCLOSED SOUND FIELDS WITH PARTICULAR APPLICATION TO PROPELLER INDUCED CABIN NOISE

by Andrew John Bullmore

This work considers the use of secondary acoustic sources for the reduction of noise levels in harmonically excited enclosed sound fields. This possibility is studied initially through the use of an analytical model of a single frequency "two-dimensional" rectangular, enclosed sound field of low modal density. Quadratic optimisation theory is used to predict the effectiveness of these active techniques for reducing sound levels. It is shown that if one chooses to minimise the total acoustic potential energy of the sound field then substantial global reductions in sound pressure may be achieved. The conditions required to achieve these reductions are discussed, and in particular the effect of secondary source location is demonstrated. The unsuitability of this as a practical control system cost function is discussed, and as an alternative it is suggested that one can minimise the sum of the squared pressures over a number of discrete sensors. Both theoretical and experimental results from using this cost function are presented. These show good agreement. The importance of both secondary source and error sensor locations is discussed.

The reduction of low frequency propeller induced cabin noise is a possible application of active noise control. Simplified analytical models of the structural and internal acoustic response of a 48 seat, twin turboprop passenger aircraft are presented. These consist of the structural response of an isotropic, thin cylindrical shell of finite length and the acoustic response of the enclosed cylindrical sound field. It is shown that, provided the external acoustic pressure forcing of the shell is modelled representatively of measured propeller pressure fields, then these simple models provide results which demonstrate good agreement with measured data, at least for frequencies encompassing the first two propeller blade passage harmonics (88 Hz and 176 Hz). These models are used to predict the effectiveness of active noise control when it is applied to reduce the average sound pressure level over a typical seated head height plane in the passenger cabin. Results for the first two blade passage harmonics are presented for systems consisting of up to 24 secondary sources and 48 error sensors. In general the predictions suggest that active noise control shows promise as a potential method of reducing low frequency propeller induced cabin noise.

CHAPTER 1

AN INTRODUCTION TO THE ACTIVE CONTROL OF ENCLOSED SOUND FIELDS

1.1 Introduction

With the advent of prop-fan powered aircraft comes the promise of high fuel efficiency combined with cruising speeds comparable with those of current jet aircraft [1]. However, it is also predicted [2] that unacceptably high sound pressure levels might be produced in the passenger cabins of these aircraft. There has thus arisen a need to develop an effective method of reducing high level, low frequency tonal noise within the enclosed cabin space. Traditional passive means of noise control aimed at reducing the transmission of sound from the exterior to the interior of the fuselage generally involve large weight penalties if they are to be effective at the low frequencies (100 Hz-300 Hz) considered. Predictions [2] have shown that using noise control techniques currently available the increase in weight required to reduce the internal sound pressure levels to an acceptable level will substantially decrease the gains in fuel efficiency originally predicted for these power plants. Active noise control, however, is known to be most effective at low frequencies, and therefore offers the potential of reducing the internal noise levels whilst keeping the weight increase low.

There exist two very distinct possibilities for applying active noise control to these aircraft. There is the option of reducing the external acoustic pressure forcing over the fuselage surface [3,4]. This would involve some distribution of secondary (cancelling) acoustic transducers mounted externally on the aircraft, distributed either close to the propeller or over the areas of fuselage wall which experience the highest levels of acoustic pressure fluctuations. Alternatively, there is the option of reducing the acoustic pressure within the cabin space [5-10]. This latter choice has two major advantages over the external noise control solution. Firstly, the environment within an aircraft cabin would allow conventional transducers to be used in the control system. This is to be contrasted with the harsh external environment, with its large temperature and pressure fluctuations throughout each flight cycle, where specialised

transducers would need to be designed for use as secondary sources (Reference [4], for example, suggests the use of compressed air powered sirens although the work reported in this reference concerns the reduction of far field noise). Secondly, there is still some debate as to whether the predominant cause of the internal noise will be due to direct (airborne) or indirect (structure borne) transmission paths. Active control of the internal acoustic field will not discriminate between these two, and will therefore be equally effective whether the noise is due to direct or indirect paths. In contrast, active control of the external acoustic field will only reduce internal noise due to the airborne path. If it is subsequently discovered that structure borne transmission is the dominant cause of the internal noise, then this external method will be ineffective in producing any substantial reduction in internal cabin sound pressure levels.

The work presented in this thesis assesses the feasibility of applying internal active noise control. In particular it reveals some of the fundamental physical limitations of active control systems when applied to harmonic enclosed sound fields and, with these fundamental constraints in mind, the practical difficulties of actively reducing cabin noise in a typical medium range propeller aircraft are studied.

1.2 A Review of Active Noise Control in Enclosed Spaces

The first reference to the active control of enclosed sound fields appeared as early as 1953. In this, Olson and May [11] described some experimental results obtained using their "electronic sound absorber". This device involved a single microphone and a single secondary source placed adjacent to each other. By suitable phasing of the control loudspeaker with respect to the pressure at the microphone it could be configured to either absorb acoustic energy, or to "null" the pressure at the microphone location. Olson and May made the important observation from their results that active noise control is most effective at low frequencies and can therefore be used to complement passive noise control measures. They then proceeded to suggest some practical uses for their system. With the device in its energy absorbing configuration they suggested that several individual

elements could be placed close to the corners of a room so as to provide additional acoustic damping, in effect producing global sound pressure reductions. With the system configured as a "spot sound reducer" they suggested that it could be placed close to the heads of people exposed to high level, low frequency noise, be they in shops, factories, offices or aircraft. Olson and May also suggested many other possible uses for their invention. However, those mentioned above have been highlighted as they pertain directly to the possible control of enclosed sound fields. It is not intended in this introduction to review the chronological development of active noise control in general. If a general review is required then several have been published elsewhere, and it is recommended that the reader refers to one of Warnaka [12], Ffowcs Williams [13] or Lindqvist [14]. These reviews adequately cover the development of the subject up until 1985. For the remainder of this section, only the contributions of those references which directly address the problem of actively controlling enclosed sound fields shall be reviewed.

Since the suggestions of Olson and May [11] in 1953, there have been several publications concerning the control of enclosed sound fields. Many of them have addressed the problem of "nulling" the pressure at a point within the enclosed sound field, with generally only passing reference as to what occurs at locations away from the cancelling microphone. In some cases it is of course only desired to produce a highly localized "zone of silence", and what happens away from this zone is of little importance. For example, Brewer *et al* [15] presented results for a "virtual earth" system applied to create a pressure null at the occupier's ear position in an audiometric booth. In this type of controlled situation it may be possible to limit the occupier's head movements to stay within the "zone of silence". However, results given in the same paper demonstrate that this zone is very small, with a reduction of 44.8 dB at 64 Hz at the cancelling microphone falling to a reduction of 25 dB within 3 cm (a distance of one two hundredth of a wavelength). The solution in this instance could be to mount the system in headsets to ensure its close proximity to the users' ears [16,17]. In many practical applications, however, it may not be acceptable to place constraints on the location of users'/occupiers' heads.

One such example where there is a low frequency noise problem is in vehicle cabs, particularly tractor and heavy goods vehicle cabs. The acoustical virtual earth principle has been applied to this problem by Berge [18,19]. He used an 18" loudspeaker located behind the driver's head, and a sensor just above the driver's head. Berge reported reductions of 15 dB at the cancelling microphone at 30 Hz, with the cancellation region extending over both the driver's and passengers' head locations. This is not too surprising since 30 Hz is below the frequency of the first acoustic resonance of the cab, and therefore the pressure would be reasonably uniform throughout the cabin volume. Regions of cancellation obtained at higher frequencies (above the first acoustic mode resonance frequency) are not reported. Nadim *et al* [20] have also described experimental results obtained in a vehicle cab, this time a tractor cab. However, rather than using a close coupled negative feedback system they used the "Essex Synchronous System" [21,22] to effect a pressure null at the single microphone location. This has the advantage that the microphone and loudspeakers do not have to be close to each other. Reductions at the cancelling microphone location were measured up to the tenth engine firing frequency harmonic (about 170 Hz), and at 50 Hz the local reduction obtained was greater than 25 dB. The observation was also made that "although the degree of cancellation deteriorated at positions progressively further away from the residual microphone, the effect was still substantial in all the normal operator head positions". No formal spatial cancellation results are presented; however, from the information provided it appears that the predominant noise is produced by the first three harmonics which are all below 60 Hz, and consequently below the cut on frequency of the lowest order acoustic mode within the cabin.

Oswald [23] also implemented an adaptive control system in a vehicle passenger compartment, with the aims of evaluating the amount of noise reduction achievable and the size of the cancellation zone which could be obtained when minimising the pressure at a single microphone location. He reports reductions of up to 30 dB at the microphone for the second to sixth harmonics of the engine firing frequency. He also notes that for frequencies less than 200 Hz the cancellation region was larger than head size but, more importantly, that at cabin resonances the noise reductions were large and occurred

over the whole cabin volume. Recognizing that the cabin modes were being excited by a non-compact source, he placed the cancelling loudspeakers in the corners of the cabin to increase their coupling with the resonant modes. This interaction of secondary sources with resonant modes has also been pointed out by Chaplin [24]. He suggests the necessary placement of secondary sources required to cancel out two modes in a noisy machinery room, thus hopefully providing global cancellation. However, no mention is made of where to put the cancelling microphone to achieve the desired effect, nor is there any discussion about the number of microphones required. Chaplin also suggests the method for global reductions in aircraft cabins.

Warnaka *et al* [5], also stress the need for global cancellation in certain applications. They report experiments involving a single cancelling microphone in a reverberation chamber, but report that reductions could be heard throughout the chamber for frequencies from 12 Hz to 400 Hz. They also describe experiments performed on a model aircraft fuselage, where a single secondary source was used to produce global reductions in sound pressure level. For these experiments the primary source was the model fuselage wall vibration produced by an external excitation. The method of producing the quoted reductions is not clear, and the paper does not consider the issue of microphone locations. In a later paper, [25], Zalas *et al* report tests performed in flight within small, twin-engined propeller aircraft. Again the desire for global reductions is emphasized, but the purpose of this work was primarily to evaluate various control reference signals. Consequently, only results for a single loudspeaker/single microphone system are presented, from which only small areas of cancellation around the microphone are achieved. From this the authors concluded that the primary noise source could not be considered compact, and therefore the single secondary source used was inadequate. This latter characteristic, that a compact primary source requires only a simple secondary source configuration in order to produce global cancellations had been experimentally proved by Short [26] in 1980. Short's experiments demonstrated that global reductions in sound pressure level throughout a reverberant chamber can be achieved using a single secondary source provided that both the primary and secondary sources are acoustically compact, and can therefore be placed within one half

wavelength of each other (of the maximum frequency to be attenuated). Cancellation in this case was effected simply by ensuring that the primary and secondary sources combined to produce a dipole type radiator, thus decreasing their radiation efficiency.

This relationship between primary source complexity and the complexity of the control system configuration required in order to ensure global reductions has been pointed out by Guicking *et al* [27]. In this paper he described experimental and theoretical results of actively controlling the reflection coefficient over a small area of anechoic chamber wall using a 3 × 3 array of loudspeakers. In a later paper [28] Guicking reported similar tests in an enclosed resonant sound field, but limited these to a one-dimensional Kundt tube. This idea was first suggested in Olson and May's original paper [11] where they suggested placing such devices, set to have reflection coefficients as close to zero as possible, in the corners of a room so as to most effectively damp out the acoustic response, thus producing global reductions throughout the three dimensional volume.

Ross [10,29], too, has commented on the complexity of the secondary source distribution required with reference to both the primary source compactness and complexity and also to the complexity of the resulting sound field in terms of the number of modes that are dominantly excited. He suggests that for global reductions one must use as many secondary sources as are required to effectively mimic the primary source velocity distribution, although 180° out of phase. Alternatively one could use as many secondary sources as there are dominant modes so as to suppress the contribution of these modes. A method of determining the number of sources required in such cases has been presented by Eatwell [30]. However, in reference [10], where Ross suggests these methods for globally reducing the sound levels within a medium size propeller aircraft, it is not clear what practical variable is to be used as the control system error signal.

All the papers mentioned above demonstrate important features of active noise control systems when they are applied to enclosed sound fields. However, particular emphasis appears to have been placed on producing fast, efficient, stable control systems, rather than trying

to fully appreciate what physical limits acoustical factors place on the active control system chosen. This approach to the problem is understandable, as it has traditionally been the advances in electronics which have enabled the development of successful practical applications of the technique. Since the 1970's the development of electronic hardware has been accelerating, particularly with the advent of dedicated digital signal processing micro- processors. Now it is possible to design control systems with extremely accurate gain and phase responses, and ones which are capable of processing data in very short periods of time. Both of these factors are generally accepted as being central to the success of most active noise control applications. Consequently, many papers in the past decade have tended to concentrate on these developments in electronics. Although this rapid progress has been essential, it has revealed in some cases a lack of full physical understanding of the acoustical problem under consideration, and this is felt to be particularly true of the active control of enclosed sound fields (see also Swinbanks [31]).

Despite this emphasis on the development of digital electronic control systems, some papers have been published that have approached the problem at a more fundamental level. Piraux *et al* [32] presented a theoretical method of minimising the total acoustic energy in a volume of space, and this was followed by an experimental verification of the technique [33]. However, the reported experiments were performed in an anechoic chamber. The same theoretical approach, namely that of quadratic optimisation, has also been used by Nelson *et al* [34,35,36] in the study of globally minimising the total acoustic potential energy in harmonically excited enclosed sound fields. These papers discuss diffuse acoustic fields (i.e., well above the Schroeder frequency [37]), for which theoretical results demonstrate that appreciable global reduction can only be obtained using relatively few secondary sources if these sources are placed less than half a wavelength of the operating frequency away from the primary source. Again using quadratic optimization theory, Bullmore *et al* [38] and Elliott *et al* [39] have studied the companion problem of reducing the total acoustic potential energy in a harmonically excited enclosed sound field at frequencies well below the Schroeder frequency, but above the first acoustic mode cut on frequency. In these papers it is demonstrated,

both theoretically and experimentally, that a practical control system can produce global reductions, but that the locations of the sources and microphones are critical to ensure these reductions. It is also demonstrated that, in general, driving the pressure to zero at a single location will not ensure global reductions. The methods by which these reductions are achieved is the topic of further papers by Bullmore *et al* [40] and also Curtis *et al* [41,42]. The latter present a time domain formulation of the problem in a one dimensional sound field. An important conclusion of this work is that, in order to achieve the optimal reduction predicted by the frequency domain formulations of references [34] to [40], the secondary source must act non-causally with respect to the primary source and hence the results of these papers may only be applied to harmonic disturbances. The problem of constrained optimisation for non- periodic disturbances has been addressed more recently by Nelson *et al* [43], who formulate the problem in terms of a Wiener-Hopf integral equation, and the levels of global cancellation which can be obtained are shown to be dependent on the predictability of the primary source output.

1.3 Contents of the Thesis

The work contained within this thesis has been undertaken as a direct consequence of the need to find a lightweight but effective noise control measure for the new generation advanced turbo propeller/ unducted fan powered aircraft that have already been referred to in Section 1.1. The ultimate aim of the work presented is to predict the levels of reduction that can be achieved using active noise control in this type of situation. However, at the initiation of the project it was clear that, although several publications had appeared on actively controlling enclosed sound fields, little had been done to resolve the basic physical mechanisms by which active noise control achieves reductions. Of course it was evident that, in order to produce a pressure null at a single microphone location, the cancelling source(s) must recreate the acoustic pressure produced by the primary source alone at that same point, but 180° out of phase. Not so evident was the use of active noise control to produce global reductions in acoustic energy within the enclosure. Several of the references of

the previous section have observed this possibility, but none of those published before the current work was undertaken offered full explanations as to the acoustic mechanisms involved, nor as to how global reductions are ensured using a practical control system, or even what parameters limit the global reduction of enclosed acoustic fields.

With such fundamental questions as these apparently unanswered it was decided that the problem should be approached at a fundamental level to try and resolve these questions. With the basic mechanisms and limitations understood the practical application of active noise control to propeller induced cabin noise could then be addressed with more confidence. Consequently, this thesis is split into two parts.

Part 1 contains Chapters 2 to 4, and covers the more fundamental work aimed at developing a physical understanding of the active control of harmonic enclosed sound fields. In Chapter 2 the active control problem is formulated in terms of quadratic optimisation theory, as previously derived in references [32-36]. The limitations of the frequency domain optimisation are discussed and the application of all the results obtained to harmonic signals only is stressed. Morse's [44] theoretical description of the sound field in a "two-dimensional", hard walled, rectangular enclosed sound field is then presented, and a computer model of this is described. The effects of applying active noise control to this enclosed sound field are then investigated using computer simulations. The investigation is limited to frequencies at which only a few acoustic modes contribute significantly to the internal acoustic response. First, the problem of minimising the average level of pressure fluctuations throughout the enclosure is studied, and the importance of secondary source locations is demonstrated. The practical limitations of this method are then discussed, and a practical alternative, which involves minimising the sum of the squared pressures at a number of microphone locations, is suggested. Computer simulations of this practical method reveal the critical placement of the microphones if global reductions are to be achieved. Chapter 3 presents experimental verification of all the important theoretical findings of Chapter 2. The main results of these two chapters have previously been published in references [38,39]. In Chapter 4, the theoretical model of the hard-walled enclosure described

in Chapter 2 is extended, using theory due to Morse and Bolt [45], to include the effects of damping materials over the enclosure walls. There is some discussion about the inherent limitations of the original model to produce meaningful results concerning the energetics of active control systems, and the modified theory is then used to investigate the mechanism by which global reductions are achieved [40].

Part 2 of the thesis contains Chapters 5 to 7 and concerns the specific application of active noise control to reduce propeller induced cabin noise. The aim of the work presented in Part 2 is to predict the levels of reduction which can be achieved in a medium size (approx. 50 seat) civil aircraft, and also to specify a suitable active control system configuration (i.e., how many sources/sensors are required, and where they should be placed to ensure appreciable reductions). In order to predict this it is necessary to have a theoretical model of the sound field to be controlled. Chapter 5 discusses the results of acoustic tests performed on a B.Ae. 748 48 seat, twin turboprop production standard aircraft [46]. These static tests were designed to evaluate the modal structure of the sound field at frequencies up to 200 Hz, and also to determine typical values of the acoustic damping. Results are obtained mainly from acoustic transfer impedance measurements between a loudspeaker and microphone both placed within the cabin, although some additional tests are reported using a calibrated sound power source to determine the acoustic damping. Using the results from these tests, the accuracy is assessed of modelling the sound field inside this type of aircraft as the sound field inside a cylindrical room (as done for example in references [47,48,49]). In Chapter 6 the form of primary source excitation of the cabin space is considered. In particular it is determined whether the propeller pressure field forcing of the cabin walls results in a "localised" primary source region, or whether it creates a "distributed" primary source. The experimental data used for this section are obtained from a series of in flight measurements performed by British Aerospace on the test aircraft. A simple theoretical structural model of the fuselage wall vibration is then introduced. This takes the form of a thin, isotropic cylindrical shell of finite length excited by an external pressure field which is representative of that which has been measured on the full size

aircraft. This structural model is then interfaced with the cylindrical room acoustics model. However, due to the highly selective excitation of the acoustic modes [9] by the structural modes, the results of the model are not considered representative of what occurs in practice and the model is modified in order to decrease this selective acoustic mode excitation. The structural and acoustic responses obtained using the modified model are compared favourably with those measured in practice and the model is therefore chosen to assess the effectiveness of applying active noise control. In Chapter 7 results are presented for the first two blade passage frequency harmonics and it is shown that, whilst at the fundamental blade passage frequency global reductions may be possible, at the second harmonic frequencly only local reductions can be expected. Results are presented for each of the harmonics for a range of different source/ sensor combinations and different control strategies are suggested for the two operating frequencies considered.

Finally, Chapter 8 contains some concluding remarks about the use of active noise control for the reduction of sound levels in harmonic, enclosed sound fields. Some suggestions for further research are also included.

PART I

CHAPTER 2

THE ACTIVE CONTROL OF HARMONIC ENCLOSED SOUND FIELDS OF LOW MODAL DENSITY - THEORY AND COMPUTER SIMULATIONS

2.1 Introduction

In many of the publications referred to in the previous chapter it has undoubtedly been shown that it is possible to "null" the pressure at a single microphone location using a single secondary control source. In fact, Olson and May [11] successfully demonstrated this in 1953 with their "electronic sound absorber". This philosophy has since been used to excellent effect in actively controlled headsets designed both for military aircraft pilots [16] and operators of reciprocating machinery [24]. Unfortunately, however, this may not always be a feasible strategy as in many potential applications it may be undesirable to impose any such restrictions on the user. The work in this thesis has been directed towards the active control of passenger aircraft internal noise, which is a particular situation in which the compulsory wearing of headsets may not be acceptable. In such situations the possibility of reducing the pressure fluctuations globally, i.e., throughout the entire cabin space, is a very attractive proposition. If global reductions could be achieved then no constraints need be imposed on the passengers, either in terms of the compulsory headgear or in terms of their movements around the cabin.

With this ultimate goal in mind the work in Part 1 of this thesis sets out to answer the two fundamental questions which should be resolved before the global control of aircraft cabin noise is attempted, namely: are global reductions possible? and secondly: how are these reductions effected?

In order to try and answer these questions, the problem has initially been approached at a fundamental level. Consequently, Part 1 of the thesis describes theoretical and experimental results obtained using theoretical and physical models of the acoustics in a hard walled, shallow rectangular enclosure. By simplifying the problem in this way a better understanding of the physics of the general problem can be

obtained, whilst not trivialising it to such a degree that the findings will not be applicable to more practical situations.

In this chapter the problem is addressed of applying quadratic optimisation theory to the specific case of minimising the pressure fluctuations in a shallow, lightly damped, rectangular enclosure which is excited acoustically by discrete sources operating at a single frequency such that the acoustic modal density within the enclosure is kept low.

2.2 The Sound Field in a Hard Walled, Rectangular Enclosure

The complex acoustic pressure at a frequency ω at a location specified by the vector $\underline{x}$ within an enclosed volume must satisfy the inhomogeneous scalar Helmholtz equation given by

$$(\nabla^2 + k^2)p(\underline{x},\omega) = -j\omega\rho q(\underline{x}_o,\omega) \qquad (2.1)$$

where $q(\underline{x}_o,\omega)$ is the source strength distribution within the enclosure and k is the acoustic wavenumber ω/c where c is the sound speed in and ρ is the density of the enclosed medium.. The solution to this equation can be written as [50]

$$p(\underline{x},\omega) = \int_S \left[p(\underline{x}_S) \frac{\partial G(\underline{x}|\underline{x}_S,\omega)}{\partial n} + j\omega\rho v(\underline{x}_S,\omega)G(\underline{x}|\underline{x}_S,\omega)\right]dS$$

$$+ j\omega\rho \int_V q(\underline{x}_o,\omega)G(\underline{x}|\underline{x}_o,\omega)dV \qquad (2.2)$$

where $\underline{x}_S$ denotes specifically a location on the bounding surface, $\underline{x}_o$ a location in the enclosed volume, V is the volume of the enclosed space, S the surface area of the surrounding enclosure, $v(\underline{x}_S,\omega)$ is the normal velocity distribution over the bounding surface directed in to the contained fluid, $G(\underline{x}|\underline{x}_o,\omega)$ is the Green function appropriate to the enclosed space under consideration and $\partial G(\underline{x}|\underline{x}_S,\omega)/\partial n$ is the derivative of the Green function with respect to the outward going normal at the bounding surface.. The appropriate Green function is determined as a

solution to the inhomogeneous scalar Helmholtz equation which for a point source at $\underline{x}_o$ is given by

$$(\nabla^2 + k^2)G(\underline{x}|\underline{x}_o,\omega) = -\delta(\underline{x} - \underline{x}_o) \qquad (2.3)$$

where $\delta(\underline{x} - \underline{x}_o)$ is the three dimensional Dirac delta function which has the property $\int f(\underline{x})\delta(\underline{x} - \underline{x}_o) = f(\underline{x}_o)$. If it is now assumed that the Green function can be expanded as an infinite sum of normal, rigid walled modes, or

$$G(\underline{x}|\underline{x}_o,\omega) = \sum_{n=0}^{\infty} b_n(\underline{x}_o,\omega)\psi_n(\underline{x}) \qquad (2.4)$$

such that the eigenfunctions satisfy

$$(\nabla^2 + k_n^2)\psi_n(\underline{x}) = 0 \qquad (2.5)$$

where $k_n = \omega_n/c$, then equation (2.3) may be rewritten as

$$-\sum_n k_n^2 b_n(\underline{x}_o,\omega)\psi_n(\underline{x}) + k^2 \sum_n b_n(\underline{x}_o,\omega)\psi_n(\underline{x}) = -\delta(\underline{x} - \underline{x}_o) \qquad (2.6)$$

Now multiplying both sides of equation (2.6) by $\psi_{n'}(\underline{x})$, and integrating over the enclosed volume, yields

$$b_n(\underline{x}_o,\omega) = \frac{\psi_n(\underline{x}_o)}{V(k_n^2 - k^2)} \qquad (2.7)$$

where the orthogonal properties of the eigenfunctions have been invoked [55] and where the eigenfunctions have been normalized according to

$$\int_V \psi_{n'}(\underline{x})\psi_n(\underline{x})\, dV = V \qquad n' = n \qquad (2.8)$$

$$= 0 \qquad n' \neq n$$

Therefore, the Green function may be written as

$$G(\underline{x}|\underline{x}_o,\omega) = \sum_n \frac{\psi_n(\underline{x})\psi_n(\underline{x}_o)}{V(k_n^2 - k^2)} \qquad (2.9)$$

Until now this analysis has assumed nothing about the physical shape of the enclosed volume. If it is stipulated that the enclosure is of rectangular form, having sides L_1, L_2, L_3, then specific expressions for the eigenfunctions and eigenvalues may be developed. Expanding equation (2.5) in rectangular Cartesian coordinates yields

$$\left(\frac{\partial^2}{\partial x_1^2} + \frac{\partial^2}{\partial x_2^2} + \frac{\partial^2}{\partial x_3^2}\right)\psi_n(\underline{x}) + k_n^2\psi_n(\underline{x}) = 0 \qquad (2.10)$$

Separating the variables in equation (2.10) and assuming hard wall boundary conditions for all the boundaries (i.e., $\partial p(\underline{x}_s,\omega)/\partial n = 0$ for all $\underline{x}_s$, where $\underline{x}_s$ denotes a point on the bounding surface) allows the eigenfunctions and eigenvalues to be written as [44]

$$\psi_{n_1n_2n_3}(x_1,x_2,x_3) = \sqrt{\epsilon_{n_1}\epsilon_{n_2}\epsilon_{n_3}}\cos\left(\frac{n_1\pi x_1}{L_1}\right)\cos\left(\frac{n_2\pi x_2}{L_2}\right)\cos\left(\frac{n_3\pi x_3}{L_3}\right) \qquad (2.11)$$

$$k_{n_1n_2n_3} = \sqrt{\left(\frac{n_1\pi}{L_1}\right)^2 + \left(\frac{n_2\pi}{L_2}\right)^2 + \left(\frac{n_3\pi}{L_3}\right)^2} \qquad (2.12)$$

where $\epsilon_{n_1} = 1$ if $n_1 = 0$ and $\epsilon_{n_1} = 2$ if $n_1 > 0$, (similarly for ϵ_{n_2} and ϵ_{n_3}) and where n_1, n_2, n_3 are modal integers specifying the nature of each individual mode (for brevity the single letter "n" will in future generally be used to denote a set of acoustic modal integers such as these). Note that the eigenfunctions have been normalized according to equation (2.8).

The pressure due to any surface or volume distribution of source strength can now be evaluated by substituting the Green function into equation (2.2) and performing the relevant surface and volume integrals. For the situation being considered in this work this procedure can be simplified, leading to the removal of two out of the three integrals.

Firstly, perfectly rigid walls are assumed and consequently the normal derivative of the Green function at the enclosure surfaces is zero, or

$$\frac{\partial G(\underline{x}|\underline{x}_s,\omega)}{\partial n} = 0 \qquad (2.13)$$

and the first surface integral in equation (2.2) is therefore zero. Secondly, if it is assumed that the enclosed space is excited only by some normal surface velocity distribution over the enclosure walls, then the volume integral of equation (2.2) also reduces to zero. Therefore, the pressure at a point $\underline{x}$ due to the normal surface velocity distribution denoted by $v(\underline{x}_s,\omega)$ may be written as

$$p(\underline{x},\omega) = \sum_{n=0}^{\infty} \int_S \frac{j\omega\rho v(\underline{x}_s,\omega)\psi_n(\underline{x})\psi_n(\underline{x}_s)}{V(k_n^2 - k^2)}\, ds \qquad (2.14)$$

where $\psi_n(\underline{x})$, $\psi_n(\underline{x}_s)$ and k_n are as defined in equations (2.11) and (2.12).

From equation (2.14) it is clear that whenever $k_n = k$ (i.e., a modal natural frequency, ω_n, exactly matches the driving frequency, ω) then an infinite pressure response will occur. In any physical situation this can never happen as the acoustic waves must lose energy as they propagate through the enclosed medium and as they strike the enclosure walls. In order to introduce energy loss into equation (2.14) a complex eigenvalue shall be defined as

$$k_n = \frac{\omega_n + j\xi_n\omega_n}{c} \qquad (2.15)$$

which on substitution into equation (2.14) yields, after some rearranging, and on assuming $\xi_n << 1$

$$p(\underline{x},\omega) = \frac{\omega\rho c^2}{V} \sum_{n=0}^{\infty} \frac{\psi_n(\underline{x}) \int_S v(\underline{x}_s,\omega)\psi_n(\underline{x}_s)ds}{2\xi_n\omega_n^2 - j(\omega_n^2 - \omega^2)} \qquad (2.16)$$

where ξ_n is called the modal damping ratio, and it is related to the quality factor Q_n of the resonance by the relationship [44]

$$\xi_n = (2Q_n)^{-1} \tag{2.17}$$

The accuracy of equation (2.16) and some of the assumptions involved in its derivation will be the subject of some discussion in Chapter 4. For the present, however, it shall be assumed that this expression adequately describes the sound pressure field in a relatively hard walled ($\xi_n \leq 0.1$) rectangular enclosure such that results obtained using it may be compared favourably with experimental measurements obtained using a correspondingly hard walled, rectangular enclosure.

2.3 The Theory of Quadratic Optimisation

The main thrust of the work presented in Part 1 of this thesis is to evaluate the physical limits to the performance of active noise control systems when applied to the control of harmonic, enclosed sound fields of low modal density. In order to theoretically evaluate these limits it is necessary to be able to model the effects of active noise control on the acoustic system under consideration. A suitable method with which to achieve this is quadratic optimisation theory. Although this has been previously covered by several authors in some detail (see, for example, Nelson *et al* [34], Piraux and Nayroles [32], Gaudefroy [51] and Roebuck [52]) the main features of this type of analysis will be presented here as it forms the theoretical basis of all the active noise control predictions presented within the chapters of this thesis.

Consider, as an illustrative example, the application of quadratic optimisation theory to the problem of minimising the volume averaged pressure fluctuations throughout an enclosed sound field by the introduction and control of secondary (control) sound sources.

A suitable quantity which is representative of the volume averaged pressure fluctuations is the total time averaged acoustic potential energy of the enclosed sound field, given by [35]

$$E_p = \frac{1}{4\rho c^2} \int_V |p(\underline{x},\omega)|^2 dV \qquad (2.18)$$

where V is the total enclosed volume and where $p(\underline{x},\omega)$, ρ and c are as defined in the previous section. Thus, by minimising E_p the average pressure amplitude will also be minimised. The choice of the potential energy rather than kinetic energy is an obvious one, as it is sound pressure which is usually measured. However, the choice also proves to be advantageous at low frequencies, when the total energy in the sound field is dominated by potential energy, and consequently larger reductions in the amplitude of pressure fluctuation are achieved by minimising E_p in this low frequency limit [41]. Following the procedure already outlined the pressure can be approximated as a sum of normal modes, or

$$p(\underline{x},\omega) = \sum_{n=0}^{N} \psi_n(\underline{x}) a_n(\omega) \qquad (2.19)$$

where each of the N modes is characterised by a normalised characteristic function, $\psi_n(\underline{x})$, and a complex mode amplitude, $a_n(\omega)$. For the particular case of the sound field in a hard-walled rectangular enclosure excited by some normal velocity distribution of the bounding surfaces the $\psi_n(\underline{x})$ are given by equation (2.11) and the $a_n(\omega)$ are obtained from equation (2.16) as

$$a_n(\omega) = \frac{\omega\rho c^2}{V} \int_S \frac{v(\underline{x}_s,\omega)\psi_n(\underline{x}_s)ds}{2\zeta_n\omega_n^2 - j(\omega_n^2 - \omega^2)} \qquad (2.20)$$

Substituting equation (2.19) into equation (2.18) yields

$$E_p = \frac{1}{4\rho c^2} \int_V \sum_{n=0}^{N} (a_n(\underline{\omega})\psi_n(\underline{x}))^* \sum_{n'=0}^{N} (a_{n'}(\omega)\psi_{n'}(\underline{x}))dV \qquad (2.21)$$

which on performing the volume integral and invoking the property of the normalised orthogonal modes given in equation (2.8) results in the expression

$$E_p = \frac{V}{4\rho c^2} \sum_{n=0}^{N} a_n^*(\omega) a_n(\omega) = \frac{V}{4\rho c^2} \sum_{n=0}^{N} |a_n(\omega)|^2 \qquad (2.22)$$

The superscript * is used here to denote complex conjugation.

The desired action of the active noise control system is to minimise E_p by the introduction and control of some distribution of secondary source of sound. It is thus necessary to modify the expression for $a_n(\omega)$ (equation (2.20)) to distinguish between the mode excitation due to the primary velocity distribution, $v_p(\underline{x}_s,\omega)$, and that due to the secondary source velocity distribution, $v_s(\underline{x}_s,\omega)$. In any practical situation the secondary source velocity distribution is likely to consist of a number, M, of discrete loudspeaker type sources. Consequently it is convenient to rewrite the expression for the mode amplitude as

$$a_n(\omega) = a_{np}(\omega) + \sum_{m=1}^{M} B_{nm}(\omega) q_{sm}(\omega) \qquad (2.23)$$

In equation (2.23) the first term, $a_{np}(\omega)$, represents the n'th mode's amplitude due to the primary source velocity distribution only, or

$$a_{np}(\omega) = \frac{\rho c^2}{V} A_n(\omega) \int_{S_p} v_p(\underline{x}_s,\omega) \psi_n(\underline{x}_s) dS_p \qquad (2.24)$$

where $A_n(\omega)$ defines the complex mode resonance term given by

$$A_n(\omega) = \frac{\omega}{2\xi_n\omega_n^2 - j(\omega_n^2 - \omega^2)} \qquad (2.25)$$

and where S_p is the surface area of the primary source distribution. The second term of equation (2.23) represents the n'th mode's amplitude due to the M secondary sources, each having a strength $q_{sm}(\omega)$ m^3/s. If

it is assumed that the secondary sources are all placed adjacent to the enclosure walls then $B_{nm}(\omega)$, the coupling coefficient between the m'th secondary source and the n'th mode, can be obtained from equation (2.20) as

$$B_{nm}(\omega) = \frac{\rho c^2}{V} A_n(\omega) \frac{\int_{S_m} v_{sm}(\underline{x}_s,\omega)\psi_n(\underline{x}_s)dS_m}{\int_{S_m} v_{sm}(\underline{x}_s,\omega)dS_m} \qquad (2.26)$$

and the m'th secondary source strength can similary be written as

$$q_{sm}(\omega) = \int_{S_m} v_{sm}(\underline{x}_s,\omega)dS_m \qquad (2.27)$$

where S_m is the surface area of the m'th secondary source and $v_{sm}(\underline{x}_s,\omega)$ is the normal velocity distribution over the surface of this source.

Substituting equation (2.23) into equation (2.22) yields

$$E_p = \frac{V}{4\rho c^2} \sum_{n=0}^{N} (a_{np}(\omega) + \sum_{m=1}^{M} B_{nm}(\omega)q_{sm}(\omega))^*(a_{np}(\omega) + \sum_{m=1}^{M} B_{nm}(\omega)q_{sm}(\omega))$$

which may be written more conveniently in matrix form as

$$E_p = \frac{V}{4\rho c^2} (\underline{a}_p + \underline{B}\underline{q}_s)^H(\underline{a}_p + \underline{B}\underline{q}_s) \qquad (2.29)$$

Here $\underline{a}_p$ is the vector of mode amplitudes due to the primary source only and its N elements are given by $a_{np}(\omega)$, $\underline{q}_s$ is the M'th order vector whose elements specify each of the secondary source strengths, $q_{sm}(\omega)$, and the matrix $\underline{B}$ is of order N × M and its elements are the complex modal excitation coefficients, $B_{nm}(\omega)$. The superscript "H" is used to denote the transpose of the complex conjugate of either a complex vector or a complex matrix [53]. Expanding equation (2.29) yields

$$E_p = \frac{V}{4\rho c^2} [\underline{q}_s^H \underline{B}^H \underline{B} \underline{q}_s + \underline{q}_s^H \underline{B}^H \underline{a}_p + \underline{a}_p^H \underline{B} \underline{q}_s + \underline{a}_p^H \underline{a}_p] \qquad (2.30)$$

which, following the procedure adopted in reference [35], can be written in Hermitian quadratic form to give

$$E_p = \underline{q}_s^H \underline{A} \underline{q}_s + \underline{q}_s^H \underline{b} + \underline{b}^H \underline{q}_s + c \qquad (2.31)$$

where the M × M matrix $\underline{A}$ equals $(V/4\rho c^2)\underline{B}^H\underline{B}$, the M'th order vector $\underline{b}$ equals $(V/4\rho c^2)\underline{B}^H\underline{a}_p$ and the scalar constant c equals $(V/4\rho c^2)\underline{a}_p^H\underline{a}_p$, which is the value of E_p due to the primary source operating alone.

Thus equation (2.31) is a real quadratic function relating the total time averaged acoustic potential energy within the enclosure, E_p, to the potentially complex secondary source strengths, $q_{sm}(\omega)$. A full discussion of the properties of this equation will not be given here as they are presented in considerable detail in references [34,35,36]. However, the very important property will be emphasised that, providing the matrix $\underline{A}$ is positive definite [53], then the cost function, E_p, has a unique minimum value specified by a particular value of the vector $\underline{q}_s$. This is most easily visualized by plotting the cost function, E_p, as a function of the real and imaginary source strengths of a single secondary source [35]. If this is done, then a bowl shaped surface results which clearly demonstrates the existence of a unique global minimum, as shown in Figure 2.1. This example is a simple case where there are only two variables. However, the same argument can be extended to any number of secondary sources, and although the simple visualisation aid of a bowl shaped surface in two dimensions may be lost, an equivalent surface will still exist in 2M-dimensional space, where M is the number of secondary sources. Consequently, a unique global minimum will still be specified by a similarly unique combination of the 2M variables. Therefore, by differentiating equation (2.31) with respect to the real and imaginary parts of the secondary source strengths, and setting the resulting equations to zero, the vector of secondary source strengths necessary to minimise E_p can be shown to be [35]

$$\underline{q}_{so} = -\underline{A}^{-1}\underline{b} \qquad (2.32)$$

which, in terms of the matrix $\underline{B}$ and vector $\underline{a}_p$ is equivalent to

$$\underline{q}_{so} = -[\underline{B}^H\underline{B}]^{-1}\underline{B}^H\underline{a}_p \qquad (2.33)$$

Equation (2.33) thus represents an unequivocal definition of the secondary source strengths required to minimise the volume averaged pressure fluctuation throughout the enclosed sound field. The power of this type of analysis can now be fully appreciated, because it is seen to enable the prediction of the "best possible" reductions which can be achieved by an active control system in any specified configuration. Substituting this expression for the vector of optimal secondary source strengths into equation (2.30) enables the minimum value of E_p (denoted by E_{po}) to be calculated as

$$E_{po} = \frac{V}{4\rho c^2}\,[\underline{a}_p^H\underline{a}_p - \underline{a}_p^H\underline{B}\underline{q}_{so}] \qquad (2.34)$$

Notice that whilst these expressions have been derived with reference to the sound field in a lightly damped, rectangular enclosure they are equally applicable to any shaped enclosure, provided that the elements of $\underline{a}_p$ and $\underline{B}$ can be evaluated. Furthermore, these predictions are not limited to the minimization of the total acoustic potential energy, as outlined above. Any "cost function" associated with the acoustic field may be chosen to be minimized provided only that a quadratic relationship exists between the chosen function and the chosen control variables. Other acoustic functions which may be minimised by the control of the secondary source strengths might be the total acoustic power output of all the sources, the total power absorption of all the secondary sources, the pressure at a point in the enclosure, or the sum of the squared pressures at a number of locations throughout the enclosure. The use of these cost functions will be investigated in subsequent sections.

Before leaving this section to apply the theory to more specific examples, it is worth stressing the possible dangers associated with this frequency domain approach to optimisation. In choosing frequency domain optimization no temporal constraints have been placed on the secondary source outputs. Thus it is possible that, in order to achieve the predicted optimal reductions, the secondary sources will have to act

non-causally with respect to the primary source output. This feature has been addressed by Curtis *et al* [41] and Elliott *et al* [54]. The problem does not affect any of the results of this thesis as the current work deals exclusively with periodic noise (and provided the primary signal is periodic, the output of the primary source can always be predicted). However, where non periodic signals are to be cancelled, the problem is not so straightforward and the results contained in this thesis cannot be applied directly to these situations.

2.4 The Application of Active Noise Control to Harmonic, Enclosed Sound Fields of Low Modal Density - Results of Computer Simulations

2.4.1 Introduction

Nelson *et al* [35] have shown that in the high frequency limit, when the acoustic response of a room can be described by statistical methods, appreciable global reductions in the level of sound pressure fluctuations are only possible if the secondary sources are placed within one half wavelength of the primary source excitation. Thus it would only be viable to try and apply active noise control in such a case if (a) the primary source was very localized or (b) a secondary source could be superposed spatially on the primary source, and driven such that the velocity distribution over its surface was equal in magnitude but 180° out of phase with the primary velocity distribution.

In this section the problem of applying active noise control to enclosed sound fields at frequencies well below the statistical region is to be studied. Using the theoretical basis of Sections 2.2 and 2.3, a computer model is developed to assess the effectiveness of active techniques for globally suppressing the sound field in a lightly damped, rectangular enclosure, driven at frequencies such that close to acoustic resonances of the enclosure only relatively few modes can be considered to dominate the acoustic response. It is demonstrated that, in theory, useful global reductions in sound pressure are possible, even when the secondary sources are placed greater than one half wavelength from the primary source (cf. the high frequency case [35]). The practical limitations of this theoretical method are discussed, and an alternative

implementation is suggested which involves minimising the sum of the squared pressures at a number of discrete sensor locations. Computer simulations of the latter system are performed and it is shown that near optimal reductions in global sound pressure fluctuations are possible for any given source configuration, but that the sensor locations critically affect the results.

2.4.2 The modelled enclosed sound field

The theoretical model which has been chosen for this section is that of the rectangular enclosure shown in Figure 2.2. The enclosure dimensions are 2.264 m × 1.132 m × 0.186 m. These have been chosen to coincide with the dimensions of an enclosure used in some preliminary experimental work undertaken by Lewers [56]. Thus, at low enough frequencies the sound field will be dominated by axial and tangential modes of the two larger dimensions, the pressure distribution being essentially uniform across the shorter dimension of the enclosure, giving rise to a mode structure which is relatively easy to visualize whilst not over-simplifying the problem.

The sources shown in Figure 2.2 were in practice [56] all circular 165 mm diameter loudspeakers. These have been modelled as 150 mm square pistons in the computer model. The primary source, also modelled as a 150 mm square piston, has been placed close to one corner of the enclosure to prevent it from selectively exciting the low order modes. A modal damping ratio of 0.01 has been assumed for all the modes included in the computer model (again to correspond roughly to the values deduced by Lewers [56]).

2.4.3 Convergence of the modal summation

In order for the modal representation of the sound pressure field (eqn. (2.16) to yield exact results it is necessary to include an infinite number of modes in the summation. Clearly this is impractical and, as in this work frequencies at which only one or two modes are dominantly excited are to be considered, it is also highly unnecessary. However, care must be exercised when truncating the modal summation as in certain situations, in particular in the near field of sources, the "residual" modes may combine constructively to produce a response of comparable magnitude to the "dominant" mode responses [55]. (For example, the near field of a point source requires the use of an infinite number of modes as on the source surface the pressure does not converge.) Therefore, use of equation (2.16) requires that a compromise be reached between including enough modes to ensure an accurate solution, whilst keeping the number within reasonable bounds to save on computation time. The number of modes that will give this compromise will be very problem dependent, being a function of the enclosure size, operating frequency and acoustic damping, and it is therefore suggested that a test for convergence of the summation should be made for each different problem, with the number of included modes being adjusted accordingly. For most applications it should be sufficient to ensure the convergence of, for example, the volume averaged pressure. However, in this work it will at times be necessary to evaluate the pressure at the surface of the sources, and consequently this is to be used as a much stricter criterion for convergence.

Figure 2.3 shows the convergence of equation (2.16) when the sound pressure level is evaluated on the surface of a source operating at 200 Hz and placed at the primary source location, P, of the enclosure described in Section 2.2 (see Figure 2.2). For comparison results for both a point source and a 0.15 m square piston source are shown. Even after the inclusion of 55,000 modes the pressure on the point source has not converged to a steady value, as one would anticipate in the near field of a point source [55]. In contrast the piston source pressure requires only about 1,700 modes to converge to within 1 dB of its value given by including over 400,000 modes. It should be noted that these graphs have been plotted as functions of the natural

frequency of the highest order mode included in the summation, and not as a function of the number of modes. The relationship between these latter two quantities is shown in Figure 2.4.

Figure 2.5 shows the dependence of the convergence of equation (2.16) on frequency when using the piston source as described above. The summation at the three frequencies lying midway between resonant frquencies, 112.5 Hz, 190.5 Hz and 439 Hz, all converge at different rates, this rate of convergence decreasing with increasing frequency. The value of the pressure on the source at the resonant frquency, 336.8 Hz, converges much more rapidly, despite being of a higher frequency than two of the non-resonant frequencies.

From these results it was thus concluded that, using the piston sources, if 7000 modes were included in the summation, then the computed sound pressure levels would be accurate to within 1 dB at all frequencies up to 300 Hz, even in the extreme near fields of the sources.

Having established this criterion, the frequency response of the enclosure from 50 Hz to 300 Hz has been evaluated as the input impedance of the primary source (i.e., the ratio of the pressure at the centre of the primary source to the normal velocity of that source, which is assumed to be constant). This frequency response function is shown on Figure 2.6, together with the natural frequencies of each of the resonances and their associated modal integers (n_1,n_2,n_3). It is seen that in this frequency range only seven resonances occur, and by virtue of the low damping these are easily discernible as separate resonant peaks (with the exception of the two degenerate resonances at 150.6 Hz). Thus, at most frequencies over this range, the requirement that only one or two modes contribute significantly to the acoustic response is satisfied.

2.4.4 Minimising the total time averaged acoustic potential energy, E_p

The total time averaged acoustic potential energy, E_p, has already been introduced in Section 2.3 as a convenient single quantity which is

representative of the volume averaged pressure fluctuations throughout an enclosed sound field. For any given source arrangement and enclosure size the optimal secondary source strengths which minimise E_p can be evaluated from equation (2.33) and the resulting minimum value of E_p from equation (2.34).

It is clear from the form of these equations and from the knowledge of the constituent elements of the matrix $\underline{B}$ and vector $\underline{a}_p$, that the reductions in E_p which can be achieved will be functions of the number of secondary sources used, the location of these sources, the operating frequency (with respect to the size of the enclosure) and also the acoustic damping present. However, the form of these relationships is not so evident. In order to clarify this relationship the results of some computer simulations involving the rectangular enclosure described previously, and shown schematically in Figure 2.2, will now be presented.

The results of this section aim to demonstrate the effect that the secondary source locations have on the minimisation of E_p within this frequency region. For each of the secondary source configurations considered E_p has been minimised at each 1 Hz interval between 50 Hz and 300 Hz, where the source strengths necessary to minimise E_p have been calculated using equation (2.33). The results are presented as plots of E_{po} against frequency, where E_{po} is the minimum possible value of E_p for the given source arrangement, as defined in equation (2.34).

2.4.4.1 Minimising E_p using source S1 only

Figure 2.7 shows the effect of introducing the secondary source S1 and minimising E_p by adjusting the gain and phase of S1 only. It would perhaps be expected from the analysis of reference [35], that over the entire frequency range from 50 Hz to 300 Hz large reductions in E_p should result, as the primary and secondary sources are never separated by a distance greater than half a wavelength of the driving frequency. However, at an operating frequency of around 300Hz, when the centre to centre source separation is still less than half a wavelength, the reduction in E_p is less than 1 dB. Clearly this low modal density situation differs substantially from the high modal density case

discussed in reference [35], and the criteria governing the levels of reduction which can be achieved are also different.

2.4.4.2 Minimising E_p using source S2 only

If source S2 is now introduced into the enclosure in the position shown in Figure 2.2, and E_p is minimised by adjusting the source strength of S2 only, the result is as shown on Figure 2.8. It is clear from this graph that the introduction of just a single secondary source results in substantial reductions in E_p at a number of the acoustic resonances despite the separation of the primary and secondary sources being greater than half a wavelength for two of the resonances involved. However, of the six separate resonances considered, only half of them are successfully attenuated, with E_p at the resonances of 150.6Hz, 225.9Hz and 271.5Hz being uncontrollable by the source introduced at the position S2. The reason for this becomes apparent if the source's position relative to the nodal planes of these resonances is considered (see Figure 2.9). For each of these three frequencies, the sound field is such that source S2 lies on, or close to, a nodal plane of the dominant mode at that frequency.

If the source is centred on a nodal plane of the dominant mode then it will be unable to excite this mode, and hence will not be able to set up the necessary sound field to destructively interfere with the sound field dominated by this modal contribution. If the source lies close to a nodal plane of the dominant mode, then whilst it would be possible to generate the necessary sound field to destructively interfere with this mode, the large volume velocity required would lead to an increased excitation of any residual modes having pressure antinodes near the source location, and consequently E_p would not necessarily be reduced by minimizing the contribution of the resonant mode.

2.4.4.3 Minimising E_p using source S3 only

If source S3 is now introduced, and E_p minimised by adjusting the source strength of S3 only, then only two of the resonances are attenuated (see Figure 2.10), as S3 lies on nodal planes of all the modes with odd numbered n_z modal integers.

2.4.4.4 Minimising E_p using sources S2 and S3

If now S2 and S3 are both introduced and E_p is minimised by adjusting their source strengths, the results are as shown on Figure 2.11 and all resonances except the 271.5Hz resonance are attenuated. Again, the reason for this is clear if the nodal planes are considered (Figure 2.9). It is interesting to note that the degenerate resonance at 150.6Hz, consisting of the (2,0,0) and (0,1,0) modes, is successfully attenuated when both S2 and S3 are used although neither one of these sources acting alone could appreciably reduce E_p at that frequency. This is because source S2 is positioned such that the two modal contributions are out of phase at that location and thus generation of the necessary source strength to cancel either mode would result in an increased excitation of the other mode. Source S3 is placed at a node of the (0,1,0) mode, yet an antinode of the (2,0,0) mode. Consequently S2 can be given the correct source strength to cancel the (2,0,0) mode whilst not affecting the (0,1,0) mode. With the effect of this (2,0,0) mode removed, S1 can be set up in phase opposition with the (0,1,0) mode and the sound field will be reduced. The resulting increased excitation of the (2,0,0) mode will be counteracted by an increase in strength of source S3, the final result being that source S2 will be of approximately equal magnitude and phase as the primary, and source S3 will be of approximately twice the magnitude of the primary and 180° out of phase with it.

2.4.4.5 Minimising E_p using source S4 only

The argument presented above does not necessarily imply, however, that this pair of resonances requires two sources to cancel them. Figure 2.12 shows the effect of minimising E_p using the single secondary source S4, and its position is such that all resonances up to 300Hz are successfully attenuated including the two 150.6 Hz resonances.

2.4.4.6 Minimising E_p using sources S2, S3 and S4

If the three secondary sources S2, S3 and S4 are now introduced simultaneously, the reductions in E_p shown in Figure 2.13 result. For this case the sources can drive several modes in antiphase with the primary field at most frequencies and consequently not only are all the

resonances successfully attenuated, but some of the lower non-resonant frequencies are also attenuated by approximately 5dB.

2.4.4.7 A summary of the effect of secondary source locations when minimising E_p

The results of Figures 2.7 to 2.13 have demonstrated the importance of source locations on the ability to successfully reduce E_p. Provided a secondary source is placed at a maxima of each of the major contributing mode shapes, then the effects of these modal contributions can each be substantially reduced without exciting the residual modes to any significant level. Also a single secondary source can reduce the contributions of more than one mode provided the primary modal contributions at the source location have the same relative phase and roughly equal amplitudes.

The general conclusion which results from these observations is that the determination of the optimal strength of a given secondary source (which minimises E_p) gives the source strengths which result in the best reduction in the response of the dominant mode at a given frequency whilst giving the least excitation of the remaining "residual" modes. This is demonstrated in Figure 2.14 which shows E_p due to the primary source, but with the contribution of the most dominant mode at each frequency removed (in the frequency range near the degenerate 150.6Hz resonance both the (2,0,0) and (0,1,0) modes have been subtracted). Also shown is the minimum value of Ep obtained when E_p has minimised using source S4. The 3 to 4dB discrepancy between the two curves demonstrates that whilst source S4 successfully attenuates the contribution of the dominant mode at each frequency, it also excites the residual modes and thus lessens the overall reduction in E_p.

As a final example of this observation the sound pressure field at the 150.6Hz resonance has been calculated both before and after E_p has been minimised using secondary source S4. The resulting pressure distributions in the x_1, x_2 plane of the enclosure are shown on Figures 2.15a and 2.15b respectively. Comparison of Figures 2.15a and 2.15b reveals that minimising E_p has removed the dominant (2,0,0)

(0,1,0) mode structure to leave the effect of the nearest mode (1,1,0) as the new dominant feature.

This property of active control to suppress dominant modes also leads directly to conclusions regarding the effects of acoustic damping. Increasing the damping will reduce the resonant responses of the modes. It is to be expected, therefore, that the levels of global reduction which can be obtained will also decrease. This is demonstrated in Figure 2.16, where a modal damping ratio of 0.05 has been substituted in the model used above. The individual resonant peaks are no longer so easily discernible, having been "rounded off" by the increased damping. When E_p is minimised using source S4 only, then the results indicated by the dashed line of Figure 2.16 are obtained. Whilst for the first mode a reduction of about 15 dB is achieved, for all modes above this the reduction is limited to only 2 or 3 dB. This is to be compared with the results of Figure 2.12, in which E_p was also minimised using the single secondary source S4, but the modal damping ratio in that case was only 0.01. Notice, however, that the absolute levels of the minimised fields are similar for both cases.

2.4.4.8 Minimising E_p as a practical control strategy

Whilst the analysis of this section has allowed the theoretical determination of the best possible global reduction in the amplitude of the pressure fluctuations which can be achieved for any given source configuration, it is not a viable suggestion as a practical system. The problem with the method is that it assumes a knowledge of the individual mode amplitudes, $a_n(\omega)$, as defined in equation (2.23). In practice this information will only be available if (a) the exact modal structure of the sound field and the velocity distribution of both primary and secondary sources is known, or (b) if the sound pressure field can be measured at enough locations such that it can be decomposed into its spatial Fourier components. In any practical application it is unlikely that the acoustics of the enclosed space will be known exactly, nor is it likely that the exact surface velocity distribution of the primary source will be known, and consequently the first of these two options must be ruled out. The second option, too,

must be ruled out by the complexity of the problem. Were this a one dimensional sound field, then only a line array of microphones would be required, the necessary spacing and number of the microphones being a function of the wavelength of the highest order mode to be detected and controlled. However, it would be necessary to monitor the amplitudes of modes well above the driving frequency, as the increased excitation of "residual" modes could play an important role in determining the overall reductions which could be achieved. Thus, even in the one-dimensional case the number of microphones required may become prohibitively large, and therefore for a three dimensional enclosure the three dimensional microphone array required would become an even more impractical proposition.

This is not to say, however, that the results of the preceding sections do not bear any practical relevance. Having realized the practical shortfalls of this method one must now endeavour to find an alternative, more practically applicable, method. However, it is still intended to produce global reductions in the sound field. Consequently, in any future simulation, it will be possible to assess the effectiveness of these practical methods by comparing the levels of global reductions which are predicted with the reductions which can be obtained by minimising E_p, and thus to ascertain how successful the new system has been in achieving global reductions in E_p. Note that, by the very formulation of the problem, for any given source configuration the reductions in E_p obtained by minimising E_p can <u>never</u> be improved upon.

2.4.5 <u>Minimising the sum of the squared pressures, J_p, at a number of discrete error sensors</u>

2.4.5.1 <u>Theory</u>

It is now necessary to suggest an alternative to minimising E_p. Perhaps the most obvious quantity to minimise is the acoustic pressure as this is readily measured using a microphone placed at the desired point in the sound field. This philosophy has been adopted by several workers, e.g., [20,23,25], but it does not seem very likely that minimising the pressure at a <u>point</u> in a sound field will ensure <u>global</u> reductions. An approach more likely to achieve global reductions is

the simultaneous minimisation of the pressure at a number of microphone locations.

In order for the quadratic optimisation analysis to be valid for the investigation of this proposed system, there must exist a quadratic relationship between the cost function and the secondary source strength. Therefore the cost function to be minimised shall be chosen as the sum of the squared pressures at a number, L, of microphone locations, or

$$J_p = \frac{V}{4\rho c^2 L} \sum_{\ell=1}^{L} |p(\underline{x}_\ell,\omega)|^2 \qquad (2.35)$$

where the coefficient $(V/4\rho c^2)$ has been included for compatibility with the expression for E_p (eqn. (2.18)) and where $p(\underline{x}_\ell,\omega)$ is the complex pressure amplitude at the ℓ'th microphone location, $\underline{x}_\ell$. Note that as the number of microphones locations, L, tends to an infinity of evenly spaced locations, the summation of equation (2.35) tends to an integral, and J_p tends to the value of E_p as specified in equation (2.18).

Now note that in vector notation equation (2.35) can be written as

$$J_p = \frac{V}{4\rho c^2 L} \underline{p}^H \underline{p} \qquad (2.36)$$

where the vector $\underline{p}$ is the L-th order vector whose ℓ-th component is $p(\underline{x}_\ell,\omega)$. Use of equation (2.19) enables this vector to be written as

$$\underline{p} = \underline{\Psi}_L^T \underline{a} \qquad (2.37)$$

where the matrix $\underline{\Psi}_L$ is of order L x N and is the matrix of the N characteristic functions evaluated at the L sensor locations such that the ℓ-th element is $\psi_n(\underline{x}_\ell)$. Substitution of the expression for $\underline{a}$ given by equation (2.23) then shows that

$$\underline{p} = \underline{\Psi}_L^T \left[\underline{a}_p + \underline{B}\, \underline{q}_s\right] \qquad (2.38)$$

Now let $\underline{p}_p = \underline{\Psi}_L^T \underline{a}_p$ be the vector of pressures at the L sensor locations produced by the primary source distribution only. Similarly let $\underline{Z} = \underline{\Psi}_L^T \underline{B}$ define the L x M transfer impedance matrix relating the complex pressure amplitudes at the L sensor locations to the complex strengths of the M secondary sources. Accordingly, one can simply write

$$\underline{p} = \underline{p}_p + \underline{Z}\, \underline{q}_s \qquad (2.39)$$

This shows that if the number of sensor locations L is equal to the number of secondary sources M then the pressure amplitude can be made equal to zero at all L sensors (i.e. $\underline{p}$ is made equal to zero) by choosing $\underline{q}_s$ to be the solution of the equation $\underline{p}_p + \underline{Z}\, \underline{q}_s = 0$ such that

$$\underline{q}_s = -\underline{Z}^{-1} \underline{p}_p \qquad (2.40)$$

provided that the matrix $\underline{Z}$ is non-singular. Although this result is useful in demonstrating that the pressure can be constrained to zero at a number of points in the sound field, this does not necessarily imply that the pressure at other locations will also be reduced. In fact,as will be demonstrated, the reverse may well be true. Under certain conditions, driving the pressure to zero at a number of discrete locations may produce substantial increases in the pressure amplitude at other locations. This can result in an increase of the total time averaged acoustic potential energy in the enclosure. It is thus more likely that a large number of sensors are required to produce a good approximation to E_p.Thus the situation that is more likely to be useful in practice in producing "overall" reductions in sound level is when the number of sensors is larger than the number of secondary sources (i.e. L > M). Thus one again seeks a "least squares" solution and $\underline{q}_s$ is chosen to minimise J_p. Combining equations (2.36) and (2.39) gives

$$J_p = \frac{V}{4\rho c^2 L} \left[\underline{q}_s^H \underline{Z}^H \underline{Z}\, \underline{q}_s + \underline{q}_s^H \underline{Z}^H \underline{p}_p + \underline{p}_p^H \underline{Z}\, \underline{q}_s + \underline{p}_p^H \underline{p}_p\right] \qquad (2.41)$$

This is a quadratic function of the secondary source strengths and is now of the same form as the expression for E_p, equation (2.31). The existence of a unique minimum value of the function can be argued on physical grounds [35]. Note that $(V/4\rho c^2 L)\underline{q}_s^H \underline{Z}^H \underline{Z}\, \underline{q}_s$ is equal to the sum of the squared pressures at the L sensor locations produced by the secondary sources only (in the absence of any primary sound field). This quantity must be greater than zero for all non-zero values of the vector $\underline{q}_s$. This then ensures that the matrix $(V/4\rho c^2 L)\underline{Z}^H \underline{Z}$ (which is equivalent to the matrix $\underline{A}$ in equation (2.31)) is positive definite and that J_p is minimised by a unique value of the vector $\underline{q}_s$. By analogy with the solution given in equation (2.33) the optimal vector of secondary source strengths which minimises J_p can be written as

$$\underline{q}_{s1} = - \left[\underline{Z}^H \underline{Z}\right]^{-1} \underline{Z}^H \underline{p}_p \qquad (2.42)$$

which results in the fractional reduction in J_p being given by

$$\frac{J_{po}}{J_{pp}} = 1 - \frac{\underline{p}_p^H \underline{Z}\left[\underline{Z}^H \underline{Z}\right]^{-1} \underline{Z}^H \underline{p}_p}{\underline{p}_p^H \underline{p}_p} \qquad (2.43)$$

where J_{po} is the optimal value of J_p and the quantity $J_{pp} = (V/4\rho c^2)\underline{p}_p^H \underline{p}_p$ is the value of J_p produced by the primary source only. Thus equation (2.42) provides a technique which can be used to determine a source strength vector in practice and which, if the number of evenly distributed sensors is large enough, should give a value of $\underline{q}_{s1}$ which is a good approximation to the optimal value $\underline{q}_{so}$ which minimises E_p. Note that the evaluation of equation (2.42) involves the determination of the complex primary pressure amplitude at the sensor locations and the matrix of complex transfer impedances between the secondary sources and sensor locations. Both of these quantities can in principle be determined experimentally in any given enclosure without any knowledge of the primary source distribution or the modal structure of the sound field.

2.4.5.2 A theoretical evaluation of the importance of error sensor locations required to ensure global reductions

The question can now be addressed of the optimal locations of sensors in order that $\underline{q}_{S1}$ gives the best possible approximation to $\underline{q}_{SO}$ using a limited number of sensors. Although a complete and rigorous solution to this problem has as yet not been attempted, some extremely useful initial guidelines have been deduced for the case considered here of a lightly damped sound field of low modal density. Firstly note that use of the expression $\underline{p} = \underline{\Psi}_L^T \underline{a}$ in equation (2.36) gives

$$J_p = \frac{V}{4\rho c^2 L} \underline{a}^H \underline{\Psi}_L \underline{\Psi}_L^T \underline{a} \qquad (2.44)$$

and use of the expressions $\underline{Z} = \underline{\Psi}_L^T \underline{B}$ and $\underline{p}_p = \underline{\Psi}_L^T \underline{a}_p$ in equation (2.42) gives

$$\underline{q}_{S1} = - \left[\underline{B}^H \underline{\Psi}_L \underline{\Psi}_L^T \underline{B} \right]^{-1} \underline{B}^H \underline{\Psi}_L \underline{\Psi}_L^T \underline{a}_p \qquad (2.45)$$

Thus if the matrix $(\underline{\Psi}_L \underline{\Psi}_L^T)/L$ is equal to the identity matrix, then J_p will be equal to E_p and $\underline{q}_{S1}$ will equal $\underline{q}_{SO}$ (equation (2.33)). Confirmation that $(\underline{\Psi}_L \underline{\Psi}_L^T)/L$ tends to the identity matrix as the number of evenly spaced sensors tends to infinity is given by consideration of the terms in the matrix. Expansion of the matrix $(\underline{\Psi}_L \underline{\Psi}_L^T)/L$ shows that each term of the N x N matrix is given by the product of a pair of characteristic functions summed over the L sensor locations. Thus

$$\left[\underline{\Psi}_L \underline{\Psi}_L^T\right]/L = (1/L) \times$$

$$\begin{bmatrix} \sum_{\ell=1}^{L} \Psi_1^2[\underline{x}_\ell] & \sum_{\ell=1}^{L} \Psi_1[\underline{x}_\ell]\Psi_2[\underline{x}_\ell] \cdots\cdots\cdots & \sum_{\ell=1}^{L} \Psi_1[\underline{x}_\ell]\Psi_N[\underline{x}_\ell] \\ \sum_{\ell=1}^{L} \Psi_2[\underline{x}_\ell]\Psi_1[\underline{x}_\ell] & \sum_{\ell=1}^{L} \Psi_2^2[\underline{x}_\ell] \cdots\cdots\cdots\cdots & \sum_{\ell=1}^{L} \Psi_2^2[\underline{x}_\ell]\Psi_N[\underline{x}_\ell] \\ \vdots & \vdots & \vdots \\ \sum_{\ell=1}^{L} \Psi_N[\underline{x}_\ell]\Psi_1[\underline{x}_\ell] & \sum_{\ell=1}^{L} \Psi_N[\underline{x}_\ell]\Psi_2[\underline{x}_2] \cdots\cdots\cdots\cdots & \sum_{\ell=1}^{L} \Psi_N^2[\underline{x}_\ell] \end{bmatrix}$$

(2.46)

The orthogonality property of the characteristic functions [55] shows that

$$(1/L) \sum_{\ell=1}^{L} \Psi_n[\underline{x}_\ell]\Psi_{n'}[\underline{x}_\ell] \underset{\lim L\to\infty}{\rightarrow} \frac{1}{V}\int_V \Psi_n(\underline{x}_\ell)\Psi_{n'}(\underline{x}_\ell)dV \rightarrow \begin{cases} 1 \text{ for } n' = n \\ 0 \text{ for } n' \neq n \end{cases}$$

(2.47)

which demonstrates that the matrix tends to the identity matrix as L tends to infinity. The form of the matrix also suggests that a "reasonable approximation" to the identity matrix may be obtained using a limited number of sensors such that the diagonal terms approach unity and the off-diagonal terms approach zero. The number of sensors required to ensure a "reasonable approximation" has yet to be determined for enclosures of an arbitrary modal density.

However, attention will initially be restricted to the case currently being considered, that is a sound field where the response is dominated by only a few modes.Thus at frequencies close to one of the natural frequencies of the enclosure, one mode's contribution will dominate, except in the case of the degenerate resonance, where two modes dominate. At "off resonance" frequencies, since the enclosure is relatively lightly damped, the response is generally dominated by a few modes whose natural frequencies lie closest to the frequency considered. Firstly consider the case where the sound field is dominated by a single mode and a single appropriately placed secondary source is used to suppress the field. Under these circumstances,

equation (2.45) for the secondary source strength necessary to minimise J_p can be written as

$$q_{S1}(\omega) = -\frac{\left[B_n^{*}\, a_{pn} \sum_{\ell=1}^{L} \psi_n^2[\underline{x}_\ell] + \delta_1\right]}{\left[|B_n|^2 \sum_{\ell=1}^{L} \psi_n^2[\underline{x}_\ell] + \delta_2\right]} \qquad (2.48)$$

where the n'th mode has been assumed to be dominant and the terms δ_1 and δ_2 are small quantities arising from the additive contributions from all the residual modes and where the superscript * again denotes complex conjugation. Note that under these circumstances the optimal secondary source strength which minimises E_p is given by

$$q_{SO}(\omega) = \frac{[B_n^{*}a_{pn} + \delta_3]}{[|B_n|^2 + \delta_4]} \qquad (2.49)$$

where δ_3 and δ_4 are again small quantities arising from residual mode contributions. It is clear that the expression for $q_{S1}(\omega)$ will give a close approximation to that for $q_{SO}(\omega)$ provided that the term

$\sum_{\ell=1}^{L} \psi_n^2[\underline{x}_\ell]$ is sufficiently large to ensure that the residual terms

δ_1 and δ_2 remain small compared to the dominant terms in the numerator and denominator respectively of equation (2.48). This can easily be achieved using a single sensor located at a maximum of the dominant mode shape $\psi_n(\underline{x})$. However, the location of a sensor, or number of sensors, at positions where $\psi_n(\underline{x})$ is zero will clearly give a value of $q_{S1}(\omega)$ which bears no relationship to that of $q_{SO}(\omega)$. Also note that the value of

$\sum_{\ell=1}^{L} \psi_n^2[\underline{x}_\ell]$ is of little relevance provided it is sufficiently large.

Thus if, for example, a single sensor is used at a maximum of $\psi_n(\underline{x})$, then the value of $\psi_n^2(\underline{x})$ will be given by the square of the normalisation constant $\sqrt{(\epsilon_{n1}\ \epsilon_{n2}\ \epsilon_{n3})}$ and will therefore be equal to 2, 4 and 8 for "axial", "tangential" and "oblique" modes respectively.

Now consider the case where two modes dominate the response of the sound field. Under these circumstances, equation (2.45) can be written as

$$q_{S1}(\omega) =$$

$$\frac{-\left[B_n^* a_{pn} \sum_{\ell=1}^{L} \psi_n^2[\underline{x}_\ell] + B_k^* a_{pk} \sum_{\ell=1}^{L} \psi_k^2[\underline{x}_\ell] + [B_n^* a_{pk} + B_k^* a_{pn}] \sum_{\ell=1}^{L} \psi_n[\underline{x}_\ell]\psi_k[\underline{x}_\ell] + \delta_5\right]}{\left[|B_n|^2 \sum_{\ell=1}^{L} \psi_n^2[\underline{x}_\ell] + |B_k|^2 \sum_{\ell=1}^{L} \psi_k^2[\underline{x}_\ell] + [B_n^* B_k + B_k^* B_n] \sum_{\ell=1}^{L} \psi_n[\underline{x}_\ell]\psi_k[\underline{x}_\ell] + \delta_6\right]} \qquad (2.50)$$

where it has been assumed that the n'th and k'th modes dominate the response and δ_5 and δ_6 are small residual contributions. Now note that the equivalent expression for $q_{SO}(\omega)$ for the case of two dominant modes can be written as

$$q_{SO}(\omega) = -\frac{\left[B_n^* a_{pn} + B_k^* a_{pk} + \delta_7\right]}{\left[|B_n|^2 + |B_k|^2 + \delta_8\right]} \qquad (2.51)$$

where δ_7 and δ_8 are again assumed small. Thus the major discrepancy between equation (2.50) and (2.51) arises from the presence of the term

$\sum_{\ell=1}^{L} \psi_n[\underline{x}_\ell]\psi_k[\underline{x}_\ell]$ in equation (2.50). This is one of the off-diagonal terms in the matrix $(\underline{\psi}_L\underline{\psi}_L^T)$. If this term can be made equal to zero by the appropriate placing of sensors, and if

$\sum_{\ell=1}^{L} \psi_n^2[\underline{x}_\ell]$ and $\sum_{\ell=1}^{L} \psi_k^2[\underline{x}_\ell]$ can be made large and equal, then $q_{S1}(\omega)$

will give a good approximation to $q_{SO}(\omega)$. An arrangement of sensors which very often but not always fulfils these requirements for a given pair of modes is to place a sensor in each corner of the enclosure. For the two dimensional case considered here, examination of the mode shapes illustrated in Figure 2.9 shows that

$\sum_{\ell=1}^{L} \psi_n[\underline{x}_\ell]\psi_n[\underline{x}_k]$ is equal to zero for these sensor locations for

each successive pair of modes up to a frequency of 300 Hz. This also includes the degenerate resonance at 150.6 Hz. Corner sensor locations also ensure that a maximum of any mode shape is always detected such that

$\sum_{\ell=1}^{L} \psi_n^2[\underline{x}_\ell]$ is always large for any mode. These observations will now

be illustrated using a further computer simulation.

2.4.5.3 Results of computer simulations

In order to keep the visualization of the modal structure simple, the results of this section have all been obtained using the single secondary source S4. It has already been demonstrated (Figure 2.12) that when this source is controlled to minimise E_p all resonances up to 300 Hz can be attenuated. Thus any inability to reduce E_p will be due to sensor locations and not source location.

The analysis of section 2.4.5.2 has demonstrated that if global reductions in acoustic energy are required then the worst possible place to locate sensors is on nodal planes of the primary sound field. Figure 2.17 shows a situation where three sensors (M5,M6 and M7) have been equispaced along the x_1=1.132m plane of the enclosure. Even though the secondary source strength has been adjusted to minimise the sum of the squared pressures at the three sensor locations, for many frequencies an increase in E_p has resulted. Note that although the pressure has only been constrained at three discrete points in the enclosure, the plot shows the resulting E_p evaluated over the whole of the enclosed space. Reference to Figure 2.9 reveals that the frequencies where the greatest increase in E_p are produced are those where the sensors are placed at

nodal planes of the primary sound field, and thus the contribution of the dominant mode is undetected.

The analysis of Section 2.4.5.2 also suggests that placing a sensor in each corner of the enclosure will ensure the detection of a single dominant mode, and that this is also the best arrangement for a limited number of sensors when two modes dominate the response. Figure 2.18 shows the result of minimising J_p using four sensors positioned at locations M1, M2, M3 and M4 of Figure 2.2, and close agreement between E_{pJ} (the value of E_p produced by minimising J_p) and E_{pO} is evident, particularly at the resonant frequencies where a single mode dominates the response. Even at the 150.6 Hz degenerate resonance E_{pJ} and E_{pO} show good agreement, implying that the off diagonal terms of the matrix $(\underline{\psi}_L\underline{\psi}_L^T)/L$ are small. Reference to Figure 2.9 confirms that the sum of the products of the two modes over the four corners of the enclosure does equal zero, and hence the matrix is diagonal. Furthermore, the two modes are both axial and thus have the same normalisation constants. Therefore, apart from the residual δ terms equations (2.50) and (2.51) are equal, and $q_{S1}(\omega)$ closely resembles $q_{SO}(\omega)$. The frequency regions where the E_{pO} and E_{pJ} curves differ significantly are at some non-resonant frequencies, where generally two modes "dominate" the sound field. Whilst for all of these cases the two "dominant" modes are such that the important off diagonal terms of the matrix $(\underline{\psi}_L\underline{\psi}_L^T)/L$ are all zero, the classes of the two modes are different and the diagonal terms therefore differ by the square of the normalisation constants. Hence the modes are weighted and, for instance, twice as much importance is placed on the contribution of a tangential wave as that of an axial wave, even though both modes are detected at their maxima. Consequently $q_{S1}(\omega)$ and $q_{SO}(\omega)$, from equations (2.50) and (2.51) respectively, will not be equal and minimising J_p will not result in E_p also being minimised. Where the dominant modes are of the same class, for example the three axial modes between the 75 Hz and 150 Hz resonances, then equations (2.50) and (2.51) differ only by the residual terms, δ, and minimising J_p does result in virtually minimising E_p.

2.5 Conclusions

(i) Substantial global reductions of sound pressure amplitude can in theory be achieved in sound fields of low modal density using only one or two secondary sources by minimising the total time averaged acoustic potential energy, E_p, of the sound field. Reductions can be achieved even if the secondary sources are placed greater than half a wavelength from the primary source. However, the sources must be placed such that they can couple efficiently with the dominant acoustic modes.

(ii) If the acoustical system is operating at, or close to, a lightly damped resonance then large global reductions (> 20 dB) should be possible using a single, sensibly placed secondary source. If the acoustical system is either heavily damped, or it is operating well away from a resonance frequency, then only small ($\simeq$ 1–2 dB) global reductions are likely to be possible using a single secondary source.

(iii) A possible practical strategy for producing global reductions is to minimise the sum of the squared pressures, J_p, at a number of discrete error sensor locations. In general it is advisable to use more error sensors than secondary sources to prevent the pressure being driven to zero at any points in the sound field.

(iv) When minimising J_p with the aim of producing global reductions the rules for secondary source placement are the same for minimising E_p. However, the locations of the error sensors are equally important, and as a general rule these should be placed close to maxima of the primary sound field. For the specific case of a sound field of low modal density in a rectangular enclosure this corresponds to placing error sensors in the corners of the enclosure.

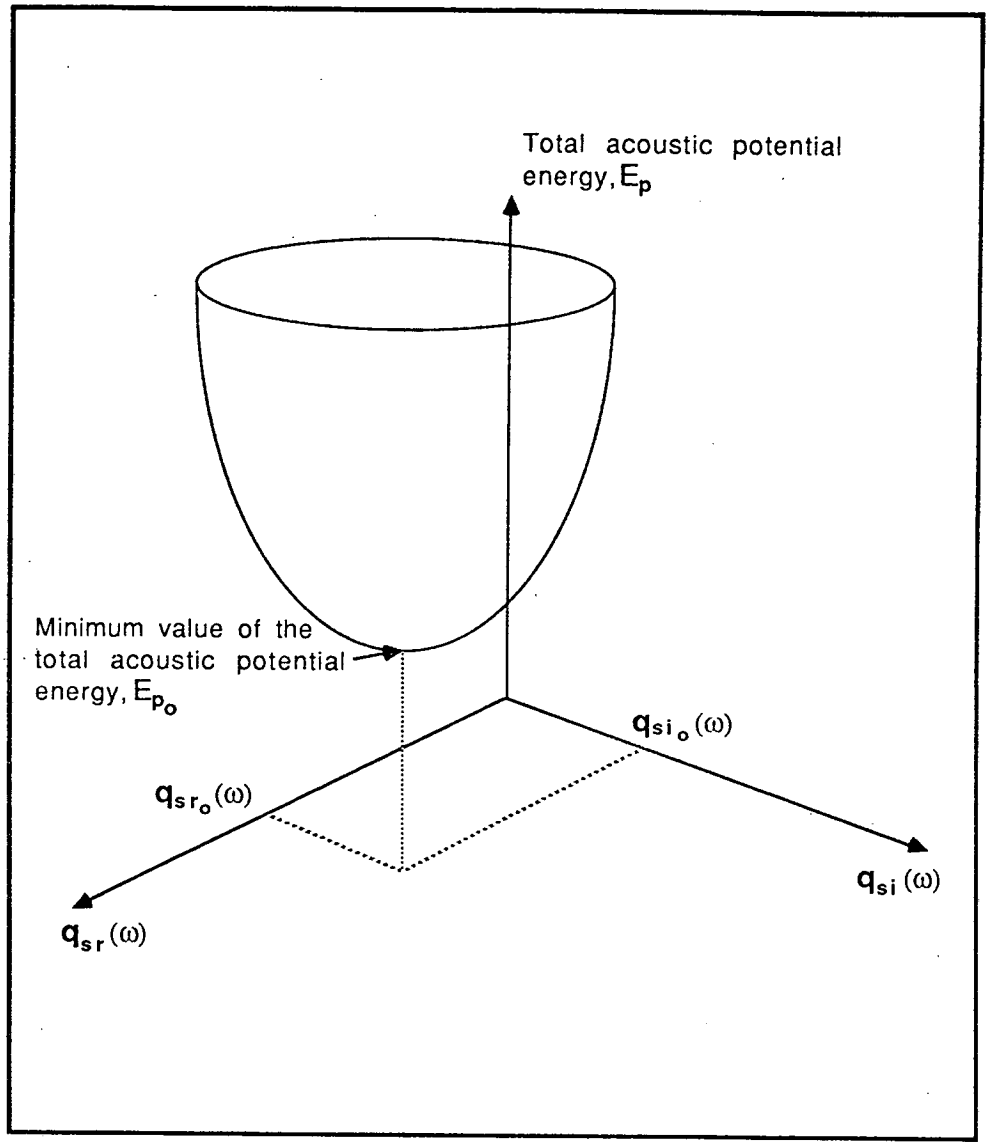

FIGURE 2.1. The total acoustic potential energy in an enclosed sound field as a function of the real and imaginary parts of the complex strength of a single secondary source.

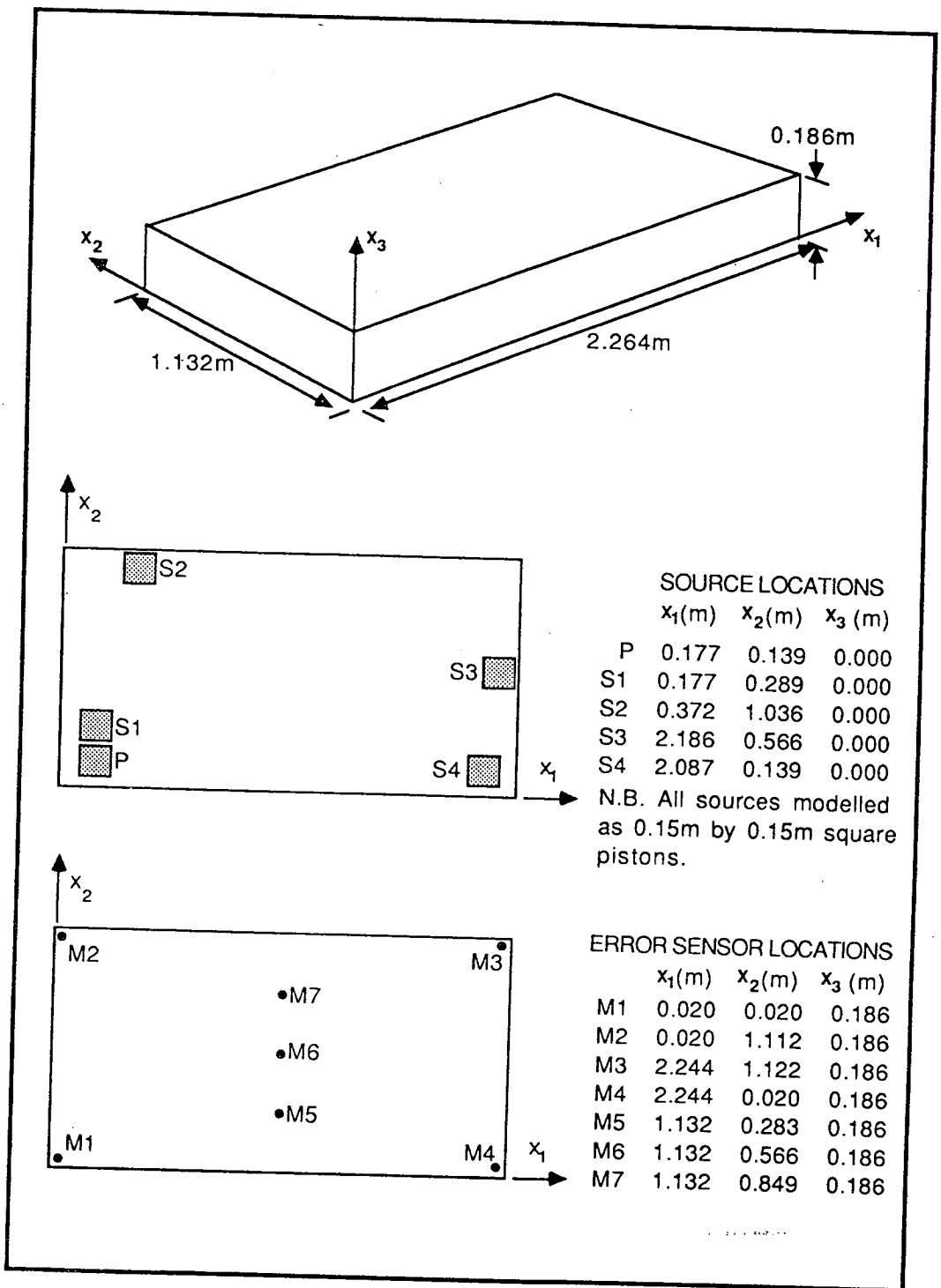

SOURCE LOCATIONS

	x_1(m)	x_2(m)	x_3 (m)
P	0.177	0.139	0.000
S1	0.177	0.289	0.000
S2	0.372	1.036	0.000
S3	2.186	0.566	0.000
S4	2.087	0.139	0.000

N.B. All sources modelled as 0.15m by 0.15m square pistons.

ERROR SENSOR LOCATIONS

	x_1(m)	x_2(m)	x_3 (m)
M1	0.020	0.020	0.186
M2	0.020	1.112	0.186
M3	2.244	1.122	0.186
M4	2.244	0.020	0.186
M5	1.132	0.283	0.186
M6	1.132	0.566	0.186
M7	1.132	0.849	0.186

FIGURE 2.2. Schematic diagram of the enclosure modelled for all the results of Chapter 2. The source and error sensor locations are also shown.

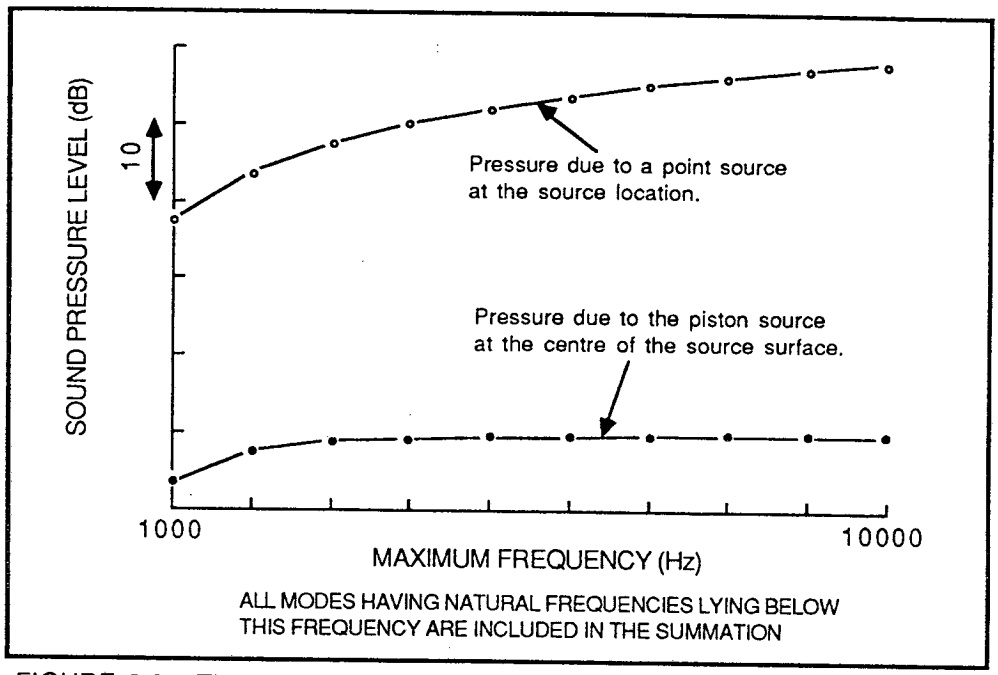

FIGURE 2.3. The convergence of the modal summation used to calculate the pressure in the enclosure shown in Figure 2.2. ∘—∘—∘ the pressure evaluated at the location of a point source , •—•—• the pressure evaluated at the centre of the surface of a 0.15m by 0.15m piston source. Both sources are placed at the primary source location shown on Figure 2.2 and are operating at 200Hz. A modal damping ratio of 0.01 has been used for all the modes.

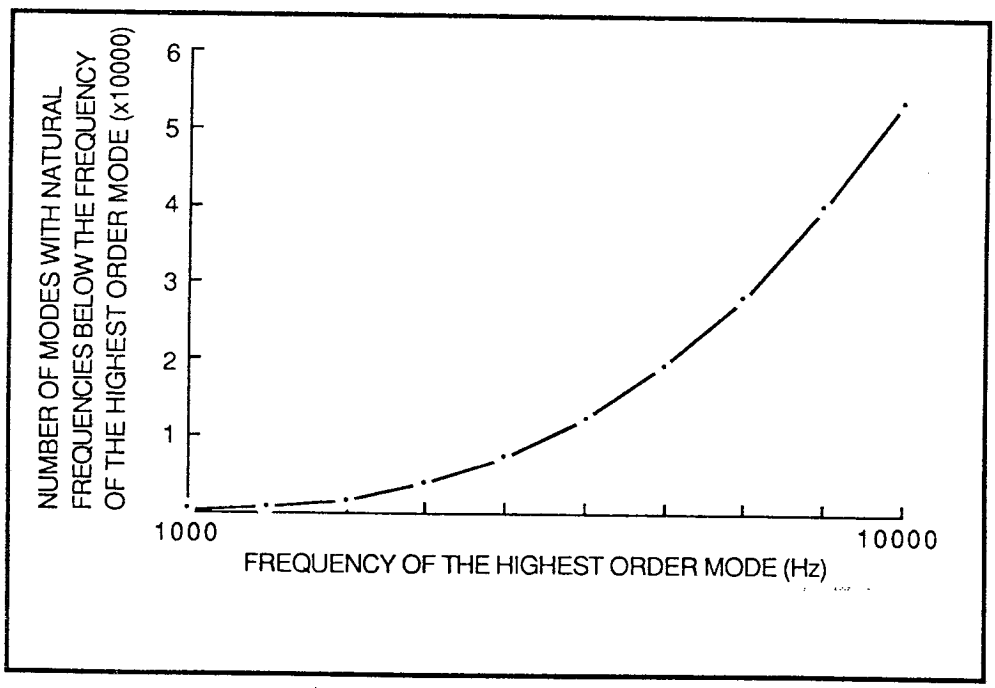

FIGURE 2.4. The relationship between the natural frequency of the highest order mode included in the modal summation and the number of modes having natural frequencies lying below this frequency.

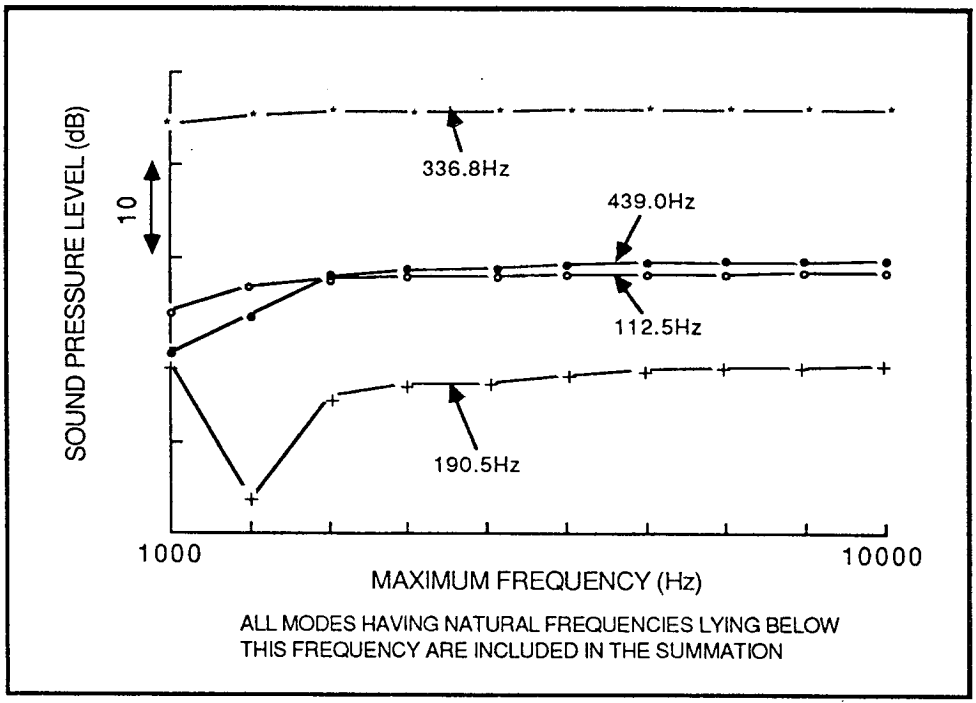

FIGURE 2.5. The dependence of the convergence of the modal summation on frequency. For each of the four different operating frequencies the pressure has been evaluated at the centre of the surface of the 0.15m by 0.15m piston source located at the primary source location shown in Figure 2.2. A modal damping ratio of 0.01 has been used for all the modes.

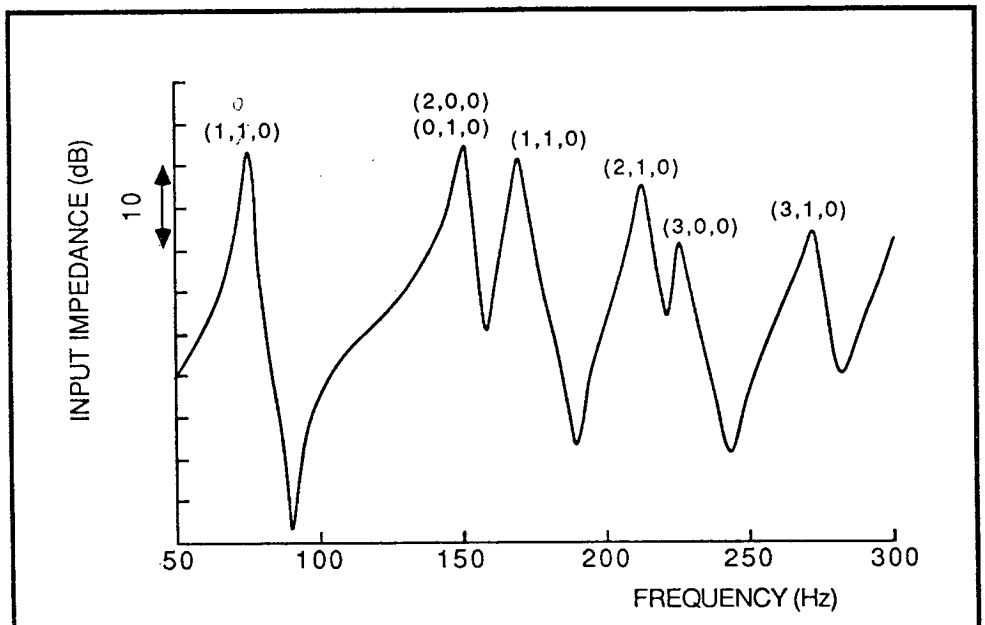

FREQUENCIES OF THE PEAKS IN THE RESPONSE

Mode number	Frequency (Hz)
1,0,0	75.3
2,0,0	150.6
0,1,0	150.6
1,1,0	168.4
2,1,0	213.0
3,0,0	225.9
3,1,0	271.5

FIGURE 2.6. The ratio of the sound pressure evaluated at the centre of the primary source surface to the velocity of the primary source when the enclosure of Figure 2.2 is excited by the primary source ,P, only. The modal integers (n_1,n_2,n_3) are also listed for each resonant mode.

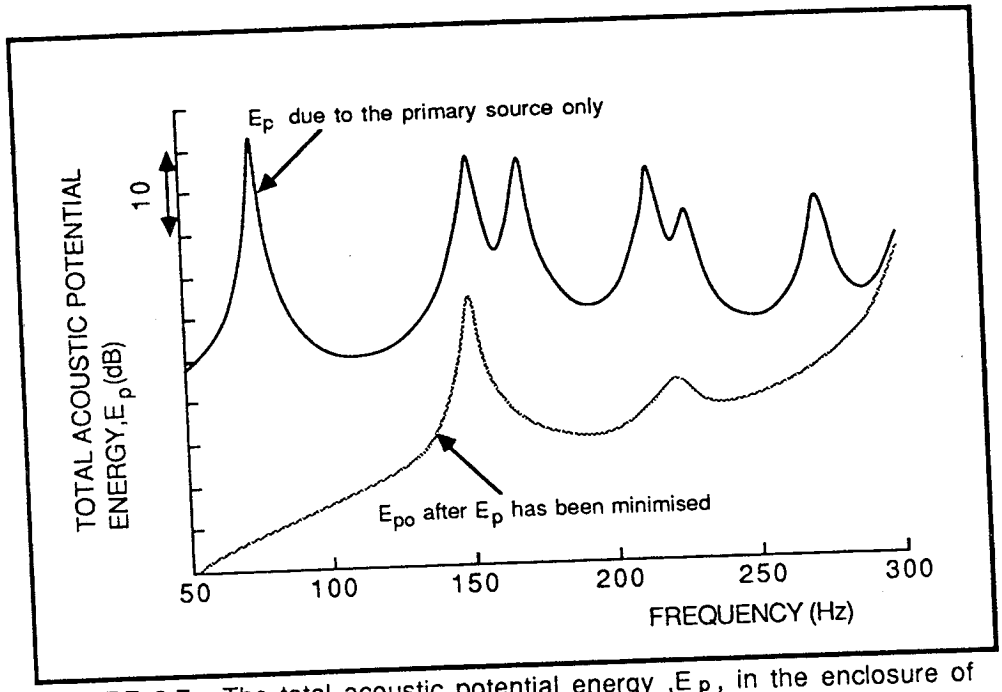

FIGURE 2.7. The total acoustic potential energy ,E_p, in the enclosure of Figure 2.2 before and after E_p has been minimised using the single secondary source S1.

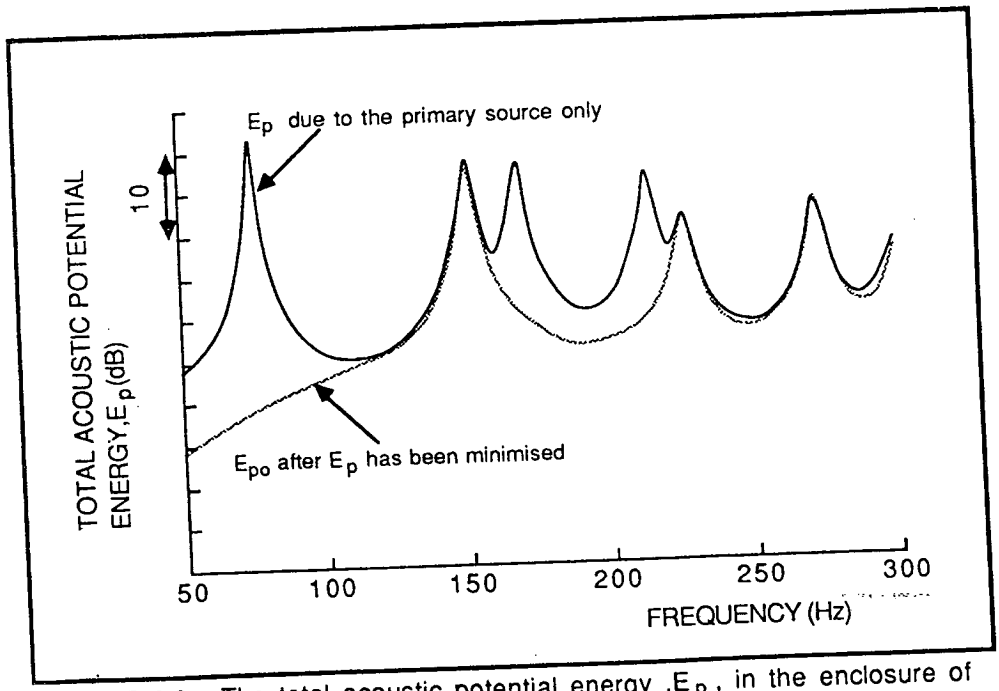

FIGURE 2.8. The total acoustic potential energy ,E_p, in the enclosure of Figure 2.2 before and after E_p has been minimised using the single secondary source S2.

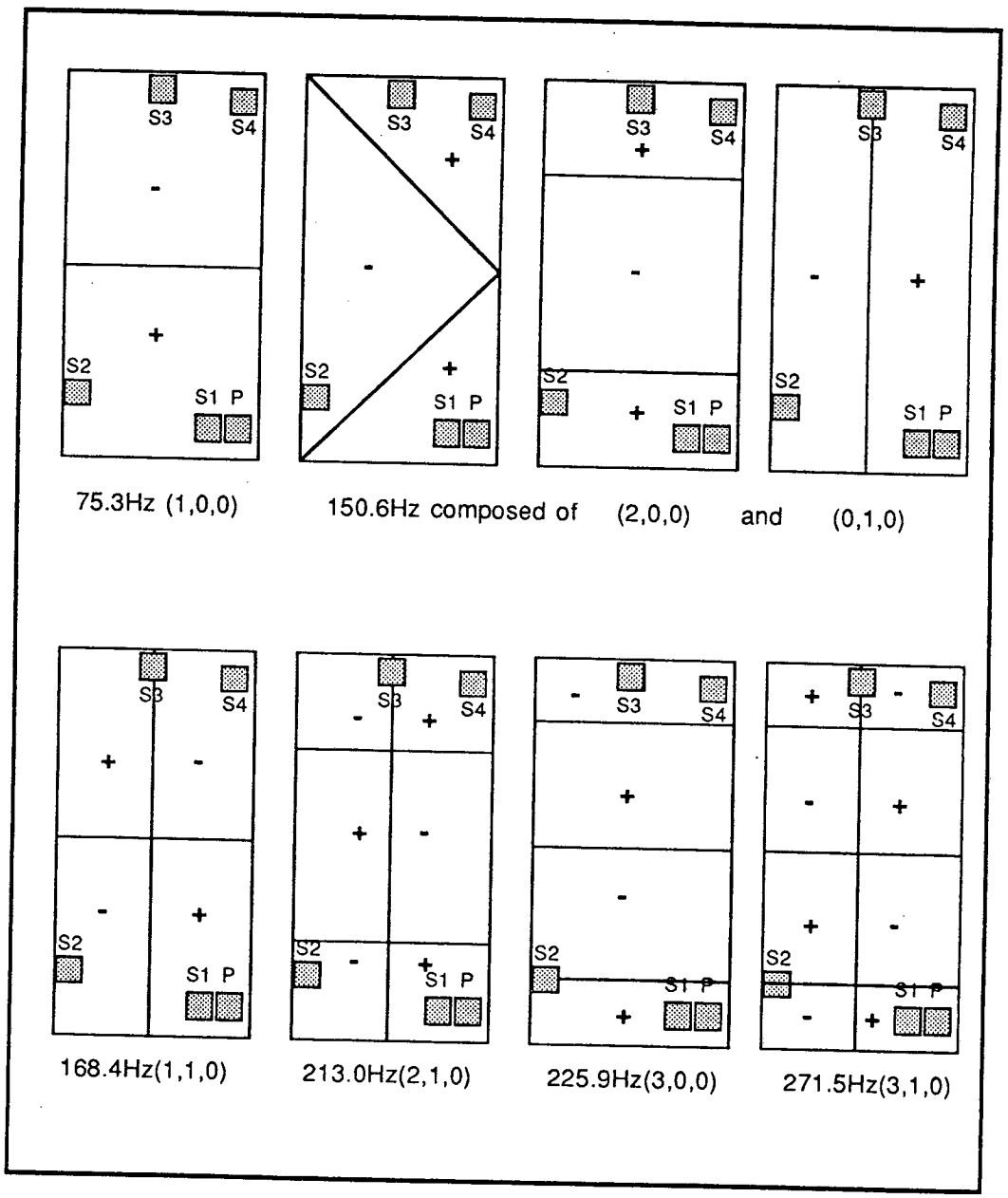

FIGURE 2.9. The distribution of nodal planes for the first six resonances of the enclosure shown in Figure 2.2. The relative phases of the responses are also shown for the case when only the primary source is operating.

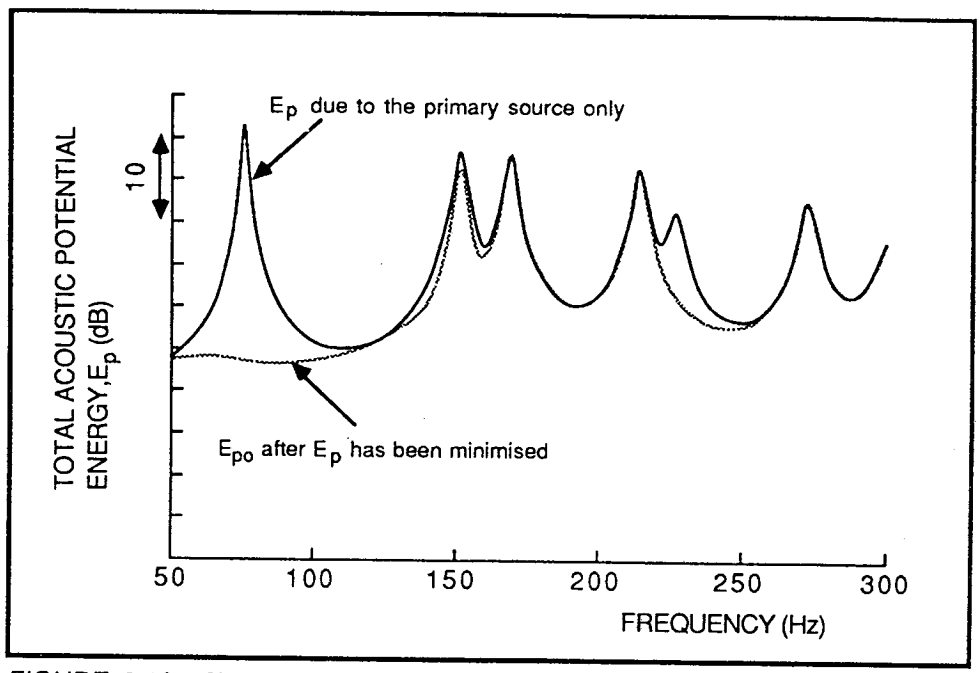

FIGURE 2.10. The total acoustic potential energy ,E_p , in the enclosure of Figure 2.2 before and after E_p has been minimised using the single secondary source S3.

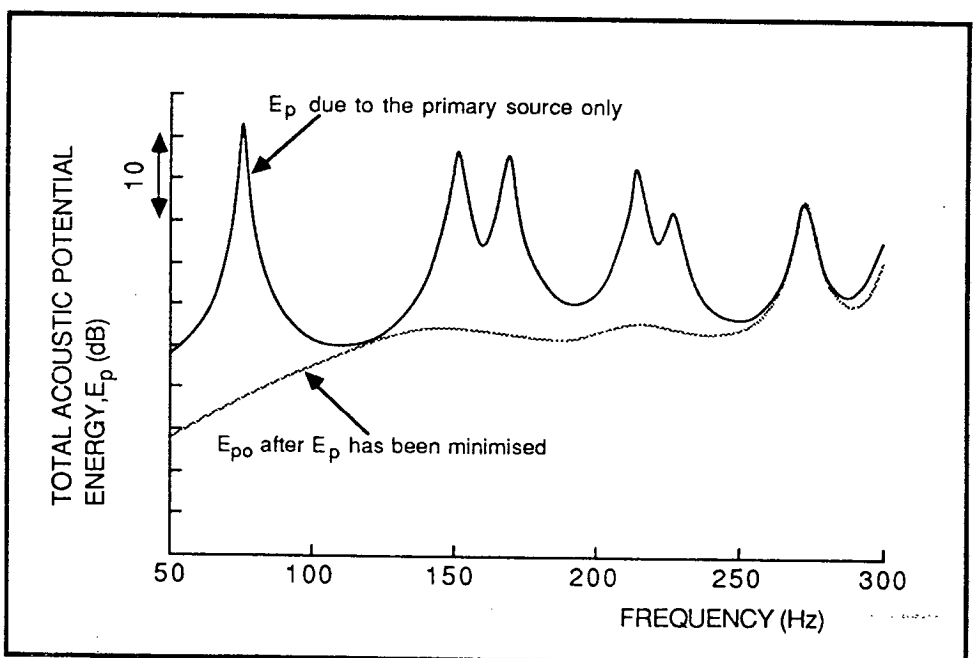

FIGURE 2.11. The total acoustic potential energy ,E_p , in the enclosure of Figure 2.2 before and after E_p has been minimised using the secondary sources S2 and S3.

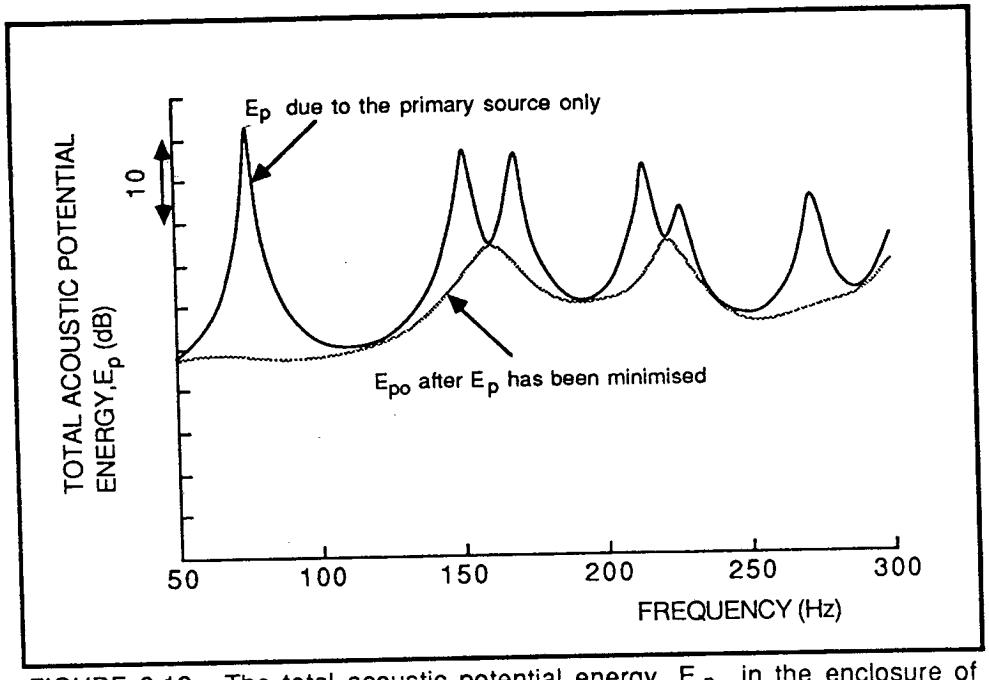

FIGURE 2.12. The total acoustic potential energy ,E_p, in the enclosure of Figure 2.2 before and after E_p has been minimised using the single secondary source S4.

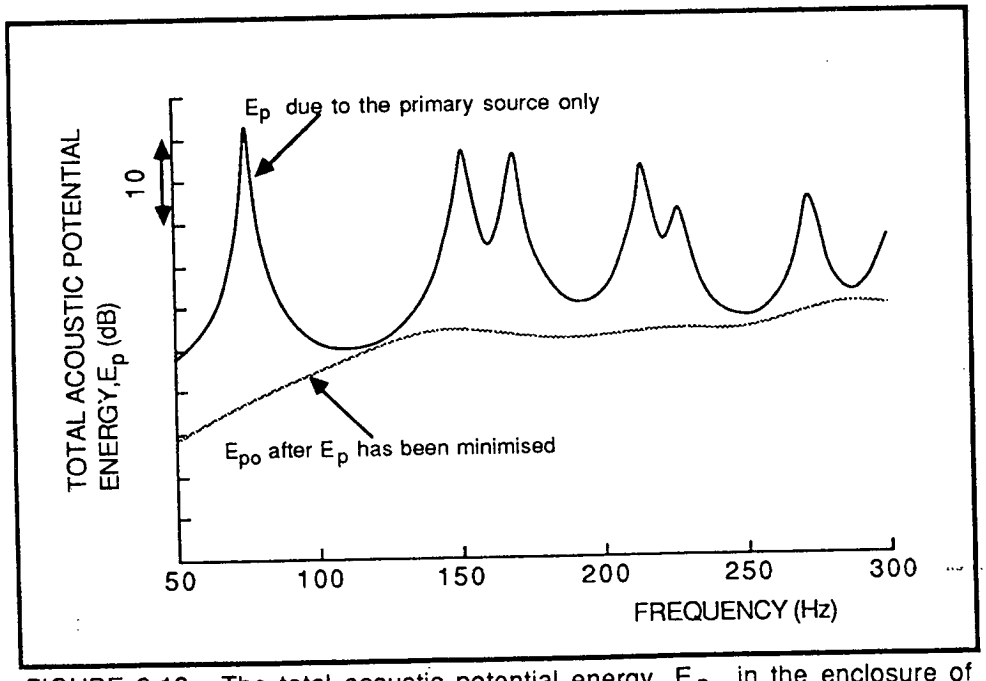

FIGURE 2.13. The total acoustic potential energy ,E_p, in the enclosure of Figure 2.2 before and after E_p has been minimised using the three secondary sources S2,S3 and S4.

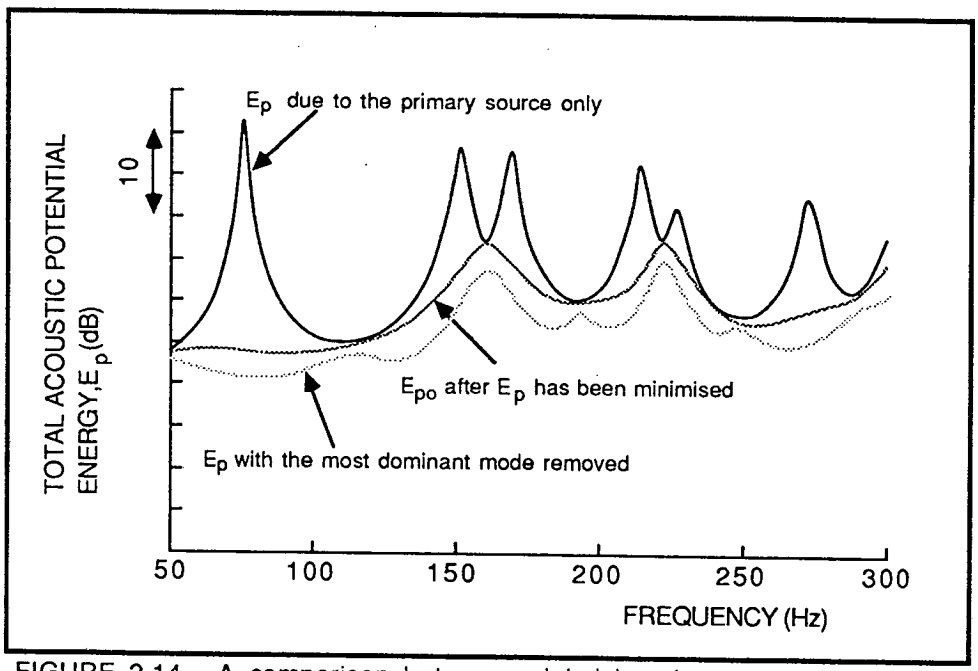

FIGURE 2.14. A comparison between minimising the total acoustic potential energy ,E_p,using the single secondary source S4 and the effect of removing the most dominant mode from the modal summation used to calculate E_p.Two modes have been removed for the 150.6Hz resonance.

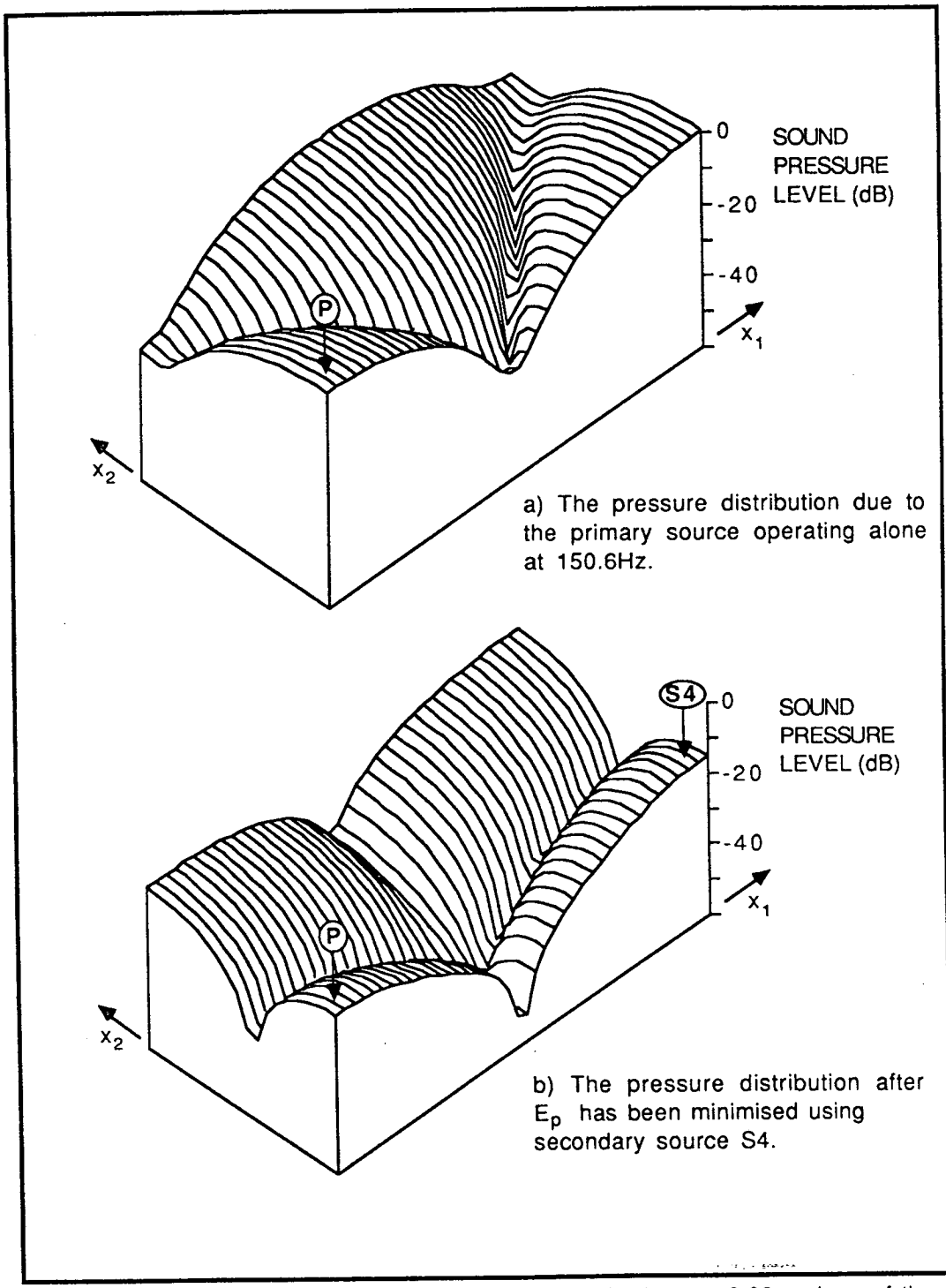

FIGURE 2.15. The sound pressure field at 150.6Hz in the x_3 =0.09m plane of the enclosure shown in Figure 2.2 for the cases when a) the primary source is operating alone and b) the total acoustic potential energy ,E_p ,in the enclosure has been minimised using the single secondary source S4.

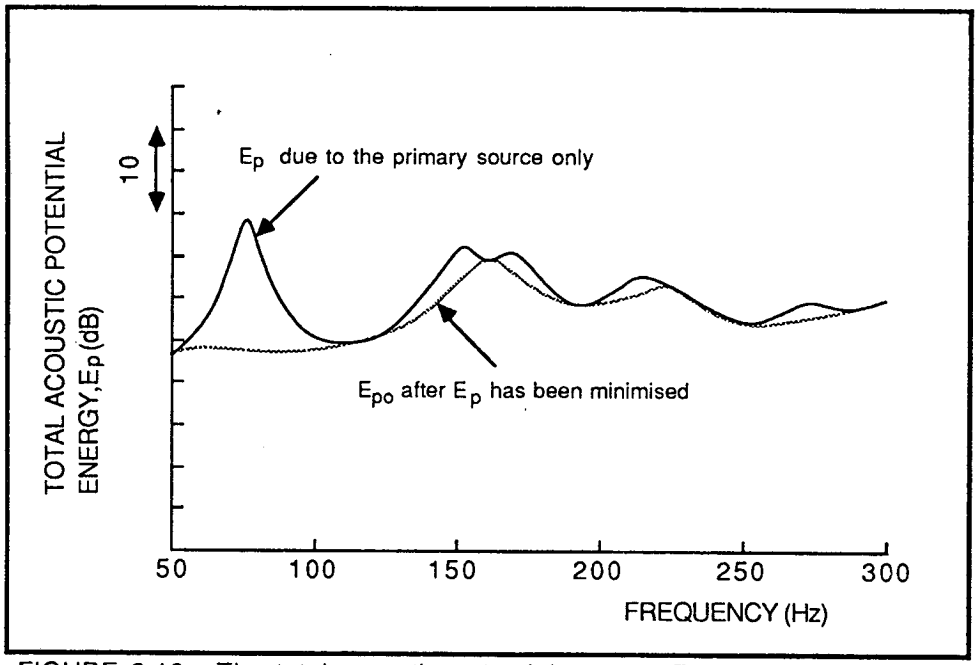

FIGURE 2.16. The total acoustic potential energy ,E_p ,in the enclosure of Figure 2.2 before and after E_p has been minimised using the single secondary source S4. The acoustic modal damping ratio has been taken as 0.05 compared to a value of 0.01 used for all the other results of Chapter 2.

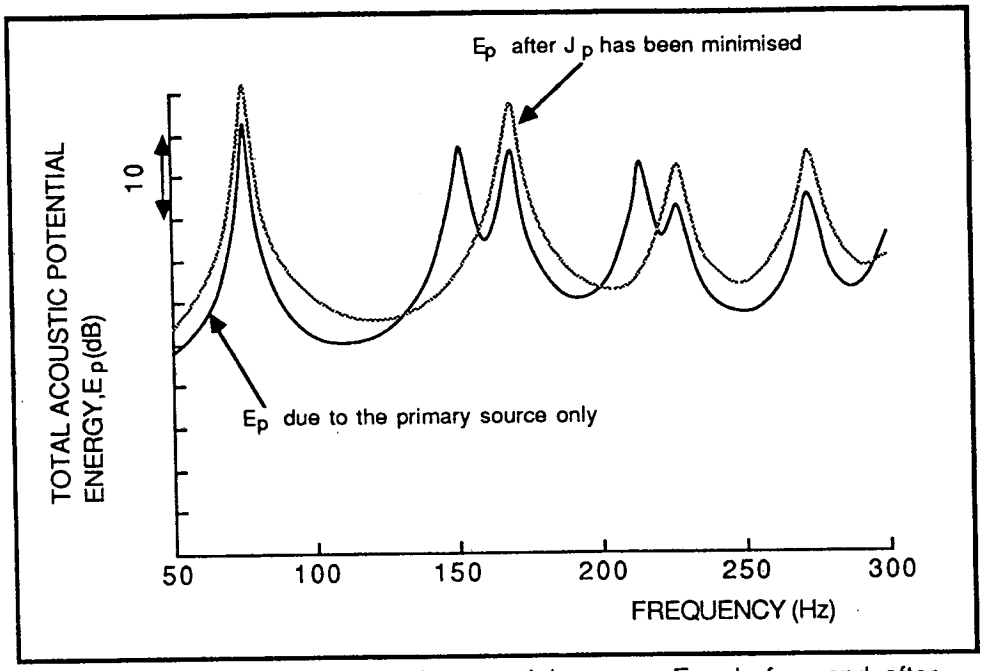

FIGURE 2.17. The total acoustic potential energy ,E_p , before and after the sum of the squared pressures ,J_p , at the three error sensor locations M5,M6 and M7 (see Figure 2.2) has been minimised using the single secondary source S4.

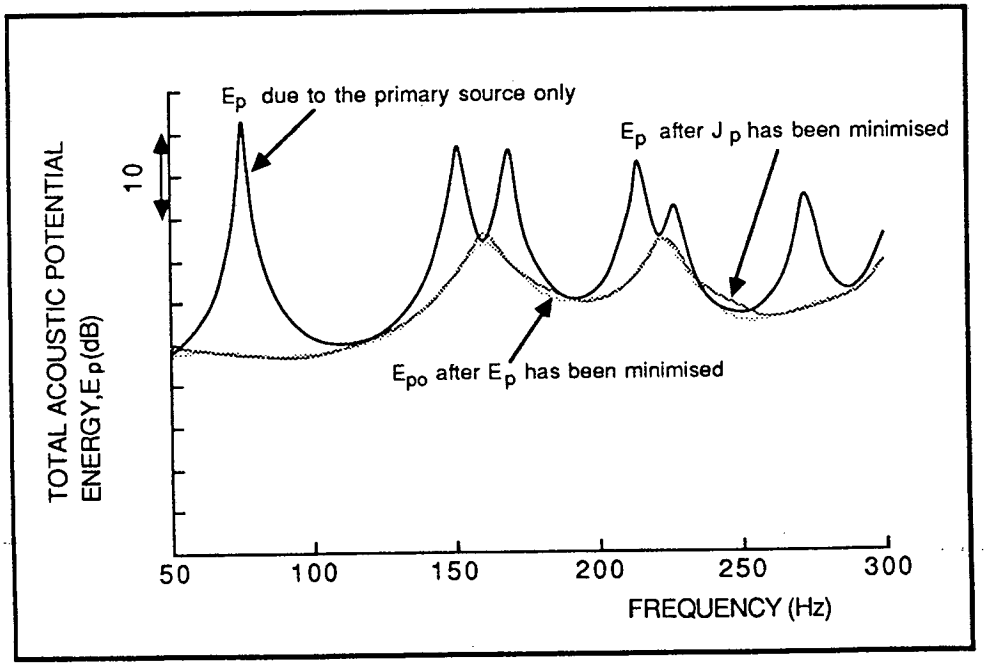

FIGURE 2.18. The total acoustic potential energy ,E_p , before and after the sum of the squared pressures ,J_p , at the four error sensor locations M1,M2,M3 and M4 (see Figure 2.2) has been minimised using the single secondary source S4. Also shown for comparison is the minimum value of E_p which can be achieved using this secondary source.

CHAPTER 3

THE ACTIVE CONTROL OF HARMONIC ENCLOSED SOUND FIELDS OF LOW MODAL DENSITY - EXPERIMENTAL RESULTS

3.1 Introduction

The theoretical results of Chapter 2 have all been obtained using a computer model of the plywood enclosure designed by Lewers [56] for some preliminary work on the active control of harmonic enclosed sound fields. It was initially intended to use this enclosure to validate the theoretical results obtained in Chapter 2, and further to investigate the spatial effects on the sound field of applying active noise control. Reference [57] describes some preliminary experimental results obtained using this enclosure, but unfortunately poor agreement between experiment and theory was obtained. The reason for this was traced to the coupling together of the acoustic modes by the vibration response of the enclosure walls. One of the implicit assumptions made in deriving the internal acoustic response equations of Chapter 2 was that the walls should be rigid, thus giving rise to an orthogonal set of acoustic modes. However, the large side walls of the enclosure (2.264 m × 1.132 m), made out of only 3/8 in. plywood, did not fulfil this condition. Even when these sides were braced with 1½ in × ¾ in timber struts the experimental and theoretical input impedances of the primary source could not be matched sufficiently well for the purposes of validating the model. Having identified this as being the main reason for the poor agreement between experiment and theory, another experimental enclosure was constructed, which was much smaller, in order to eliminate the problem outlined above. The parameters of the computer model were then adapted to match this new enclosure for the purposes of validating the theory.

3.2 The Experimental Enclosure

The experimental enclosure used to obtain the results of this section is shown schematically in Figure 3.1. The enclosure has internal dimensions of 0.668 m × 0.265 m × 0.050 m and is constructed from 18 mm thick medium density fibreboard. Thus the sides are substantially more

rigid than those of the plywood enclosure described in the previous section and therefore better agreement between experimental and theoretical results should be expected. Figure 3.1 also shows the locations on the two larger sides of the enclosure of the four sources used, where the single primary source is indicated by the P and the three secondary sources are denoted by S1, S2 and S3. Also shown are the locations of the five microphones at which the pressure is to be minimised, denoted by M1, M2, M3, M4 and M5. All sources used were KEF T27a dome tweeter units, having dome diameters of 20 mm, and all microphones were 12 mm B & K type 4133. Notice that the enclosure is still essentially "two-dimensional" for sufficiently low frequencies and consequently the pressure variation across the shorter (x_3) dimension of the enclosure should be uniform. In order to measure the pressure field in the x_1x_2 plane of the sound field, 20 evenly spaced holes were drilled along one of the long sides of the enclosure to allow the insertion of a 2 mm probe microphone (made from a B & K probe attachment kit UA0040 attached to a B & K 4133 microphone). Thus by traversing the probe microphone to ten evenly spaced locations in the x_2 direction, for each of the twenty x_1 locations, a grid of 200 evenly spaced pressure measurements was possible. To facilitate the rather laborious task of taking these measurements, the DC output of the B & K type 2609 microphone amplifier was passed through a 3-D "Inlab" interface system analogue-to-digital converter to an HP85 desktop computer, which stored the sound pressure amplitudes for later analysis.

In order to determine the acoustic response of the enclosure it was necessary to measure the input impedance of the primary source, which was deliberately placed in one corner of the enclosure to excite all the lower order acoustic modes with the least possible spatial selectivity. If this were to be done by evaluating the transfer function between the electrical output of the pressure microphone placed at location M1, and the electrical input signal to the primary source, then it is quite possible that a true estimate of the acoustic response would not be realized. This is because this method would assume that both the microphone and the loudspeaker have a flat frequency response over the frequency range of interest. This should not be an unreasonable assumption for the pressure signal, but the loudspeaker dome velocity is not likely to remain constant for a constant input voltage over such a

large frequency range. This is particularly so because it is driving into such a small enclosure, and therefore the effects of the acoustic loading on the finite internal impedance source are likely to be non-negligible.

To circumvent this problem a perspex window 10 mm in diameter was flush-mounted into the enclosure wall directly opposite the primary loudspeaker dome. It was then possible to measure the velocity of the dome directly by using the ISVR Laser Doppler Vibrometer (LDV)*. An estimate of the input impedance was thus obtained (using a Solartron 1200 Dual Channel Analyser) as the transfer function between the pressure signal from the microphone at location M1 and the velocity signal from the LDV. As the frequency responses of both the microphone and the LDV are given by the manufacturers as being essentially flat over a frequency range that extends well above 1000 Hz, and as neither of these responses is highly sensitive to the environment in which the measurements are made, it is a reasonable assumption that the transfer function measured as described above should be a good estimate of the acoustic input impedance of the enclosure.

Figure (3.2) shows the measured input impedance of the primary source over the frequency range from 0 Hz to 1000 Hz. The average modal damping ratio in this frequency band was estimated to be $\zeta_n = 0.01$ by using the centre frequencies and half power bandwidths of the peaks in the measured input impedance. Substituting this into the computer model, together with the correct enclosure dimensions and source and sensor locations, and modelling the source as a 20 mm square piston, resulted in the theoretical response shown as the dotted line in Figure 3.2. The general agreement between the theoretical and experimental results is excellent, except below about 30 Hz. Also listed in Figure 3.2 are the measured and predicted natural frequencies of the resonances, together with their associated modal integers.

---

*As the LDV measures the point velocity, it must be assumed that the dome acts as a piston. At frequencies below about 1 kHz this is a safe assumption.

It is evident from this input impedance measurement that working in the frequency range from 0 to 1000 Hz with this enclosure still results in the desired properties of the sound field being achieved; that is, well spaced, clearly discernible resonances such that at most frequencies only one or two modes can be considered to be dominating the response. These features are functions of both the frequency range being considered which, being kept below 1000 Hz, ensures that the modes are well spaced, and also of the very light damping which ensures the large response of the modes near their resonance frequencies. Particular care was taken over the choice of a suitable combination of enclosure dimensions and loudspeaker type with regard to the latter point. Previous experience had shown that at frequencies near to loudspeaker mechanical resonances, the loudspeakers can offer the dominant source of damping due to their low mechanical impedance. The free air resonance of the KEF T27a dome units is quoted by the manufacturer as being 1200 Hz. Consequently, the enclosure was designed such that only frequencies well below this resonance frequency need be used.

3.3 The Minimisation Procedure

It has already been stated in the introduction to this thesis that it is not intended to discuss the technical details of implementing a practical control system, either in terms of suitable algorithms or in terms of the hardware components of the system. Efficient, high speed algorithms and their implementation have been discussed in some detail by Elliott *et al* in a number of publications [58,59,60], where the physical implementation of these algorithms have used, as their central component, a high speed digital signal processing chip. The speed of these dedicated signal processing chips has allowed an ever increasing speed of convergence of the adaptive algorithms used. In reference [58] the use of active noise control to reduce the internal noise levels inside a commercial car is discussed, and results are presented which show the ability of the algorithm and control system used to adapt in a time less than the response time of the engine as the accelerator pedal is dipped. This example has been included to demonstrate that current electronic technology is at a stage whereby practical control systems can be built, although of course any further increase in the speed of the

signal processing capabilities of microprocessors can only be welcomed as making future control systems more flexible. For the purposes of the work described in the thesis, however, all experiments were performed under laboratory conditions where the primary noise source characteristics could be held constant over long periods of time. Consequently, the minimisation procedure was achieved using a relatively slow (convergence time of the order of several minutes) but simple to implement, pattern search algorithm.

A detailed discussion of the pattern search algorithm is given by Adby and Dempster [61], and the reasons for its choice for these particular experiments are discussed by Elliott *et al* [39]. Basically, the pattern search constantly adjusts the gains and phases of each of the secondary sources being used to ensure that the chosen cost function is always at, or converging towards, its minimum. If a quadratic cost function is chosen it is ensured that there exists only a single minimum, no matter how many secondary sources are used. Consequently, for any given source arrangement and at any given frequency there will be a unique combination of complex secondary source strengths which minimises the cost function, and the pattern search algorithm should always converge to this solution.

The experimental set up used is shown in Figure 3.3. The basic procedure for minimisation was as follows. The primary source was driven by a single frequency signal derived from a two phase oscillator (Feedback VBF 602) and power amplified. The pressures at up to four of the five microphones, denoted M1 to M5 (all B & K type 4133) were each passed through a B & K type 2609 measuring amplifier. With the measuring amplifiers adjusted such that each channel had an equal sensitivity, the DC outputs of the measuring amplifiers were proportional to the rms pressures at each microphone location. Using a 3-D "Inlab" interface, consisting of an eight channel multiplexer board, a twelve bit A/D converter, a 3 × 12 bit output port and an HPIB compatible interface board, these pressure signals were then sequentially sampled, analogue to digital converted and passed to the HP85 desktop computer, where they were squared and summed in accordance with the procedure for minimising J_p (equation (2.35)). This single quantity, the squared and summed

pressures at the microphones, thus provided the cost function for the pattern search algorithm to minimise.

The secondary source driving signals were derived from the same two phase oscillator as the primary source. However, they were driven with a combination of both the primary signal and another signal which was set to be in quadrature with the primary signal. Both these outputs were connected to a bank of programmable attenuators. These programmable attenuators consisted of 12 bit multiplying digital to analogue converters (Analogue Devices type AD7541 JN). The outputs of these devices are proportional to the reference signal (i.e., the in-phase or quadrature output of the two phase oscillator) multiplied by the digital input (derived from the pattern search algorithm on the computer, which was interfaced with the programmable attenuators via the Inlab digital output port), and thus the converters acted as linear attenuators. The output from each pair of converters, driven from the two phases of the oscillator, were then added together electronically and the single output, which may now have both a gain and phase variation with respect to the primary source signal, was fed via a power amplifier to one of the secondary sources.

Notice that the control parameters that have been chosen for the minimisation procedure are the squared and summed voltage signals from the microphones and the electrical input signals to the secondary sources. In the computer model these correspond to the squared and summed pressures, and the actual source strength. Despite the secondary source strengths not necessarily being directly proportional to the input voltage to the loudspeakers, particularly in this situation where the loudspeaker domes can be acoustically loaded by the other sources, whose strengths will not necessarily be constant, the pattern search algorithm should still converge to minimise the sum of the squared pressure signals and so from this point of view the results obtained should be directly comparable with the theoretical results. However, because the pressure due to the secondary sources can potentially load the primary source there is no guarantee that the primary field being minimised is the same as the primary field with no secondary sources acting. This effect could lead to a discrepancy between the measured and computed results, as

the computer model assumes infinite internal impedance sources. The error incurred by this mechanism will be discussed later.

3.4 Experimental Results

3.4.1 Experimental evaluation of E_p

Although the theoretical results of Chapter 2 were obtained using a model of a different enclosure the general findings should be equally applicable to the new enclosure, as it has been ensured that both enclosures have similar acoustical properties over the frequency ranges considered. One of the important conclusions of Chapter 2 was that appreciable global reductions (reductions in E_p, the total time averaged acoustic potential energy) can be achieved at, or close to, frequencies corresponding to modal resonances. Ideally, a graph similar to Figure 2.10 should be produced, showing the experimentally measured values of E_p in the enclosure both before and after minimisation of the sum of the squared pressures at the four corner microphones, for each frequency over a range from 0 Hz to 1000 Hz. However, in order to evaluate E_p experimentally, the pressure must be measured at an infinite number of locations throughout the enclosure volume. Clearly this is not possible, so as an estimate of E_p the pressure has been averaged over the previously described grid of 200 measurement points, evenly spaced over the x_1x_2 plane of the enclosure. This measurement will be denoted by $J_{p_{200}}$. Even having made this approximation, the time taken to measure the pressures at 200 locations was still appreciable, especially as it was necessary to measure it twice for each configuration, once before active noise control was applied, and again after the noise control had been applied. Furthermore, if this had been done over a 1000 Hz range, the time involved would have increased proportionately. Consequently, results of the form of Figure 2.10 have not been reproduced experimentally, although later in this chapter the effects over a smaller frequency range are considered. Instead the effects of applying active control at two single frequencies have been investigated. One of these, 680 Hz, corresponds to a resonant frequency, whilst the other, 730 Hz, corresponds to a frequency lying midway between two resonances. By choosing these two, the important features demonstrated in the analysis of Chapter 2 can be demonstrated experimentally.

3.4.2 Minimising J_p at a resonant frequency

3.4.2.1 A comparison of the theoretical and experimental primary pressure fields

The frequency of 680 Hz will be considered first. This is the resonant frequency of the third (1,1,0) mode. The nodal planes of this mode, and of the fourth (3,0,0) mode which will be used later, are shown on Figure 3.4. An isometric plot of the pressure field due to the primary source only, being driven with a 680 Hz pure tone signal, is shown in Figure 3.5a. This experimental result was obtained by measuring the pressure over the grid of 200 measurement locations described in Section 3.2. For this and all other experimental results the terminals of all the other sources, which were mounted on the enclosure but not driven, were short circuited. This ensured that the acoustic impedance the sources presented to the enclosed field was constant, whether they were driven or not. Figure 3.5b shows the theoretical pressure distribution for this condition, and it appears to be in close agreement with the experimentally measured pressure distribution. The parameters used in the computer model matched those of the experimental enclosure, with a damping ratio of 0.01 being used, and with this source (and all subsequent sources) being modelled as a 0.02 m square piston source. The frequency used in the computer simulation, however, was chosen as 692 Hz from Figure 3.1. The primary source strength was adjusted to match the amplitudes of the two responses. This close agreement between the theoretical and experimental primary fields thus validates the computer model of the acoustic response, and it must now be seen whether the optimization part of the computer routine can also predict the experimental results so accurately.

3.4.2.2 Minimising J_p using source S1 and error sensor M3

One of the most important conclusions obtained from the computer simulations was that appreciable reductions in E_p can be obtained using a limited number of secondary sources and sensors, but only if these sources are not located too close to nodal planes of the dominant primary mode(s). In order to validate this an initial series of experiments was performed using the secondary source S1, which can be seen from Figure 3.1 to be the closest secondary source to the primary source, P.

First the pressure was minimised at the single microphone M3, which is in the opposite corner to the primary source, by optimising the electrical input to the single secondary source using the automatic control system described previously. This resulted in the measured pressure field shown in Figure 3.6a. The computed residual pressure field is shown in Figure 3.6b, and again there is good agreement between the two. The reduction in the "total" acoustic potential energy was evaluated experimentally using the $J_{p_{200}}$ approximation (i.e., the average over 200 points) and found to be 16.8 dB. The theoretical reduction in $J_{p_{200}}$ was 16.0 dB. The theoretical reductions in E_p and $J_{p_{200}}$ were found to be within 0.5 dB of each other, indicating that $J_{p_{200}}$ is a reasonable approximation to E_p. (A summary of the results of this chapter can be found in Table 3.1.)

One possible error incurred by directly comparing the theoretical and experimental results was mentioned in Section 3.2. That is, because the primary source has a finite internal acoustic impedance, it is possible that the acoustic loading imposed by the secondary sources may alter its dome velocity, and hence its source strength. The velocity of the primary loudspeaker dome was monitored using the LDV during all the experiments and it was found that this source of error was less than 0.1 dB. This effect can consequently be ignored.

This initial experiment has proved that substantial global reductions can be achieved at a resonant frequency using a single secondary source and sensor, provided that both of these are placed away from the nodal planes of the resonant mode. The physical reasons for this were discussed in Section 3.4 where it was concluded that, provided the pressure at the sensor is dominated by a contribution from the mode which also dominates the modal contributions to E_p, then minimising the pressure at that microphone should ensure that E_p is also substantially reduced as the secondary source will act to reduce the contribution of the dominant mode. This is clearly demonstrated in Figures 3.5 and 3.6. The primary field of Figure 3.5 is dominated by the shape of the (1,1,0) mode. The residual field of Figure 3.6, however, has lost this dominant (1,1,0) structure, and the field which remains appears to be composed of several residual modes, none of which may be considered to

nate the others, and none of which are excited to as high a level as original (1,1,0) mode.

3.4.2.3 A note on the strategy of placing error sensors at maxima of the primary sound field

The final conclusion of the previous section is in itself an portant result, although it is to some extent problem dependent, even n considering sound fields of low modal density. This problem endency shall be illustrated using an example.

Imagine that the enclosure were nearly square, or that its sides had gths which were very nearly integer multiples of each other. In this e it would be possible for two resonances to exist at nearly the same equency. Now assume that the primary source is placed such that it es at an antinode of one of these two modes, which shall be denoted as de M_1, and at a node of the other mode, M_2. Similarly, assume that the ngle microphone is also placed at an antinode of mode M_1 and at a node mode M_2. Now what would be the effect of minimising the pressure at e microphone? If the secondary source were placed at an antinode of and at a node of M_2, then minimising the pressure would also bstantially reduce E_p, as described above. However, if the secondary urce were placed close to antinodes of both modes M_1 and M_2, then nimising the pressure at the microphone would effectively reduce the plitude of mode M_1, but no account would be taken of mode M_2's plitude, as the pressure at the microphone contains no information garding this mode. Consequently, it is possible that the reduction in would be very small, and an increase in E_p could even result for rtain conditions. Notice that this could occur despite following the nitial guidelines for optimal sensor locations disussed in Chapter 2, hich stated that secondary sources and sensors should be placed at axima of the primary sound field to ensure the detection and control of he dominant modes. The reason for the discrepancy is that, in the heoretical analysis of Chapter 2, it was assumed that the primary source as not selective in its spatial excitation of the lower order acoustic odes. This situation, too, has been arranged for in the experimental nclosure, where the primary source has been placed in one corner of the rectangular box. However, in practical situations the primary source is

likely to be selective in which modes it excites, particularly in situations where it is distributed over large areas of the bounding surface. Indeed, it was not until this latter situation was studied that the importance of this effect was realized [9]. However, because of the design of the experimental enclosure being used for the results of this chapter, an experimental result showing this behaviour was not possible, although the possibility of such an event in other cases should not be forgotten.

3.4.2.4 Minimising J_p using source S1 and error sensor M5

Returning now to the experimental results for the enclosure of Figure 3.1, it has been shown that minimising the pressure at the single microphone, M3, in one corner of the enclosure results in global reductions in E_p of about 16.0 dB. This is to be expected from the analysis of Section 2.4. However, in that section it was also concluded that if the single sensor is placed near a nodal plane of the dominant mode then global reductions will not be ensured, and increases in E_p are almost certain to result.

Figure 3.7 shows the results of minimising the pressure at microphone M5, again using the single secondary source S1. The experimental and theoretical results show good agreement, with the common factor that the residual pressure field is very similar in form to the primary pressure field, although increased in amplitude. The increase in $J_{p_{200}}$ was measured as 5.6 dB experimentally and predicted as 11.3 dB theoretically. This discrepancy is thought to be due to the secondary source strength being critically dependent on the exact position of M5, and because the pressure at M5 was minimised using the probe microphone there was some uncertainty (about ± 3 mm in each direction) as to its exact location. However, the important feature has been successfully demonstrated in this test: that is, unless the pressure at the minimisation point contains a substantial contribution from the mode which contributes most to E_p, then minimising this pressure will certainly not ensure a reduction in E_p.

3.4.2.5 Minimising J_p using source S2 and error sensor M3

In both the experiments described above, the secondary source S1 was placed within a half wavelength of the primary source. If attention is

now turned to source S2, then the centre of this souce is 0.65m from the centre of the primary source, compared to a half wavelength at 680 Hz of 0.25m. Thus S2 may be considered as being remote from the primary source. Figure 3.8 shows the result of minimising the pressure at microphone M3 by adjusting the gain and phase of source S2 only. Again the experimental and theoretical forms of the pressure field agree well, as do the measured and predicted reductions in $J_{p_{200}}$ which are 10.9 dB and 11.6 dB respectively. Therefore, in accordance with the theoretical results of Chapter 2, it has been shown that appreciable reductions in E_p are possible, using remote secondary sources, provided the system is operating close to an acoustic resonance.

3.4.2.6 Minimising J_p using source S2 and error sensors M1,M2,M3 and M4

It is also suggested in Chapter 2 that by minimising the sum of the squared pressures at the four corners of the enclosure, J_{p_4}, then the resulting reduction in E_p should closely approximate the optimal reduction in E_p obtainable using the same secondary source distribution. The results of minimising J_{p_4} using the single secondary source S2 are given in Figure 3.9, with the measured and predicted reductions in $J_{p_{200}}$ being 11.4 dB and 11.7 dB respectively. Using the computer model to minimise E_p using S2 only, it is predicted that a reduction in $J_{p_{200}}$ of 12.0 dB would result. Thus minimising J_{p_4} has resulted in near optimal reductions in $J_{p_{200}}$, although because there is only one dominant mode in this case, minimising the pressure at the single corner microphone M3 also resulted in similar, if not quite so good, global reductions.

3.4.2.7 A note on control system accuracy

Before moving on to investigate the effects of minimising J_p at a non-resonant frequency, a few words on the importance of control system finite word length effects are considered worthwhile. From Figures 3.5 to 3.9 it is seen that generally the theoretical and experimental results are in good agreement. However, close examination of the results revealed large differences in the levels of pressure reductions at the error sensors. Typical measured reductions were of the order of 30-40 dB and typical theoretical reductions were of the order of 100 dB. This is due largely to the finite precision of the computation involved

in each case. Experimentally 12 bit word lengths were used, and theoretically 16 bit floating point number representation was used. However, despite the local discrepancies, the experimental and theoretical pressure fields are elsewhere in excellent agreement, as are the measured and predicted global reductions. Thus, unless one were actually interested in producing very high reductions at the cancelling microphone, which would also be likely to be very localized reductions, then ensuring very high accuracy in the control system by using longer word lengths would be wasted effort. This feature has also been pointed out by Swinbanks [31].

3.4.3 Minimising J_p at a non-resonant frequency

3.4.3.1 A comparison of the theoretical and experimental primary pressure fields

From the computer simulations of Chapter 2 it is expected that only small global reductions will be achievable using a single secondary source which is placed remotely from the primary source if the system is being driven at a non-resonant frequency. In order to check these predictions a frequency of 723 Hz experimentally, and 730 Hz theoretically, was chosen to perform some experimental/theoretical comparisons. These frequencies were chosen as they lie at the minimum of the measured and predicted input impedance curves beween the third (1,1,0) and fourth (3,0,0) resonances. Figures 3.10 show the measured and predicted sound pressure fields due to the primary source alone operating at these frequencies. The two plots are in close agreement in general form. As with the resonant frequency results the theoretical primary source amplitude has been adjusted to set the average amplitude of the two fields equal to aid comparison.

Figure 3.11 shows the theoretical contributions of the first eight modes to E_p due to the primary source only over the frequency range 0 Hz to 1000 Hz. The operating frequency used for the current tests, 730 Hz, is indicated by an arrow. It is obvious from this plot that residual modes will play a much more important role in not just local effects, but also global effects concerning the sound field when compared to the resonant frequency of 692 Hz (1,1,0) considered in the previous section. It now becomes difficult to talk of a clear distinction between "dominant" and "residual" modes. For example, at 730 Hz the two modes

(1,1,0) and (3,0,0) are the most dominant, but the next mode, the (2,1,0) mode, contributes only 5 dB less to E_p, and below this the tails of many other "residual" modes also contribute to a significant degree. Thus even if the two most dominant modes could be suppressed by the action of an active control system, global reductions of no more than 5 dB could be expected.

3.4.3.2 Minimising J_p using source S1 and error sensor M3

In order to demonstrate most effectively the contrast between resonant and non-resonant suppression, the pressure was minimised at microphone M3 using source S1, which for the resonant results of the previous section produced a measured reduction in J_{pz00} of 16.8 dB. Figures 3.12 show the measured and predicted results for the non-resonant case, where the reduction in J_{pz00} was measured as an increase of 7.5 dB, compared to a predicted increase of 3.6 dB. The reason for this behaviour is apparent if one refers back to Figure 3.4, which shows the nodal lines of the (1,1,0) and (3,0,0) modes. Although the microphone M3 has been placed in a corner of the enclosure, thus ensuring that all modes will exhibit maxima there, in this case the (1,1,0) and (3,0,0) modes are out of phase with respect to the primary source at the location of M3. Therefore, as the two modes are excited to an equal amplitude by the primary source, they add to give zero contribution to the pressure at M3. Consequently, S1 concentrates on minimising the pressure at M3 by appropriately driving the "less dominant" modes, and as a result E_p is increased. The discrepancy between measured and predicted reductions is in this case thought to be due to the slight non-compatibility of the experimental and theoretical frequencies used. If the enclosure is not excited exactly at the frequency corresponding to the minimum of the input impedance curve then the relative contributions of the two nearest modes will be significantly altered. During the course of the experiments the frequency was held constant to within 0.1 Hz, but a temperature drift of up to 1°C was measured corresponding to an effective change in frequency of about 1.2 Hz.

3.4.3.3 Minimising J_p using source S1 and error sensors M1, M2, M3 and M4

The results of the above experiment have demonstrated yet again the importance of the cancelling microphone location. They also serve to strengthen the argument presented in Section 2, which suggested the use of several microphones to increase the chances of detecting the contribution of the dominant modes. Following this philosophy the sum of the squared pressures at microphone locations M1, M2, M3 and M4 was minimised, again using secondary source S1 only, and the pressure fields of Figure 3.13 resulted. In this case the reductions in $J_{p_{200}}$ are 0.8 dB measured and 1.9 dB predicted. Notice that now a reduction in the overall energy has resulted, although it is not as great as may have been hoped for, particularly when it is considered that source S1 is less than half a wavelength away from the primary source which was the criterion presented by Nelson *et al* [35] for good reductions in enclosed sound fields of high modal density. Once more reference to Figure 3.4 will provide a reason for this behaviour. It is because a nodal plane of the (3,0,0) mode lies between the primary source and source S1, thus preventing the secondary source from driving both modes with the same phase as the primary source. The optimal secondary source strength must therefore compromise between cancelling the (1,1,0) mode whilst increasing the excitation of the (3,0,0) mode or vice versa, with the result that the source can provide little net global cancellation. The predicted reduction in E_p which can be obtained by adjusting the source strength of S1 to minimise E_p is only 2.0 dB, so the use of four corner microphones is producing near optimal results.

3.4.3.4 Minimising J_p using source S2 and error sensors M1, M2, M3 and M4

If the sum of the squared pressures at the four corner microphones is now minimised using secondary source S2 only, then the pressure fields of Figure 3.14 result, and $J_{p_{200}}$ is increased by 0.1 dB theoretically, and increased by 0.5 dB experimentally. This poor reduction is again caused by the relative phases of the two most dominant modes at the secondary source location. As in the previous example, the two modes are out of phase with respect to the primary source and any action source S2 takes to decrease the amplitude of one mode will increase the amplitude of the other.

3.4.3.5 Minimising J_p using source S3 and error sensors M1, M2, M3 and M4

If one now chooses secondary source S3 alone and again minimises Jp_4 using microphones M1, M2, M3 and M4 then the pressure fields of Figure 3.15 result. The predicted and measured reductions in Jp_{200} are 0.7 dB and 1.8 dB respectively. The location of source S3 is such that it can cancel the (3,0,0) mode whilst leaving the (1,1,0) mode relatively unchanged, as evidenced by the residual pressure field (Figure 3.15(b)). The use of both secondary sources S2 and S3 simultaneously to cancel Jp_4 should, therefore, enable the amplitudes of both the (3,0,0) and the (1,1,0) modes to be reduced. In this situation, source S3 will be able to suppress the (3,0,0) mode, whilst source S2 concentrates on suppressing the (1,1,0) mode, any additional excitation of the (3,0,0) mode being counteracted by an appropriate increase in the gain of source S3. (A case entirely analogous to this was studied in Section 2.4.4, except in that context the two modes being considered were degenerate, resonant modes).

3.4.3.6 Minimising J_p using sources S2 and S3 and error sensors M1, M2, M3 and M4

Figures 3.16 show the pressure fields after Jp_4 has been minimised using sources S2 and S3 simultaneously, and the corresponding reductions in Jp_{200} are 2.0 dB measured and 1.6 dB predicted. These reductions still do not seem particularly impressive, particularly when compared to the theoretical predictions for the two degenerate, resonant modes mentioned above, where an optimal reduction in E_p of over 20 dB was predicted using two similarly placed secondary sources. The reason is, of course, that at frequencies between resonances, the "tails" of many modes can significantly contribute to the acoustic response (see Figure 3.11). In this current example, effort has been concentrated on suppressing the two most dominant modes, but Figure 3.11 reveals that the next most dominant mode's contribution to E_p is less than 5 dB down. Thus one is limited to overall reductions of this order of magnitude for this situation. However, this assumes that the contributions of the (3,0,0) and (1,1,0) modes can be suppressed without affecting the residual mode amplitudes. In practice, using discrete sources as in this case this is not possible, and the theoretical optimum reduction in E_p which can be achieved using sources S2 and S3 is just 2.8 dB.

The general conclusion of this section is, therefore, that global reductions are possible at non-resonant frequencies, using a small number of remote secondary sources, but the levels of reduction which can be achieved are much less than those which can be achieved for a comparable resonant frequency using the same number of secondary sources.

3.4.4 Minimising the squared and summed pressure at the enclosure's four corners over a range of frequencies

In the previous two sections the major theoretical predictions of Chapter 2 have been successfully demonstrated by looking at two specific frequencies, one lying exactly at an acoustic resonance, the other lying at an acoustic antiresonance. It has been shown that, for both these cases for the low modal density sound fields being considered, by minimising the sum of the squared pressures in the four corners of the enclosure, J_{p_4}, reductions in E_p result which are close to those which would be obtained with an infinite number of microphones. This section presents the experimental and theoretical results of minimising J_{p_4} over a range of frequencies.

The frequency range chosen was from 600 Hz to 750 Hz, thus including the two frequencies studied earlier. For each 5 Hz interval J_{p_4} was measured with just the primary source operating, and then again when J_{p_4} had been minimised using source S2 alone. The measured values of J_{p_4} before and after cancellation are plotted in Figure 3.17 as a function of frequency. During the course of taking these measurements the primary source dome velocity was constantly monitored using a Laser Doppler Vibrometer, and the results given in Figure 3.17 have been normalized with respect to this measured primary source velocity. Thus these experimental results are directly comparable with those predicted from the computer simulation. The computed values of J_{p_4} before and after minimising J_{p_4} using secondary source S2 only are presented in Figure 3.18. Comparison beween Figures 3.17 and 3.18 shows that the general trend has been predicted well by the theoretical model, with large reductions in J_{p_4} being obtained at resonant frequencies decreasing gradually to negligible reductions at the antiresonances.

The close agreement between the experimental and theoretical results over a frequency range which includes resonances, antiresonances and

transition regions between the two serves to successfully validate the computer model, and one can now proceed with some confidence to predict the effect of minimising J_{p_4} on E_p, the total acoustic potential energy. Figure 3.19 shows the theoretical values of E_p resulting from minimising J_{p_4} using source S2 over the chosen frequency range. Also plotted for comparison are the optimum reductions in E_p which can be achieved if source S2 is set to minimise E_p. Thus, minimising J_{p_4} has provided a good approximation to minimising E_p over the majority of the frequency range or, put alternatively, using just four microphones placed in the corners of the enclosure has produced reductions in the total acoustic potential energy comparable with those which could have been obtained using an infinite number of evenly spaced microphones.

However, at the antiresonances minimising J_{p_4} has resulted in E_p increasing, in particular over the frequency range from 640 Hz to 660 Hz where E_p has increased by as much as 2 dB. Referring back to Figure 3.18 shows that the reduction in J_{p_4} over this range is typically 0.01 dB, yet if the source strength of S2 is evaluated it is found to be of comparable magnitude to the primary source strength. Thus the secondary source is expending considerable effort for very little return in the reduction of the cost function, J_{p_4}, which over this frequency range is clearly to the detriment of the total energy. Because of the location of source S2, even if its optimal source strength is calculated to minimise E_p, then only a negligible (about 0.01 dB) reduction in E_p is possible at this antiresonance (the reason for this poor reduction has been discussed in Section 3.4.2.4). Consequently it may be sensible to try an alternative cost function which compensates for this problem by minimising some combination of the "error" (i.e., J_p) and the "effort" (i.e., q_s, the secondary source strength). A suitable quadratic cost function, J_T, can be defined as

$$J_T = \frac{V}{4\rho c^2 z_L} [\underline{p}^H \underline{p} + r \underline{q}^H \underline{q}] \qquad (3.1)$$

where r is a scalar constant which weights the importance of each of the secondary source strengths equally. When r equals zero, equation (3.1) reduces to equation (2.36) and no account is taken of the secondary source strengths, but as r is increased, then more importance is placed

on keeping the secondary source strengths as small as possible with respect to the reduction in J_p which is achieved. Figure 3.20 shows a result of applying the cost function of equation (3.1) to the current situation. The value of r has been chosen to suppress the increases in E_p previously encountered at the antiresonances. However, this has had the undesirable effect of decreasing the reductions which can be achieved near the resonances. In fact, if the integral of E_p after minimisation is evaluated over the frequency range from 600 Hz to 750 Hz then its value monotonically increases as the value of r is increased from zero. Therefore, if it is desired to achieve the maximum possible reduction in E_p over a large frequency range it is better to use the simple cost function J_p.

3.5 Conclusions

(i) The major conclusions of Chapter 2 have been verified experimentally, and the use of the computer model has been convincingly validated.

(ii) Global reductions in volume averaged sound pressure can be achieved in practice in a lightly damped sound field of low modal density using very few (1 or 2) secondary sources and error sensors provided these are sensibly placed.

(iii) The potential global reductions are much larger if the system is operating close to an acoustic resonance than if it is at a frequency midway between two resonances.

(iv) Error sensors should never be placed solely at minima of the primary noise field if global reductions are desired.

e 3.1: Summary of Results of Chapter 3

tion	Exp. freq. (Hz)	Condition	Secondary Source(s)	Sensor(s)	Reduction in J_{p2oo} (dB) Exp.	Theory
.1.2	680	Resonant	S1	M3	16.8	16.0
.1.4	680	Resonant	S1	M5	-5.6	-11.3
.1.5	680	Resonant	S2	M3	10.9	11.6
.1.6	680	Resonant	S2	M1,M2,M3,M4	11.4	11.7
4.2.2	723	Non-resonant	S1	M3	-7.5	-3.6
4.2.3	723	Non-resonant	S1	M1,M2,M3,M4	0.8	1.9
4.2.4	723	Non-resonoant	S2	M1,M2,M3,M4	-0.5	-0.1
4.2.5	723	Non-resonant	S3	M1,M2,M3,M4	1.8	0.7
4.2.6	723	Non-resonant	S2,S3	M1,M2,M3,M4	2.0	1.6

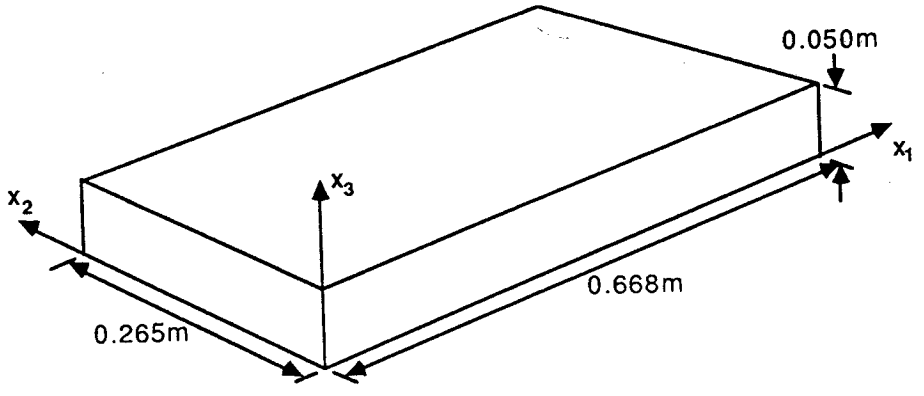

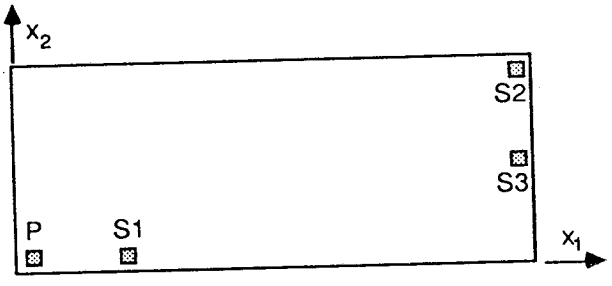

SOURCE LOCATIONS

	x_1(m)	x_2(m)	x_3 (m)
P	0.025	0.025	0.000
S1	0.135	0.025	0.000
S2	0.643	0.240	0.000
S3	0.643	0.133	0.000

N.B. Experimentally all sources 0.02m diameter dome tweeters
Theoretically all sources modelled as 0.02m by 0.02m pistons.

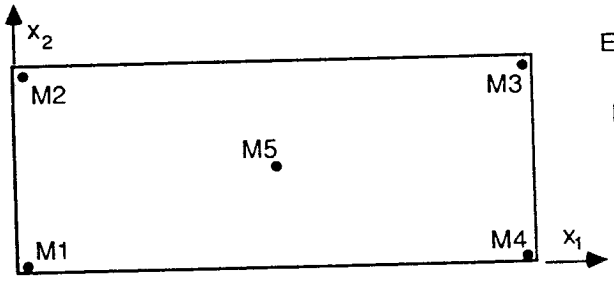

ERROR SENSOR LOCATIONS

	x_1(m)	x_2(m)	x_3 (m)
M1	0.005	0.005	0.050
M2	0.005	0.260	0.050
M3	0.663	0.005	0.050
M4	0.663	0.260	0.050
M5	0.350	0.133	0.025

FIGURE 3.1. Schematic diagram of the enclosure used for all the theoretical and experimental results of Chapter 3. The source and error sensor locations are also shown.

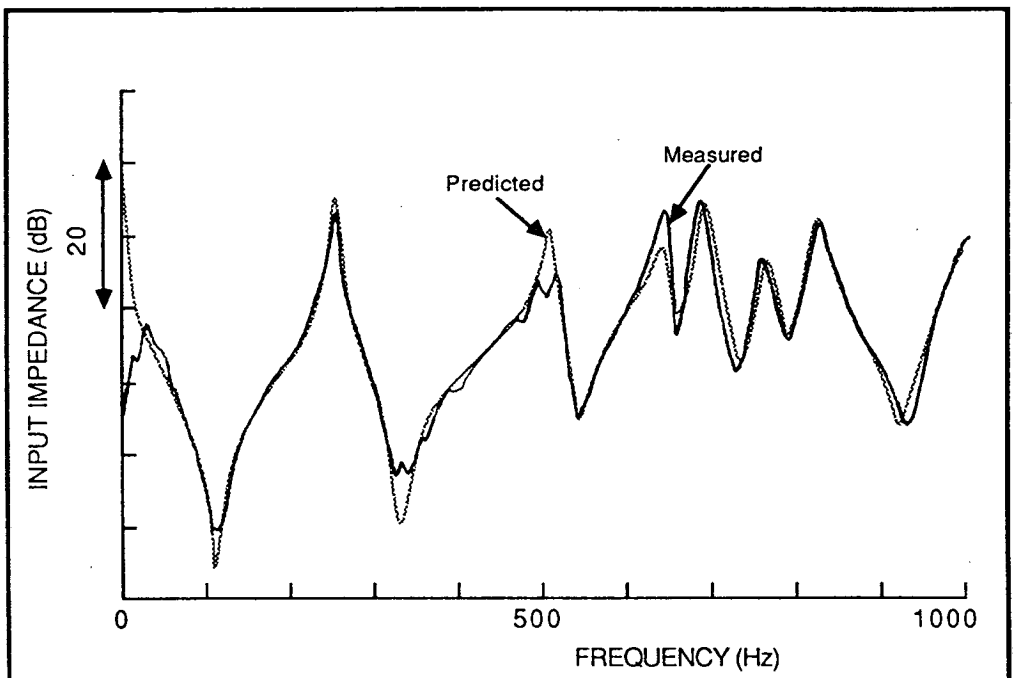

FREQUENCIES OF THE PEAKS IN THE RESPONSE.

Mode number	Computed frequency (Hz)	Measured frequency (Hz)
1,1,0	255	248
2,0,0	510	514
0,1,0	643	634
1,1,0	692	680
3,0,0	765	756
2,1,0	821	812

FIGURE 3.2. The ratio of the sound pressure at the centre of the primary source surface to the velocity of the primary source. The modal integers (n_1, n_2, n_3) are also listed for each resonant mode. Both measured and computed results are presented.

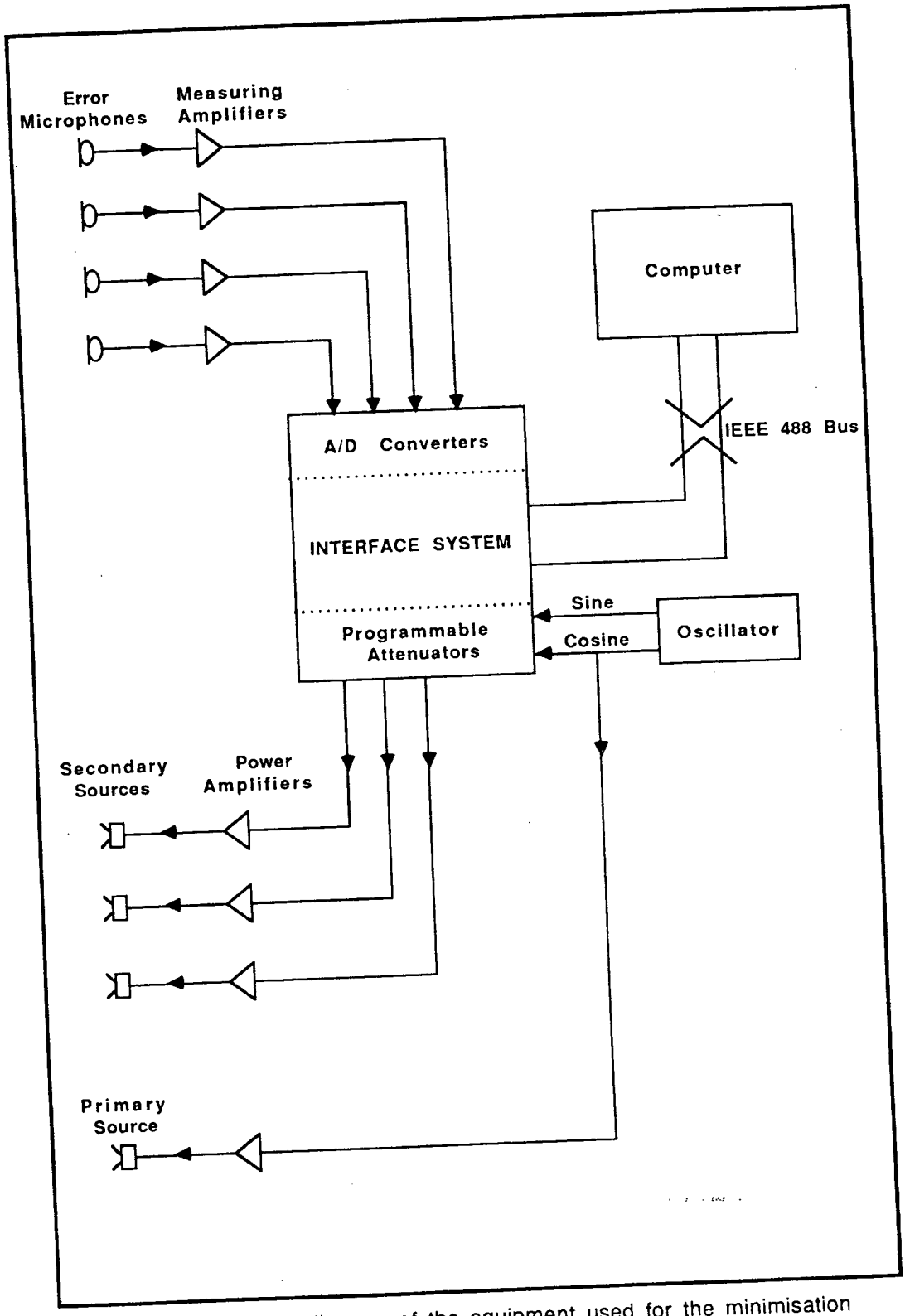

FIGURE 3.3. Block diagram of the equipment used for the minimisation procedure.

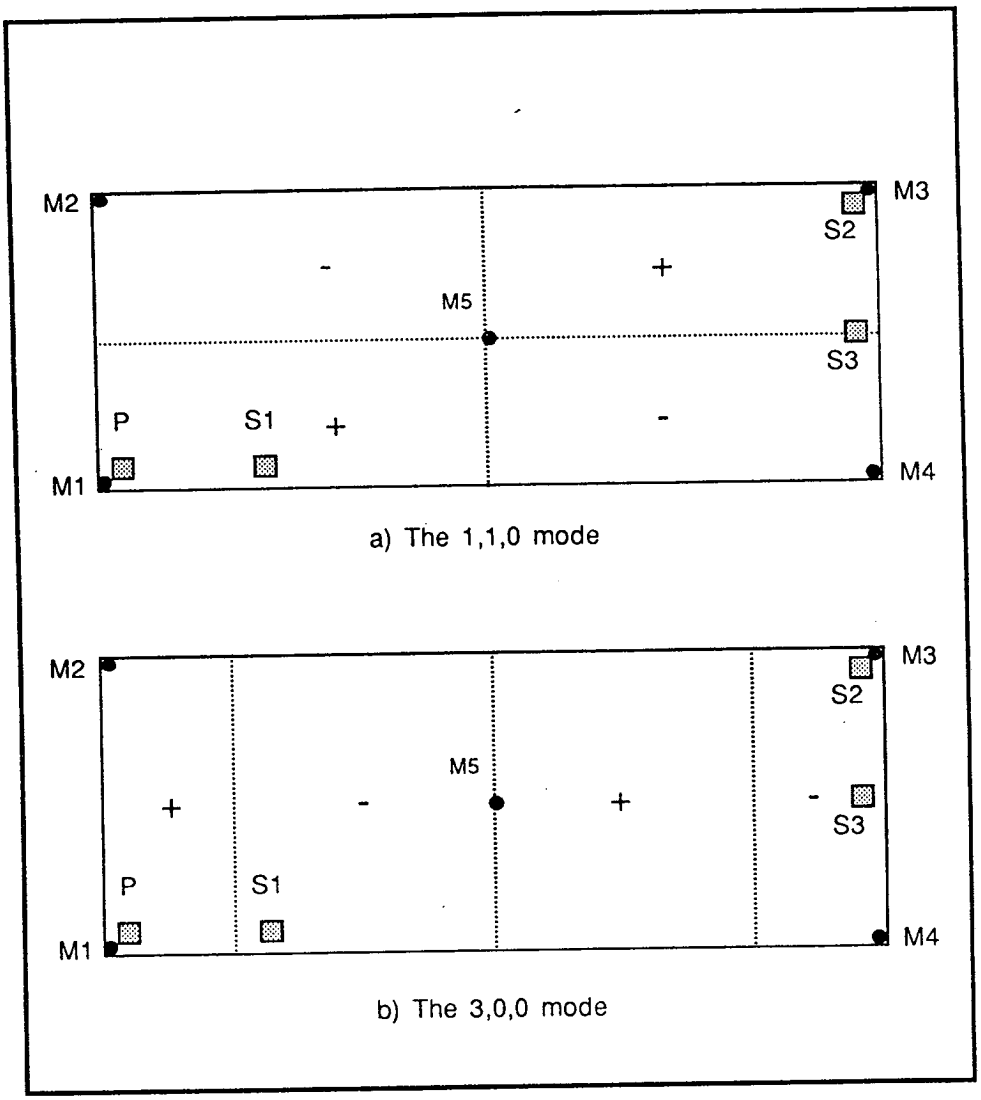

FIGURE 3.4. The nodal planes of a) the (1,1,0) and b) the (3,0,0) modes, together with the positions of the sources and sensors. The relative phases of the responses are also indicated for the case when only the primary source is operating.

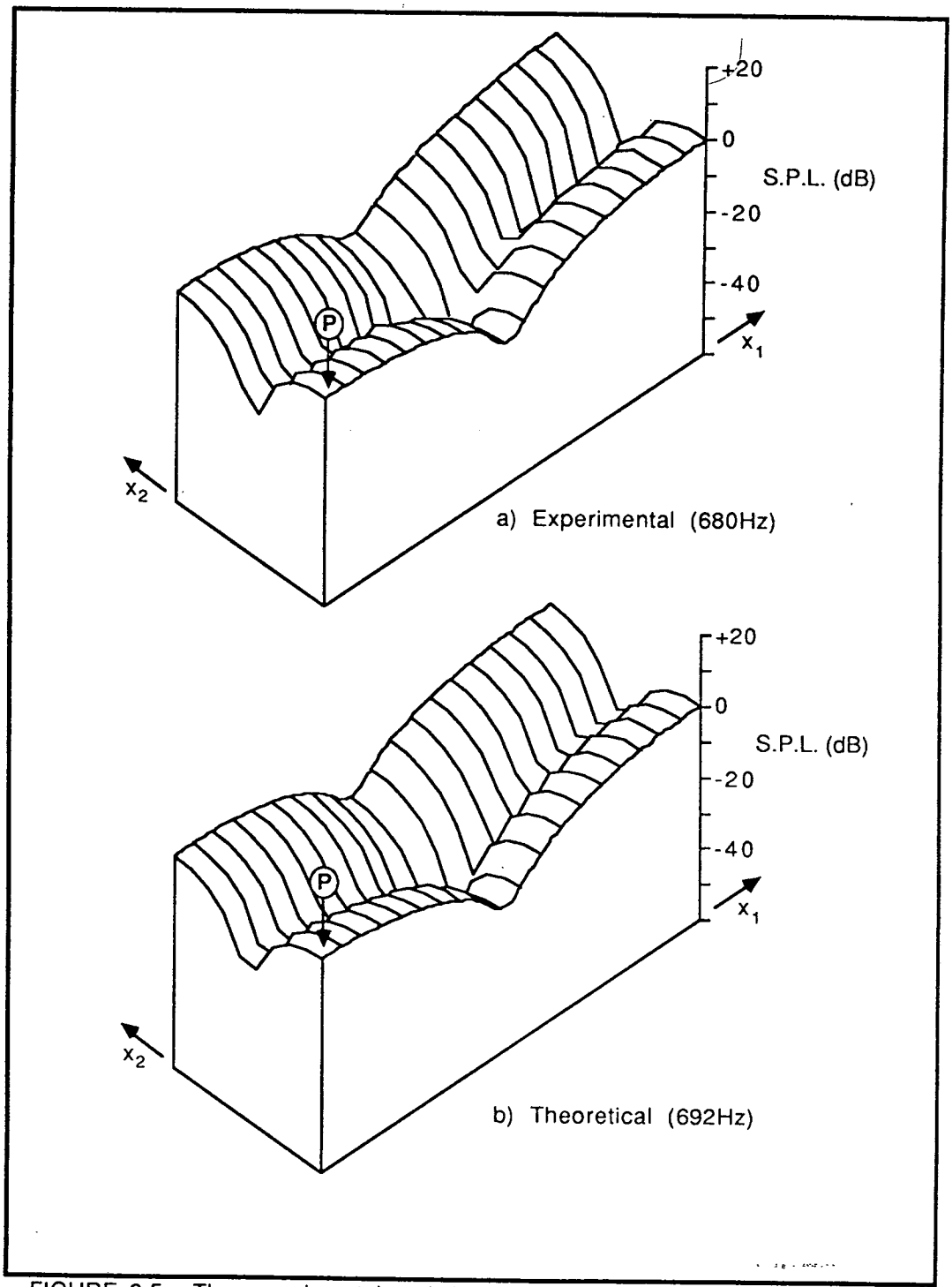

FIGURE 3.5. The experimental and theoretical sound pressure fields at 680Hz and 692Hz respectively in the x_3=0.025m plane of the enclosure shown in Figure 3.1 when it is excited by the primary source, P ,only.

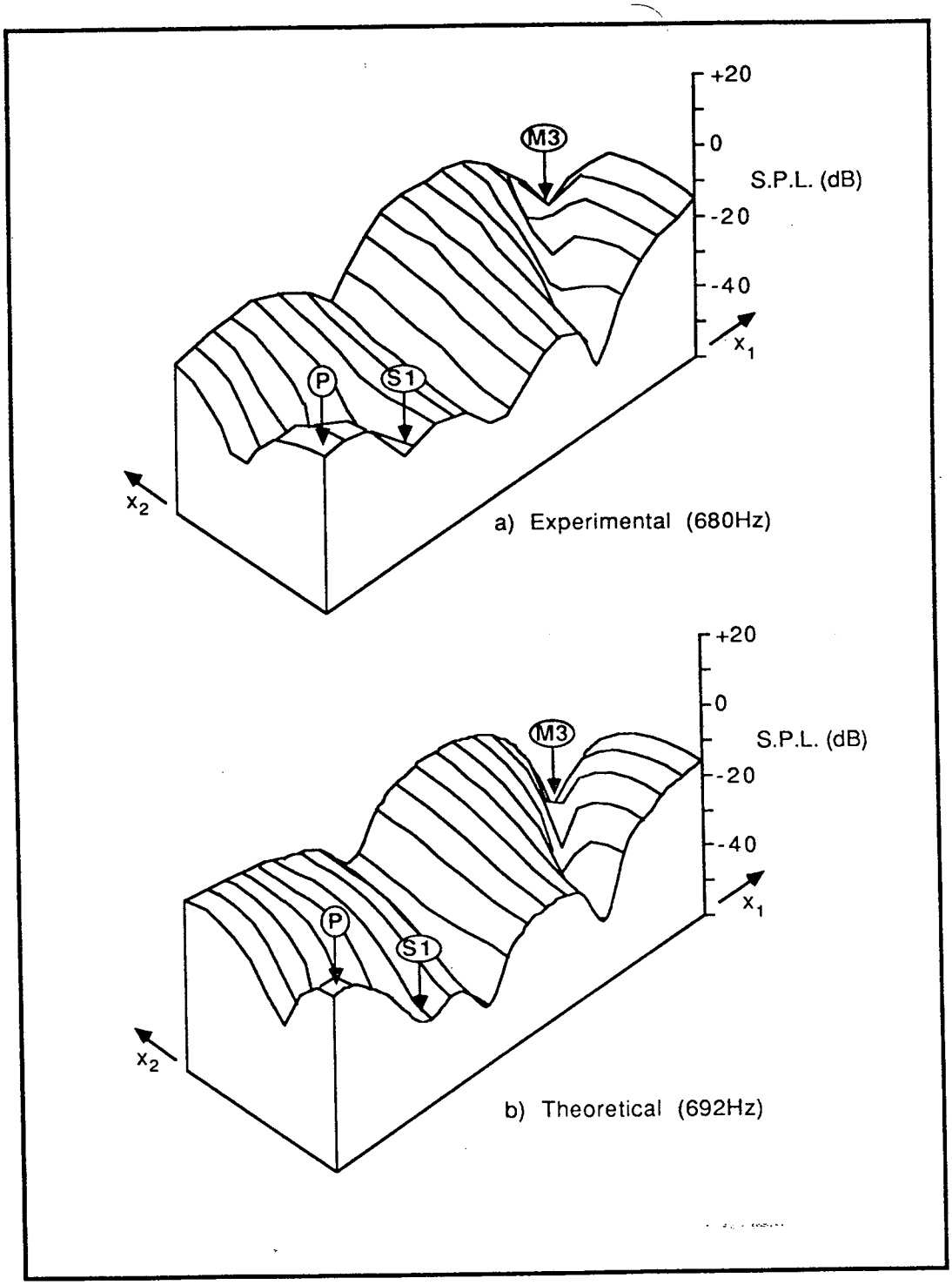

FIGURE 3.6. The experimental and theoretical sound pressure fields at 680Hz (692Hz) in the x_3=0.025m plane of the enclosure shown in Figure 3.1 when the pressure has been minimised at microphone M3 using secondary source S1.

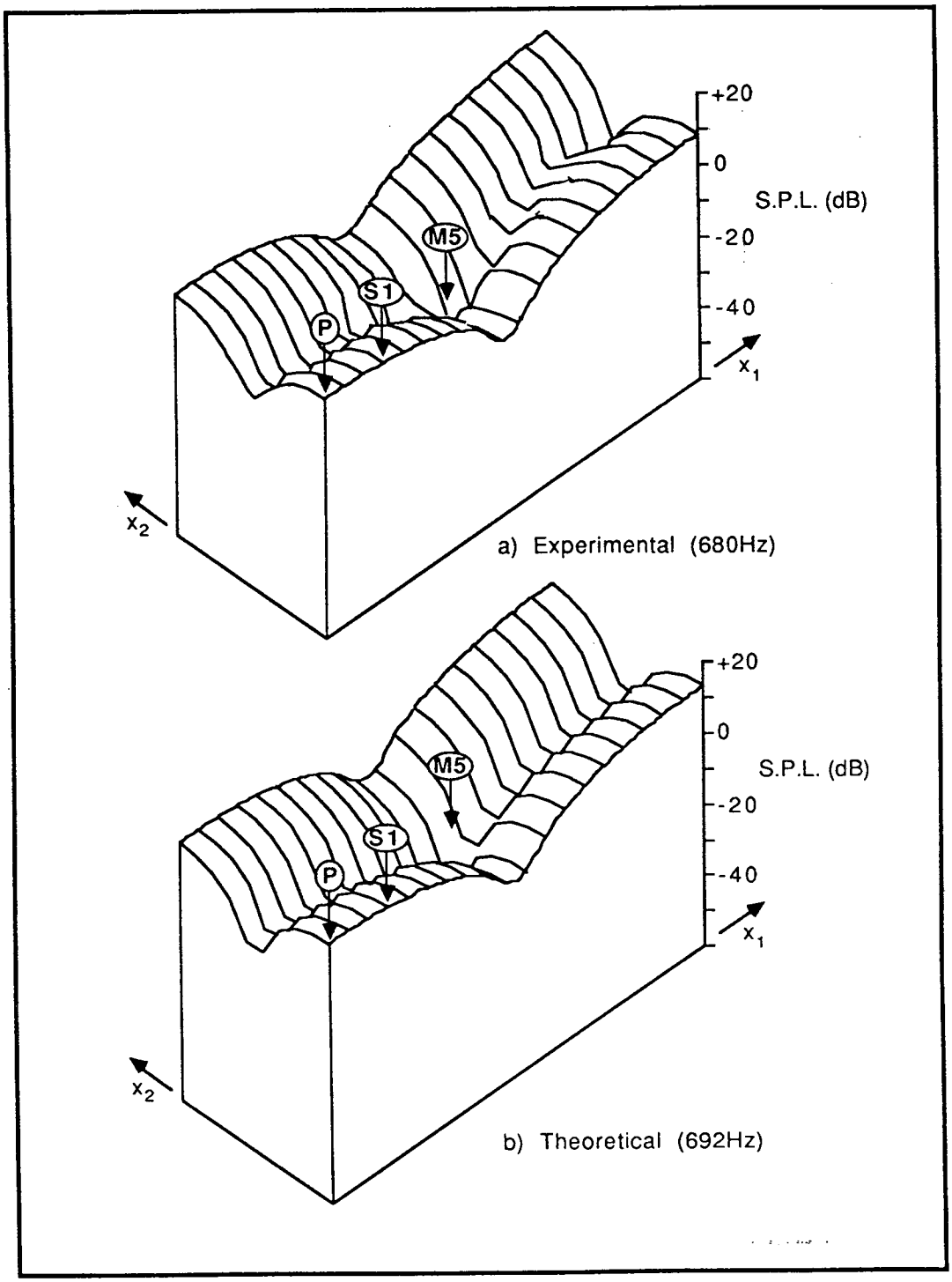

FIGURE 3.7. The experimental and theoretical sound pressure fields at 680Hz (692Hz) in the x_3=0.025m plane of the enclosure shown in Figure 3.1 when the pressure has been minimised at microphone M5 using secondary source S1.

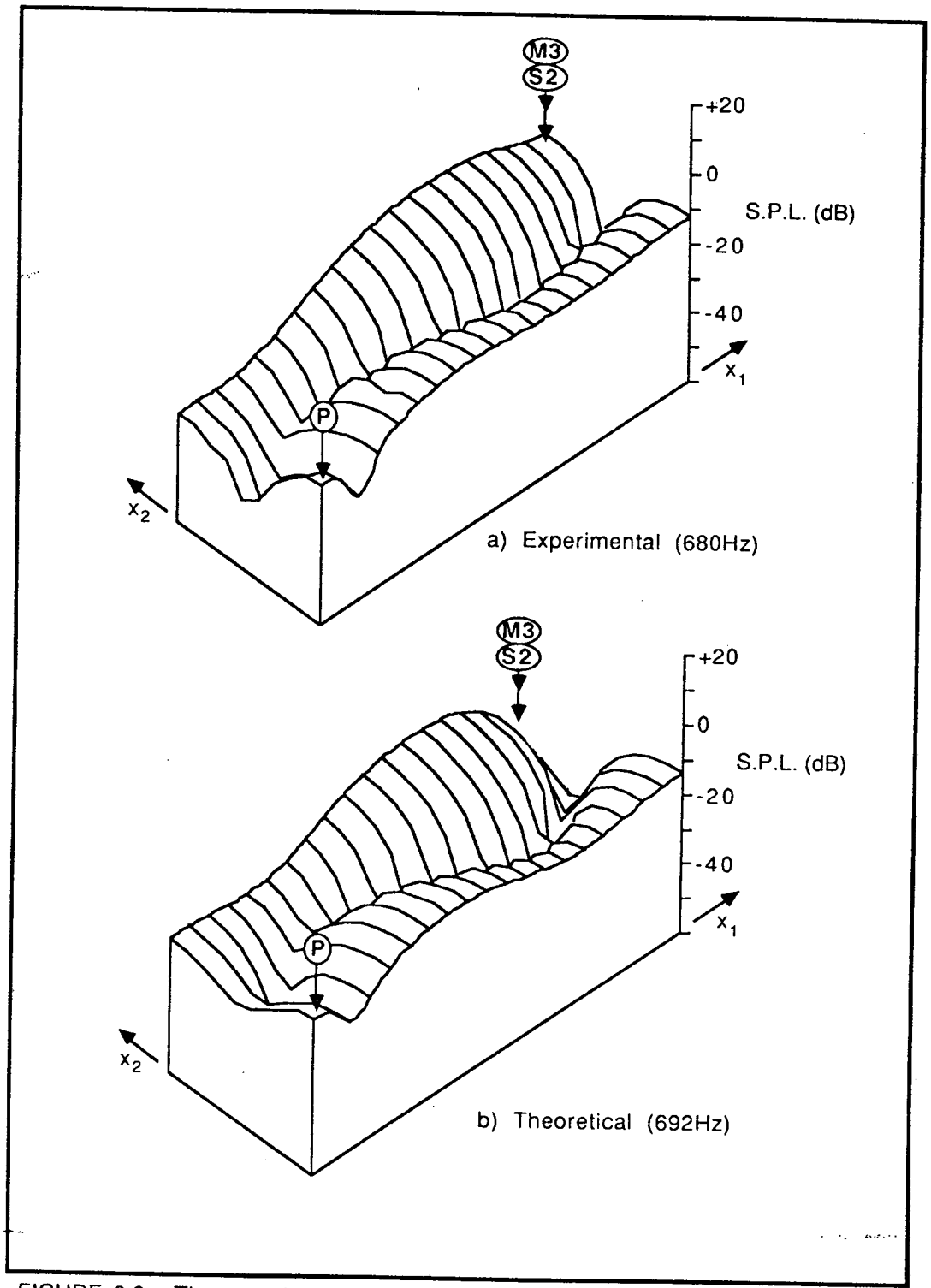

FIGURE 3.8. The experimental and theoretical sound pressure fields at 680Hz (692Hz) in the x_3 =0.025m plane of the enclosure shown in Figure 3.1 when the pressure has been minimised at microphone M3 using secondary source S2.

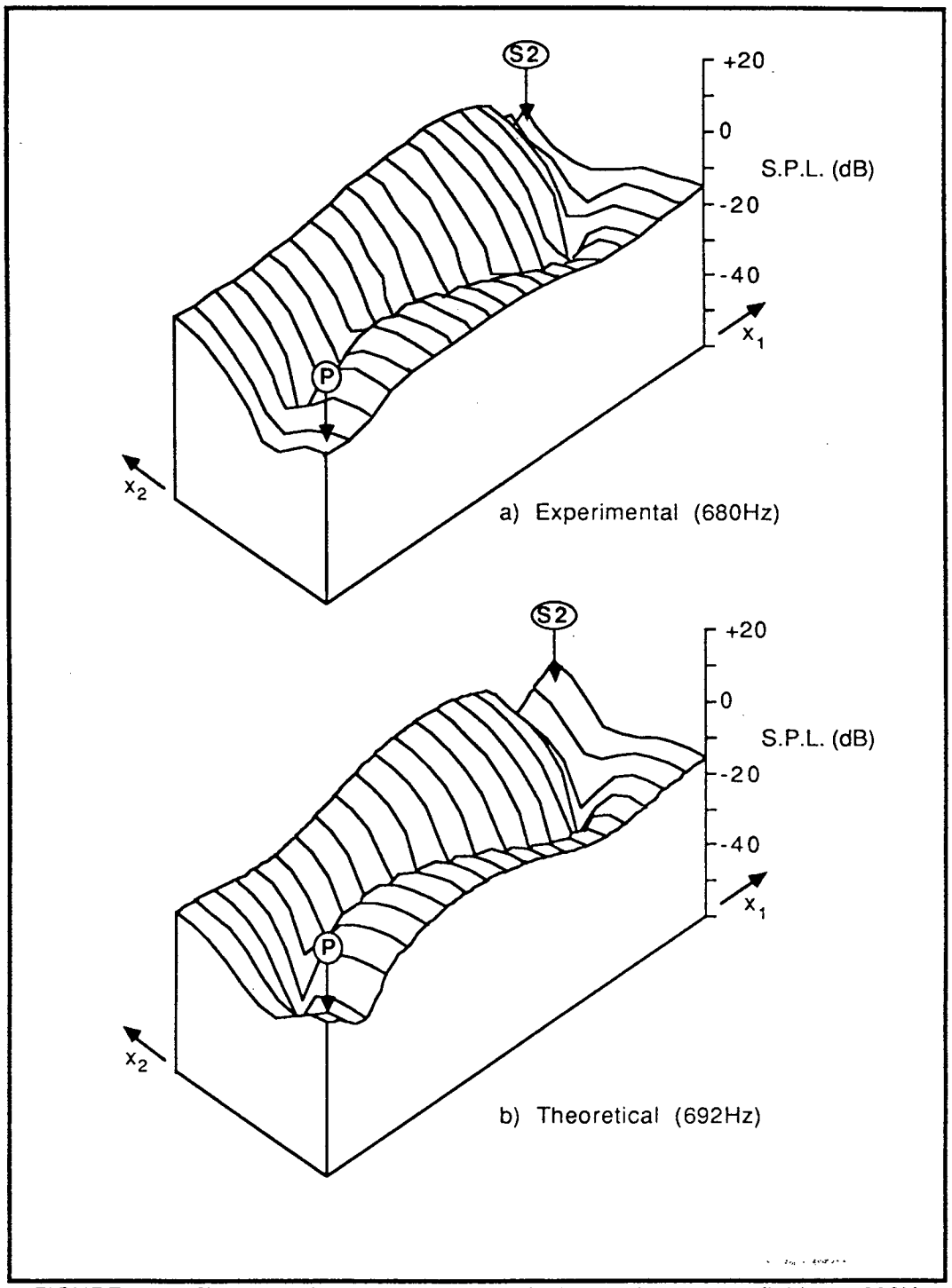

FIGURE 3.9. The experimental and theoretical sound pressure fields at 680Hz (692Hz) in the x_3=0.025m plane of the enclosure shown in Figure 3.1 when the sum of the squared pressures in the four corners (M1,M2,M3 & M4) has been minimised using secondary source S2.

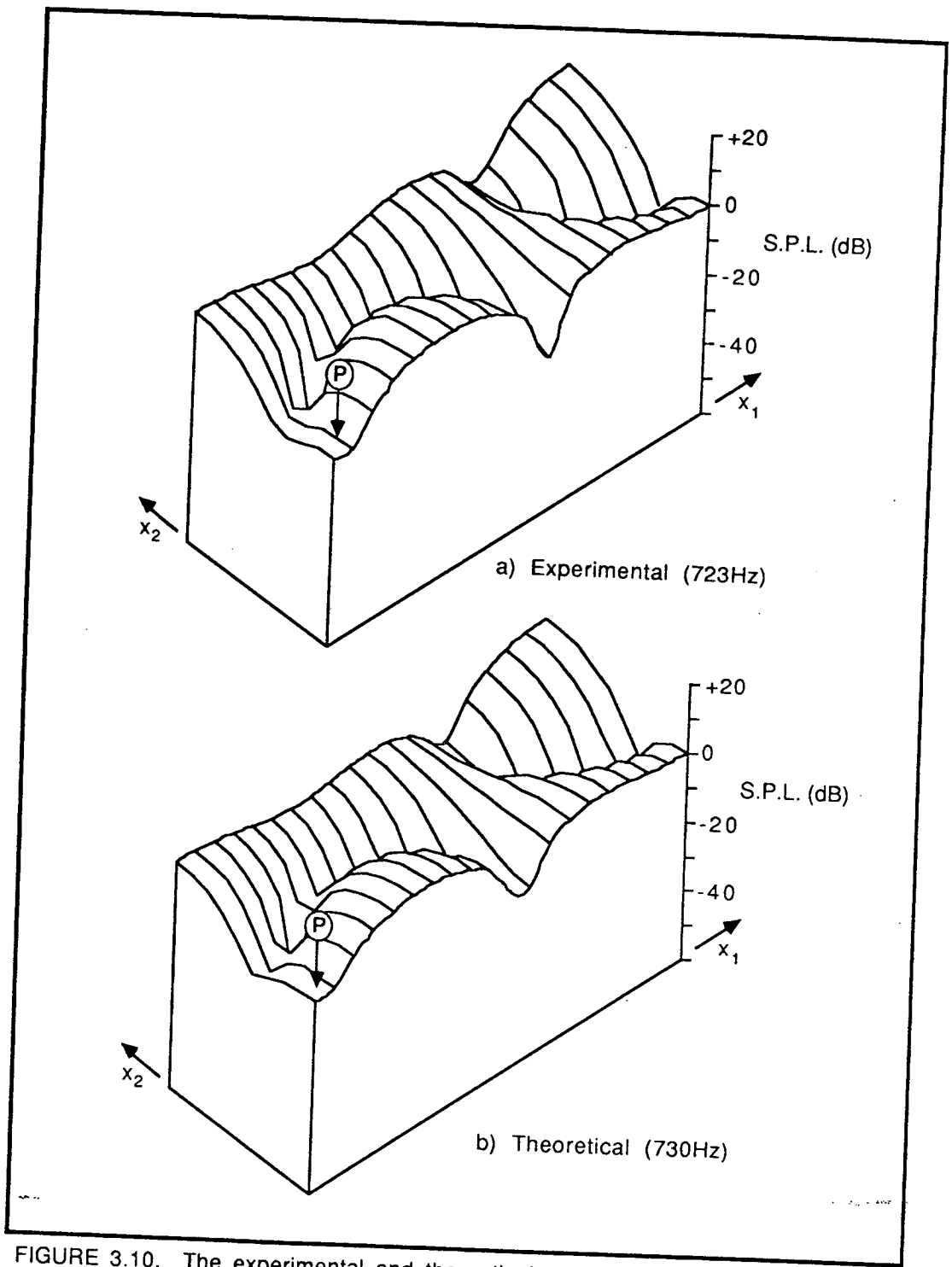

FIGURE 3.10. The experimental and theoretical sound pressure fields at 723Hz and 730Hz respectively in the x_3=0.025m plane of the enclosure shown in Figure 3.1 when it is excited by the primary source, P ,only.

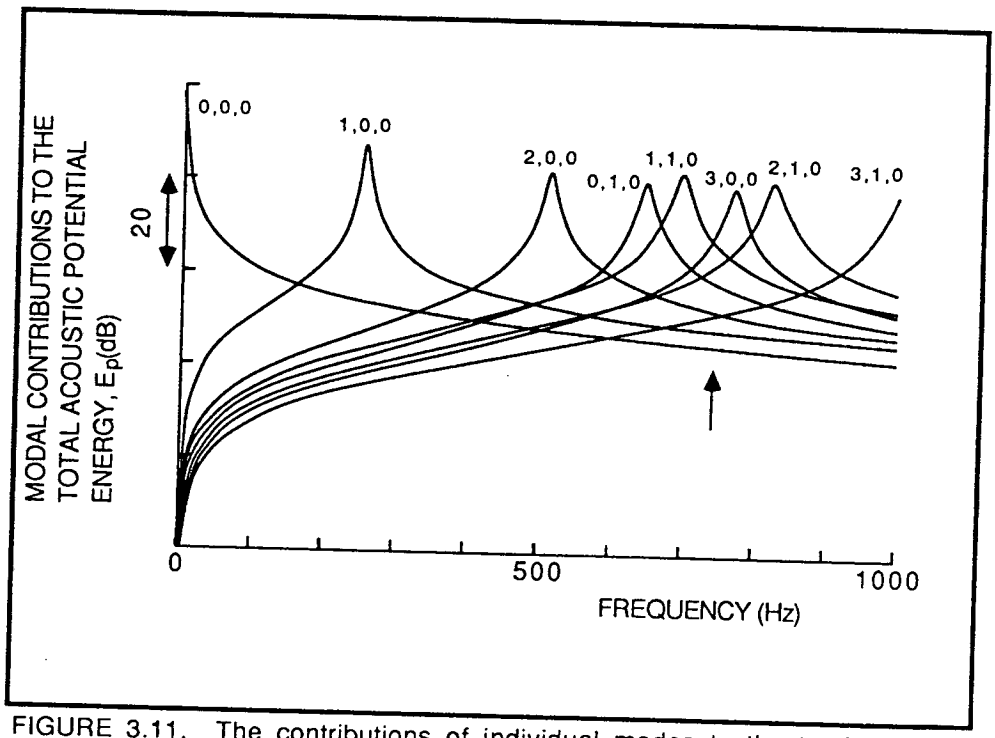

FIGURE 3.11. The contributions of individual modes to the total acoustic potential energy in the enclosure shown in Figure 3.1 when it is excited by the primary source, P , only. The arrow indicates the excitation frequency for the off resonance experiments.

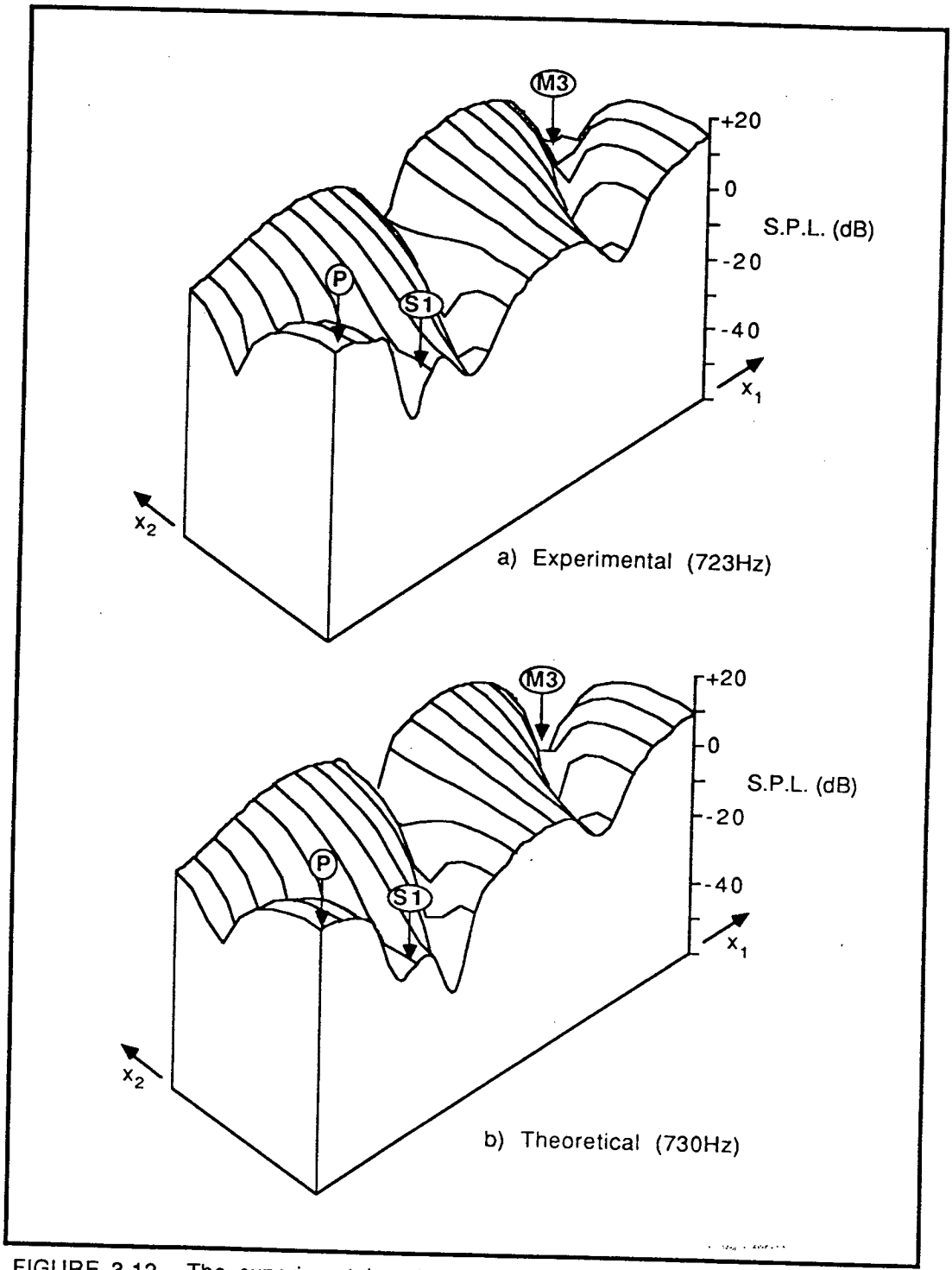

FIGURE 3.12. The experimental and theoretical sound pressure fields at 723Hz (730Hz) in the x_3 =0.025m plane of the enclosure shown in Figure 3.1 when the pressure has been minimised at microphone M3 using secondary source S1.

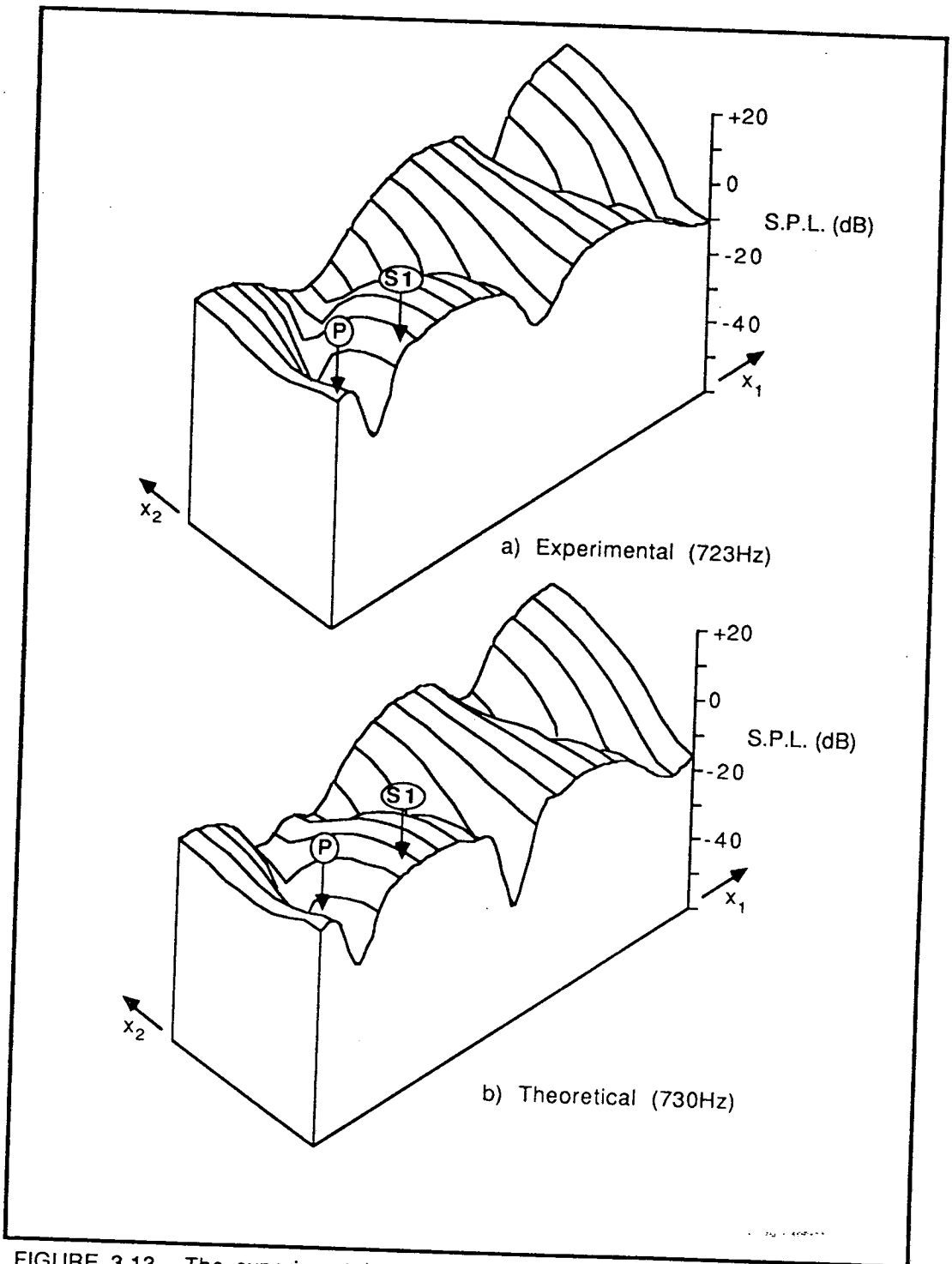

FIGURE 3.13. The experimental and theoretical sound pressure fields at 723Hz (730Hz) in the x_3=0.025m plane of the enclosure shown in Figure 3.1 when the sum of the squared pressures at the four corners (M1,M2,M3 &M4) has been minimised using secondary source S1.

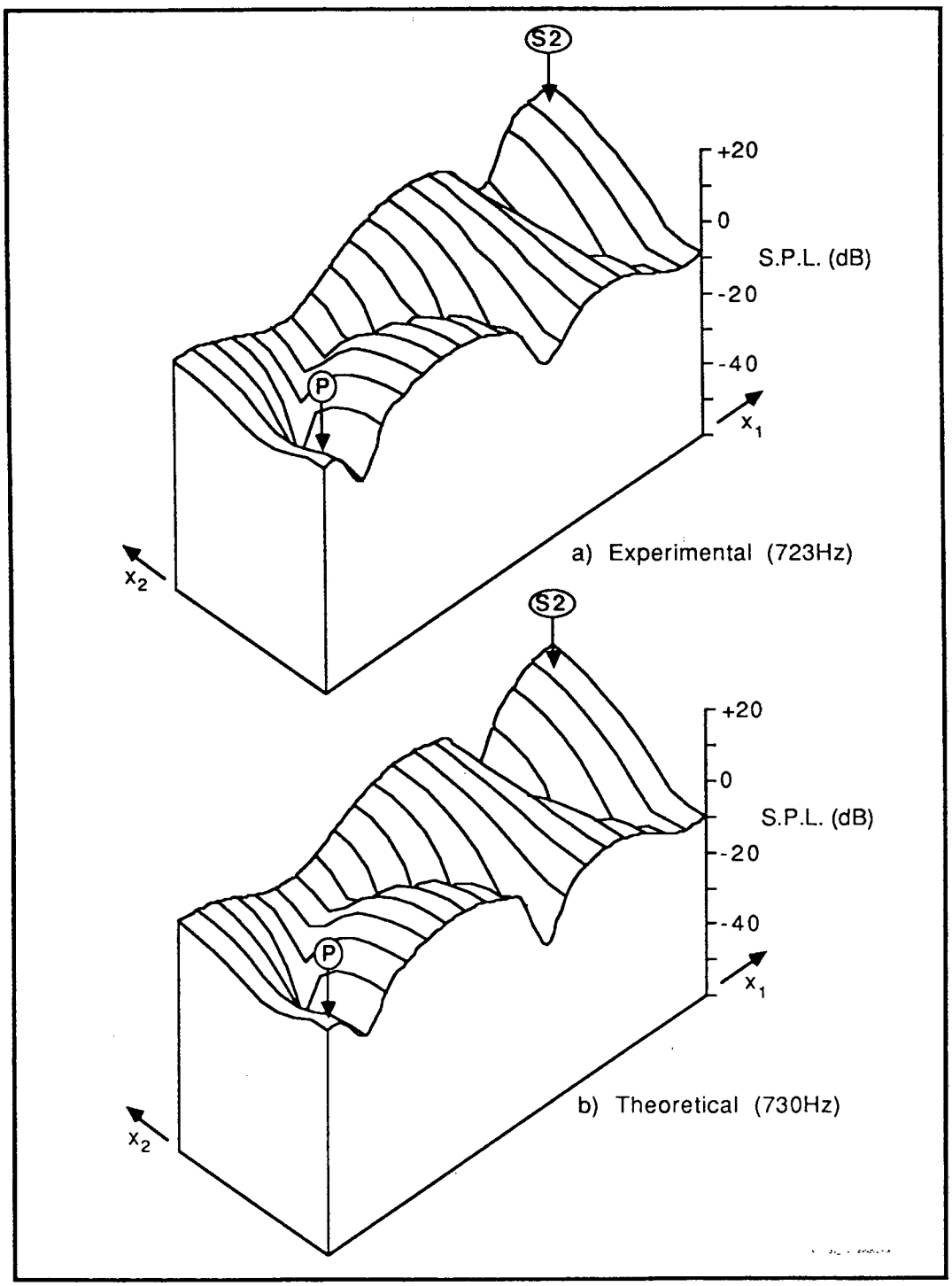

FIGURE 3.14. The experimental and theoretical sound pressure fields at 723Hz (730Hz) in the x_3=0.025m plane of the enclosure shown in Figure 3.1 when the sum of the squared pressures at the four corners (M1,M2,M3 &M4) has been minimised using secondary source S2.

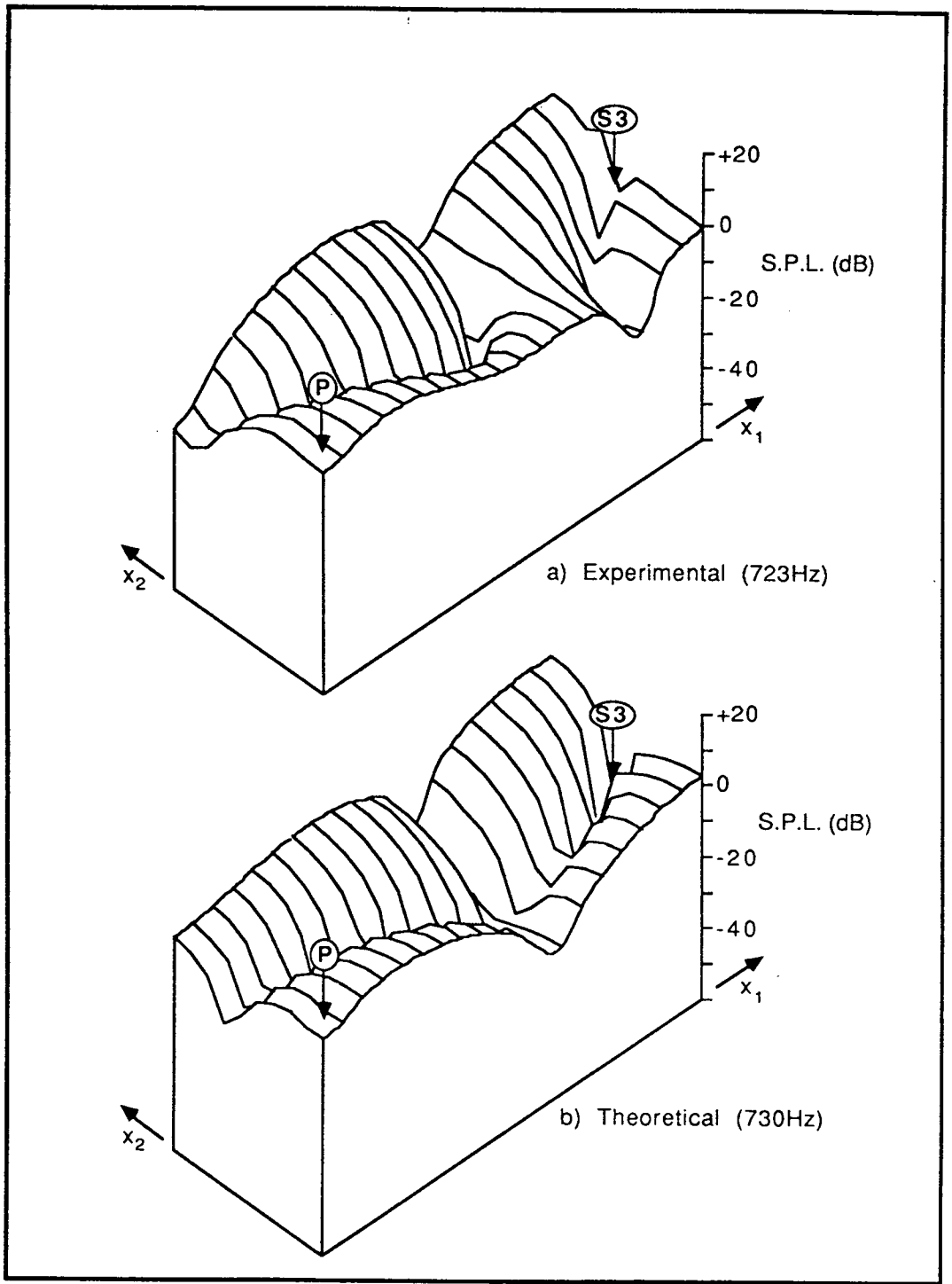

FIGURE 3.15. The experimental and theoretical sound pressure fields at 723Hz (730Hz) in the x_3=0.025m plane of the enclosure shown in Figure 3.1 when the sum of the squared pressures at the four corners (M1,M2,M3 &M4) has been minimised using secondary source S3.

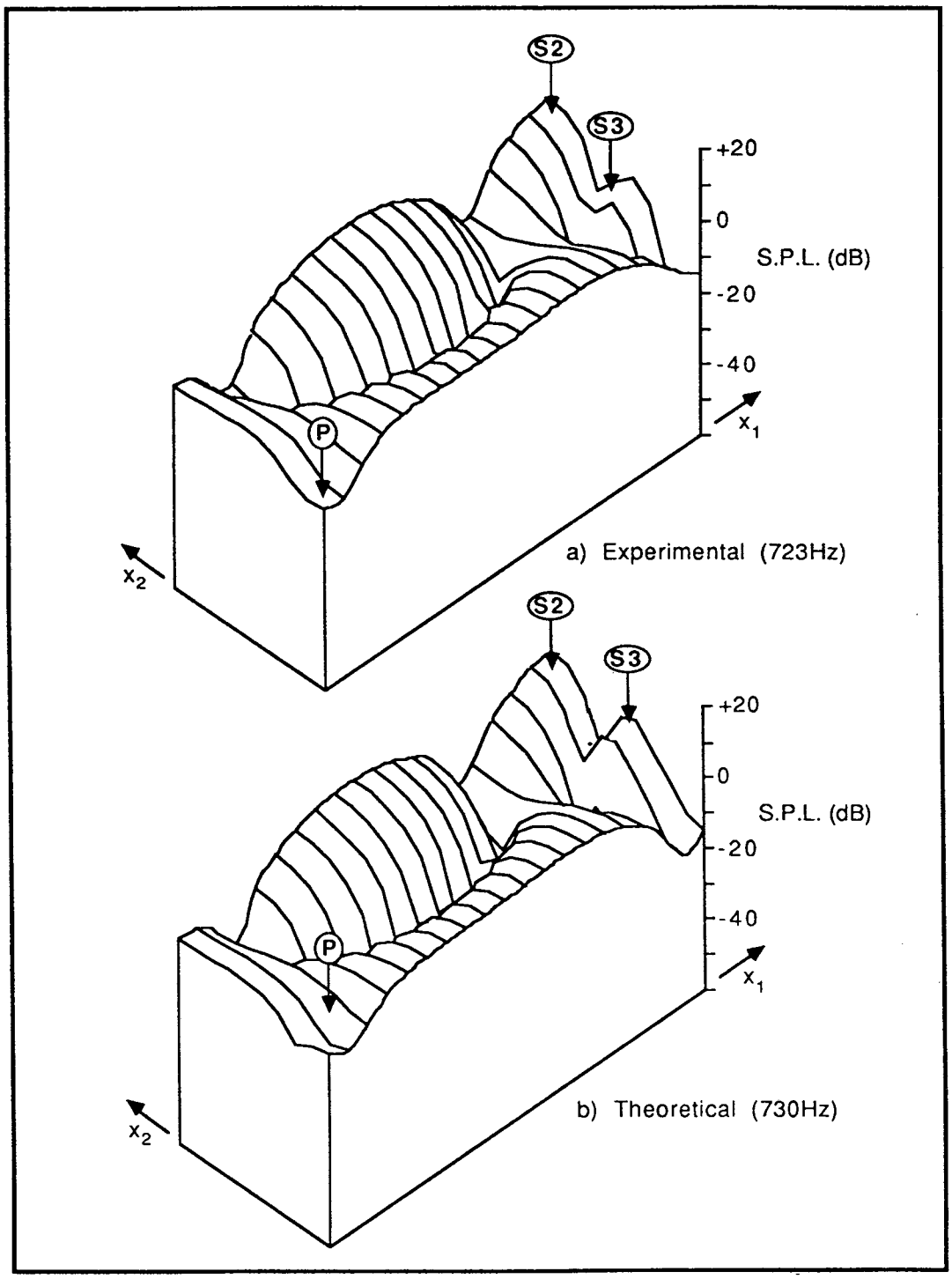

FIGURE 3.16. The experimental and theoretical sound pressure fields at 723Hz (730Hz) in the x_3=0.025m plane of the enclosure shown in Figure 3.1 when the sum of the squared pressures at the four corners (M1,M2,M3 &M4) has been minimised using secondary sources S2 & S3.

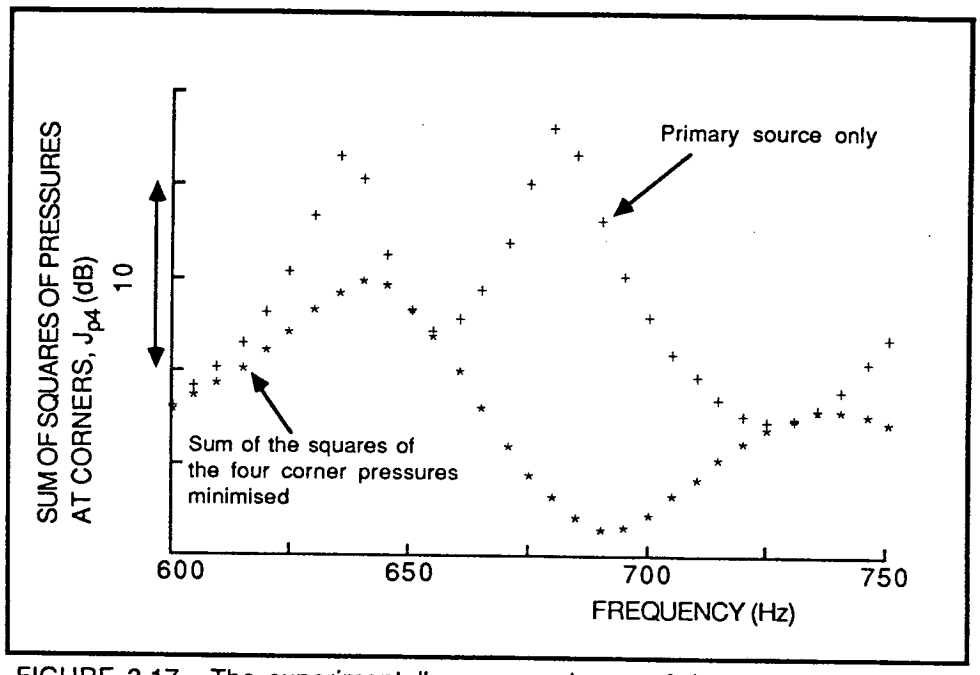

FIGURE 3.17. The experimentally measured sum of the squares of the pressures, J_{p4} , in the four corners of the enclosure (M1,M2,M3 & M4) plotted over a range of frequencies before and after J_{p4} has been minimised at these four sensor locations using secondary source S2.

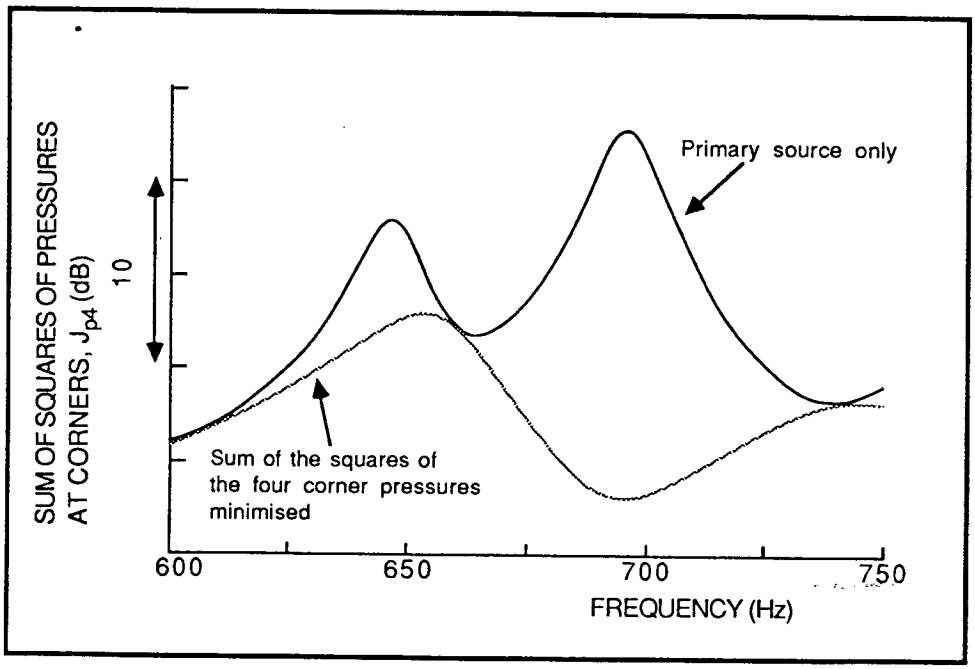

FIGURE 3.18. The theoretically calculated sum of the squares of the pressures, J_{p4} , in the four corners of the enclosure (M1,M2,M3 & M4) plotted over a range of frequencies before and after J_{p4} has been minimised at these four sensor locations using secondary source S2.

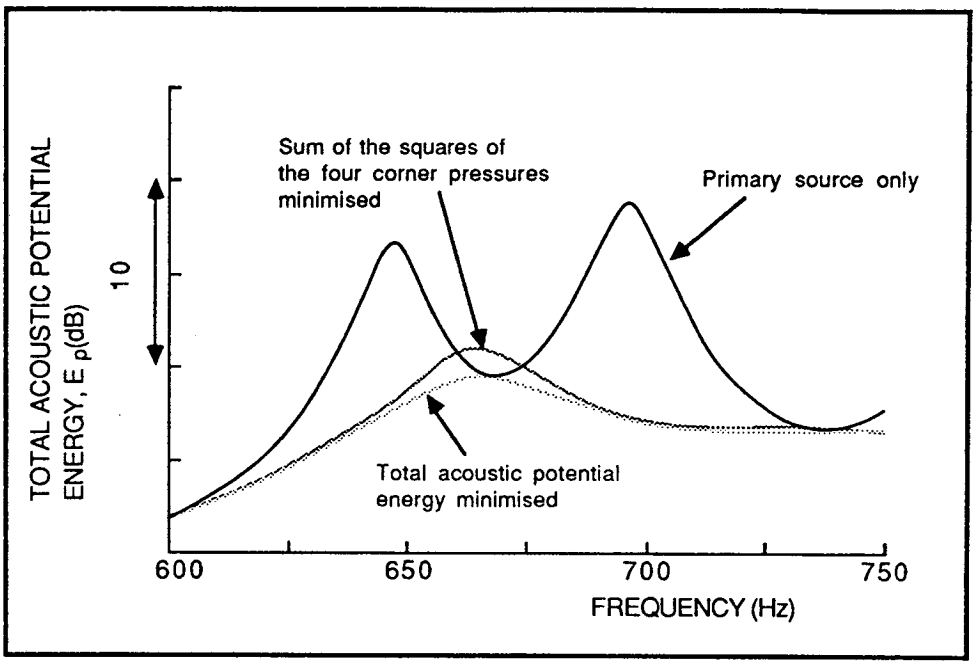

FIGURE 3.19. The calculated values of the total acoustic potential energy ,E_p , in the enclosure plotted over a range of frequencies before and after the sum of the squares of the pressures, J_{p4} ,in the four corners (M1,M2,M3 & M4) has been minimised using secondary source S2. The minimum values of E_p achievable using this source are also shown.

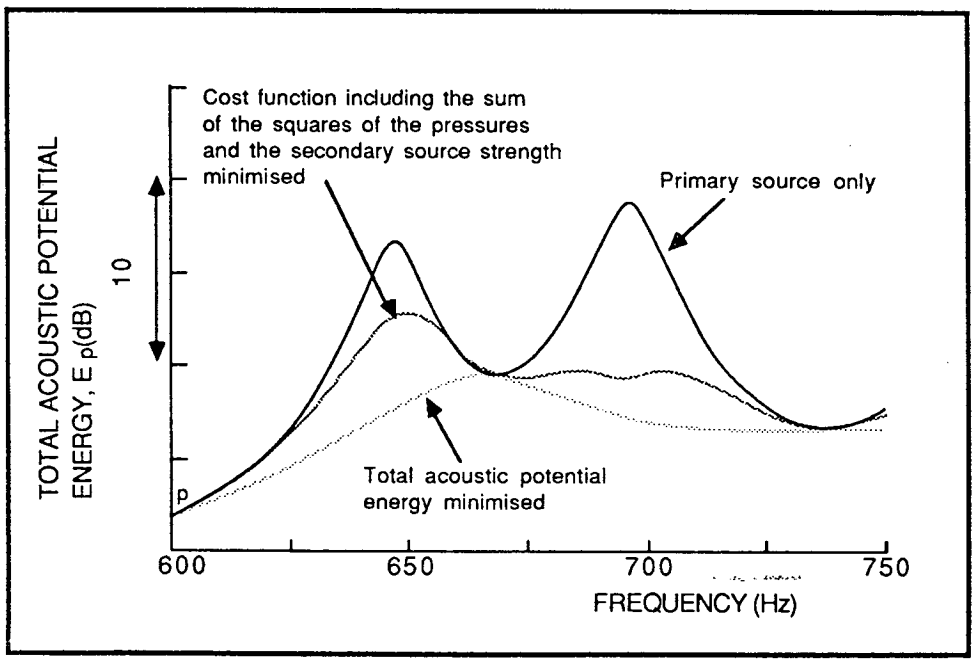

FIGURE 3.20. The calculated values of the total acoustic potential energy ,E_p , in the enclosure before and after a cost function involving the sum of the squares of the pressures, J_{p4} ,in the four corners and the secondary source strength has been minimised using secondary source S2. The minimum values of E_p achievable using this source are also shown.

CHAPTER 4

MECHANISMS OF THE ACTIVE CONTROL OF HARMONIC ENCLOSED SOUND FIELDS

4.1 Introduction

Although the results of Chapters 2 and 3 have adequately demonstrated the capability of an active control system to produce global reductions, and the requirements for both source and microphone locations in order to achieve these reductions, no conclusions have yet been drawn about the mechanisms by which these reductions are effected. The work in this chapter investigates, by computer simulation, the acoustic energy flow in these active control systems. It is shown that, whilst the room acoustics model used in Chapters 2 and 3 was perfectly adequate for the purposes for which it was used in those chapters, it is not sufficiently accurate to be used to study the acoustic intensity within the enclosure, particularly close to the enclosure walls. Consequently, the first two sections of this chapter describe the modifications which must be made to the original theory used which assumed hard enclosure walls. The modified model is then used to determine the energetics of various configurations of active control systems.

4.2 A Comparison of "Hard Walled" and "Soft Walled" Room Acoustics Theory for Determining Acoustic Intensity

4.2.1 The inclusion of damping in the hard walled model

The time averaged acoustic intensity for a harmonic pressure fluctuation of frequency ω may be evaluated as [55]

$$\underline{I}(\underline{x},\omega) = \tfrac{1}{2}\mathrm{Re}\{p^*(\underline{x},\omega)\underline{v}(\underline{x},\omega)\} \qquad (4.1)$$

where superscript * denotes complex conjugation, and $\underline{v}(\underline{x},\omega)$ is the acoustic particle velocity vector in the direction of the intensity vector. The particle velocity at the location specified by the vector $\underline{x}$ can be obtained from the acoustic pressure at the same location by the relationship

$$\underline{v}(\underline{x},\omega) = -\frac{1}{j\omega\rho}\nabla p(\underline{x},\omega) \qquad (4.2)$$

If the pressure is evaluated using the hard walled eigenfunctions derived previously as equation (2.11) and the result is substituted into equation (4.2), then the resulting velocity normal to the enclosure walls will be zero. Therefore, the intensity must also be zero, and consequently no energy may be dissipated at the enclosure boundaries, even though the effects of damping have apparently been accounted for in equation (2.16) by the inclusion of the complex eigenvalues. If acoustic intensity is to be used to determine the energetics of active noise control it is important to resolve this apparent anomaly, particularly as it has been suggested in other situations [11,62] that active noise control can work by increasing the acoustic volume velocity at lossy passive boundaries, thus increasing the energy absorption.

The assumptions used to derive equation (2.16) were that the enclosure surfaces were perfectly hard, but that energy dissipation could occur by some acoustic damping mechanism, the physical nature of which was unspecified. Looking at this in its most elementary form, the equation of free motion for a single mode of vibration, n, may be written as

$$m_n \frac{d^2 x_n}{dt^2} + c_n \frac{dx_n}{dt} + k_n x_n = 0 \qquad (4.3)$$

where m_n is the mass, c_n is the damping and k_n is the stiffness force acting on the mode. Now assuming a solution of the form $x_n = X_n e^{s_n t}$ and substituting this into equation (4.3) yields

$$s_n^2 + (2\xi_n\omega_n)s_n + \omega_n^2 = 0 \qquad (4.4)$$

where ω_n is the undamped natural frequency of the system, given by $\omega_n = \sqrt{k_n/m_n}$, and ξ_n is the damping ratio, given by $\xi_n = c_n/(2\sqrt{k_n m_n})$. Solving equation (4.4) for s_n gives

$$s_n = -\frac{2\xi_n\omega_n \pm \sqrt{4\xi_n^2\omega_n^2 - 4\omega_n^2}}{2} \qquad (4.5)$$

which, if it is now assumed the damping is very small so that $\xi_n^2 >> 1$ reduces to

$$s_n \simeq -\xi_n\omega_n \pm j\omega_n \qquad (4.6)$$

leading to a possible solution of equation (4.3) being written as

$$x_n = X_n e^{-\xi_n\omega_n t + j\omega_n t} \qquad (4.7)$$

Therefore, the harmonic term in the undamped solution has been replaced by two terms. The first of these is again a harmonic term (strictly speaking of a different frequency than the original motion, although this difference has been ignored due to the small damping assumption) and the second of these is a damping term, which causes the mode amplitude to decay at a rate $e^{-\xi_n\omega_n t}$.

The factor $\xi_n\omega_n$ may therefore be considered as a damping constant (using Morse's terminology [44]) which shall be denoted as C_n. This damping constant can be related to the "Q" of the mode resonance by the relationship

$$C_n = \frac{\omega_n}{2Q_n} \qquad (4.8)$$

where the Q has an identifying subscript because, in general, all modes will have a different sharpness of their resonance peaks.

4.2.2 The theory of Morse and Bolt

By introducing damping in the manner described above it is important to realize the physical constraints imposed. Perhaps most importantly it has not been specified what physical form the damping takes. The results obtained using the above model and presented in Chapters 2 and 3 all involved frequencies below 500 Hz. At such low frequencies the

majority of energy absorption is likely to occur at the enclosure boundaries rather than by damping within the enclosed medium [37]. If this is the case, then there must exist a particle velocity component normal to the enclosure walls, and the boundary condition $\partial p/\partial n = 0$, where n is the outward normal to the boundary, no longer applies. Consequently a more accurate theory must be used. One such possible theory will be outlined in the following paragraphs. This is the "first order theory" as suggested by Morse and Bolt [45], so called because, although it allows the effects of damping over the walls to be modelled, the assumptions made for its derivation still limit its applicability to cases where the damping consists of absorbing material which is locally reacting, evenly spread over each wall of the enclosure and produces only small damping. The method of solution still uses a modal representation of the pressure response, as given in equation (2.14). However, the modal characteristic functions and values are modified to suit the appropriate boundary conditions.

Assume that each wall of the rectangular enclosure is evenly covered with a locally reacting damping material which may be characterised by its specific acoustic admittance, $\beta = \kappa + j\sigma$, where κ is the specific acoustic conductance and σ is the specific acoustic susceptance. The values of the admittance, however, may vary from wall to wall and they shall be identified using subscripts, so $\beta_{x_1}^{0}$ and $\beta_{x_1}^{L_1}$ are the specific acoustic admittances of the walls at $x_1 = 0$ and $x_1 = L_1$ respectively, $\beta_{x_2}^{0}$ and $\beta_{x_2}^{L_2}$ are the acoustic specific admittances of the walls at $x_2 = 0$ and $x_2 = L_2$ respectively and $\beta_{x_3}^{0}$ and $\beta_{x_3}^{L_3}$ are those of the walls at $x_3 = 0$ and $x_3 = L_3$ respectively. The constituent modes of the acoustic response still satisfy the homogeneous Helmholtz equation, so

$$(\nabla^2 + k_n^2)\psi_n(\underline{x}) = 0 \qquad (4.9)$$

but now they must also satisfy the boundary conditions given by

$$\frac{\partial \psi_n(\underline{x}_s)}{\partial n} = \pm jk\beta\psi_n(\underline{x}_s) \qquad (4.10)$$

where it has been implicitly assumed that all the modes are being driven at the common frequency, ω. Therefore, from equations (4.9) and (4.10),

because $k\beta$ is a function of this driving frequency, then both the eigenfunctions and eigenvalues are functions of ω. It also follows from these two equations that if β is complex, then so too must the eigenfunctions and eigenvalues also be complex, which clearly results directly from energy absorption at the boundaries. Now proceeding as in Chapter 2 we can use equation (2.9) for the form of the Green function provided we can identify the appropriate forms of the eigenvalues and eigenfunctions consistent with equations (4.9) and (4.10). We thus separate each of equations (4.9) and (4.10) into three equations, each equation having a dependence on only one of the spatial coordinates x_1, x_2 or x_3 yielding, for example, for the x_1 coordinate

$$\frac{\partial^2 \psi_{n_1}(x_1)}{\partial x_1^2} + k_{n_1}^2 \psi_{n_1}(x_1) = 0 \qquad (4.11)$$

and

$$\frac{\partial \psi_{n_1}(0)}{\partial x_1} = jk\beta_{x_1}^{0} \psi_{n_1}(0) \qquad (x_1 = 0) \qquad (4.12)$$

$$\frac{\partial \psi_{n_1}(L_1)}{\partial x_1} = -jk\beta_{x_1}^{L} \psi_{n_1}(L_1) \qquad (x_1 = L_1) \qquad (4.13)$$

where the eigenfunctions and eigenvalues of equations (4.9) and (4.10) are given by

$$\psi_n(\underline{x}) = \psi_{n_1}(x_1)\psi_{n_2}(x_2)\psi_{n_3}(x_3) \qquad (4.14)$$

and

$$k_n^2 = k_{n_1}^2 + k_{n_2}^2 + k_{n_3}^2 \qquad (4.15)$$

As for the hard walled case of Section 2.2, a cosine function could be chosen as a suitable solution of equation (4.11) but this would have a complex argument. The analysis is therefore simpler if one chooses a solution of the form [55]

$$\psi_{n_1}(x_1) = \cosh(jk_{n_1}x_1 - \Phi_{n_1}) \qquad (4.16)$$

A better physical understanding of this may be obtained by rewriting equation (4.16) in terms of exponentials, so

$$\psi_{n_1}(x_1) = \tfrac{1}{2}\{e^{(jk_{n_1}x_1 - \Phi_{n_1})} + e^{(-jk_{n_1}x_1 + \Phi_{n_1})}\} \qquad (4.17)$$

Written like this the solution is seen to represent two waves, travelling in opposite directions, the ratio of the amplitudes of the two waves being given by $e^{-2Re\{\Phi_{n_1}\}}$ and the phase change by $-2\ Im\{\Phi_{n_1}\}$ [55].

Appendix 4.1 details the determination of the k_n's and Φ_n's of equation (4.16) for the case of the small admittance boundaries as considered here. Once these have been evaluated the resulting expressions for equations (4.14) and (4.15) can be substituted directly into equation (2.14) of Section 2.2 and the pressure response can be calculated.

4.2.3 The relationship between the mode damping constant and the random incidence absorption coefficient

It is often useful in practice to relate the mode damping constants to the random incidence energy absorption coefficients which are often used to describe surface properties in the study of diffuse sound fields. Full derivations of this relationship may be found in, for example, reference [63], consequently it will only be outlined here. The plane wave energy absorption coefficient, α_θ, due to a plane wave striking a plane surface at an angle θ to the surface normal may be written in terms of the specific acoustic conductance of the surface as [63]

$$\alpha_\theta = \frac{4\kappa^o_{x_1}\cos(\theta)}{(\kappa^o_{x_1}\cos(\theta) + 1)^2} \qquad (4.18)$$

where the wall at $x_1 = 0$ is being considered.

The random incidence energy absorption coefficient, α, may be related to the plane wave energy absorption coefficient, α_θ, by evaluating the fractional amount of energy absorbed by a surface element due to plane

waves impinging on that element with random angles of incidence, so

$$\alpha^{o}_{x_1} = 2\int_{o}^{\pi/2} \alpha^{o}_{\theta_1} \sin\theta\cos\theta\, d\theta \qquad (4.19)$$

which, on substituting equation (4.18) and performing the integral, yields for the $x_1 = 0$ wall

$$\alpha^{o}_{x_1} \simeq 8\kappa^{o}_{x_1} \qquad (4.20)$$

where it has been assumed that the wall is not too absorptive (provided $\alpha \leq 0.08$, an error of less than 10% is introduced by the approximation [63]). Substituting this result into equation (A4.1.11) for the mode damping constant gives

$$C_n \simeq \frac{c}{16V}\left[\epsilon_{n_1}(\alpha^{o}_{x_1} + \alpha^{L}_{x_1})S_1 + \epsilon_{n_2}(\alpha^{o}_{x_2} + \alpha^{L}_{x_2})S_2 + \epsilon_{n_3}(\alpha^{o}_{x_3} + \alpha^{L}_{x_3})S_3\right] \qquad (4.21)$$

Thus the extent to which each mode is damped depends not only on the distribution of the absorption material, but also on the type of mode. This analysis thus enables the damping effect of acoustic materials on individual modes to be written in terms of classical, diffuse field material properties. It must be remembered, however, that as a result of the effort to derive this convenient relationship it has been chosen to ignore some of the properties of modal sound fields. A more accurate solution must take account of the fact that each mode has only eight constituent plane waves having fixed angles of incidence with each of the walls. Therefore the random incidence energy absorption coefficient is not, strictly speaking, applicable to this analysis, and the damping constants should more accurately be written in terms of the plane wave energy absorption coefficients.

An alternative method of evaluating the relationships derived above is presented by Morse [44] where he uses the fact that the damping constant is equal to one half times the ratio between the power loss and the total energy of vibration, or

$$C_n \simeq \frac{Sc}{2V} \frac{(\text{average value of } \kappa_x \psi_n^2 \text{ over all walls})}{(\text{average value of } \psi_n^2 \text{ over room volume})} \qquad (4.22)$$

and thus by comparing the decay of energy in a single mode, given by $e^{-2C_n t}$, with the decay of sound energy in a diffuse field, given by Sabine as $e^{-S\bar{\alpha}ct/4V}$, where S is the total surface area and $\bar{\alpha}$ is the surface averaged random incidence energy absorption coefficient, he concludes that the quantity which takes the place of $\bar{\alpha}$ in the case of a single standing wave is the "average wall coefficient", $\bar{\alpha}_n$, where

$$\bar{\alpha}_n \simeq \frac{\text{average value of } 4\kappa_x \psi_n^2 \text{ over all walls}}{\text{average value of } \psi_n^2 \text{ over room volume}} \qquad (4.23)$$

If the eigenfunctions are substituted into equation (4.22) and the appropriate integrals evaluated, then the expression for C_n reduces to that of equation (4.21) following the application of equation (4.20).

4.2.4 Evaluation of the acoustic intensity in a "soft walled" rectangular enclosure

The theory presented above may now be used to calculate the energy flow in the active noise control systems presented in Chapters 2 and 3. It will be useful to be able to calculate both the power output of the primary and secondary sources and the time averaged acoustic intensity throughout the volume of the enclosure. Comparison of these quantities before and after the application of active control should lead to a better understanding of how the active control is effecting any reductions obtained.

From equations (4.1) and (4.2) the time averaged acoustic intensity vector at $\underline{x}$ in the x_1 direction, assuming harmonic excitation, is given by

$$I_1(\underline{x},\omega) = \tfrac{1}{2}\mathrm{Re}\left\{ - \frac{p^*(\underline{x},\omega)\, \frac{\partial p(\underline{x},\omega)}{\partial x_1}}{j\omega\rho} \right\} \qquad (4.24)$$

with similar expressions for the intensity in the x_2 and x_3 directions. The time averaged power output of each of the sources may be similarly evaluated by noting that the acoustic particle velocity over the source surface must be equal to the velocity of the source. Thus, for the plane piston sources used this becomes

$$W = \int_S \tfrac{1}{2}\mathrm{Re}\{p^*(\underline{x}_S,\omega)v(\omega)\}dS \qquad (4.25)$$

where the integration is performed over the surface, S, of the source whose normal velocity is $v(\omega)$. In some instances it may also be of use to evaluate the energy dissipation at the enclosure boundaries. This can be obtained by integrating the intensity normal to the enclosure walls over all the bounding surfaces having non-zero admittance. Thus, for example, the total time averaged power absorbed by the walls at $x_1 = 0$ and $x_1 = L_1$ respectively is given by

$$W^{\,o}_{x_1}(\omega) = \tfrac{1}{2}\mathrm{Re}\int_{x_2=0}^{L_2}\int_{x_3=0}^{L_3} \frac{\{p^*(0,x_2,x_3,\omega)p(0,x_2,x_3,\omega)\beta^{o}_{x_1}\}}{\rho c}\,dx_3dx_2$$

$$W^{\,L}_{x_1}(\omega) = \tfrac{1}{2}\mathrm{Re}\int_{x_2=0}^{L_2}\int_{x_3=0}^{L_3} \frac{\{p^*(L_1,x_2,x_3,\omega)p(L_1,x_2,x_3,\omega)\beta^{L}_{x_1}\}}{\rho c}\,dx_3dx_2 \qquad (4.26)$$

Equations (4.24) and (4.25) are relatively straightforward to implement computationally. All that is required in addition to the formulae already evaluated are the derivative and integral forms of the coshine function. Equation (4.26) is not so straightforward to evaluate, either computationally or analytically. However, as the absorptive enclosure walls are the only form of passive damping included in the current theory, the total energy flux into all the walls can be calculated simply from the relationship

Power input by primary source + Power input by M secondary sources

= Power absorbed at the boundaries (4.27)

The disadvantage of this approach is that the power loss over individual walls cannot be calculated. In order to do this simply, equation (4.26) can be simplified by noting that, for small admittance ratios, the eigenfunctions will not alter too much from the hard walled eigenfunctions. Consequently, the hard walled eigenfunctions of equation (2.11) can be substituted into equations (4.26) and, as shown by Bodlund in reference [64], their evaluation then becomes straightforward, yielding

$$W^{O}_{x_1} = \sum_{n=0}^{\infty} \frac{|a_n(\omega)|^2}{2\rho c}\{\epsilon_{n_1} L_2 L_3 \kappa^{O}_{x_1}\} \tag{4.28}$$

$$W^{L}_{x_1} = \sum_{n}^{\infty} \frac{|a_n(\omega)|^2}{2\rho c}\{\epsilon_{n_1} L_2 L_3 \kappa^{L}_{x_1}\}$$

where $a_n(\omega)$ can be written from equation (2.16) as

$$a_n(\omega) = \frac{\omega\rho c^2}{V} \frac{\int\int_S v(\underline{x}_S,\omega)\psi_n(\underline{x}_S)dS}{2\omega_n C_n - j(\omega_n^2 - \omega^2)} \tag{4.29}$$

Similar expressions are obtained for the energy absorbed by the remaining four walls of the enclosure. Note that in the surface integral of equation (4.29) the surface, S, refers to the surfaces of all sources which contribute to the energy of the sound field, not necessarily to the bounding surface of the enclosure. Of course, in performing this simplification some error will inevitably be introduced into the calculated energy absorption. However, the magnitude of this error can easily be checked by summing the energies absorbed by each of the walls calculated using the simplified theory of equations (4.28) and

by comparing this with the more accurate* value obtained using equation (4.27).

4.3 Computed Results for the Mechanisms of Active Control

4.3.1 A comparison of computed pressure and intensity fields using the "hard" and "soft" wall theories

The analytic results presented in the previous section have been implemented in the active minimisation computer prediction routine described in Chapter 2. Thus, as before, the modified computer program allows the minimisation of E_p or J_p using any number of sensors and piston sources in a rectangular enclosure, but now the specific acoustic admittance of each of the walls, rather than the modal damping ratio, must be specified. For any operating frequency the program will output the overall reduction in E_p, the power outputs of each of the sources both before and after the minimisation has been performed and also the energy absorbed by each of the enclosure walls. In addition, the acoustic pressure and intensity vectors may be plotted over any plane within the enclosure. This section presents results obtained using this program. The results have all been obtained using a theoretical model of the enclosure described in Section 3.2, and redrawn in Figure 4.1. For the present work only two possible secondary source locations and four error sensor locations shall be considered, indicated on Figure 4.1 as sources S1 and S2 and sensors M1, M2, M3 and M4. All the sources have again been modelled as 0.02 m square pistons. It is assumed that the specific acoustic admittance is constant over each of the four smaller walls of the enclosure and that its value is $\beta = 0.01 + j0.0$, whilst its value over the two larger walls is zero. This results in a modal damping ratio of 0.008 for the 692 Hz (1,1,0) mode.

** i.e., accurate to within the validity of the assumptions made to derive equations (8), (10), (11) and (13) of Appendix 4.1.*

Before considering the application of active noise control to this situation it will be instructive to compare a typical primary pressure and intensity distributions obtained using the "soft" walled theory of this chapter with the equivalent pressure and intensity distributions obtained using the "hard" walled theory of Chapter 2. Figure 4.2 show the sound pressure field in the x_3 = 0.025 m plane of the enclosure due to the primary source operating alone at 692 Hz with a normal surface velocity of 1 ms^{-1} (as was stated in Chapter 3, the pressure across the shortest dimension of the enclosure can be considered to be uniform and therefore results shall only be presented for this x_1 x_2 plane). Figure 4.2(a) shows the pressure field at 692 Hz evaluated using the "hard" walled theory where the damping constant has been determined from equation (4.28) and Figure 4.2(c) shows the equivalent pressure field evaluated using the "soft" walled theory. The differences between the two are indiscernible. Figures 4.2(b) and (d), however, show the acoustic intensity fields for this case plotted over the same x_1 x_2 plane. The intensity has been plotted as intensity level (re 1×10^{-12} W) and the arrow lengths are proportional to the intensity level. The difference between the two theories now becomes apparent. Figure 4.2(b), the intensity field obtained using the "hard" wall theory, indicates zero energy flux into the enclosure boundaries. Figure 4.2(d) on the other hand, clearly illustrates the absorption of acoustic energy at the boundaries, and in particular near the corners of the enclosure as one might expect [55]. However, despite these significant differences, it is interesting to note that there is surprisingly little error introduced by using the hard wall theory to evaluate the power balance within the enclosure. For example, using the hard wall theory the power output of the primary source is 0.0420 W and, from equations (4.28) which use the eigenfunctions of the hard walled theory, the total power absorption of the walls is -0.0418 W. Using the soft wall theory the primary source power output is 0.0423 W and therefore, on a power balance basis (equation (4.27)), the total power absorption of the walls is -0.0423 W.

Figures 4.3(a) to (d) show a similar set of results to those of Figures 4.2, but the primary source driving frequency is now 669 Hz and it therefore lies mid-way between two resonance frequencies. Once again,

the pressure fields are in excellent agreement, but the intensity fields differ substantially in regions close to the absorptive boundaries.

These results imply that, provided the damping is sufficiently small, the hard wall theory should provide accurate predictions of the power balance in the enclosed space. However, it will not be able to provide accurate predictions of the acoustic intensity distribution at all points in the enclosure, especially those points close to boundaries where energy absorption may occur. Because the results of this chapter will be making reference to intensity plots similar to those shown in Figures 4.2 and 4.3 all the results presented subsequently have been obtained using the soft wall theory.

4.3.2 Minimising the total time averaged acoustic potential energy, E_p

In reference [38] it has been suggested that when secondary sources are introduced and their source strengths are optimised to minimise the total time averaged acoustic potential energy, E_p, in the enclosure then the mechanism by which the reduction occurs is a mutual "unloading" of the primary and secondary sources. In other words, the phases of the pressure over each of the sources and the normal surface velocity of the source are arranged, as well as is possible from the physical constraints imposed, to be in quadrature. In order to demonstrate that this is what occurs, we shall investigate the effects of minimising E_p at each 1 Hz interval over a frequency range from 600 to 750 Hz using the single secondary source S2. Figure 4.4 shows the reduction in E_p which is obtained using this secondary source when its source strength is optimised to minimise E_p. Figure 4.5 shows the calculated power outputs of the sources.

The primary source power output before E_p has been minimised clearly follows the form of the primary E_p curve of Figure 4.4, as would be expected. After E_p has been minimised the primary source power output substantially decreases. It is therefore apparent from Figure 4.4 that the secondary source can neither inject nor absorb any great amount of power, and this is demonstrated on Figure 4.5, where the calculated power output of the secondary source is seen to be close to zero over the

entire frequency range considered. This effect can be demonstrated further by evaluating the acoustic pressure distribution over each of the source surfaces and seeing how this changes in relation to the source velocity when the active control is applied. Figure 4.6 shows the primary and secondary source velocities, where the upper graph shows the modulus of the velocities and the lower graph the phase relative to the primary source velocity. Both the primary and secondary sources are assumed to have an infinite internal impedance. Therefore the primary source velocity is unaffected by the pressure loading over its surface and its velocity remains constant both before and after minimisation. Also, the secondary source velocity is zero when only the primary source is operating. Figures 4.7 and 4.8 show the surface averaged pressures acting on the primary and secondary sources respectively. Again the information has been presented in modulus and phase form, with the phase being expressed relative to the primary source velocity. Comparing Figures 4,6, 4.7 and 4.8, two main effects are observed. Firstly, over both the primary and secondary source surfaces the minimisation of E_p has generally resulted in a decrease in the pressure amplitude acting on the source surfaces. The only frequency regions where the pressure has increased are those where it was initially low. Secondly, the action of minimising E_p has tended to cause the pressure over each source to adopt a 90° phase difference relative to that source's velocity. In the case of the secondary source (Figures 4.6 and 4.8) this quadrature phase relationship between the pressure and velocity has been achieved to an accuracy of greater than 10° over the entire frequency range. The phase matching for the primary source (Figures 4.6 and 4.7) is not so good, although this is understandable when it is considered that in this case only the phase of the pressure can be varied by the action of the active control, whereas over the secondary source both the pressure and velocity can be varied to obtain a better phase match.

Both of the effects mentioned above will result in the total source power outputs after E_p has been minimised being lower than the initial power output of the primary source operating alone.

Thus it appears that, in order to minimise the total acoustic potential energy within the enclosure, it is generally more effective for

the primary and secondary sources to mutually load each other to prevent energy radiation than for the secondary source to absorb energy.

Although the results presented in Figures 4.4 to 4.8 have clearly demonstrated the mechanism by which reductions in E_p are effected when the secondary source is set to minimise E_p, it may still be instructive to evaluate the time averaged acoustic intensity fields at specific frequencies. Two frequencies shall be considered. The first of these is 692 Hz, corresponding to the resonance frequency of the (1,1,0) mode. The acoustic pressure and intensity fields due to the primary source operating alone at this frequency have already been presented in Figures 4.2(c) and (d) respectively. When E_p is minimised using the single secondary source S2 a reduction in E_p of 11.1 dB is obtained and the pressure and intensity fields of Figures 4.9(a) and (b) result. Whilst there are differences between the primary and residual intensity fields of Figures 4.2(d) and 4.9(b) respectively there are no obvious regions in the residual intensity field where new sources or sinks of energy have been created. Consequently, it is difficult to obtain any more useful information from this result. Figures 4.10(a) and (b) show the acoustic pressure and intensity fields after E_p has been minimised again using source S2 but now at a frequency of 669 Hz. This frequency lies midway between two resonances. The pressure and intensity fields due to the primary source operating alone at this frequency have already been presented in Figures 4.3(c) and (d). In this case, the intensity and pressure fields following the minimisation of E_p are very similar to those before, although this is not too surprising as at this frequency using this source it is only possible to obtain an optimal reduction in E_p of 0.02 dB.

4.3.3 Minimising the sum of the squared pressures, J_p, in the four corners of the enclosure

It has been noted previously in Chapter 3 that minimising the sum of the squared pressures in the four corners of the enclosure, J_{p4}, will result in a near optimal reduction in E_p. The mathematical analysis presented in Section 2.4.5.2 gave an indication as to why this behaviour occurs and it was concluded that minimising the squared and summed corner pressures in sound fields of low modal density does indeed result in a

very similar effect to minimising E_p. This has been checked for the present situation and it has been shown to be true. Figure 4.11 shows the reduction in E_p obtained when J_{p_4} is minimised using the single secondary source S2 and the four error sensors M1, M2, M3 and M4. Figure 4.12 shows the power outputs of the sources and, as with the comparable results when E_p is minimised using source S2 (Figure 4.5), the reduction in E_p occurs not by energy absorption, but by the prevention of energy radiation. Although not presented here for conciseness, results very similar to those of Figures 4.6 to 4.10 have also been obtained for the case when J_{p_4} is minimised, further demonstrating the similarity between minimising E_p and J_{p_4} in this type of situation.

4.3.4 Minimising the total power output of the secondary sources, W_s

Although minimising E_p can, in some instances, result in a relatively small amount of energy being absorbed by the secondary sources, it has been shown in Section 4.3.2 that energy absorption is not the main mechanism involved in the minimisation process. However, in their 1953 paper [11], Olson and May suggested a possible use for their energy absorbing active noise control system. The suggestion was to place several of the single microphone/single loudspeaker active control systems near the corners of a room and to phase the pressure over the source surface relative to the source velocity such that they act as active dampers, thus dissipating energy from the acoustic field. As the total power output of the secondary sources, W_s, is a quadratic function of the secondary source strengths it is a straightforward matter to formulate the minimisation of W_s in the same manner as the minimisation of E_p or J_p in Chapter 2. However, because the minimum total power output of the secondary sources will be negative, minimising W_s will result in the power absorption of the secondary sources being maximised [86].

The total power output, W_s, of M secondary sources can be written from equation (4.25) as

$$W_s = \tfrac{1}{2}\mathrm{Re}\{(\underline{p}_{ss}^T + \underline{p}_{sp}^T)\underline{q}_s^*\} \qquad (4.29)$$

where $\underline{p}_{ss}$† is a complex vector of order M whose m'th element specifies the component of the pressure due to the M secondary sources which acts over the m'th secondary source surface, $\underline{p}_{sp}$† is a complex vector of order M whose m'th element specifies the component of the pressure due to the primary source only which acts over the m'th secondary source, and $\underline{q}_s$ is a complex vector of order M whose m'th element specifies the strength of the m'th secondary source. The vector $\underline{p}_{ss}$ can be expressed in terms of the secondary source strengths via a transfer impedance matrix, $\underline{z}_{ss}$†, such that equation (4.29) can be rewritten as

$$W_s = \tfrac{1}{2}\mathrm{Re}\{(\underline{z}_{ss}\underline{q}_s + \underline{p}_{sp})^T\underline{q}_s^*\} \qquad (4.30)$$

which on expanding yields

$$W_s = \tfrac{1}{2}\mathrm{Re}\{\underline{q}_s^T\underline{z}_{ss}^T\underline{q}_s^* + \underline{p}_{sp}^T\underline{q}_s^*\} \qquad (4.31)$$

Taking the real part of equation (4.31) gives

$$W_s = \tfrac{1}{4}\{\underline{q}_s^T\underline{z}_{ss}^T\underline{q}_s^* + \underline{q}_s^H\underline{z}_{ss}^H\underline{q}_s + \underline{p}_{sp}^T\underline{q}_s^* + \underline{p}_{sp}^H\underline{q}_s\} \qquad (4.32)$$

Since each of these terms is a scalar then it is equal to its own transpose and thus the equation can be rearranged to give

$$W_s = \tfrac{1}{4}\{\underline{q}_s^H\underline{z}_{ss}\underline{q}_s + \underline{q}_s^H\underline{z}_{ss}^*\underline{q}_s + \underline{q}_s^H\underline{p}_{sp} + \underline{p}_{sp}^H\underline{q}_s\} \qquad (4.33)$$

which can be written as

$$W_s = \underline{q}_s^H\{\tfrac{1}{4}(\underline{z}_{ss} + \underline{z}_{ss}^*)\}\underline{q}_s + \underline{q}_s^H(\tfrac{1}{4}\underline{p}_{sp}) + (\tfrac{1}{4}\underline{p}_{sp}^H)\underline{q}_s \qquad (4.34)$$

Equation (4.34) is now in the Hermitian quadratic form, as a quadratic function of the complex secondary source strengths, or

$$W_s = \underline{q}_s^H\underline{A}\underline{q}_s + \underline{q}_s^H\underline{b} + \underline{b}^H\underline{q}_s \qquad (4.35)$$

---

†*Note that because piston sources are assumed, the elements of the vectors* $\underline{p}_{ss}$ *and* $\underline{p}_{sp}$ *and the matrix* $\underline{z}_{ss}$ *all involve surface integrals over the relevant source's surface*

where the matrix $\underline{A}$ equals $\frac{1}{2}Re(\underline{Z}_{ss})$ and the vector $\underline{b}$ equals $\frac{1}{4}\underline{p}_{sp}$. Differentiating equation (4.35) with respect to the real and imaginary parts of the secondary source strengths and setting the result equal to zero enables the optimal secondary source strengths which minimise W_s to be evaluated as

$$\underline{q}_{s2} = -[\tfrac{1}{2}Re(\underline{Z}_{ss})]^{-1}[\tfrac{1}{4}\underline{p}_{sp}] \qquad (4.36)$$

This result has been included in the computer program used to derive the results of the previous two sections, thus enabling the effect of maximising the secondary source power absorption to be theoretically evaluated.

Figure 4.13 shows the reduction in E_p which is obtained over the frequency range 600 Hz to 750 Hz when the single secondary source S2 is introduced and its source strength optimised according to equation (4.36). At first sight the result is rather surprising because, at frequencies away from the two resonance frequencies included in the frequency range, the total energy <u>increases</u> despite the secondary source <u>absorbing</u> energy. Figure 4.14 shows the power outputs of the sources involved and the secondary source is clearly absorbing energy. However, what is also occurring is that, at frequencies at which the power output of the primary source is initially low, the secondary source is loading the primary source such that it radiates more energy, thus enabling the secondary source to absorb more energy. This can be shown more clearly by studying the pressures over the source surfaces, together with the source velocities, as was done in Section 4.3.2. Figure 4.15 shows the constant primary source velocity and the velocity of secondary source S2 which is required to minimise W_s. Figure 4.16 shows the modulus and phase of the pressure averaged over the primary source surface both before and after W_s has been minimised. The action of setting source S2 to minimise W_s has had two main effects. It has generally increased the pressure amplitude acting on primary source surface and it has also tended to drive this pressure such that it is in phase with the primary source velocity, thus increasing the power output of the primary source. Figure 4.17 shows the pressure acting on the secondary source S2 both before and after W_s has been minimised. Notice that the optimal

secondary source velocity is 180° out of phase with the pressure acting on the source due to the primary source, thus ensuring energy absorption.

This effect of the secondary source acting to increase the power output of the primary source in order to maximise its own absorption has been checked using other secondary source configurations and has been found to occur frequently in many different situations. For example, Figures 4.18 and 4.19 show the effects of minimising W_s using secondary source S1 and similar results to those using source S2 are obtained. from these results it is therefore concluded that an adaptive scheme which seeks to maximise the total secondary source power absorption would not in general be an effective global control strategy. If such a system were to be successful then the cost function to be minimised should take account of the primary source power output as well as the secondary source power absorption.

Returning to the case of minimising W_s using the single secondary source S2, Figures 4.20 and 4.21 show the pressure and intensity fields after minimisation at 692 Hz and 669 Hz respectively (the corresponding fields prior to minimisation have already been presented in Figures 4.2(c) and (d) and 4.3(c) and (d) respectively).

For the 692 Hz case of Figure 4.20 it is interesting to note that, whilst a reduction in E_p of 3.7 dB has occurred following the minimisation of W_s, the residual pressure field is still dominated by the resonant (1,1,0) mode. It can also be seen from the intensity fields of both Figures 4.20 and 4.21 that the energy flux in the enclosure changes in a more definable manner when W_s is minimised compared to when E_p is minimised (Figures 4.9 and 4.10). In the present case there is a more definite flow of energy towards the secondary source which is acting as an energy sink.

4.4 Conclusions

(i) When an active noise control system is configured to minimise the total acoustic potential energy of an enclosed sound field then it does so by effectively minimising the total power output of all the

sources, primary and secondary. Thus the secondary sources act so as to mutually "unload" each other, and the primary source, by reducing the pressure acting over each of the sources and by ensuring that this pressure bears a close to quadrature phase relationship with the source velocity.

(ii) Minimising the total acoustic potential energy does not generally involve the secondary sources absorbing any significant amount of energy and may result in some radiation from the secondary sources.

(iii) If the secondary sources are configured to optimally absorb energy from the acoustic field then this does not necessarily mean that the total acoustic potential energy will decrease, particularly at frequencies away from acoustic resonances. At such frequencies the secondary sources generally act so as to increase the acoustic power output of the primary source thus increasing the total energy of the sound field and enabling more energy to be absorbed by the secondary sources.

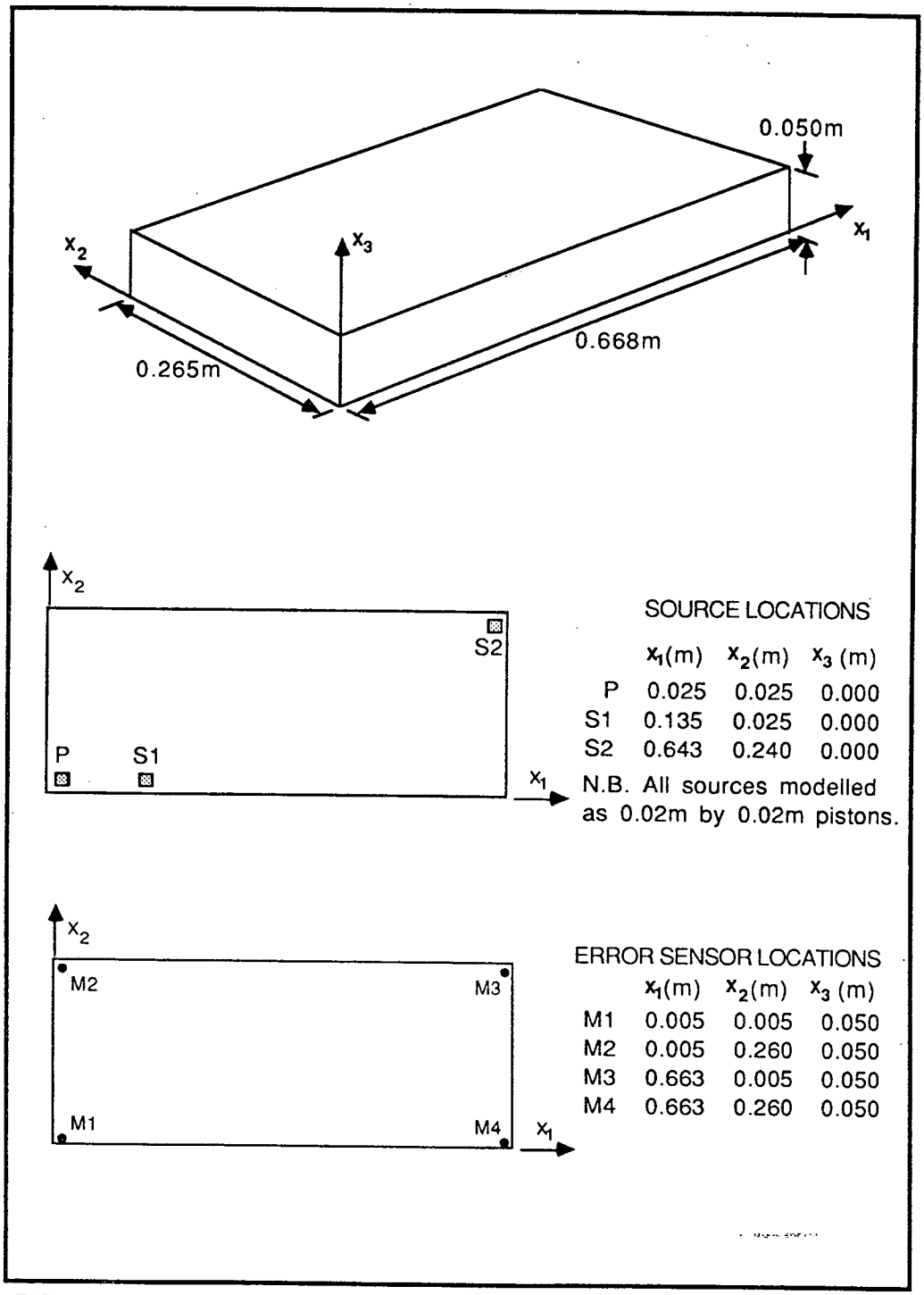

FIGURE 4.1. Schematic diagram of the enclosure modelled for all the results of Chapter 4. The source and error sensor locations are also shown.

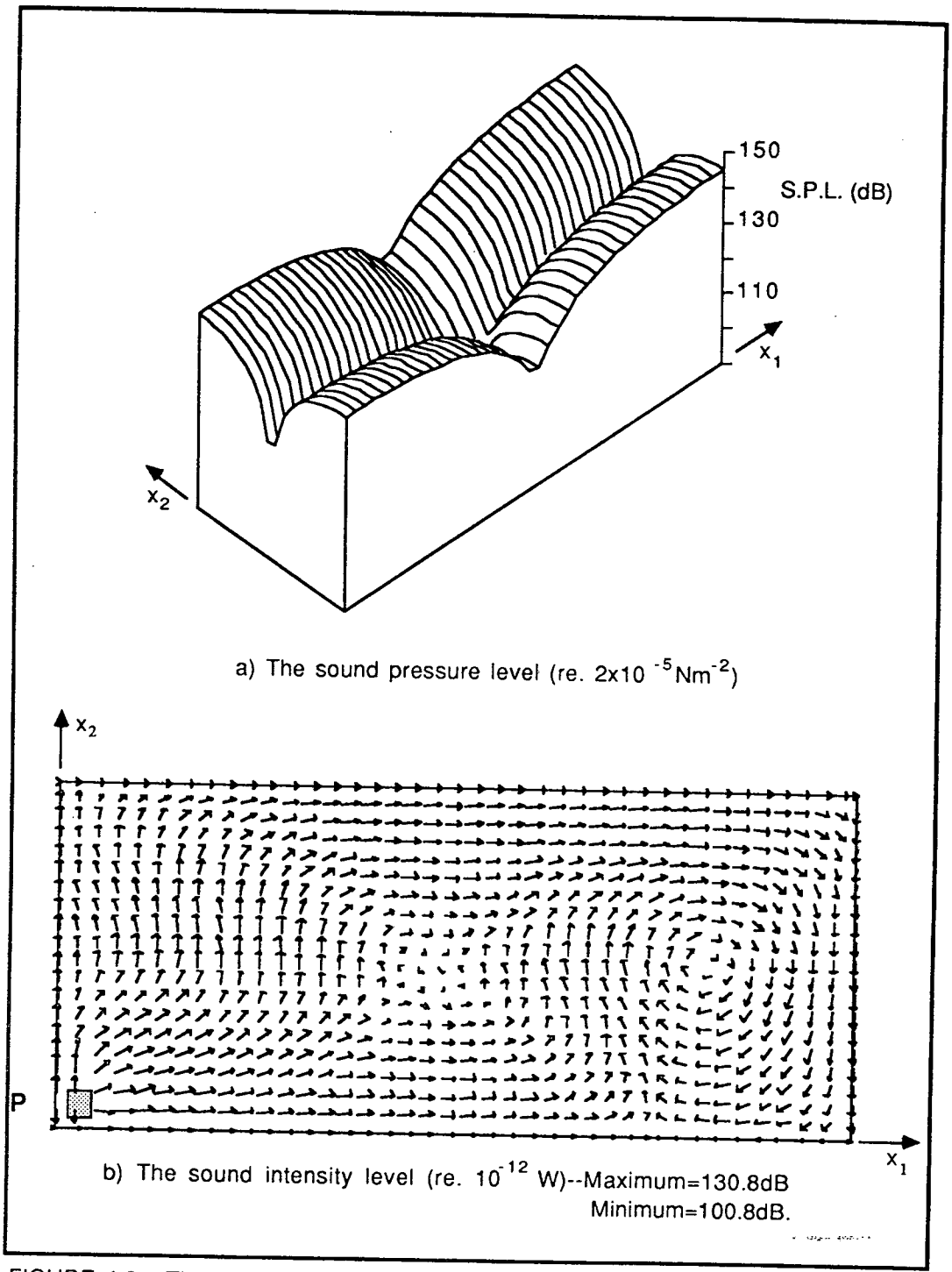

FIGURE 4.2. The sound pressure and intensity fields in the x_3 =0.025m plane of the enclosure shown in Figure 4.1. The fields have been evaluated using the hard wall theory for the situation when the primary source is operating alone at a frequency of 692Hz.

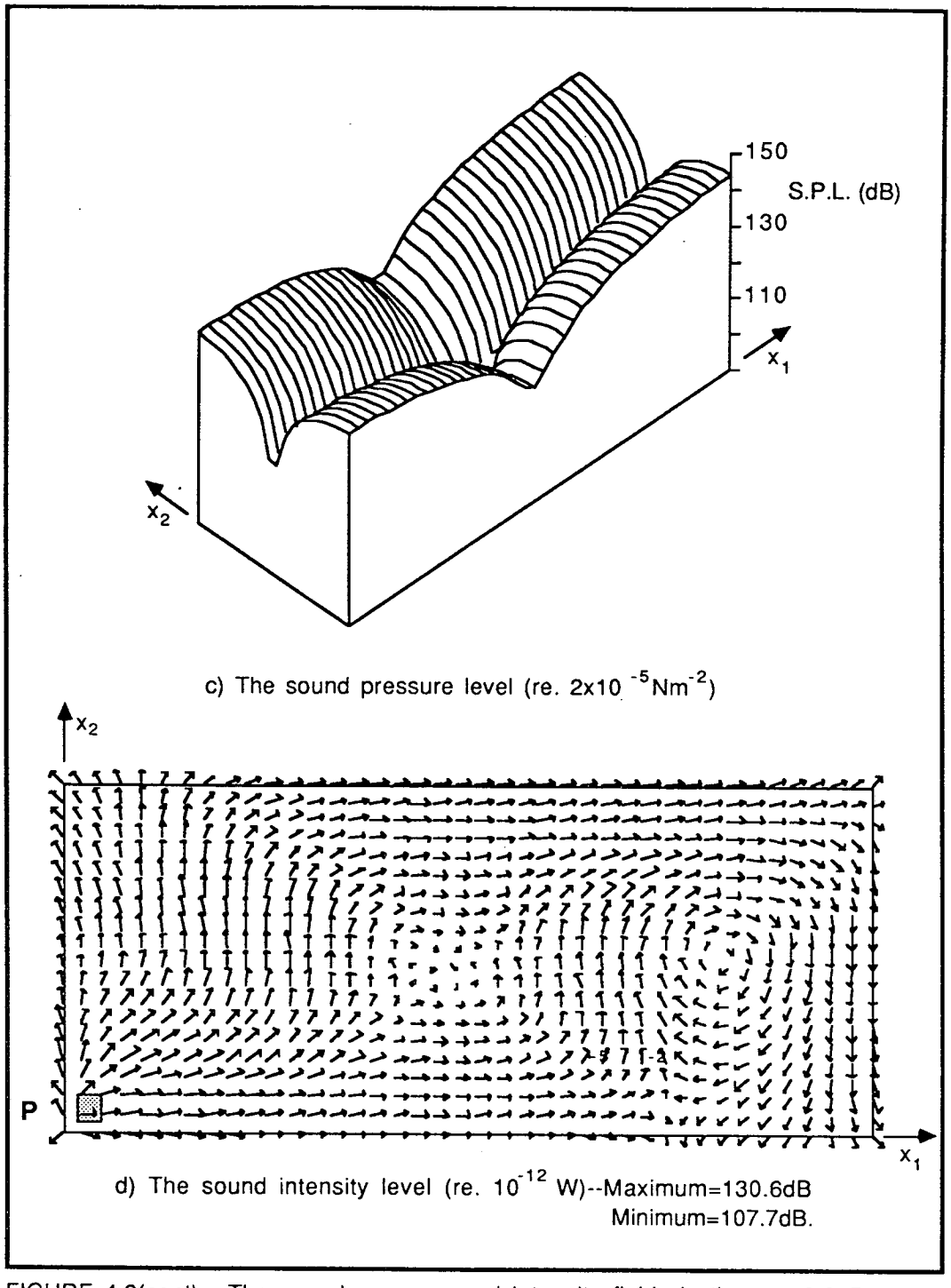

FIGURE 4.2(cont). The sound pressure and intensity fields in the x_3=0.025m plane of the enclosure shown in Figure 4.1. The fields have been evaluated using the soft wall theory for the situation when the primary source is operating alone at a frequency of 692Hz. Note the energy dissipation at the corners of the enclosure compared to that of the hard wall case shown in Figure 4.2(b).

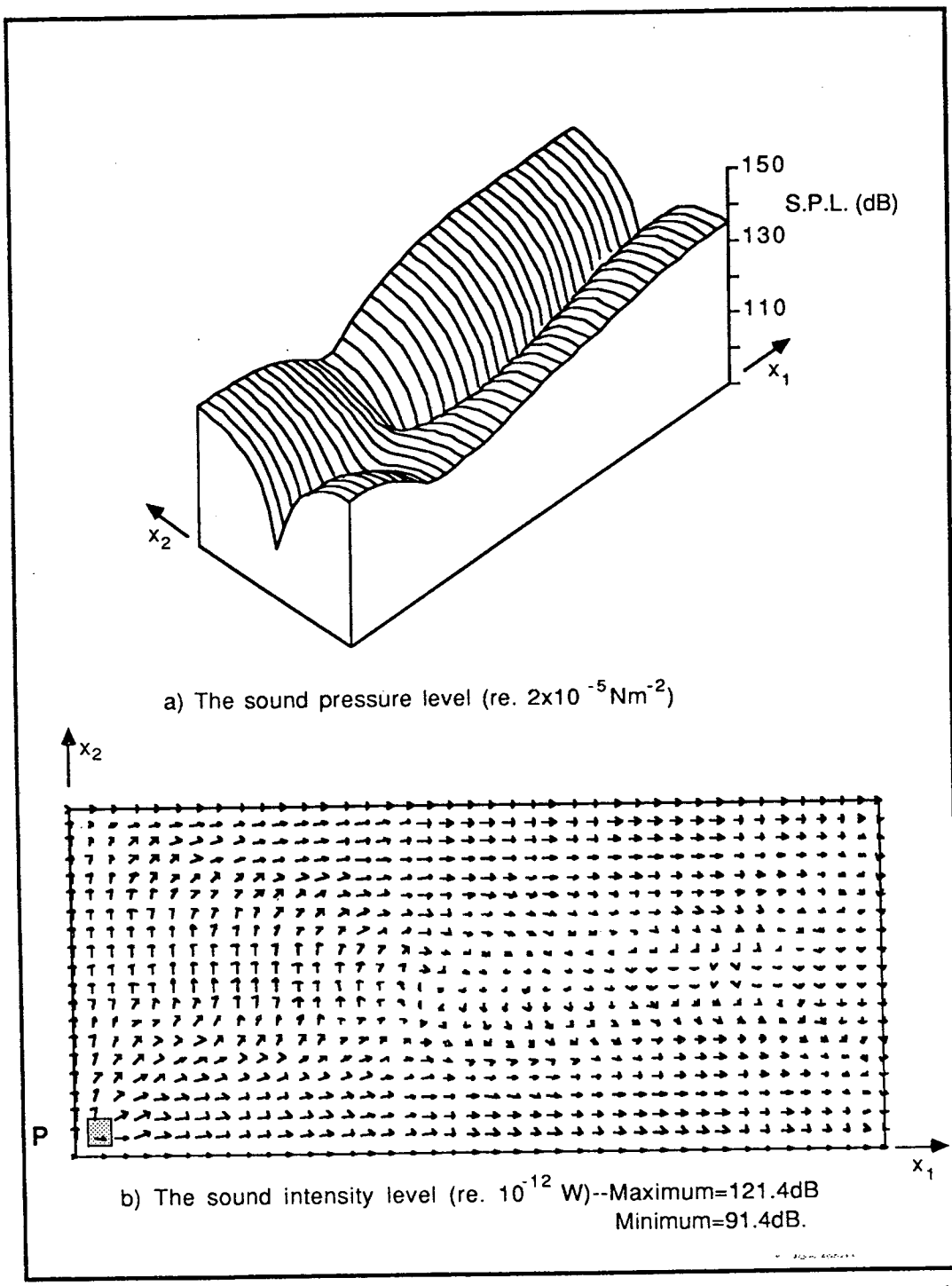

FIGURE 4.3. The sound pressure and intensity fields in the x_3 =0.025m plane of the enclosure shown in Figure 4.1. The fields have been evaluated using the hard wall theory for the situation when the primary source is operating alone at a frequency of 669Hz.

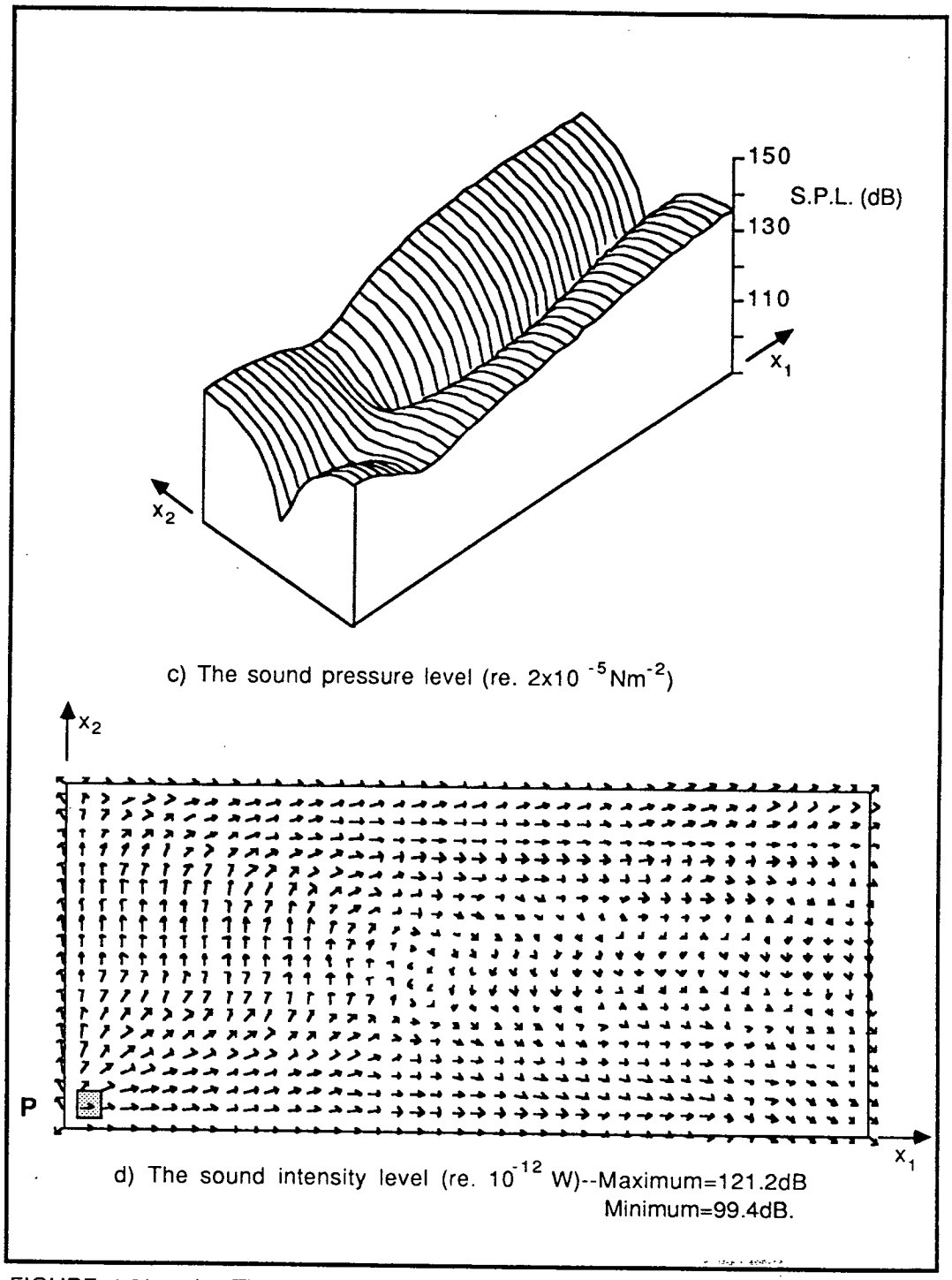

FIGURE 4.3(cont). The sound pressure and intensity fields in the x_3 =0.025m plane of the enclosure shown in Figure 4.1. The fields have been evaluated using the hardwall theory for the situation when the primary source is operating alone at a frequency of 669Hz. Note the energy dissipation at the corners of the enclosure compared to that of the hard wall case shown in Figure 4.3(b).

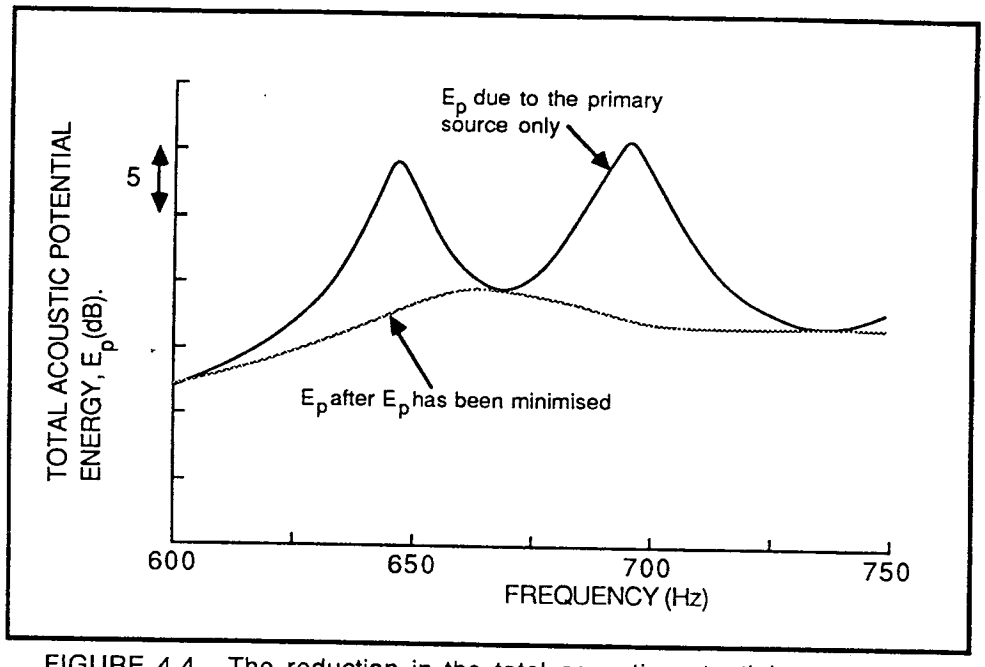

FIGURE 4.4. The reduction in the total acoustic potential energy, E_p, when E_p has been minimised using secondary source S2.

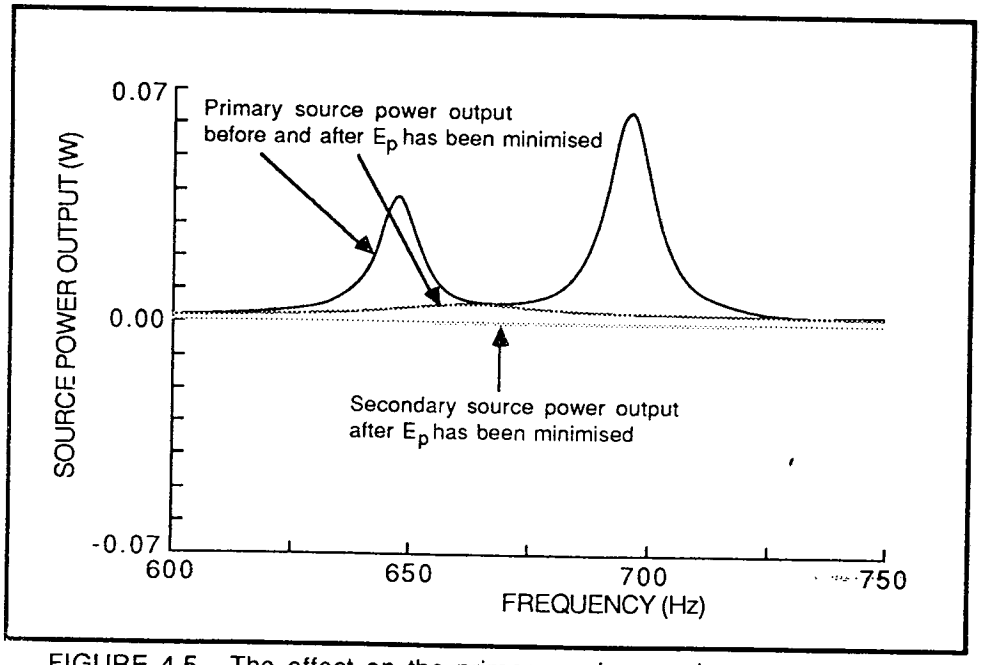

FIGURE 4.5. The effect on the primary and secondary source power outputs when the total acoustic potential energy, E_p, has been minimised using secondary source S2.

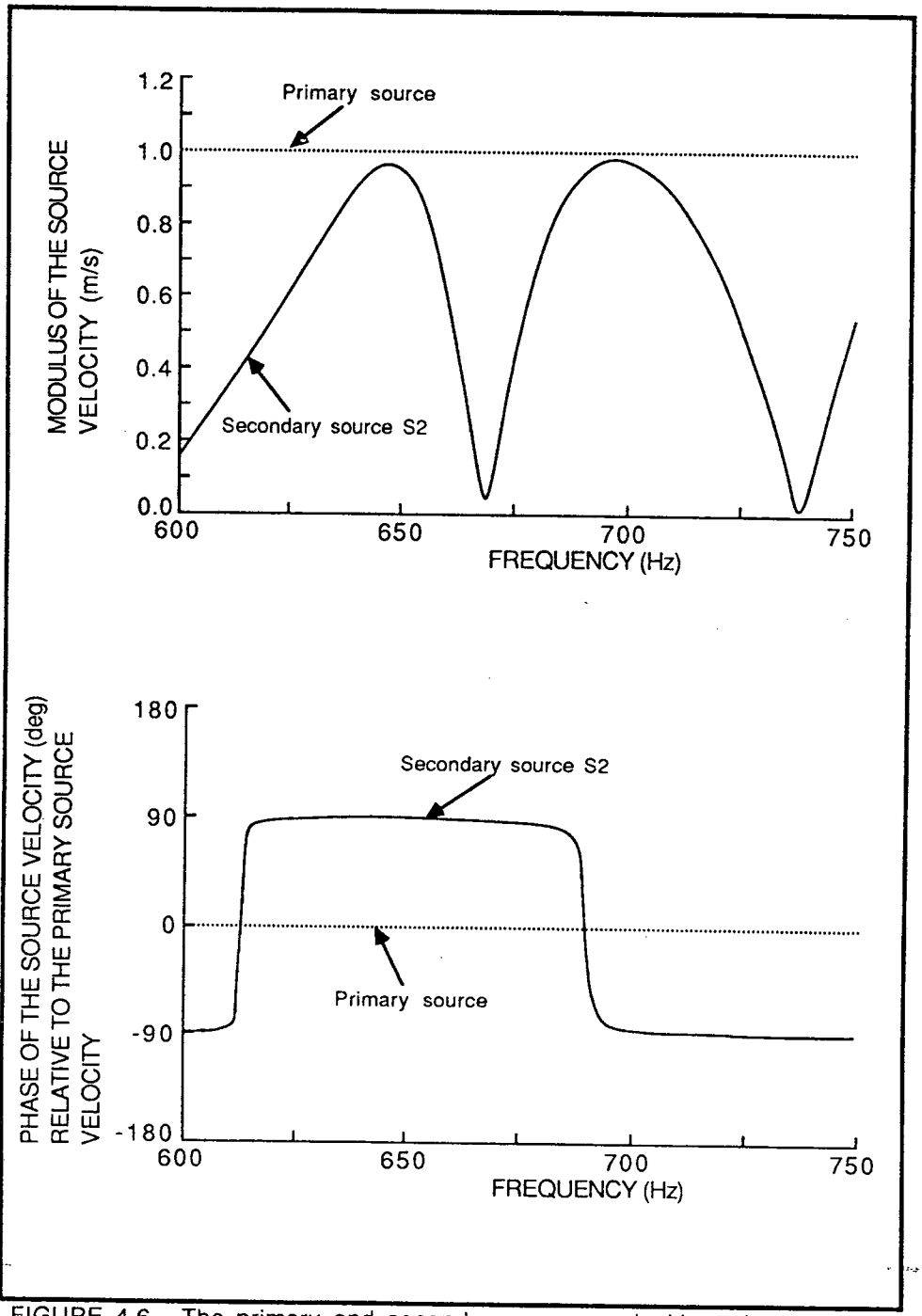

FIGURE 4.6. The primary and secondary source velocities when the total acoustic potential energy, E_p, has been minimised using secondary source S2.

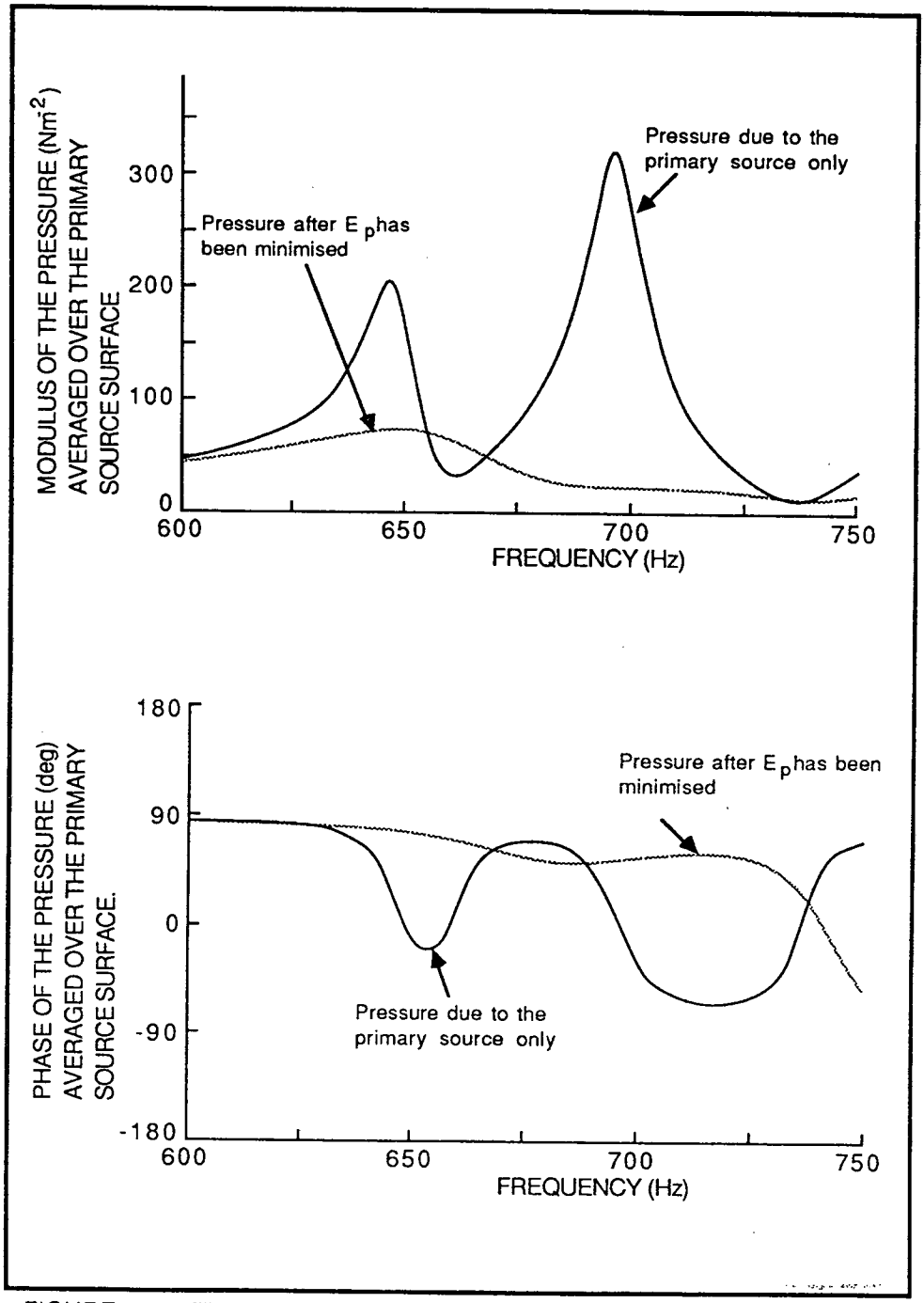

FIGURE 4.7. The surface averaged pressure over the primary source surface before and after the total acoustic potential energy, E_p, has been minimised using secondary source S2.

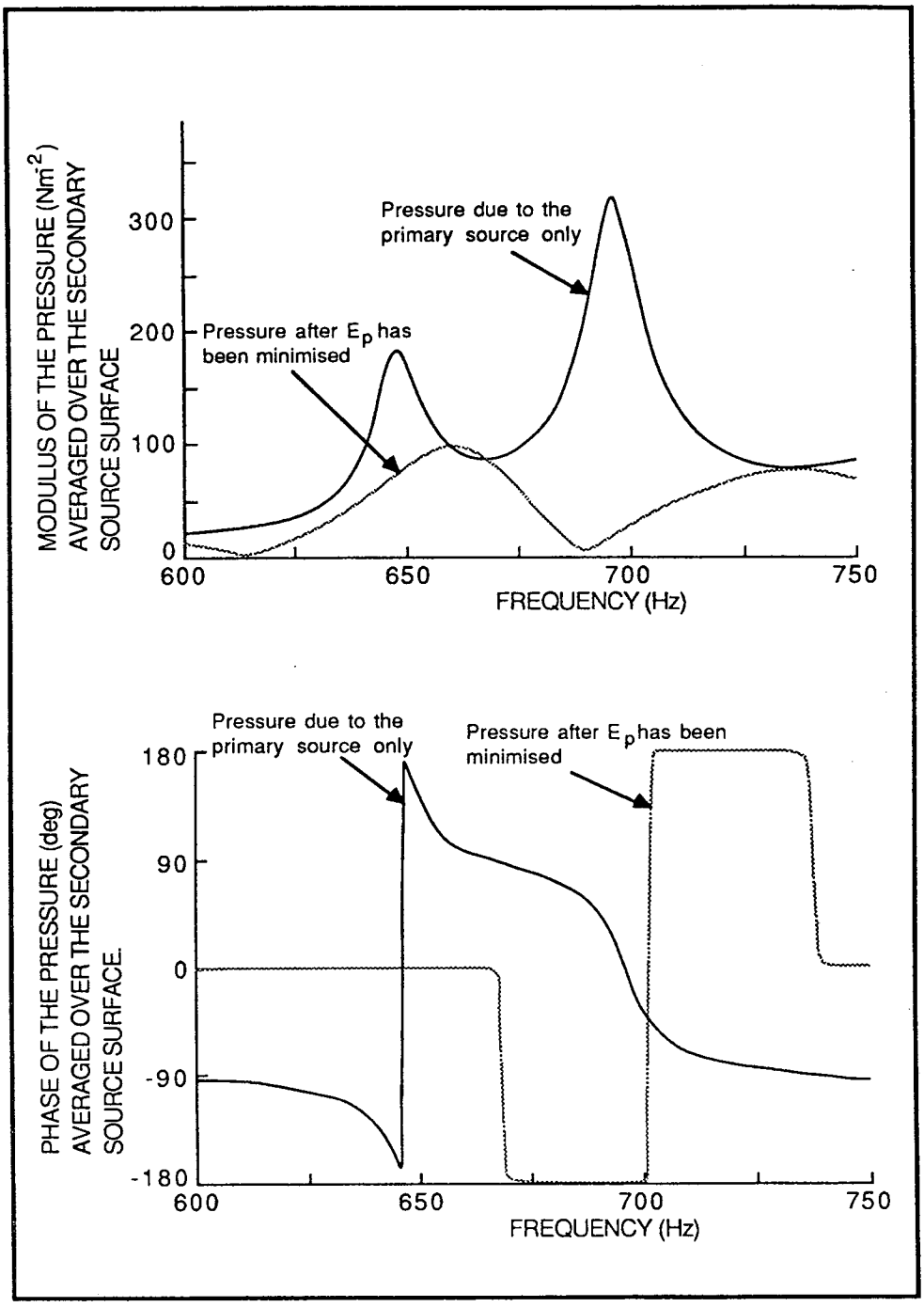

FIGURE 4.8. The surface averaged pressure over the secondary source surface before and after the total acoustic potential energy, E_p, has been minimised using secondary source S2.

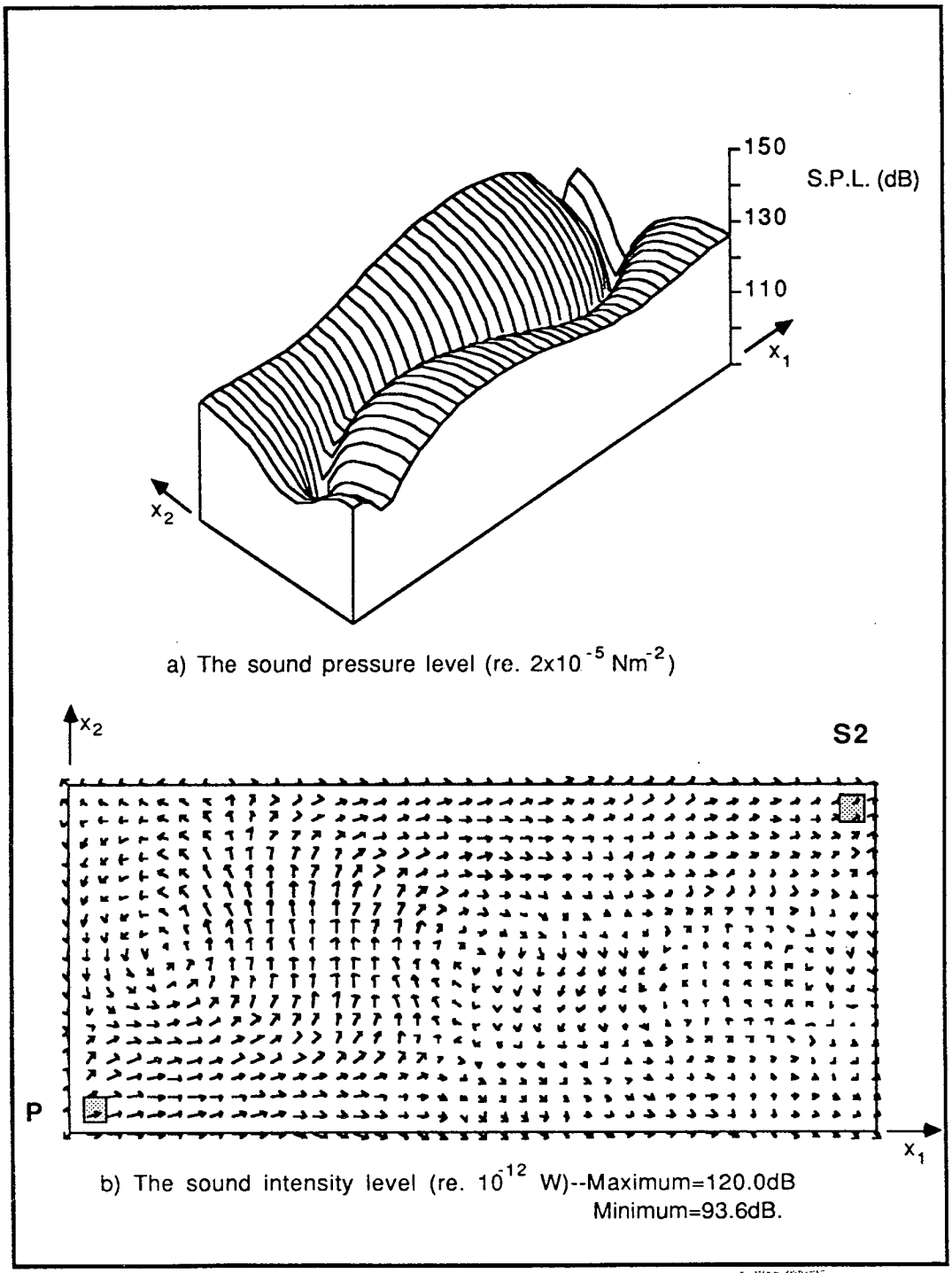

FIGURE 4.9. The sound pressure and intensity fields in the x_3 =0.025m plane of the enclosure shown in Figure 4.1. The fields have been evaluated using the soft wall theory for the situation when the secondary source strength has been set to minimise the total acoustic potential energy. The frequency is 692Hz.

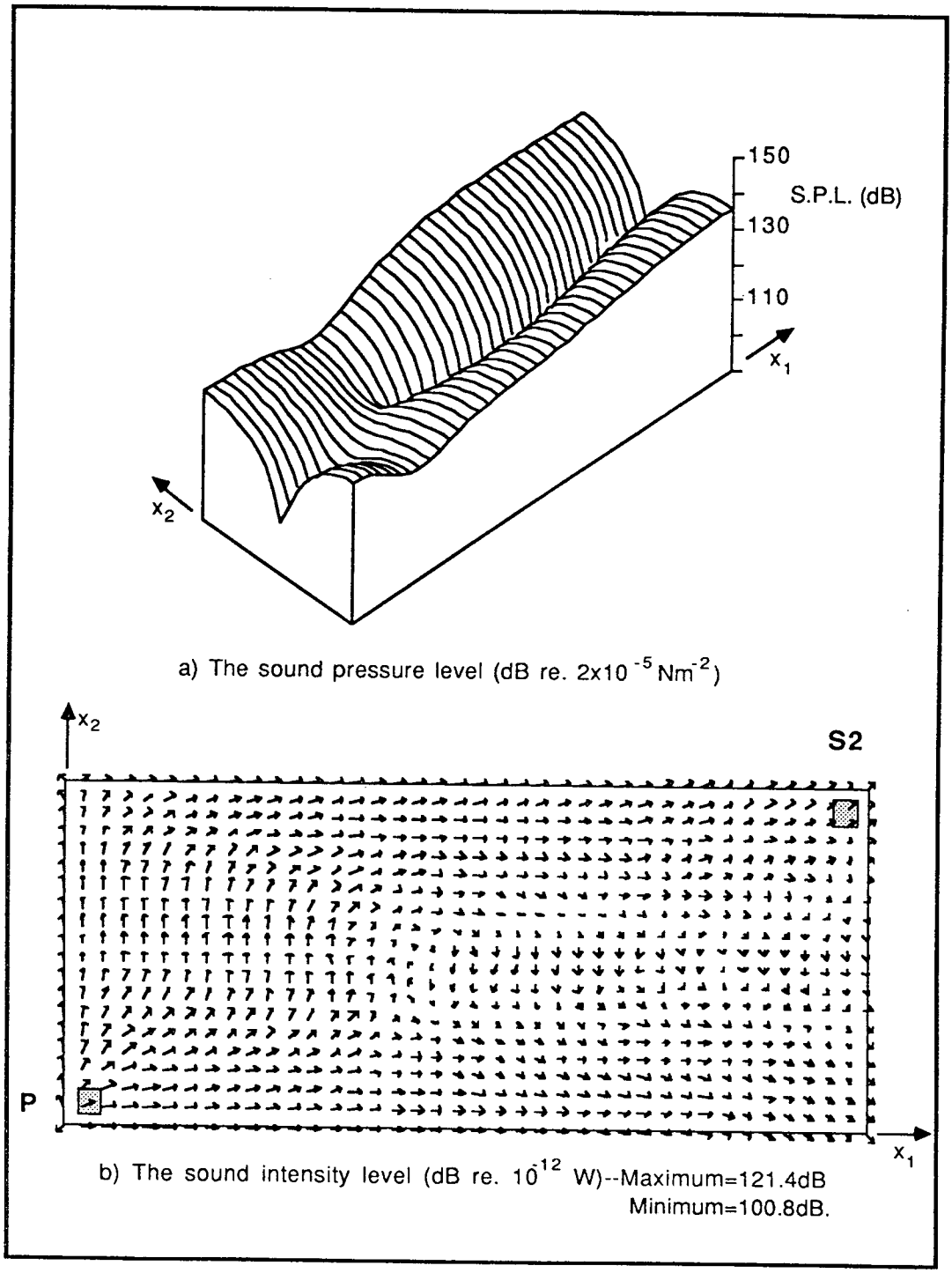

FIGURE 4.10. The sound pressure and intensity fields in the x_3 =0.025m plane of the enclosure shown in Figure 4.1. The fields have been evaluated using the soft wall theory for the situation when the secondary source strength has been set to minimise the total acoustic potential energy. The frequency is 669Hz.

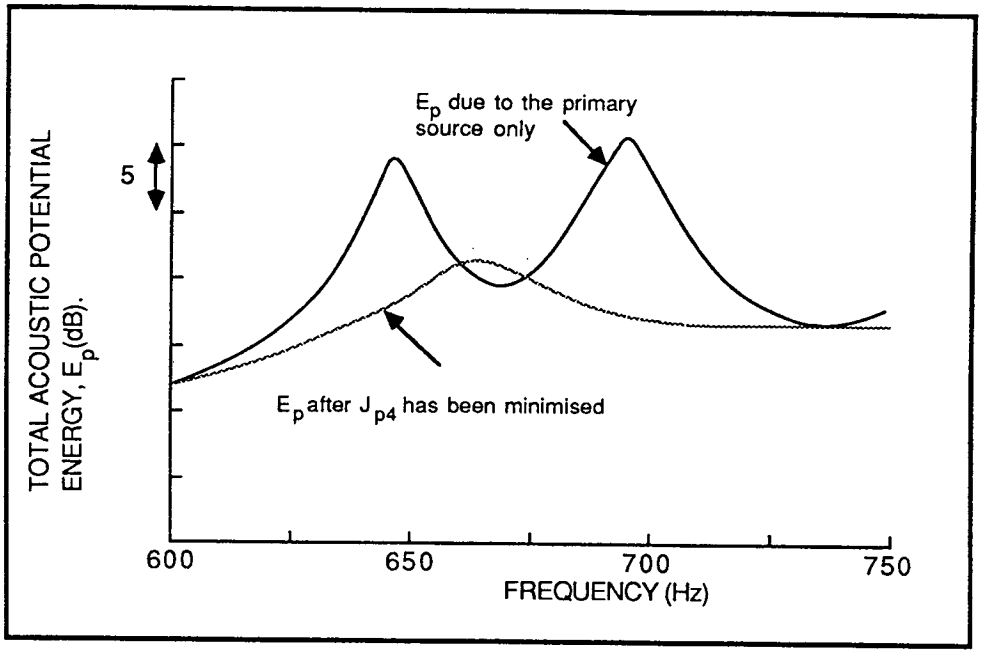

FIGURE 4.11. The reduction in the total acoustic potential energy, E_p, when the sum of the squares of the pressures, J_{p4}, at the four corners (M1,M2,M3,M4) has been minimised using secondary source S2.

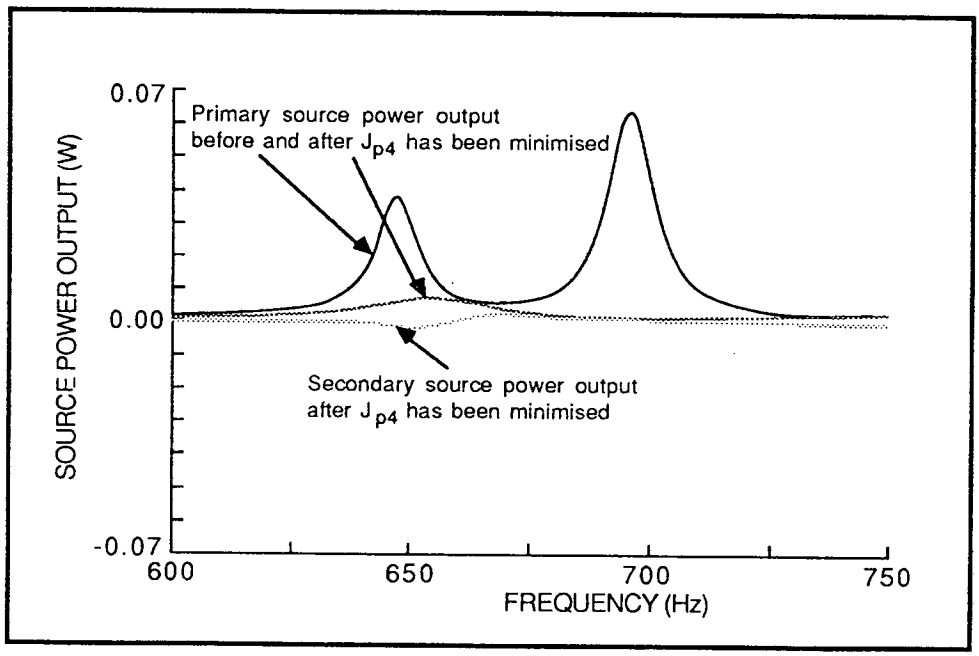

FIGURE 4.12. The effect on the primary and secondary source power outputs when the sum of the squares of the pressures, J_{p4}, at the four corners (M1,M2,M3,M4) has been minimised using secondary source S2.

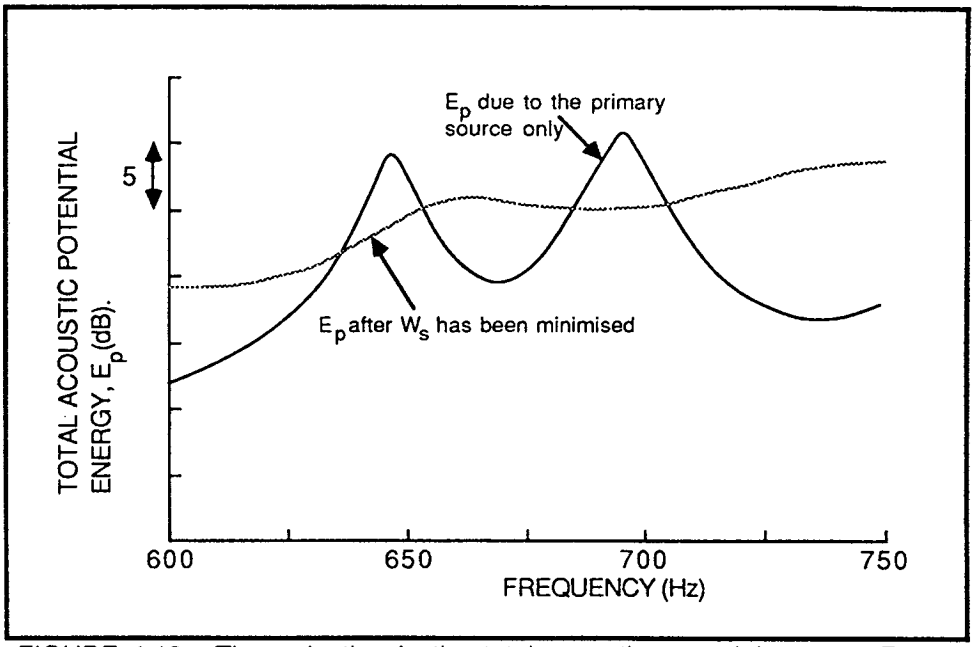

FIGURE 4.13. The reduction in the total acoustic potential energy, E_p, when the power output, W_s, of secondary source S2 has been minimised using secondary source S2 only.

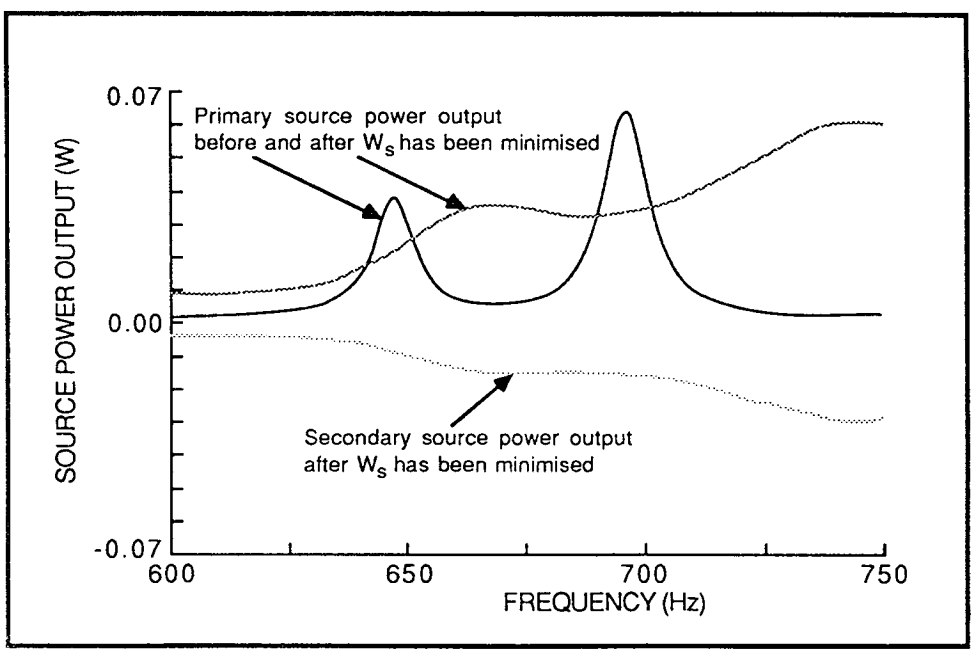

FIGURE 4.14. The effect on the primary and secondary source power outputs when the power output, W_s, of secondary source S2 has been minimised using secondary source S2 only.

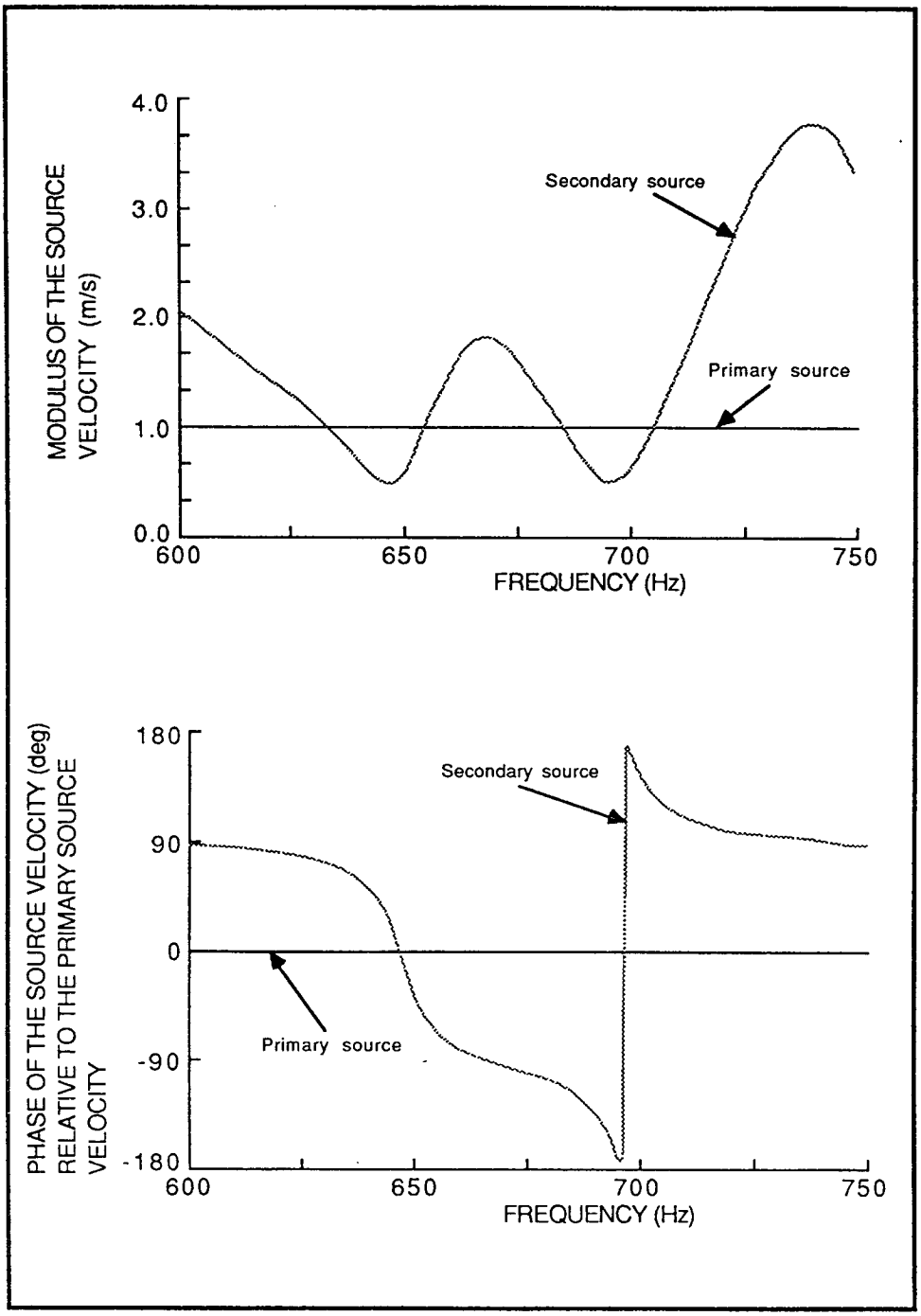

FIGURE 4.15. The primary and secondary source velocities when the power output, W_s , of secondary source S2 has been minimised using secondary source S2 only.

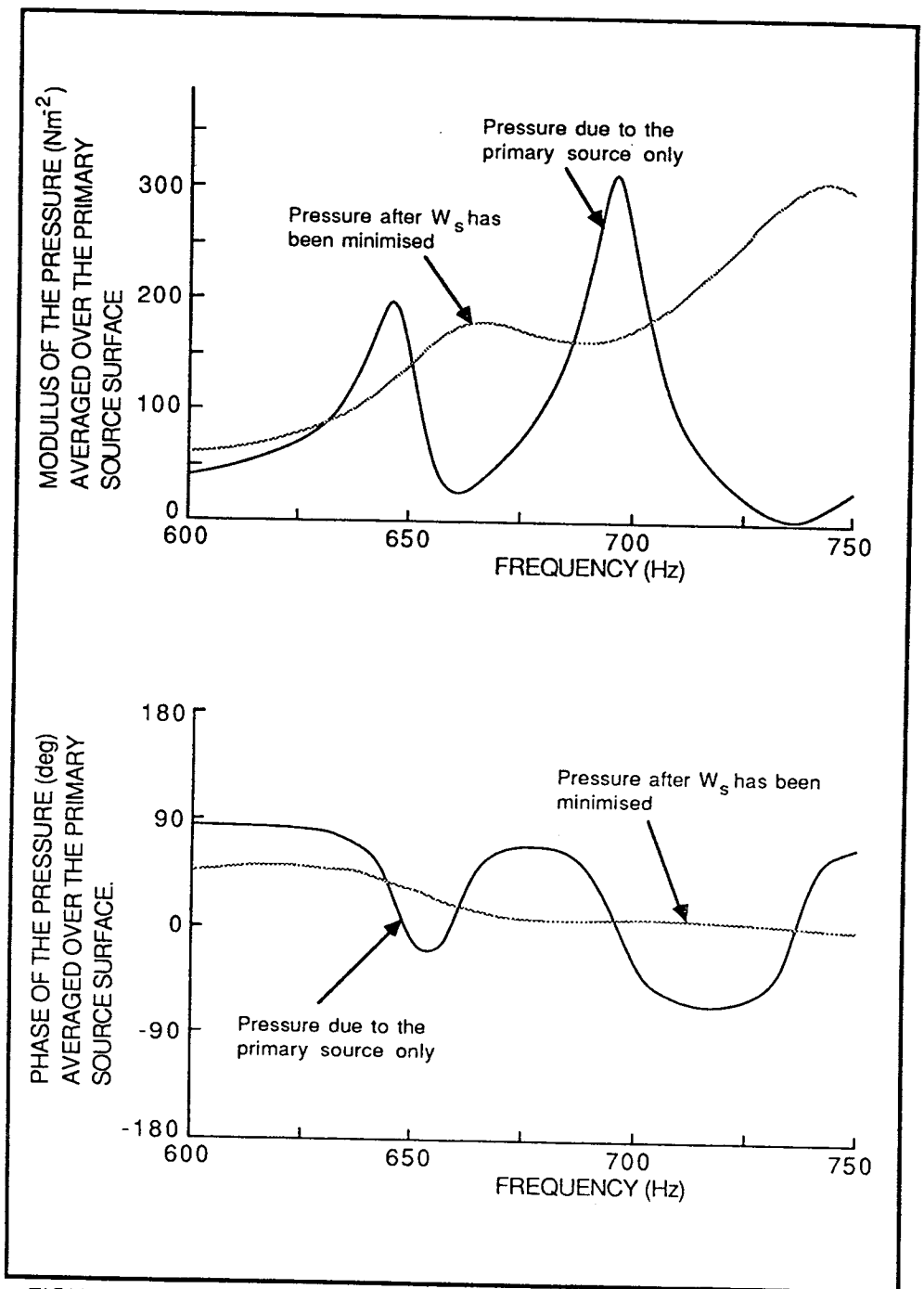

FIGURE 4.16. The surface averaged pressure over the primary source surface before and after the power output, W_s , of secondary source S2 has been minimised using secondary source S2 only.

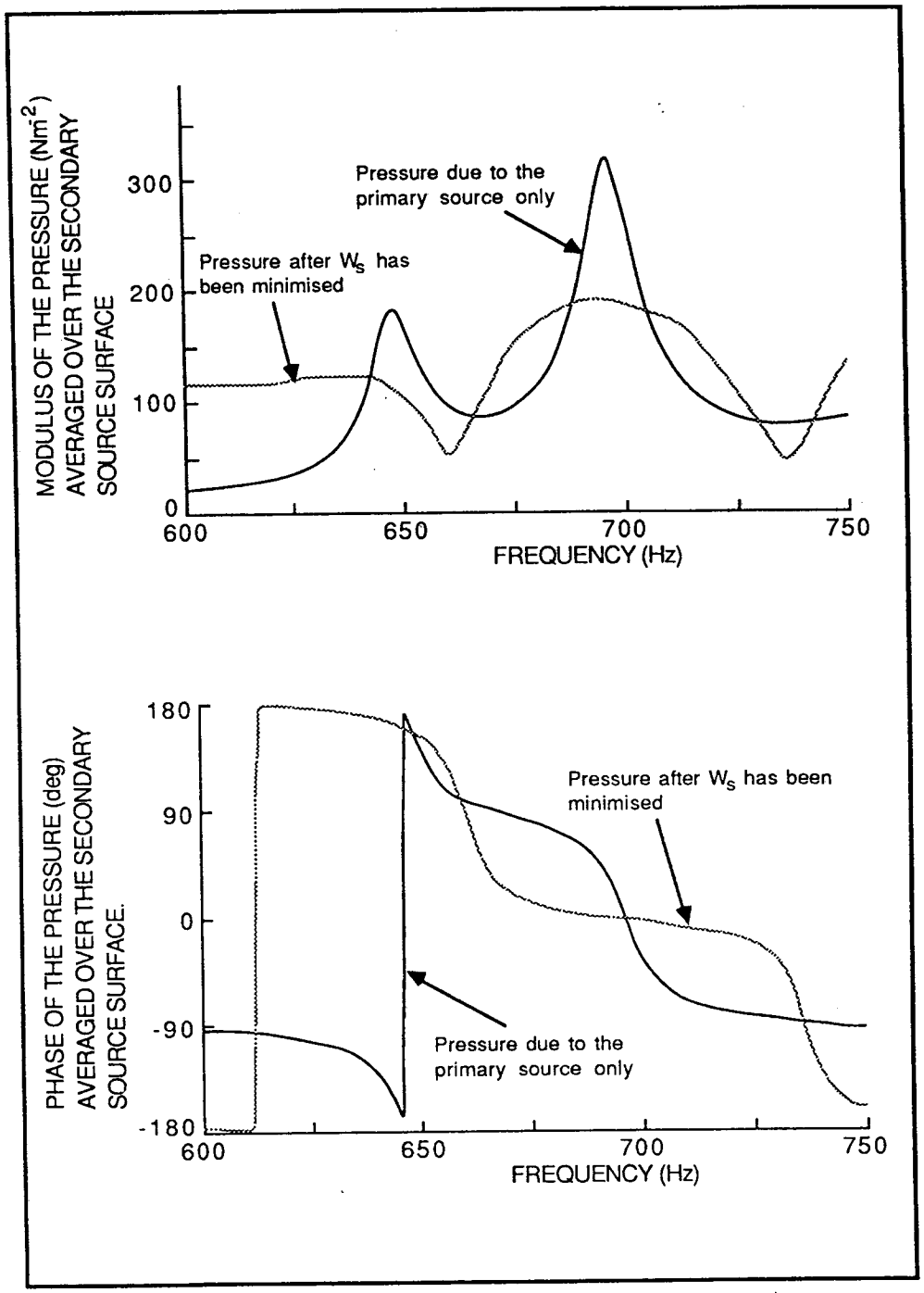

FIGURE 4.17. The surface averaged pressure over the secondary source surface before and after the power output, W_s, of secondary source S2 has been minimised using secondary source S2 only.

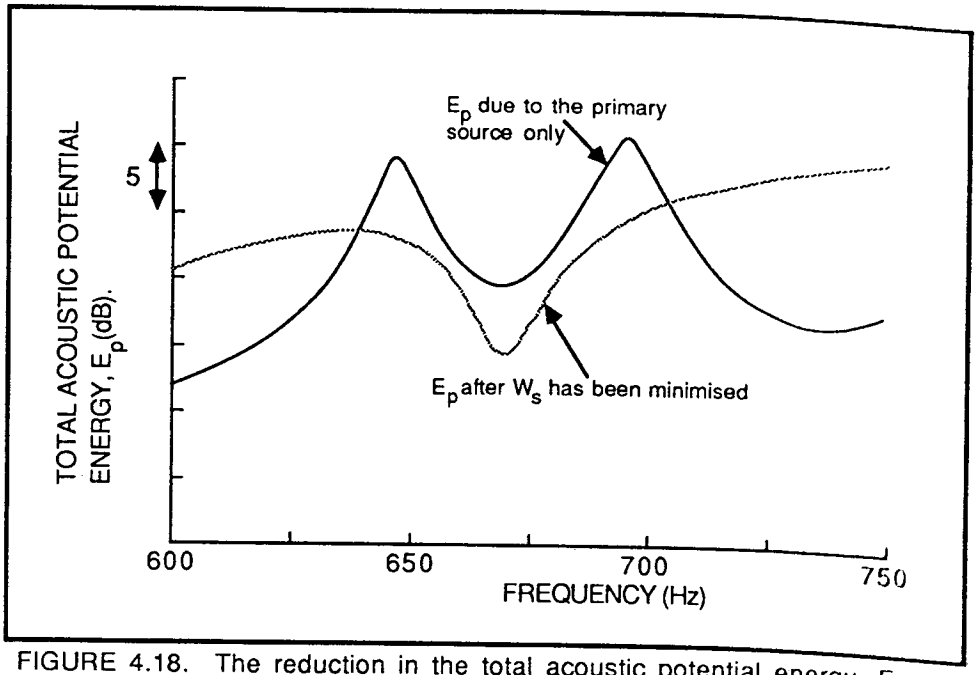

FIGURE 4.18. The reduction in the total acoustic potential energy, E_p, when the power output, W_s, of secondary source S1 has been minimised using secondary source S1 only.

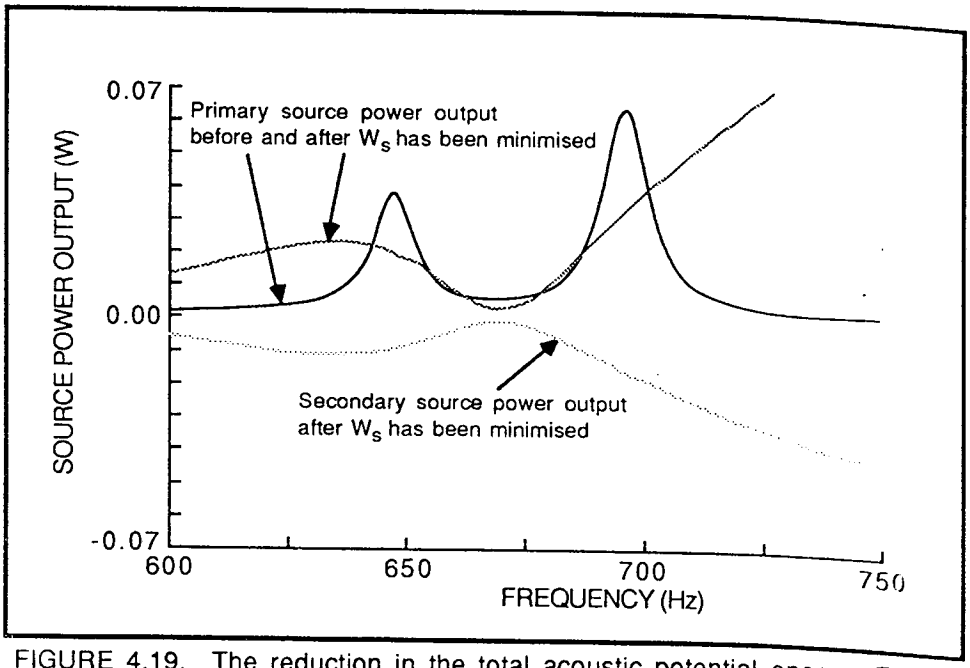

FIGURE 4.19. The reduction in the total acoustic potential energy, E_p, when the power output, W_s, of secondary source S1 has been minimised using secondary source S1 only.

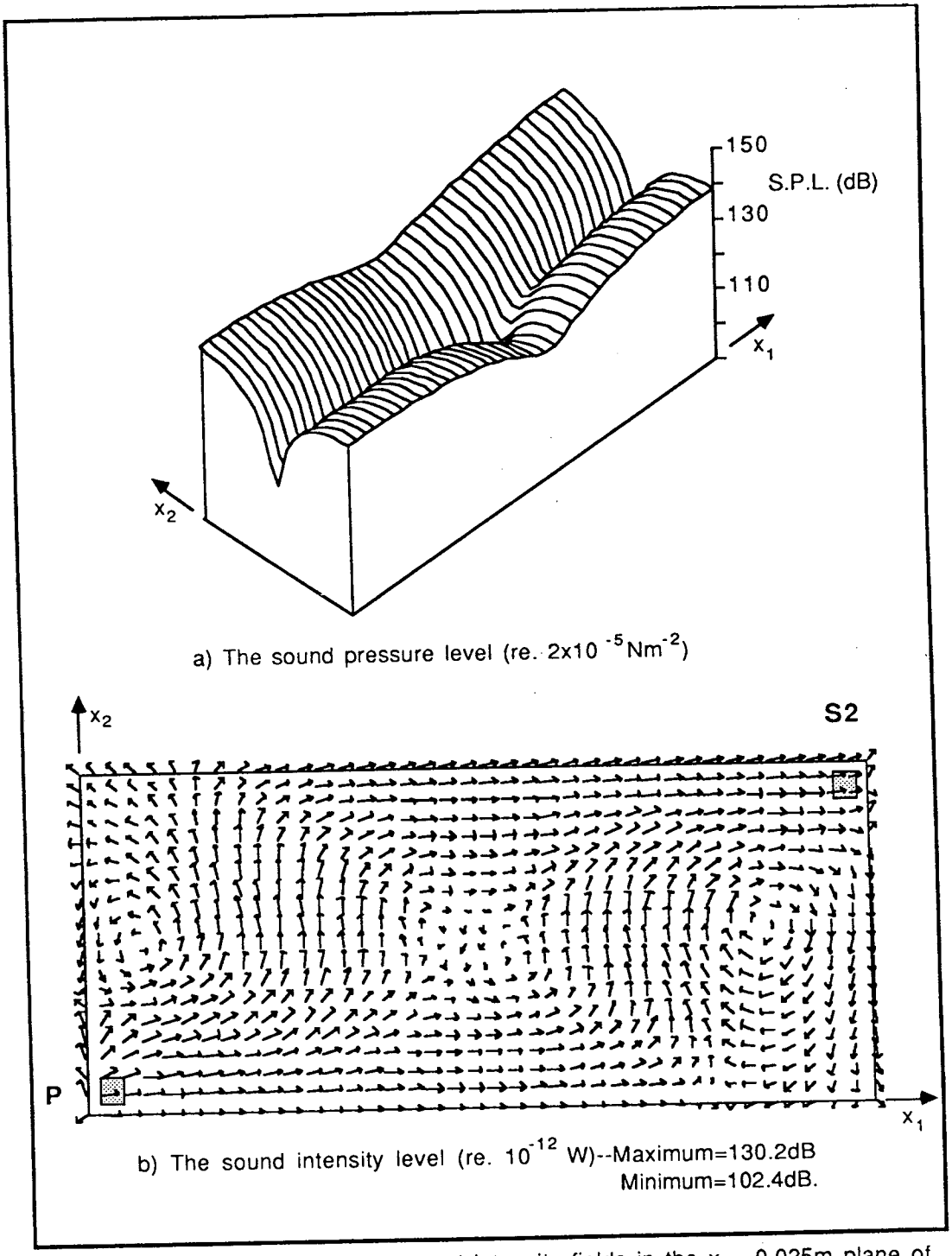

FIGURE 4.20. The sound pressure and intensity fields in the x_3 =0.025m plane of the enclosure shown in Figure 4.1. The fields have been evaluated using the soft wall theory for the situation when the secondary source strength has been set to minimise its own power output, W_s. The frequency is 692Hz.

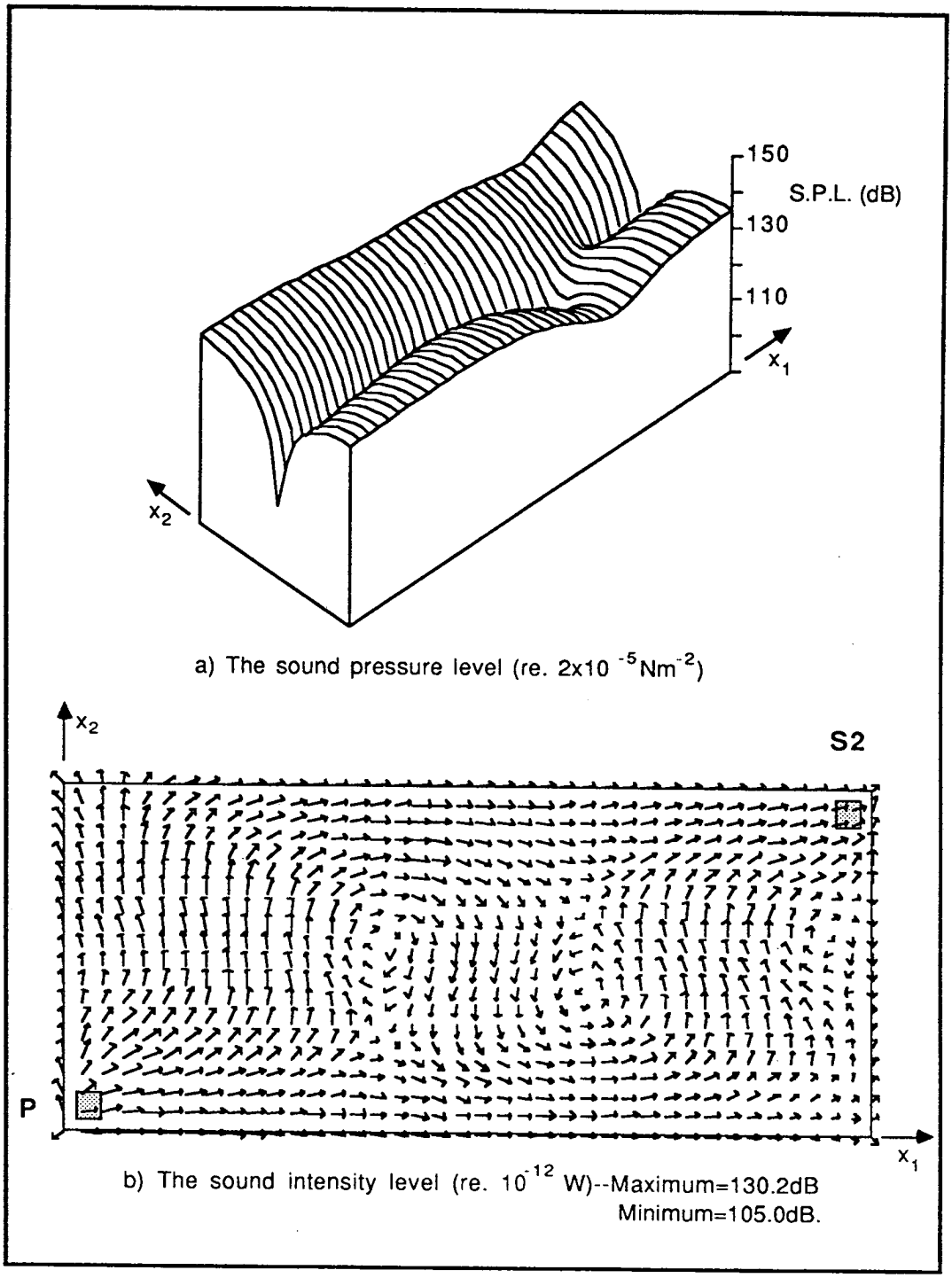

FIGURE 4.21. The sound pressure and intensity fields in the x_3=0.025m plane of the enclosure shown in Figure 4.1. The fields have been evaluated using the soft wall theory for the situation when the secondary source strength has been set to minimise its own power output, W_s . The frequency is 669Hz.

PART II

CHAPTER 5

EXPERIMENTAL DETERMINATION OF THE ACOUSTIC RESPONSE OF THE CABIN OF A BRITISH AEROSPACE 748 AIRCRAFT

5.1 Introduction

The theoretical and experimental results of Part I have demonstrated the feasibility of applying active noise control to reduce sound levels in harmonic enclosed sound fields and they have also revealed the physical mechanisms by which these reductions are obtained. However, in order to reveal these mechanisms, the sound fields to which the active control was applied were deliberately kept very simple, with a low modal density and light damping. The work to be presented in Part II of the thesis will use the same basic theory of Part I, but it is now intended to apply it to a much more practical situation. The situation to be considered is the application of active noise control to reduce the propeller induced cabin noise of a B.Ae. 748 aircraft [46]. This is a 48 seat, short-medium range, twin turbopropeller passenger aircraft (see Figure 5.1) which uses conventional four-bladed propellers giving it a fundamental blade passage frequency of less than 100 Hz.

The sound field inside the aircraft is dominated by harmonics of this blade passage frequency and therefore an active noise control system would only be required to attenuate the contribution due to these harmonics. Consequently the frequency domain quadratic minimisation theory presented in Part I will still be applicable to this problem. However, what is likely to differ substantially from the situations addressed in Part I is the nature of the acoustic field. Even at the fundamental blade passage frequency of 88 Hz the acoustic field is neither likely to be of very low modal density, nor very lightly damped, especially when it is considered that the passenger compartment alone of the test aircraft has a length of 9.0 m, a maximum diameter of 2.6 m, and is to be fully trimmed and fitted with its full complement of 48 seats. Also likely to differ considerably from the model used in Part I is the primary source distribution. In Part I this was always modelled as a discrete loudspeaker type piston source whose maximum dimensions were much less than a wavelength of the sound being considered. In the case of the aircraft the "primary source" distribution consists of the normal

vibrations of the cabin walls, and therefore there is no longer any guarantee that it will be so compact.

These three factors, the acoustic modal density, the acoustic damping, and the extent of the primary source distribution were all shown in Part I to affect the levels of reduction which could be obtained using an active noise control system. It is therefore to be expected that the theoretical results obtained for the application of active noise control to this more practical situation will differ considerably from the results of Part I. This also implies that, if these predictions are to be representative of what will occur in practice, then it is important that the acoustic modal density, the acoustic damping and the primary source distribution should be modelled accurately. Because of the importance of specifying these quantities accurately, a series of tests were performed on the test aircraft. The work presented in this chapter describes some experiments performed on the static aircraft to determine the modal structure of the sound field and the acoustic damping. These tests included reverberation time measurements, steady state power measurements and internal cabin acoustic transfer impedance measurements. The extent of the normal velocity distribution of the cabin walls will be considered in Chapter 6.

The acoustic theory used to describe the sound fields of Part I was a modal model, and as such its practical application is limited to lower frequencies where the modal density of the sound field is still reasonably low. This same theory is to be used in this work, as it is only intended to consider the application of active noise control at the first two blade passage harmonic frequencies. This may appear to be restrictive, but these two harmonics tend to dominate the cabin sound field, even on an A-weighted basis [84]. This is partly due to the decreasing levels of the external propeller pressure fields as the harmonic order is increased, but it is also helped by the increasing transmission loss of the fuselage as the frequency increases. Having made this decision it is most important to obtain an accurate estimate of the sound field properties in this low frequency range. Consequently the results of this chapter concentrate on obtaining these estimates by means of the transfer impedance measurements between a loudspeaker and a microphone which are both placed within the cabin. However, it has also

been attempted to estimate the higher-frequency acoustic properties by means of reverberation time measurements and steady state power balance measurements.

5.2 The Sound Field in a Cylindrical Room

Several works [47,48,49] which have considered the problem of noise transmission into aircraft cabins have chosen to model the cabin sound field as that which exists in a purely cylindrical room. It is one of the intentions in this section to assess how good a model this is.

The acoustic pressure at a point specified by the location vector $\underline{r}$ due to some normal velocity distribution $v(\underline{r}_S,\omega)$ over the cylinder walls can be expressed as (see Figure 5.2 for the cylindrical coordinate system used)

$$p(\underline{r},\omega) = \frac{\omega\rho c^2}{V} \sum_{n_1=0}^{N_1} \sum_{n_2=0}^{N_2} \sum_{n_3=0}^{N_3} \sum_{n_4=0}^{1} \frac{\psi_n(\underline{r}) \int_S v(\underline{r}_S,\omega)\psi_n(\underline{r}_S)\, dS}{2\zeta_n\omega_n^2 - j(\omega_n^2 - \omega^2)} \qquad (5.1)$$

where harmonic time dependence of frequency ω has been assumed. The terms in equation (5.1) all have the same definitions as those of equation (2.16). However, the surface, S, now refers to the cylindrical room interior surface, and the eigenfunctions must now satisfy the assumed hard walled boundary conditions presented by the cylindrical room. Thus, by separating the variables, the eigenfunctions can be evaluated [55] as

$$\psi_{n_1n_2n_3n_4}(z,\theta,r) = \frac{\cos(\frac{n_1\pi z}{L_z})\cos(n_2\theta + \frac{n_4\pi}{2})J_{n_2}(\frac{k_{n_2n_3}r}{a})}{\Lambda_n^2} \qquad (5.2)$$

where n_1, n_2, n_3 and n_4 are the modal integers, L_z is the length of the cylinder, J_{n_2} is a Bessel function of order n_2, $k_{n_2n_3}$ are solutions of $(\partial J_{n_2}(k_{n_2n_3})/\partial r) = 0$ and a is the radius of the cylinder. The eigenfunctions have been normalised according to equation (2.8) to give

$$\Lambda_n = \frac{1}{\epsilon_{n_1}} \frac{1}{\epsilon_{n_2}} \left(1 - \frac{n_2^2}{k_{n_2 n_3}}\right) J_{n_2}^2(k_{n_2 n_3}) \qquad (5.3)$$

where $\epsilon_{n_1} = 1$ if $n_1 = 0$ or $\epsilon_{n_1} = 2$ if $n_1 > 0$ and the same applies to ϵ_{n_2}. Similarly, the natural frequency of the n'th mode is evaluated from the expression

$$\omega_n = c\left(\left(\frac{n_1 \pi}{L_z}\right)^2 + \left(\frac{k_{n_2 n_3}}{a}\right)^2\right)^{1/2} \qquad (5.4)$$

Note that these expressions have been derived using hard walled boundary conditions, and therefore the acoustic damping has been introduced by means of complex eigenvalues ($k_n = \omega_n(1 + j\xi_n)/c$) However, following the procedure of Chapter 4, the modal damping ratio, ξ_n, can be related to an effective surface averaged energy absorption coefficient, $\bar{\alpha}$, by means of the relationship

$$\xi_n \omega_n = C_n = \frac{Sc}{16V} \frac{\text{average value of } \bar{\alpha}\psi_n^2(\underline{r}) \text{ over all walls}}{\text{average value of } \psi_n^2(\underline{r}) \text{ over the room volume}} \qquad (5.5)$$

where S is the total surface area of the boundary walls, V is the enclosed volume and C_n is the effective damping constant of the n'th mode. Substituting equations (5.2) and (5.3) into equation (5.5) and performing the necessary surface and volume integrals yields

$$C_n = \frac{c}{16V}\left[S_e \bar{\alpha}_e \epsilon_{n_1} + \frac{S_c \bar{\alpha}_c}{1 - \left(\frac{n_2}{k_{n_2 n_3}}\right)^2}\right] \qquad (5.6)$$

where S_e is the surface area and $\bar{\alpha}_e$ the surface averaged absorption coefficient of the end walls and where S_c and $\bar{\alpha}_c$ are the equivalent quantities for the curved wall. As with the damping constant expression for the rectangular room, it is seen from equation (5.6) that the extent to which each mode is damped depends not only on the distribution of the damping material but also on the type of mode being considered. In the work that follows, the distribution of absorbing material over the end

and curved walls will be assumed to be equal, and therefore $\bar{\alpha}_e$ will equal $\bar{\alpha}_c$, therefore the subscript shall be dropped.

5.3 Steady State Power Balance Measurements

As a first attempt to experimentally estimate the absorption within the cabin space steady state power balance measurements were made. For these measurements a calibrated octave band white noise sound source of known power output was placed in the cabin, and for each of a number of different source locations the sound pressure level was measured at a number of randomly selected microphone locations (see Figure 5.3 for a schematic diagram of the experimental set up). Using this procedure, and assuming that the source is the only form of power input to the acoustic field and that energy is only dissipated at the walls, the mean squared pressure can be related to the power output of the source by [63]

$$\langle p_{rms}^2 \rangle = \frac{4\rho c W}{S\bar{\alpha}} \qquad (5.7)$$

where the symbol < > denotes space averaging and where W is the source power output and ρ, c, $\bar{\alpha}$ and S are as defined previously. Equation (5.7) has been derived using diffuse field theory. There are three main conditions which must be satisfied if the diffuse field assumption is to remain valid. Firstly the source frequency must be high enough and/or its bandwidth wide enough to ensure that many modes are significantly excited. Secondly, the damping must be sufficiently low that the majority of the measured sound power is due to waves that have undergone many reflections [37], and lastly, the source and microphone must always be separated by a distance, r, such that [37]

$$r > (\bar{\alpha}S/50)^{1/2} \qquad (5.8)$$

This latter condition ensures that the source near field is avoided. Also, in a truly diffuse sound field the measured mean squared pressures should be equal no matter where the source and microphone are

placed (provided regions near the surfaces of the room are avoided). However, initial tests in the aircraft cabin showed this not to be true, particularly below the 250 Hz octave band, so the source and microphone locations were "volume averaged" by using several randomly chosen source/microphone location combinations, hence the "volume averaged" quantity $\langle p_{rms}^2 \rangle$ in equation (5.7). The non uniformity of the sound field, even when excited using 125 Hz octave band white noise, is a good indication that at these frequencies and below the sound field cannot be considered as diffuse, and therefore the direct application of equation (5.7) is likely to lead to error. At these low frequencies the responses of individual modes should be taken into account. However, this formulation of the problem has been addressed in Appendix 5.1 and it has been concluded that, due to the large number of potentially inaccurate assumptions that must be made to make the problem tractable, the steady state power balance technique should not be used to estimate the absorption at these low frequencies. However, despite this realization, some results have been included for comparison with other available data.

The result of using this power balance method and the diffuse field theory (equation (5.7)) are listed in Table 5.1 for the four octave bands between 125 Hz and 1000 Hz inclusive. For each octave band the number of source and microphone locations used to achieve the "volume averaging" are given, along with the averaged source power outputs and sound pressure levels. (*N.B.* The source power output was kept constant at 99 dB re 1×10^{-12} W for all the different source locations used and for each different frequency band.) The absorption coefficients, $\bar{\alpha}$, have been evaluated using equation (5.7) by assuming the cabin to be a cylindrical room of length 16.0 m and diameter 2.6 m. Thus the total surface area, S, is 141 m^2. Also shown in Table 5.1 is the theoretical number of modes which can be excited within each of the octave bands assuming a cylindrical cabin as above.

The high values of absorption coefficient obtained are thought to be due largely to the fact that in the aircraft the absorption is not present over only the walls, but also over the seats, additonal bulkheads, luggage bins, etc. If, for example, 48 seats each having an exposed surface area of 1.5 m^2 are added to the total surface area, the

absorption coefficients are reduced by 33%. However, these values are still large and therefore, because the second of the diffuse field assumptions listed after equation (5.7) may be infringed, the results should be treated cautiously. Indeed, Table 5.2 shows a comparison of the measured results with those sugested by Wilby *et al* [2], where the total absorptions calculated using the absorption coefficient estimates from reference [2] have been evaluated assuming a cabin length of 16.0 m, a cabin diameter of 2.6 m with a carpeted floor offset from the central axis by 0.5 m and with 48 seats mounted, each having an exposed surface area of 1.5 m^2.

From Table 5.2, discrepancies in the total absorption of up to 300% are evident. The assumptions involved in obtaining the experimental absorptions will inevitably account for some error. Also, the application of the suggested absorption coefficients of reference [2] without account being taken of the extra absorbing surfaces such as luggage bins and other protrusions will lead to some underestimation of the total absorption (although this latter effect will certainly not account for 300% errors). However, because it is not clear from reference [2] how the suggested absorption coefficients have been estimated, it is difficult to comment further on the cause of the discrepancies.

5.4 Reverberation Time Measurements

It has already been demonstrated in the previous section that the cabin sound field cannot be considered diffuse when excited at frequencies below 250 Hz, and even above this frequency the assumption appears to be rather dubious. It is therefore pointless to apply reverberation time measurement techniques to estimate the low frequency cabin absorption (as discussed in Appendix 5.1). However, at the higher frequencies, the results of Section 5.3 suggest that the reverberation time method may be preferable to the steady state power method, due to the high absorption in the cabin [37]. Unfortunately, at the time the experiments were performed, only a standard chart recorder type measurement apparatus was available for use, and as the measured decay times of the chart recorder and the cabin acoustic response were

comparable in the higher frequency bands, the results were unusable. If this technique is to be tried again to improve on the absorption estimates of Section 5.3 then an electronic data capturing and averaging system must be used.

5.5 Acoustic Transfer Impedance Measurements

5.5.1 Experimental procedure

From the previous two sections it has become apparent that, in order to accurately determine the acoustic absorption at low frequencies, a method which can isolate the response of individual modes is required. The method of measuring the acoustic transfer impedance between a loudspeaker and a microphone, both placed within the cabin space, provides a means by which this can be achieved (at least at low frequencies).

The equipment used for these measurements is shown in Figure 5.4, which also shows the loudspeaker location. The microphone locations used are shown in Figures 5.5 and 5.14. The loudspeaker was driven with a Pseudo Random Binary Sequence signal generated by the Solartron 1200 analyser. The transfer function was taken as the ratio of the pressure measured at the microphone to the velocity of the source, thus ensuring measurement of the cabin acoustic response only.*

**The velocity of the source was measured at the edge of the KEF B139 loudspeaker using a laser Doppler vibrometer, the assumption being that over the frequency range of interest the speaker diaphragm moves as a flat piston. Subsequent tests have shown this to be a valid assumption only up to about 400 Hz. Figures 5.6(a), (b) and (c) show the transfer function modulus, phase and coherence between the speaker input voltage and the cone velocity at the centre of the diaphragm. Figures 5.7(a), (b) and (c) show the same variables but this time for a velocity measurement location on the top edge of the diaphragm. Even by 300 Hz there is a deviation from piston-like behaviour of about 3 dB, the worst affected area of the diaphragm being the centre.*

A sample plot of transfer modulus and phase over a frequency range of 0 to 500 Hz is presented in Figure 5.8. From this the modal response of the cabin at the lower frequencies can clearly be seen. Also evident is the transition from the "peaky" modal response to a smoother response above about 150 Hz. This is where the modes become too dense to exist individually, and "clumps" of modes appear [65]. Because it is difficult to extract any information from these higher modal density regions, and also because instrumentation problems during the test led to a lack of data being collected above 200 Hz, the work presented will concentrate mainly on the frequency range from 10 Hz to 200 Hz. The lower limit of 10 Hz is imposed by the response of the loudspeaker. In addition, the frequency range of interest regarding the applicability of active control is also restricted to this range which includes the fundamental (88 Hz) and second harmonic (176 Hz) blade passage frequencies.

5.5.2 Evaluation of the low frequency modal damping from the measured acoustic transfer impedances

Figure 5.9 shows the transfer function over the frequency range 0 to 100 Hz between the loudspeaker, located as in Figure 5.4, and the microphone placed at location 6 of Figure 5.5. The modal nature of the response at these low frequencies is evident. By performing an "expand" analysis about each of the resonance centre frequencies it has been possible to evaluate the modal damping constant, C_n, by measuring the half power point bandwidth, Δf_n, and invoking the relationship

$$C_n = 2\pi f_n \zeta_n = \pi \Delta f_n \qquad (5,9)$$

where f_n is the centre frequency of the n'th resonance. Figure 5.10 shows a sample expanded resonance. Table 5.3 lists the measured modal damping ratios for the first seven modes evaluated using equation (5.9), where the value for each particular frequency has been obtained as the average over at least three separate measurement locations. Also listed are the corresponding surface averaged absorption coefficients, evaluated using equation (5.6), and by assuming a cylindrical cabin 16.0 m long by 2.6 m in diameter. Table 5.4 lists in order of ascending natural

frequency up to 140 Hz the acoustic modes of such a cylindrical cavity. Because the first circumferential mode does not cut on until 76 Hz, all except the 81.9 Hz resonance results of Table 5.3 have been obtained assuming the modes to be axial.

5.5.3 Estimating the higher frequency modal damping from the measured acoustic transfer impedances

Whilst the technique used in Section 5.6 has enabled the accurate determination of the low frequency (< 85 Hz) modal damping ratios the intention has already been expressed to use this model at frequencies up to at least 176 Hz. Consequently it is necessary to try and estimate the damping of the higher frequency modes. If a suitable model of the cabin space could be found, it would be possible to predict the transfer impedance between any given loudspeaker and microphone locations, and then by adjusting the modal damping parameters in the model until the predicted response "matched up" with the experimental measurements, it would be possible to estimate the damping of the higher frequency modes. For reasons of mathematical simplicity it has been decided for the present study to use this matching method with a simple cylindrical room model. Although it is understood that this can only show the gross characteristics of the cabin space acoustics it is hoped that it will still be possible to obtain a reasonable estimate of the higher frequency absorption.

The length of the aircraft interior, from the front of the flight deck to the rear of the passenger compartment, is approximately 16.0 m and the maximum diameter in the passenger compartment is approximately 2.6 m (Figure 5.5). Consequently these dimensions were chosen for the cylinder model. The theoretical acoustic modes up to 140 Hz resulting from this model have already been listed in Table 5.4. Comparison of the theoretical resonance frequencies with the experimentally measured resonance frequencies of Table 5.3 does reveal some of the discrepancies to be expected from using such a simple model. However, for the present work this model will be assumed to be adequate.

Ten experimentally measured transfer functions over the frequency range 0 to 500 Hz were available for performing this matching. These were measured using the loudspeaker shown on Figure 5.4 and ten of the

microphones shown on Figure 5.5. The theoretical transfer impedances used for the matching procedure were all evaluated by modelling the loudspeaker as a 0.15 m by 0.22 m piston mounted flush with the cylinder surface and centred at z = 3.5 m, θ = 90° and r = 1.3 m, where z = 0.0 m corresponds to the front of the flightdeck and θ = 0° corresponds to the keel of the aircraft. Performing the matching of the transfer impedances as described above for each of the ten different microphone locations the absorption coefficients listed in Table 5.5 were chosen as giving the best overall agreement. A sample of the match between theoretical and experimental transfer impedances obtained using these absorption coefficients is given in Figure 5.11. This corresponds to the experimentally measured transfer impedance previously presented in Figure 5.8, which has been replotted on Figure 5.11 for direct comparison. (The experimental transfer impedance shown was obtained using a calibrated measuring system such that its units are $Pa/(ms^{-1})$. The theoretical transfer impedances have been evaluated in the same units, so the absolute levels of the experimental and theoretical results are directly comparable.) Note that whilst there are significant differences between the two responses, the general form of the experimental and theoretical responses seem to agree well, with roughly equal variations in pressure levels occurring, with the lower frequency modes being discernible for both cases, and with "clumping" of modes occurring at higher frequencies. Table 5.5 also lists the resulting absorptions obtained in the cylindrical room model from using these absorption coefficients and comparison of these values with those obtained using the steady state power measurements (Table 5.2) shows reasonable agreement. On the basis of the results of Table 5.5 the Schroeder frequency [37] for the aircraft cabin is approximately 80 Hz. However, for this situation the Schroeder frequency cannot be assumed to separate the lower frequency non diffuse region from the higher frequency diffuse sound field region. In the current situation the sound field is still essentially dominated by purely axial modes at 80 Hz so it certainly cannot be considered as diffuse. The value of the Schroeder frequency in this instance, therefore, is determined by the high levels of acoustic damping present and not by the high acoustic modal density.

5.5.4 The acoustic pressure distribution axially along the cabin centreline

In order to try and identify the shortfalls of this simple model, individual transfer impedances were measured between the loudspeaker at the location of Figure 5.4 and all 30 microphone locations of Figure 5.5, for a frequency range from 0 to 100 Hz. A sample of the experimentally measured responses is shown in Figures 5.12(a). Also shown in Figure 5.12(b) is the corresponding theoretical response. Once again the general form of the theoretical and experimental results appears to agree, but the details do not.

From the 30 transfer impedance plots it has been possible to map out the axial pressure distribution along the centreline of the cabin for the lower frequency resonances. These results are shown in Figures 5.13(a-d), and overlayed on these are the corresponding theoretical pressure distributions. The agreement between experiment and theory for the 10 Hz and 17.8 Hz resonances is reasonable. However, for the higher frequency resonances the effective length of the cabin appears to be longer than that used in the model. For example, at 33 Hz, a theoretical axial mode of order 3 is dominant, yet the dominant experimental mode is of order 4, thus suggesting a cabin length of 20.8 m. However, the maximum cabin length of 16.0 m has already been employed in the model. This feature could be caused by the effects of the four coupled cavities which make up the total length of the cabin, although this possibility has not been investigated further.

5.5.5 The acoustic pressure distribution circumferentially around the cabin circumference

The results of the preceding section have shown that even the low order axial modes are not necessarily predicted correctly by the cylindrical room model. In this section the circumferential modes are to be studied. As with the axial modes, it would not be expected that the model should be able to predict higher order circumferential modes with any accuracy, due primarily to the presence of a floor across the cylinder. However, it might be hoped that this will not distort the lower order modes too much. In order to check this, fourteen transfer impedances over the frequency range 0 to 200 Hz were measured around the

circumference of the cabin in the plane of microphone 9 of Figure 5.5, the loudspeaker being placed as indicated in Figure 5.14. The microphone locations were spaced at approximately 0.5 m intervals around the circumference (see Figure 5.14).

A sample plot of one of the 13 experimental transfer impedances is shown in Figure 5.15(a), along with the corresponding theoretical response in Figure 5.15(b). The first three theoretical circumferential modes occur at 76 Hz, 128 Hz and 176 Hz. Figures 5.16(a-c) show the sound pressure distribution around the circumference at these three frequencies. The agreement between theory and experiment for the 76 Hz and 128 Hz resonances is very good, despite the fact that the theoretical response has been evaluated at the inside surface of the cylinder over the whole circumference, with no account at all being taken of the floor. The comparison of experiment and theory at 176 Hz is not so impressive, although the limited number of fourteen experimental locations makes it difficult to interpret the experimental pressure distribution.

5.6 Conclusions

(i) Three methods have been presented to estimate the acoustic absorption and also the nature of the sound field in a fully trimmed B.Ae.748 cabin.

(ii) The reverberation time technique used in the tests failed to give accurate results for two main reasons. Firstly, the non-diffuseness of the sound field at low frequencies made it difficult to measure the reverberation time due to the non-linearity of the decay, and even if it had been measured successfully it would have been difficult to assign a meaning to what had been measured. Secondly, for higher frequencies, the reverberation time was so short that electronic techniques must be used to capture the decays. These were not available at the time of the tests.

(iii) The method of steady state power balance did yield values for the absorption, but these can be treated with only marginal confidence due to the high absorption measured.

(iv) The method of measuring the acoustic transfer impedances between two points within the cabin has been used to evaluate individual modal damping ratios for frequencies up to 80 Hz, and also to estimate the higher frequency damping. This method has demonstrated the shortfalls of using a simple cylinder model to represent the acoustics of the cabin space. However, it has been shown that whilst pointwise predictions of sound pressure levels cannot be expected using this simplified type of model, it should be adequate for showing the gross characteristics of the sound field and should be able to provide predictions for the effectiveness of applying active noise control to cabins of this type at low frequencies.

(v) The Schroeder frequency in the cabin is approximately 80 Hz. However, this cannot be taken as the transition frequency from non-diffuse to diffuse sound field behaviour as this value is determined by the high value of cabin damping.

(vi) The best estimates of the absorption coefficient at various frequencies from the acoustic transfer impedances are given in Table 5.5 and are comparable with those estimated using the power balance method. These values are used in Chapter 7 for the active noise control predictions.

TABLE 5.1. Surface averaged absorption coefficients evaluated using the steady state power balance method

Octave band centre freq. (Hz)	No. of source locations	No. of mic. locations/ source location	Source power output (dB re 10^{-12} W)	Average SPL (dB re 2×10^{-5} Nm^{-2})	No. of modes resonant within the bandwidth*			High freq. asymptotic no. of modes* resonant within the source band-withs (M_o)	Absorption coefficients $\bar{\alpha}$ (from eq. (5.7))
					Axial	Rad + circ	Combined		
125	3	6	99.0	84.8	8	3	43	37	0.77
250	3	6	99.0	82.8	17	7	241	289	1.22
500	3	6	99.0	81.1	33	31	1681	2348	1.81
1000	2	6	99.0	81.4	–	–	–	18253	1.69

*These values have been calculated by assuming the cabin space to be a 16.0 m long by 2.6 m diameter cylindrical room.

TABLE 5.2

Comparison of absorption coefficients for a typical aircraft as suggested by Wilby *et al* [2] and those measured using the power balance method

Octave band centre freq. (Hz)	Suggested absorption coefficients				Absorption (m^2)		
	Carpet	Seats	Baseline sidewall	Maximum sidewall	Base-line	Maximum	Measured (from Table 5.1)
125	0.06	0.15	0.17	0.55	28	62	108
250	0.13	0.17	0.34	0.74	48	84	172
500	0.22	0.20	0.44	0.76	62	91	255
1000	0.34	0.18	0.42	0.60	64	80	239

TABLE 5.3

Modal damping ratios evaluated from the measured half power point bandwidths

Centre freq. (Hz)	Modal damping ratio (ξ_n)	Equivalent surface averaged absorption coeff. ($\bar{\alpha}$)
22.5	0.033	0.13
24.2	0.032	0.14
30.1	0.031	0.16
49.3	0.043	0.37
56.0	0.045	0.44
66.3	0.043	0.50
81.9	0.040	0.40

TABLE 5.4

The acoustic modes of a 16.0 m long by 2.6 m diameter cylinder, arranged in order of ascending natural frequency up to 140 Hz and then selected modes to 315 Hz.

n_1	n_2	n_3	Frequency (Hz)
0	0	0	0.0
1	0	0	10.7
2	0	0	21.4
3	0	0	32.2
4	0	0	42.9
5	0	0	53.6
6	0	0	64.3
7	0	0	75.0
0	1	0	77.3
1	1	0	78.1
2	1	0	80.2
3	1	0	83.7
8	0	0	85.8
4	1	0	88.4
5	1	0	94.1
9	0	0	96.5
6	1	0	100.6
10	0	0	107.2
7	1	0	107.7
8	1	0	115.5
11	0	0	117.9
9	1	0	123.6
0	2	0	128.3
12	0	0	128.6
1	2	0	128.7
2	2	0	130.0
10	1	0	132.2
3	2	0	132.2
4	2	0	135.2
5	2	0	139.0
13	0	0	139.3
0	0	1	160.9
0	3	0	176.4
0	4	0	223.3
0	5	0	269.3
0	0	2	294.6
0	6	0	315.0

TABLE 5.5

Absorption coefficients used in the theoretical model to best match theoretical and experimental transfer responses

Frequency range (Hz)	Absorption coefficient	Absorption (m^2)
<20	0.16	14
20 < f < 200	f × 0.008	141 @ 125 Hz
>200	1.6	225

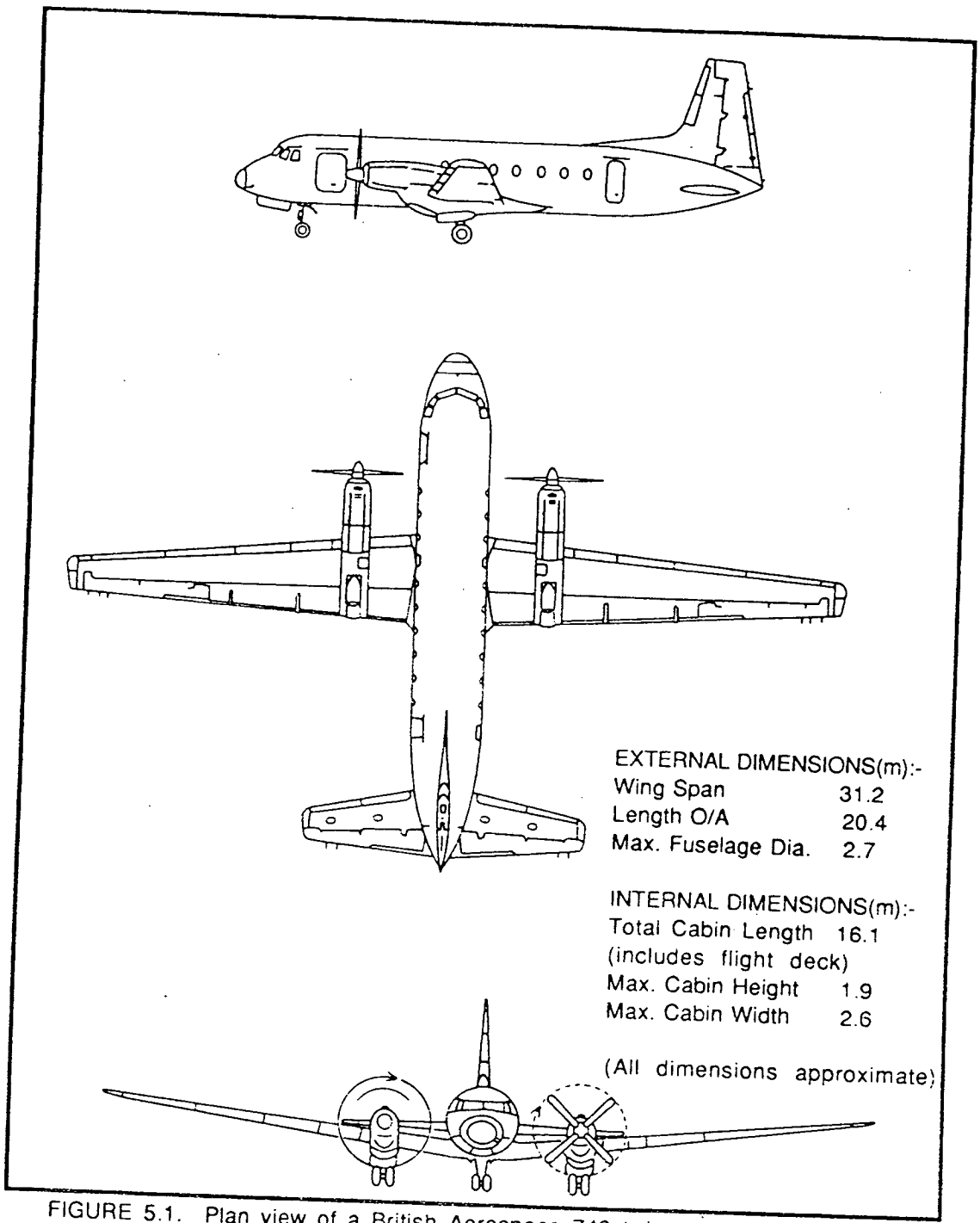

FIGURE 5.1. Plan view of a British Aerospace 748 twin turboprop , 48 seat passenger aircraft.

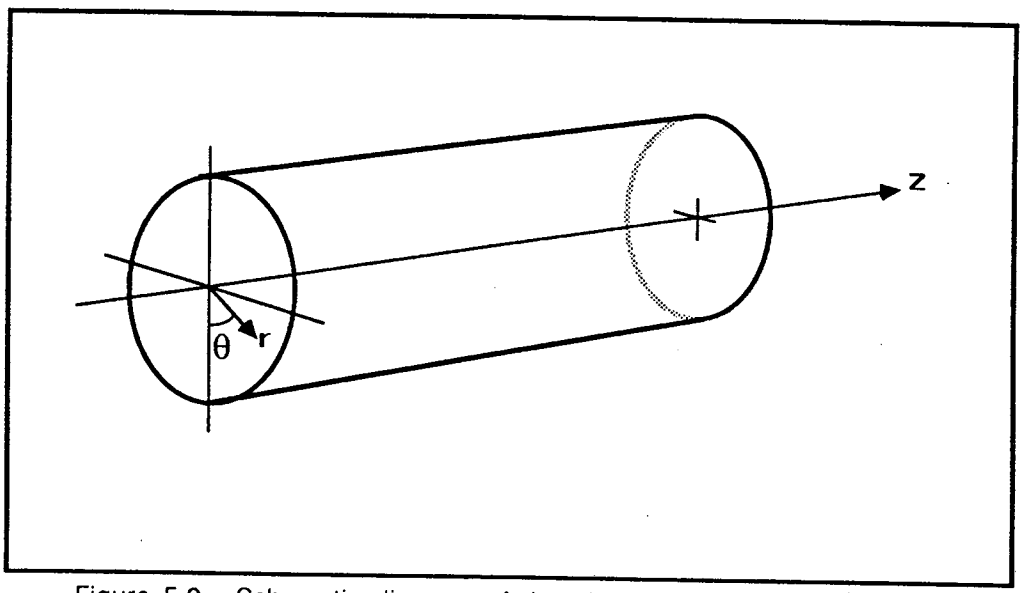

Figure 5.2. Schematic diagram of the shell coordinate system used.

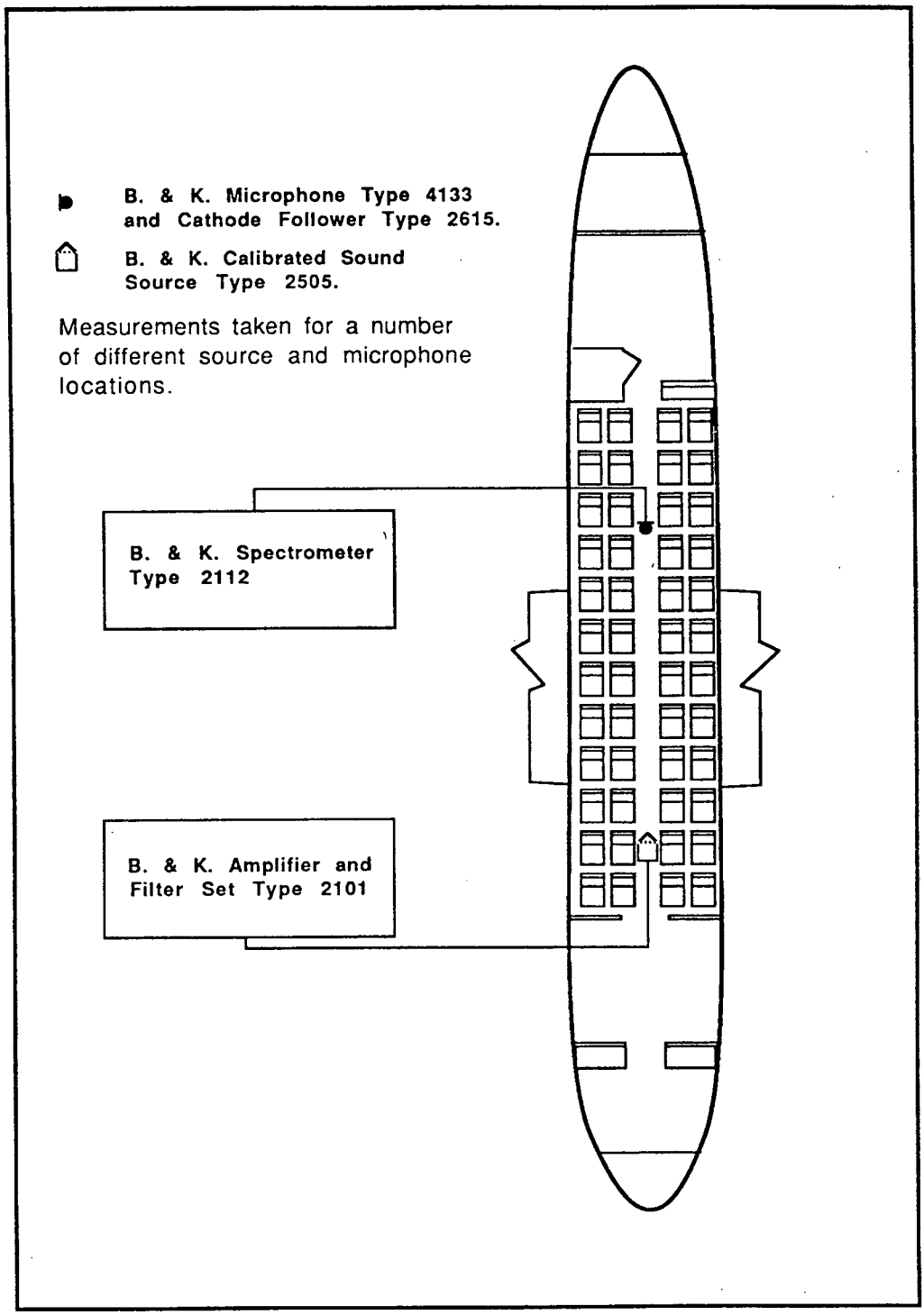

FIGURE 5.3. Block diagram of the equipment used for the steady state power measurements.

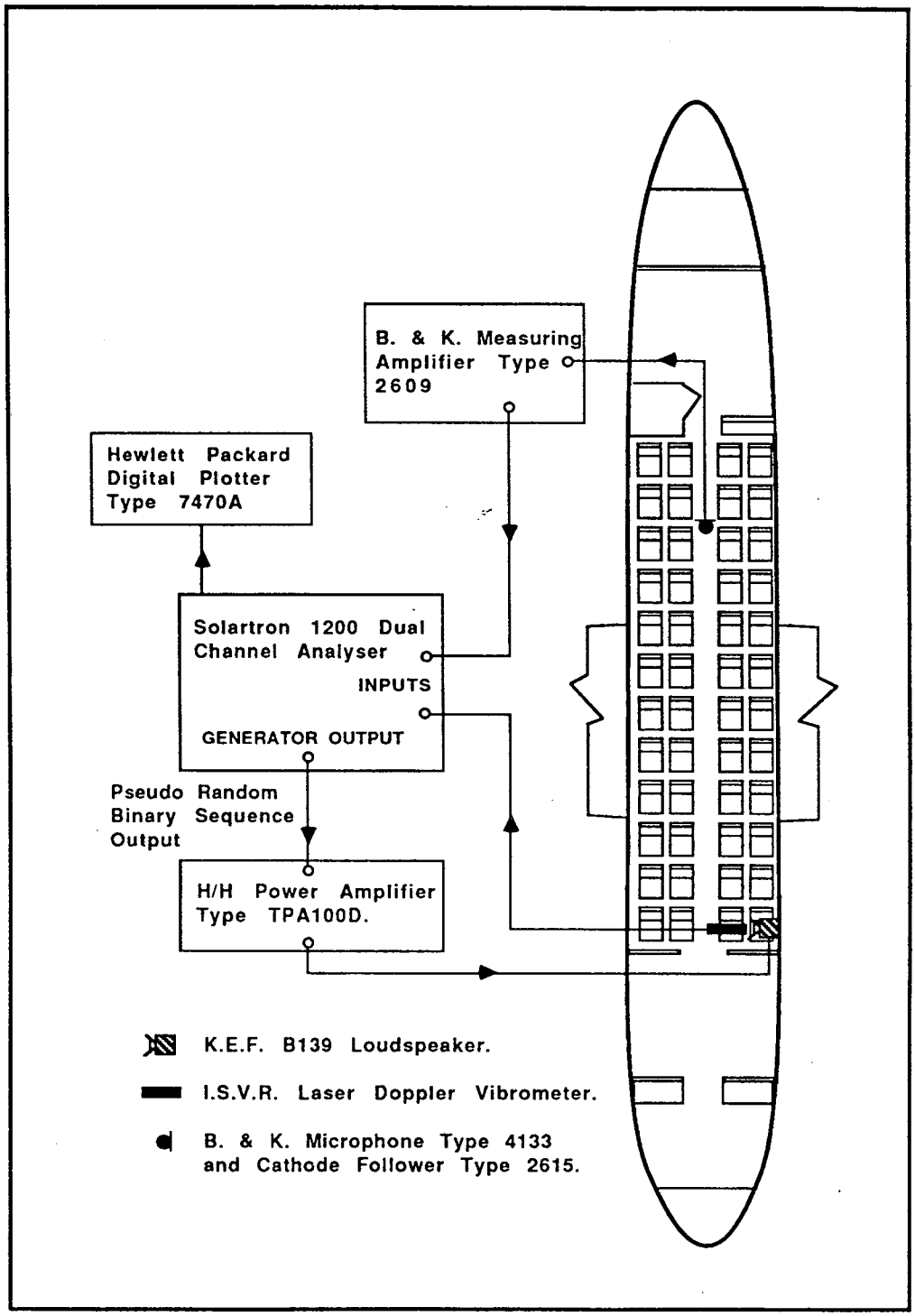

FIGURE 5.4. Block diagram of the equipment used for the cabin acoustic transfer impedance measurements.

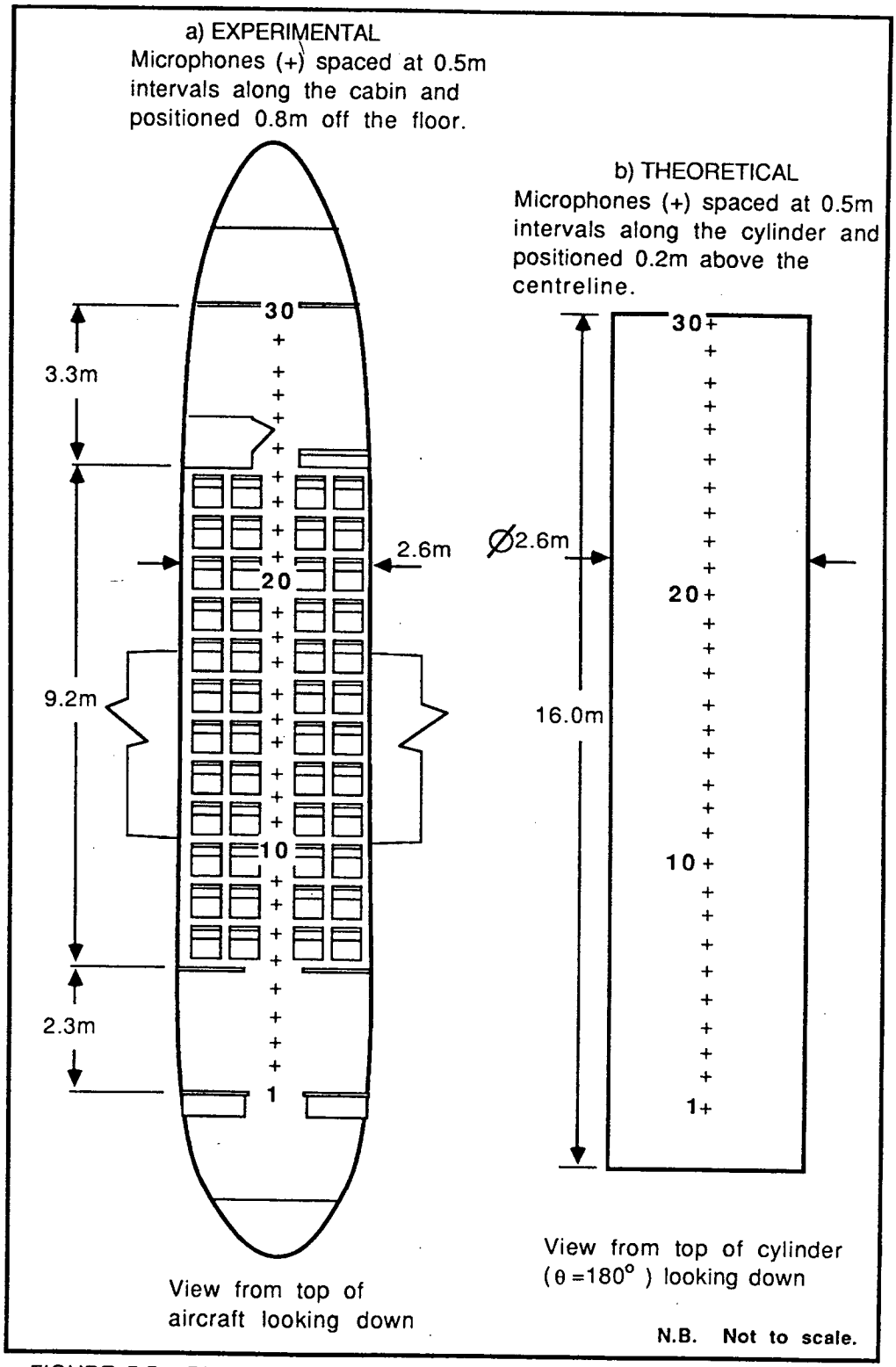

FIGURE 5.5. Diagram of the microphone locations used for the axial transfer impedance measurements and the corresponding theoretical predictions.

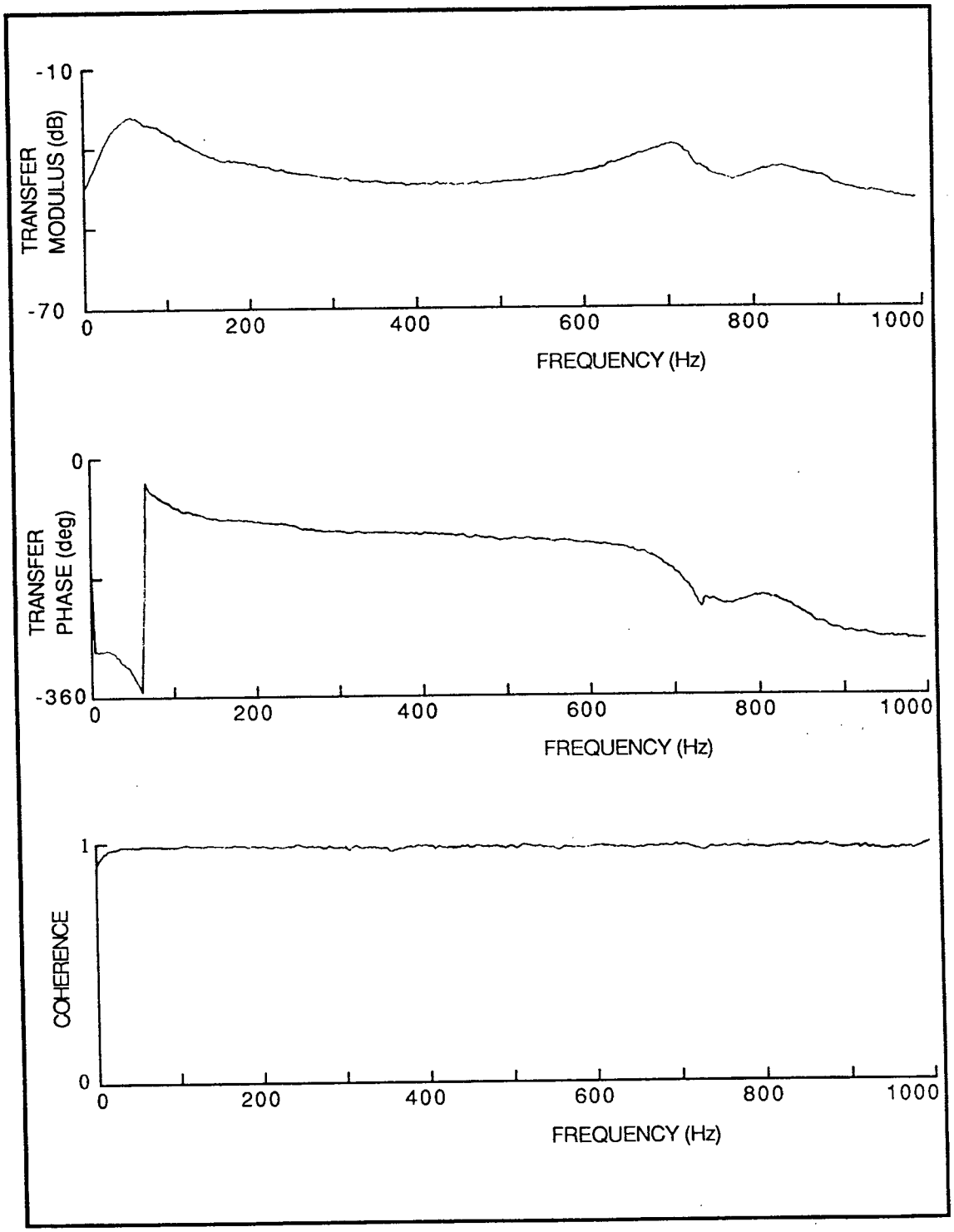

FIGURE 5.6. The transfer function between the cone velocity of the K.E.F. B139 loudspeaker measured at the centre of the diaphragm and the speaker input voltage.

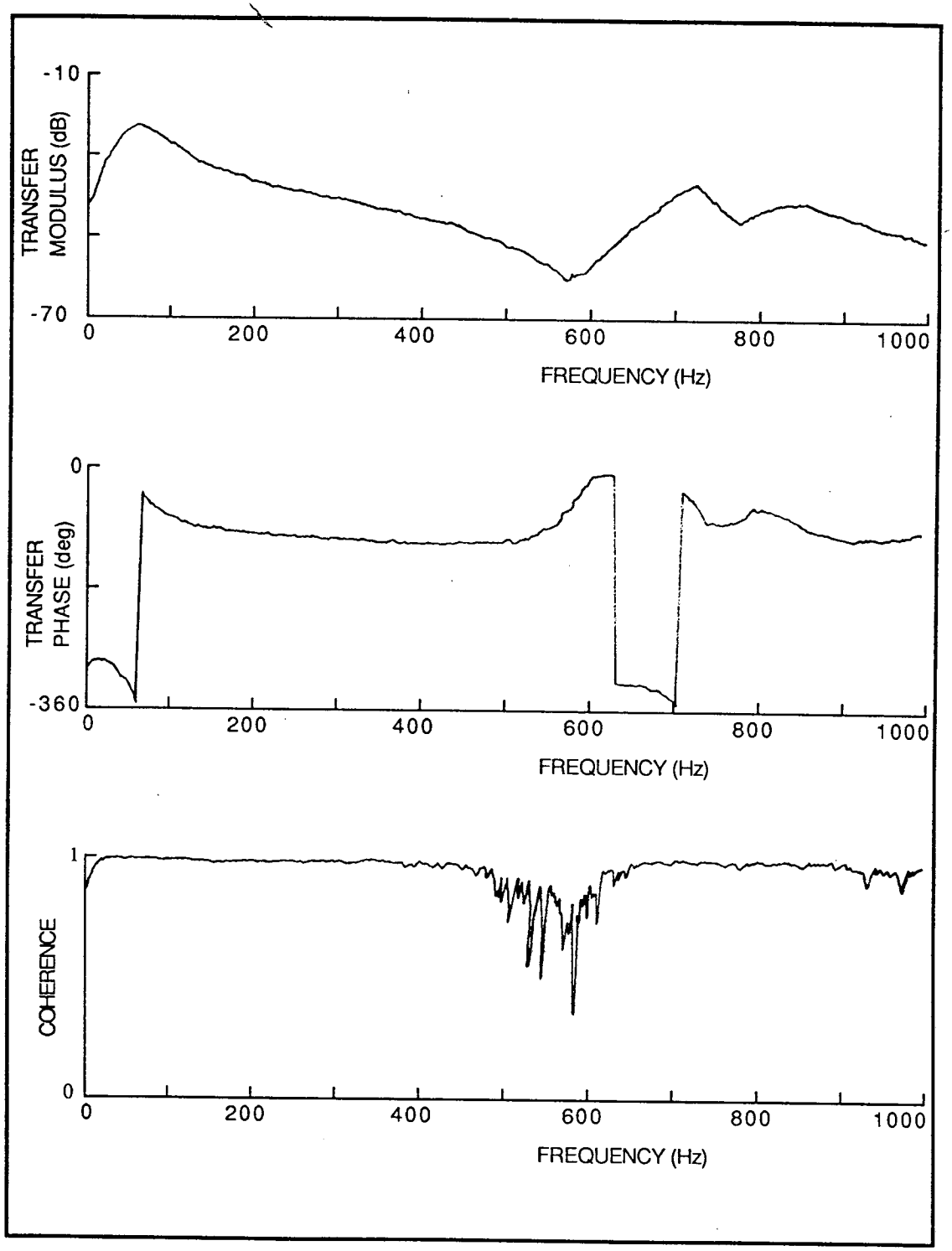

FIGURE 5.7. The transfer function between the cone velocity of the K.E.F. B139 loudspeaker measured at the outer edge of the diaphragm and the speaker input voltage.

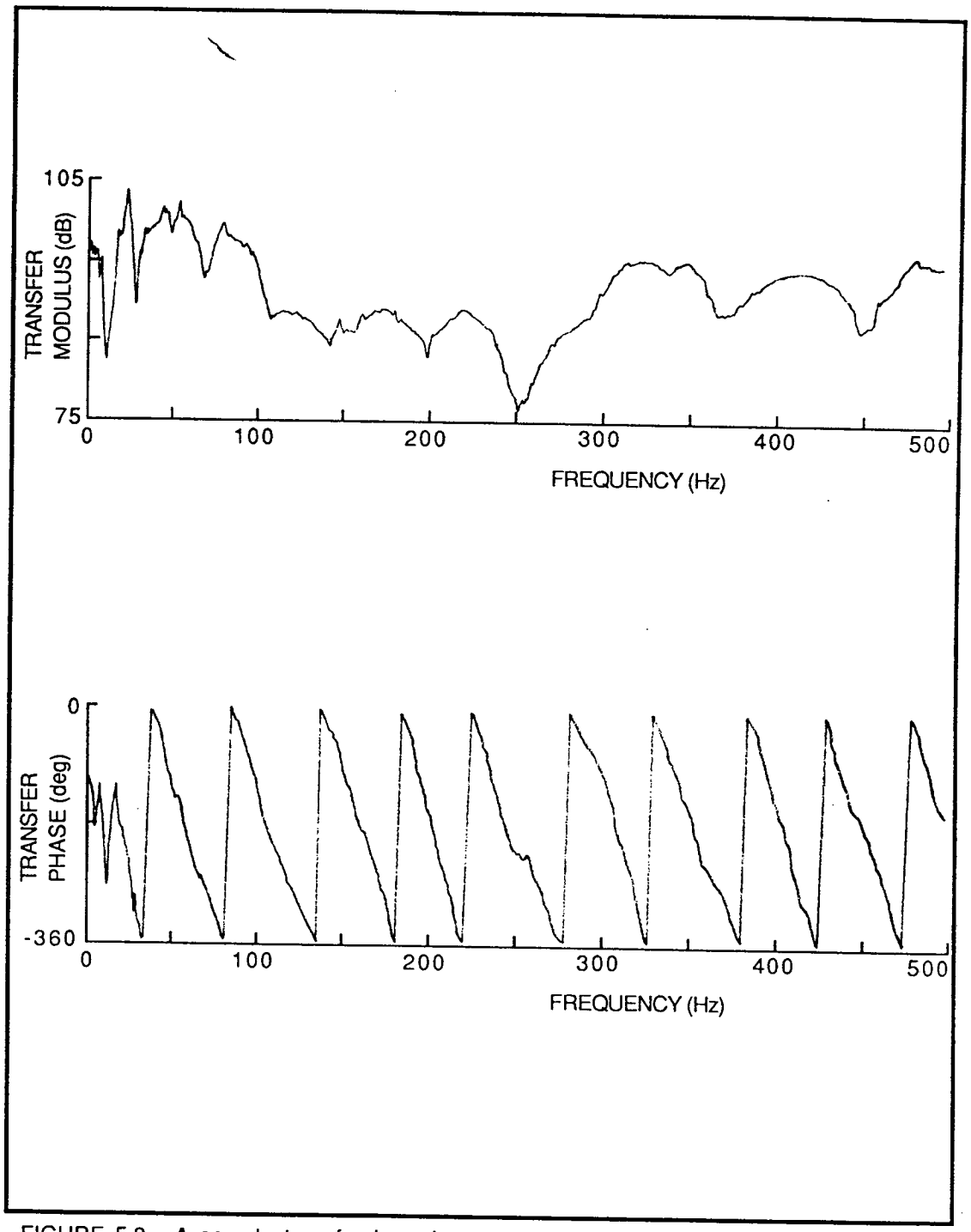

FIGURE 5.8. A sample transfer impedance measurement over the frequency range 0 to 500Hz. The loudspeaker was located as shown in Figure 5.4 and the microphone was at location 16 of Figure 5.5.

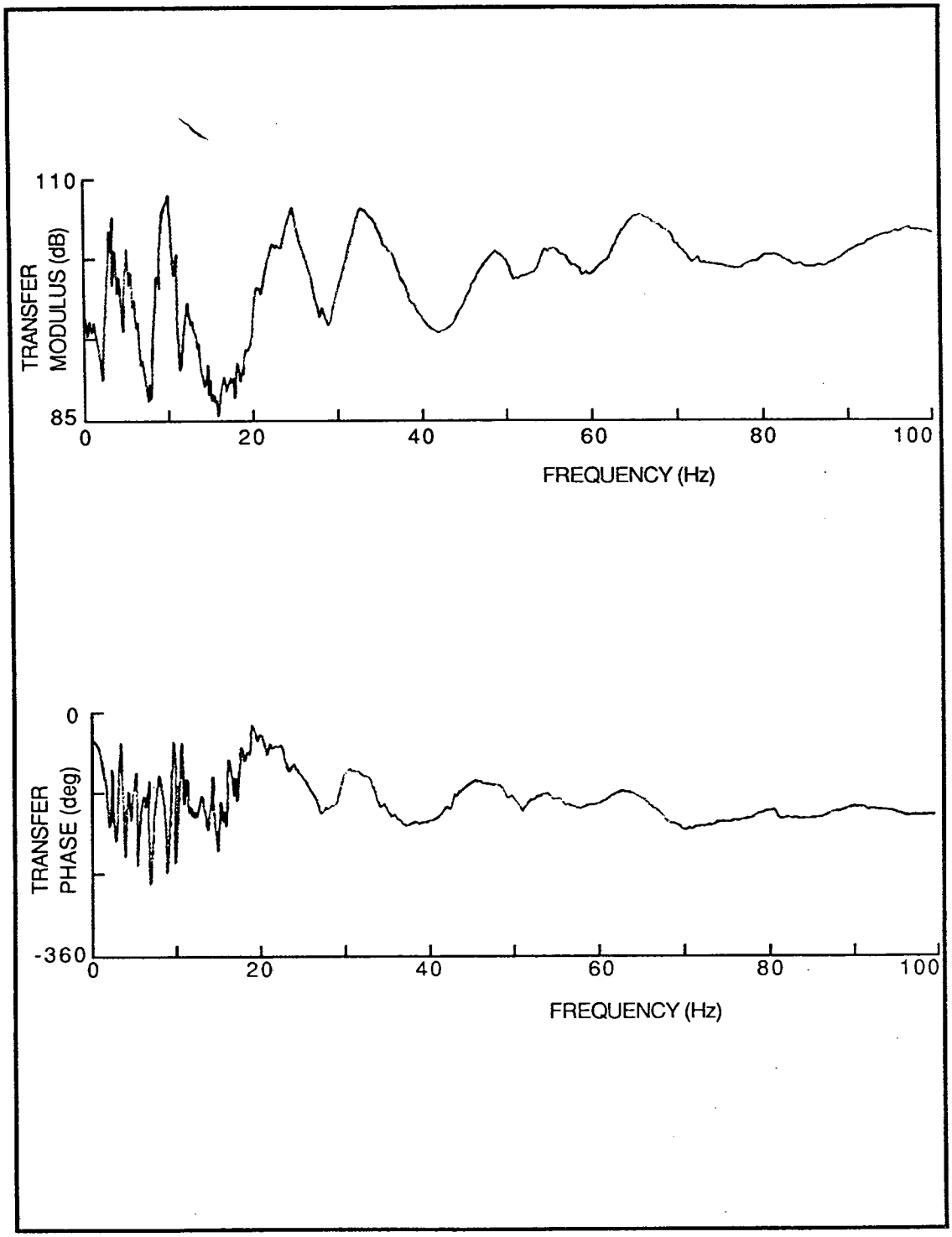

FIGURE 5.9. A sample transfer impedance measurement over the frequency range 0 to 100Hz. The loudspeaker was located as shown in Figure 5.4 and the microphone was at location 6 of Figure 5.5.

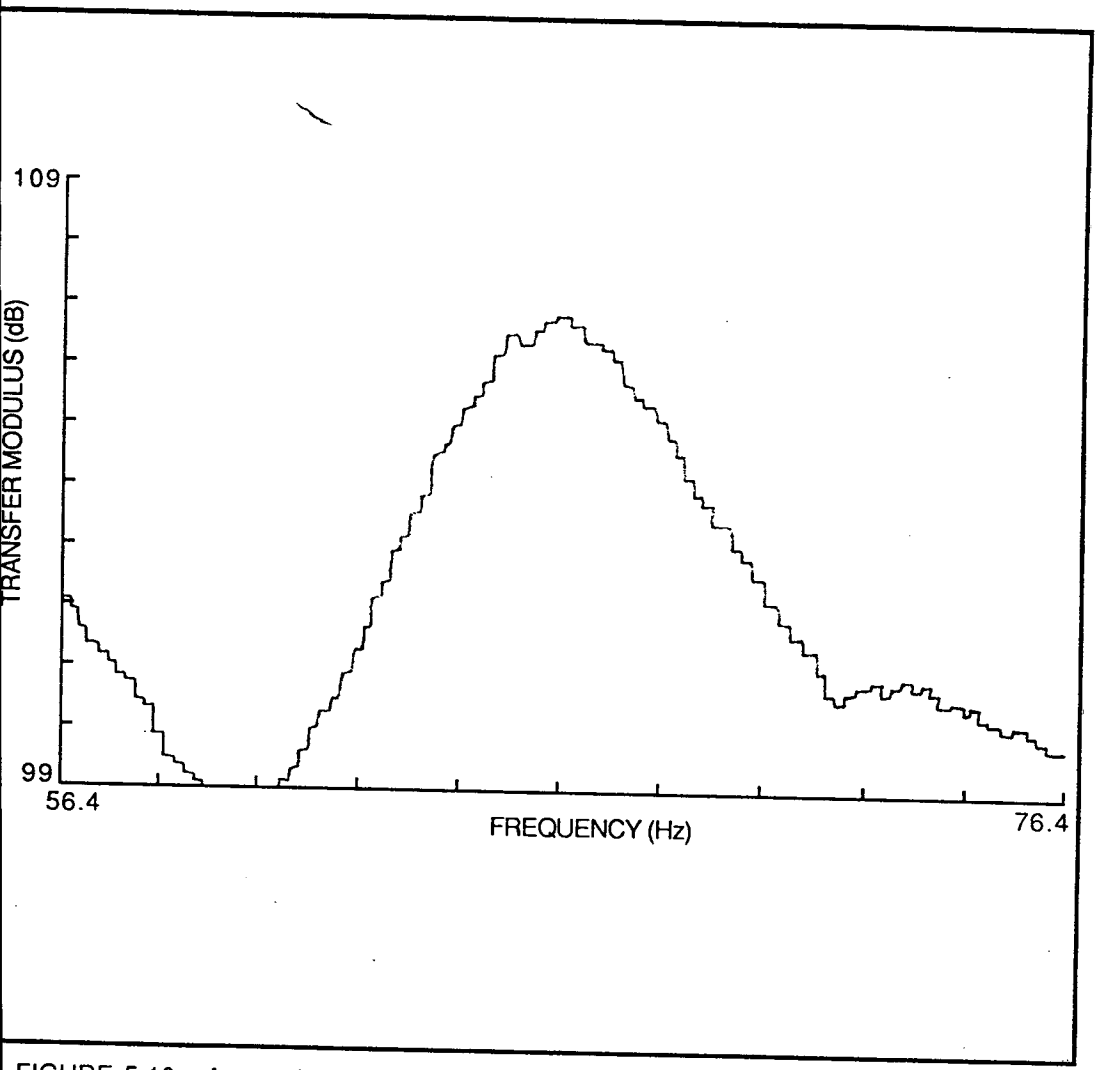

FIGURE 5.10.. A sample expand analysis of the 66Hz resonance of Figure 5.9.

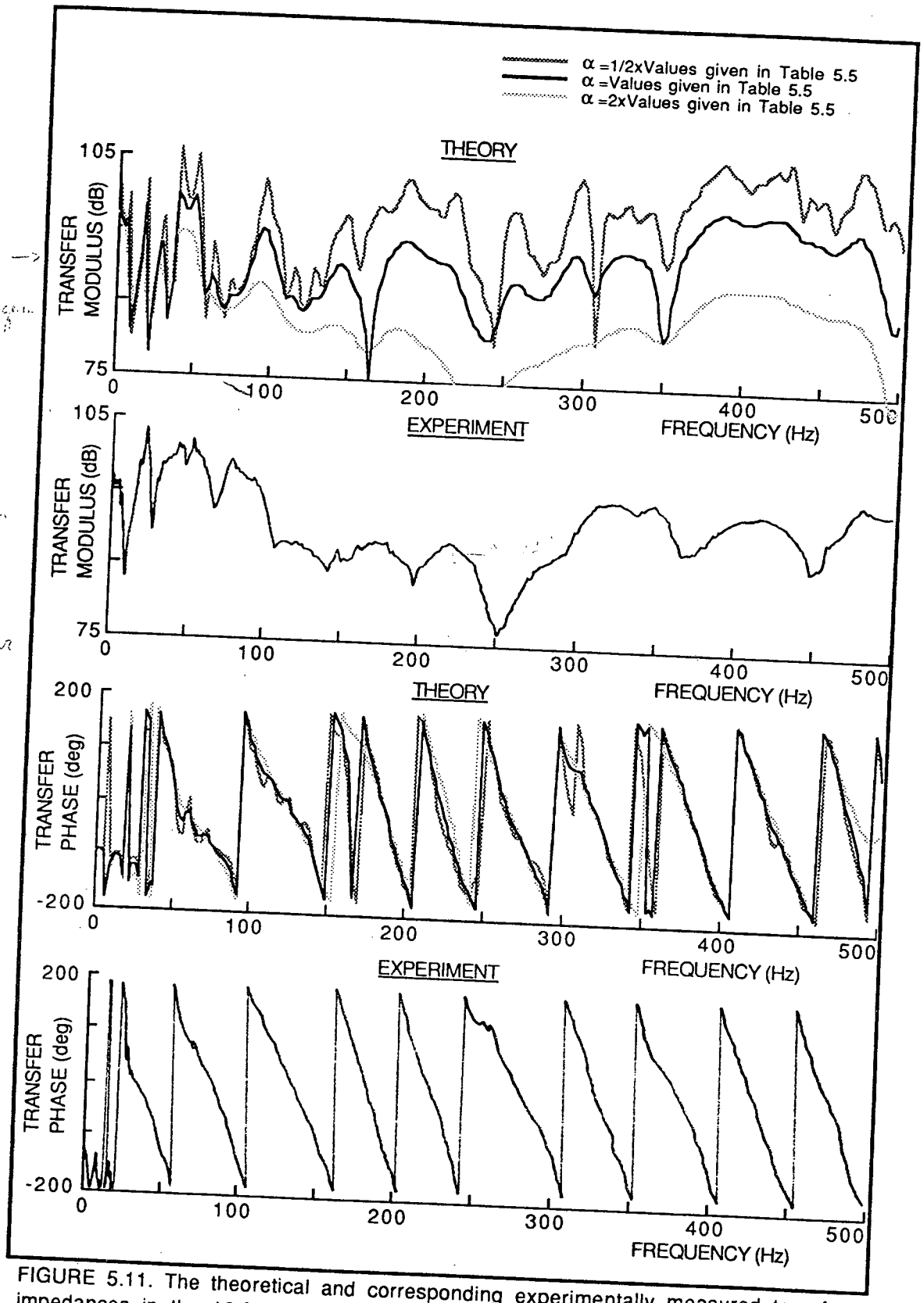

FIGURE 5.11. The theoretical and corresponding experimentally measured transfer impedances in the 16.0m long by 2.6m diameter cylindrical room/aircraft cabin over the frequency range 0 to 500Hz. The loudspeaker was located as shown in Figure 5.4 and the microphone was at location 16 of Figure 5.5. The results of using three different theoretical values of acoustic damping are shown.

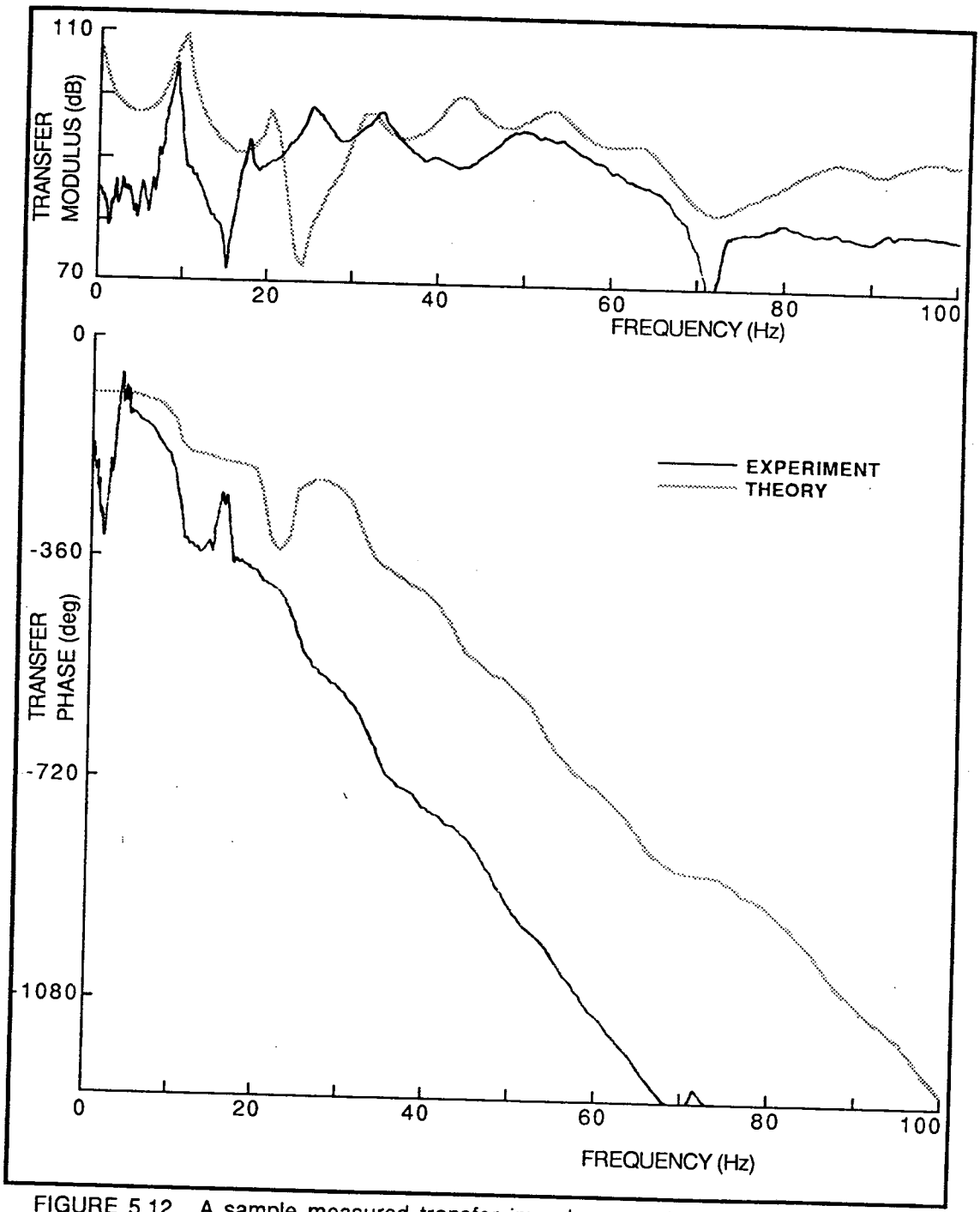

FIGURE 5.12. A sample measured transfer impedance and the corresponding theoretical response over the frequency range 0 to 100Hz. The loudspeaker was located as shown in Figure 5.4 and the microphone was at location 30 of Figure 5.5.

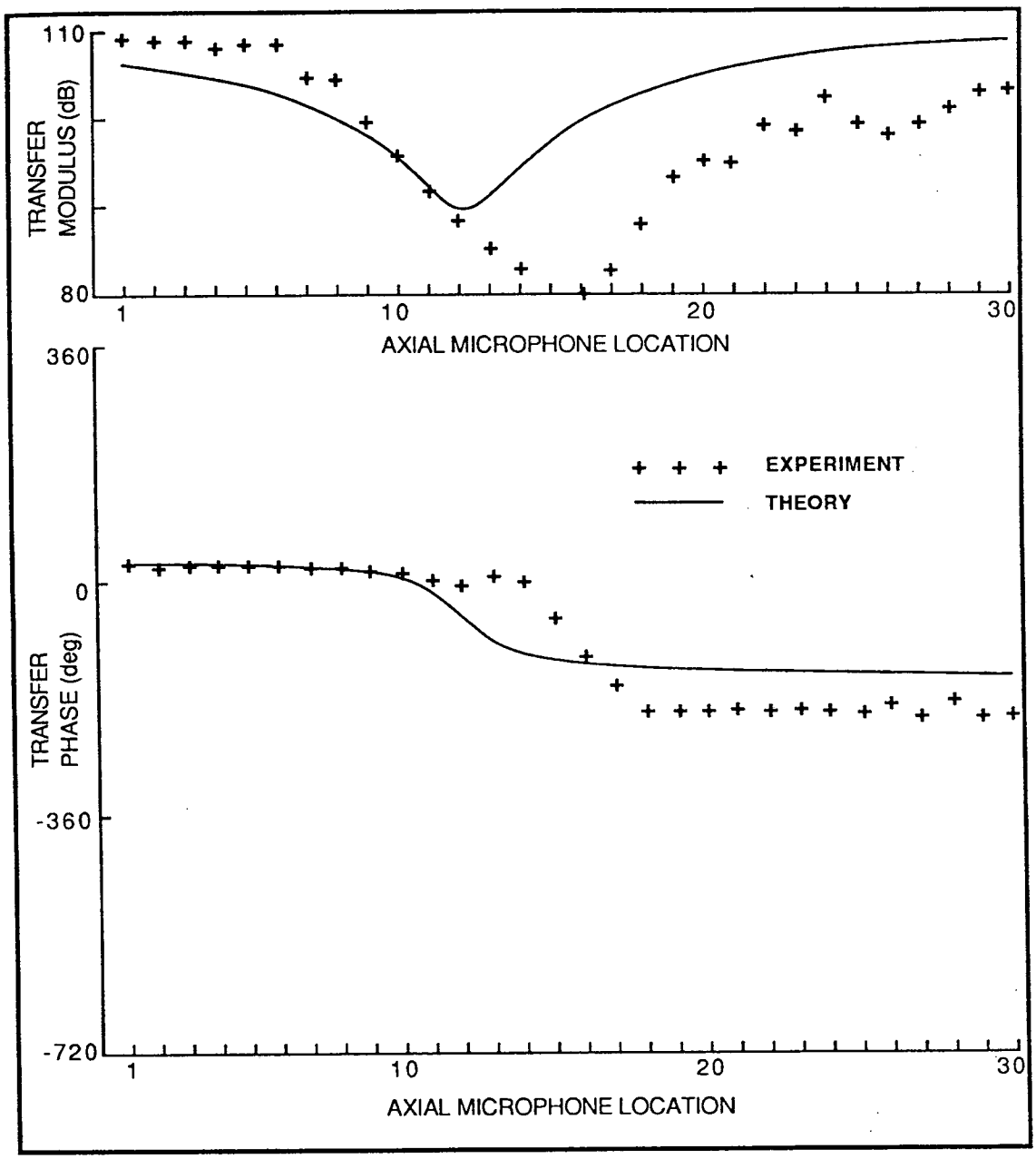

FIGURE 5.13(a). The pressure distribution along the cabin centre aisle at a frequency of 10.0Hz. The experimental distribution has been evaluated from the transfer impedance measurements taken at each of the microphone locations shown in Figure 5.5.

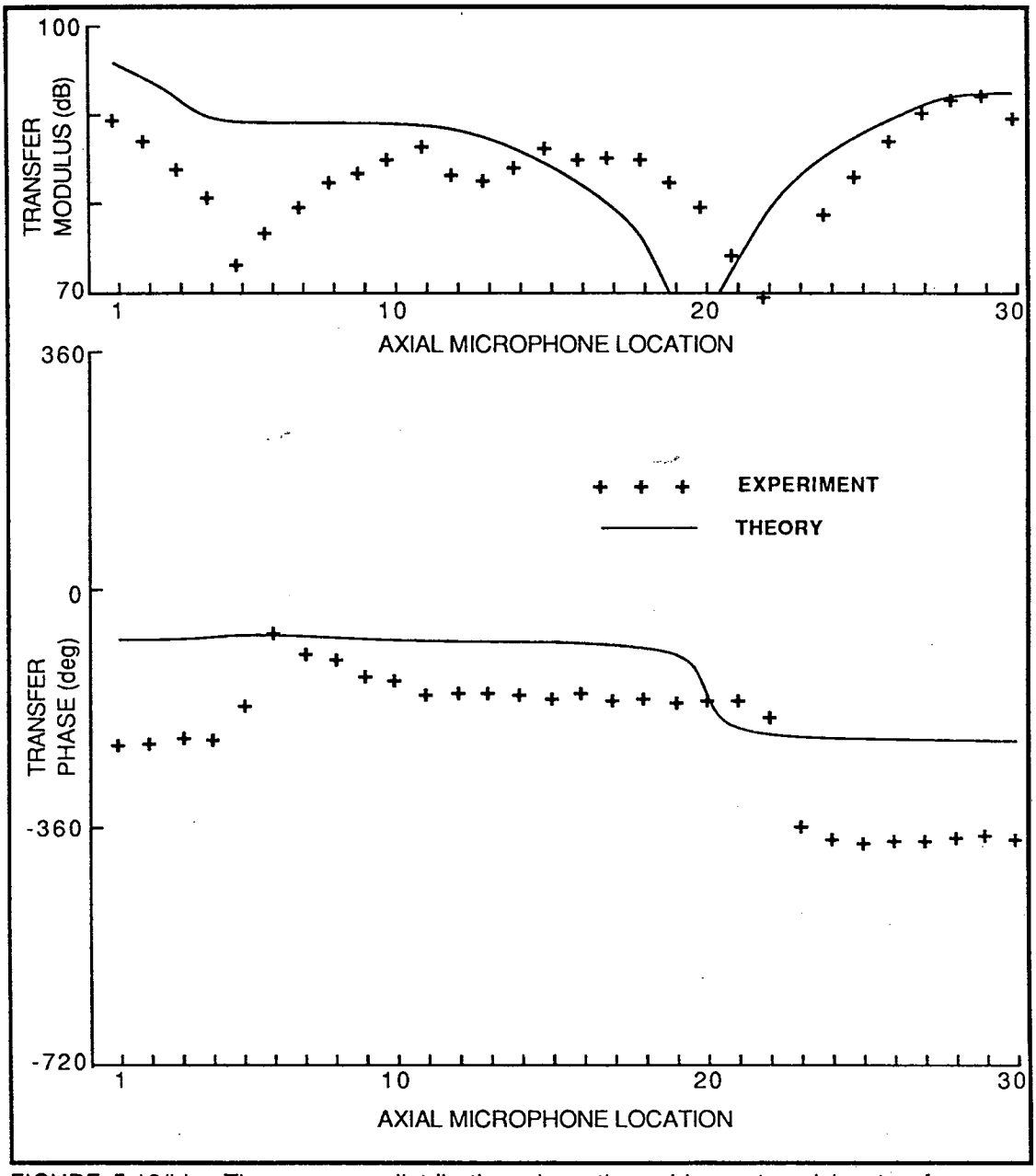

FIGURE 5.13(b). The pressure distribution along the cabin centre aisle at a frequency of 17.8Hz. The experimental distribution has been evaluated from the transfer impedance measurements taken at each of the microphone locations shown in Figure 5.5.

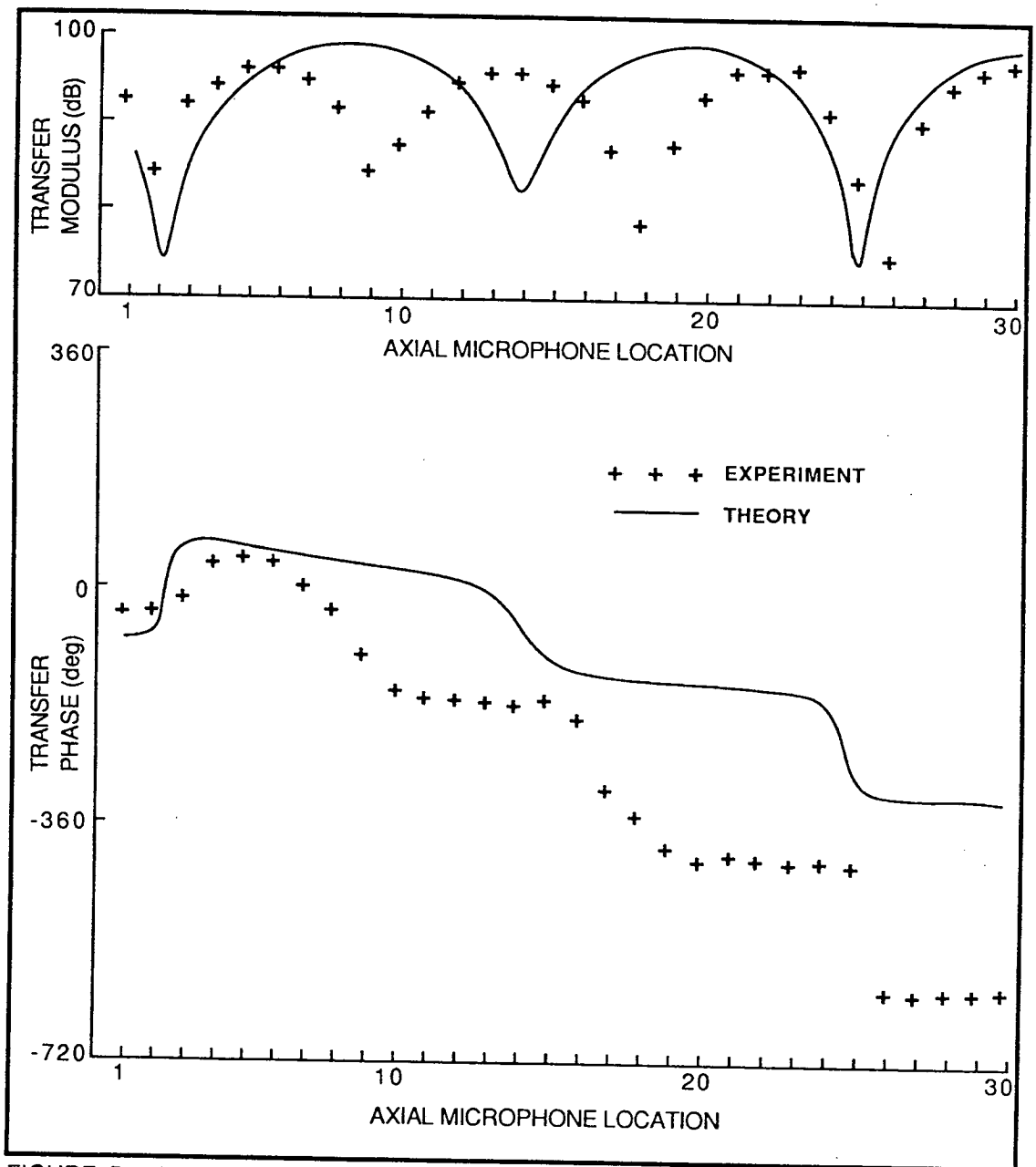

FIGURE 5.13(c). The pressure distribution along the cabin centre aisle at a frequency of 33.0Hz. The experimental distribution has been evaluated from the transfer impedance measurements taken at each of the microphone locations shown in Figure 5.5.

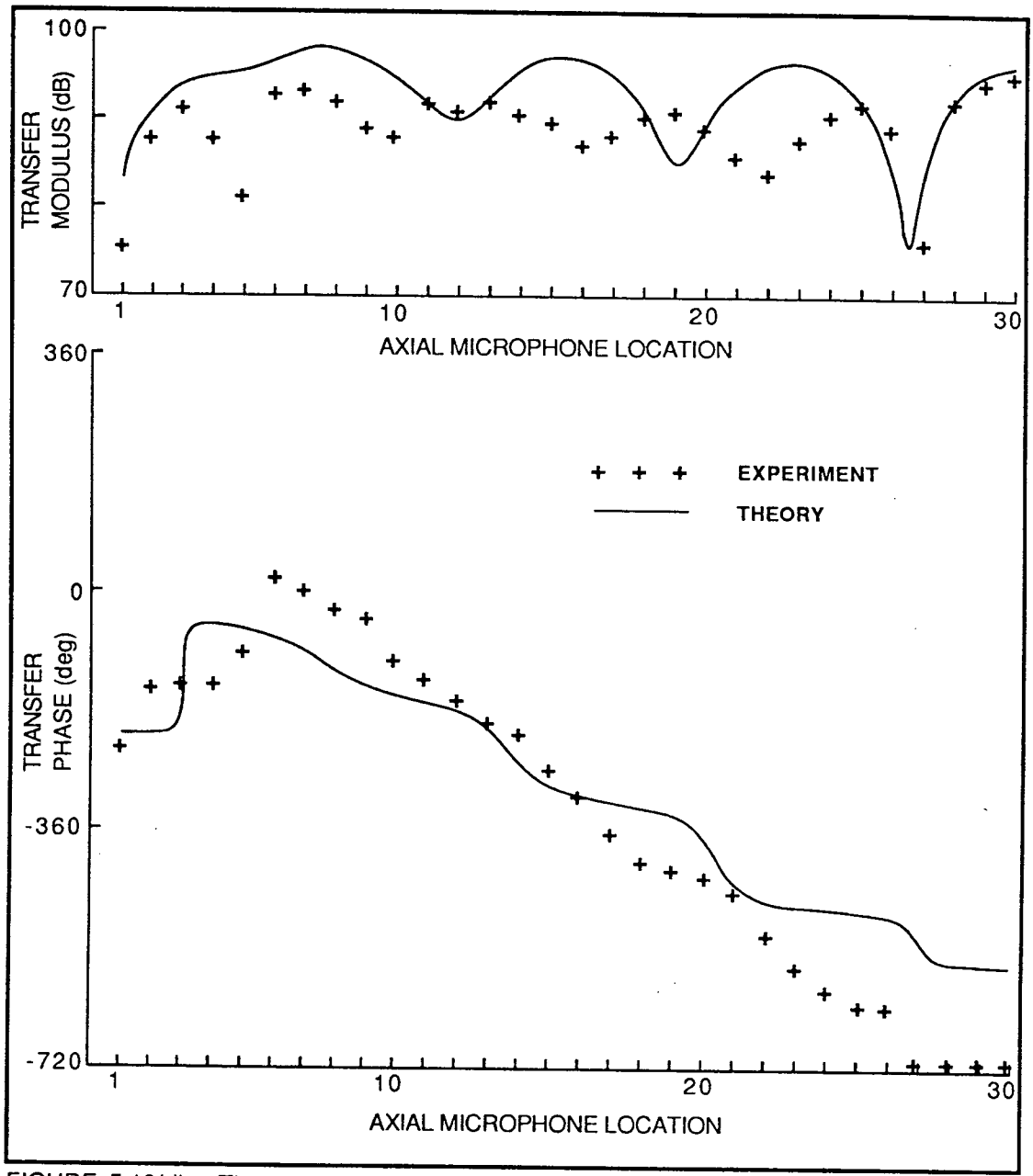

FIGURE 5.13(d). The pressure distribution along the cabin centre aisle at a frequency of 49.0Hz. The experimental distribution has been evaluated from the transfer impedance measurements taken at each of the microphone locations shown in Figure 5.5.

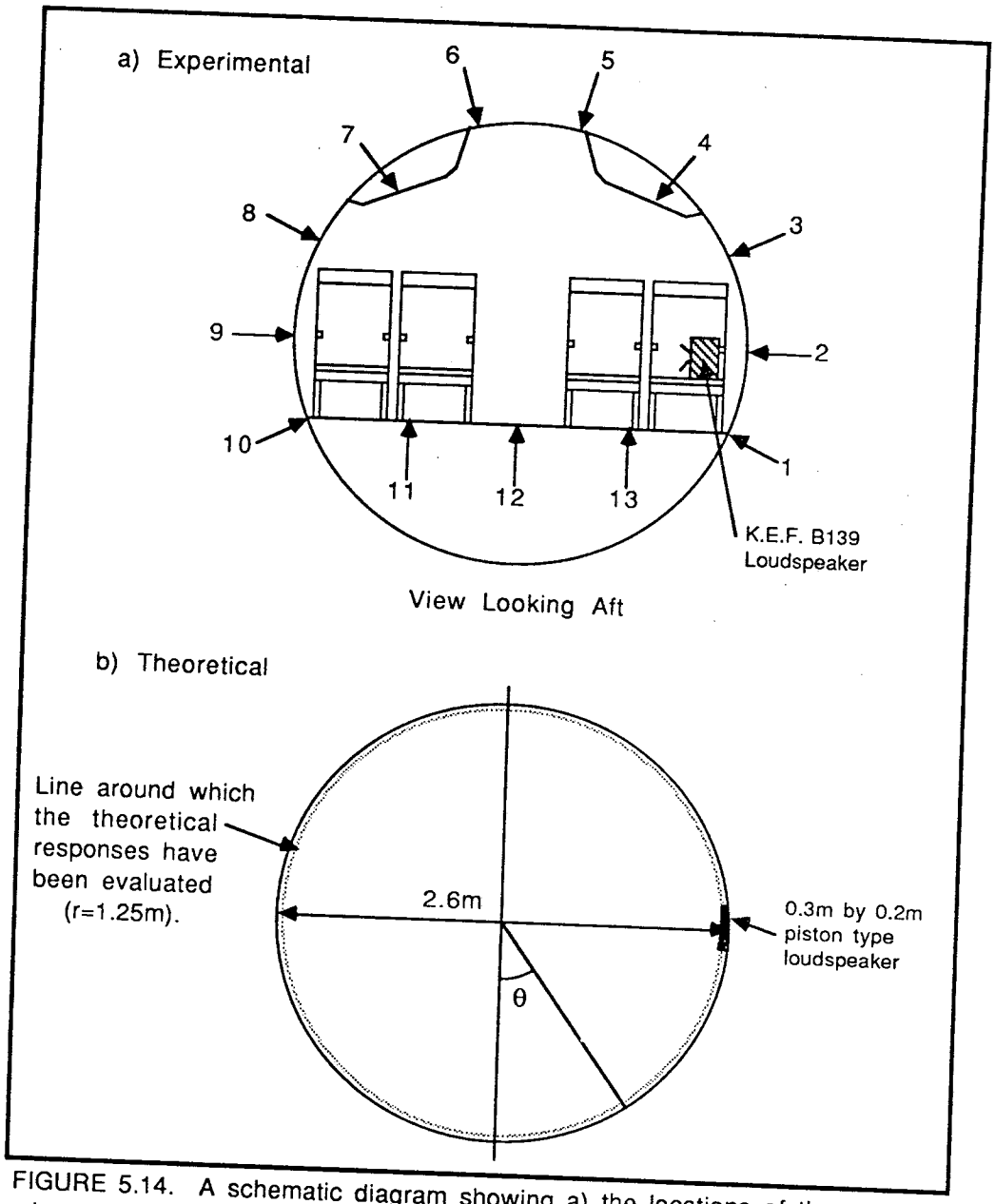

FIGURE 5.14. A schematic diagram showing a) the locations of the microphones used for the circumferential transfer impedance measurements and b) the line around which the corresponding theoretical responses have been evaluated. The axial location corresponds to microphone location 9 of Figure 5.5.

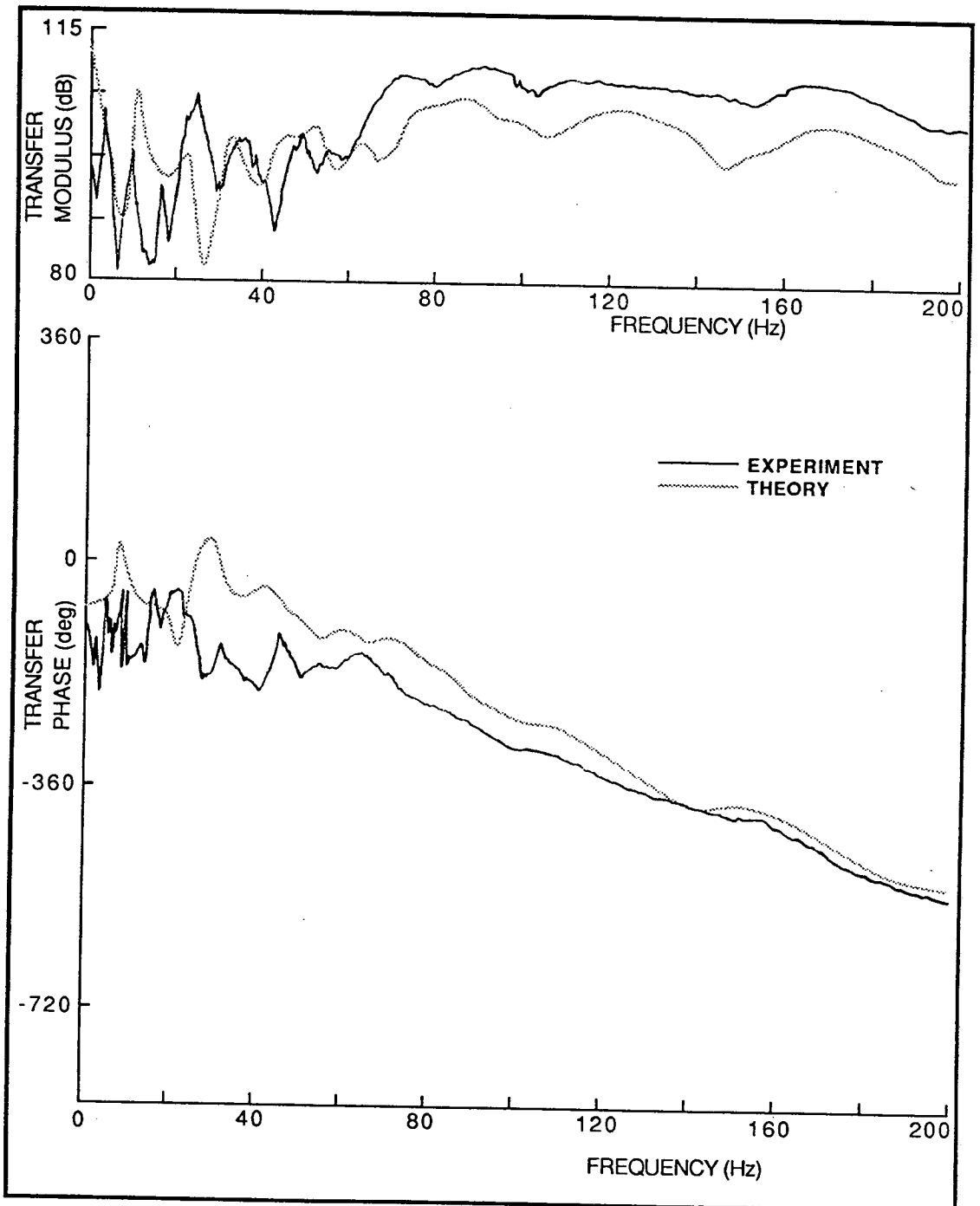

FIGURE 5.15. A sample measured transfer impedance and the corresponding theoretical response over the frequency range 0 to 200Hz. The loudspeaker was located as shown in Figure 5.14 and the microphone was at location 1 of Figure 5.14.

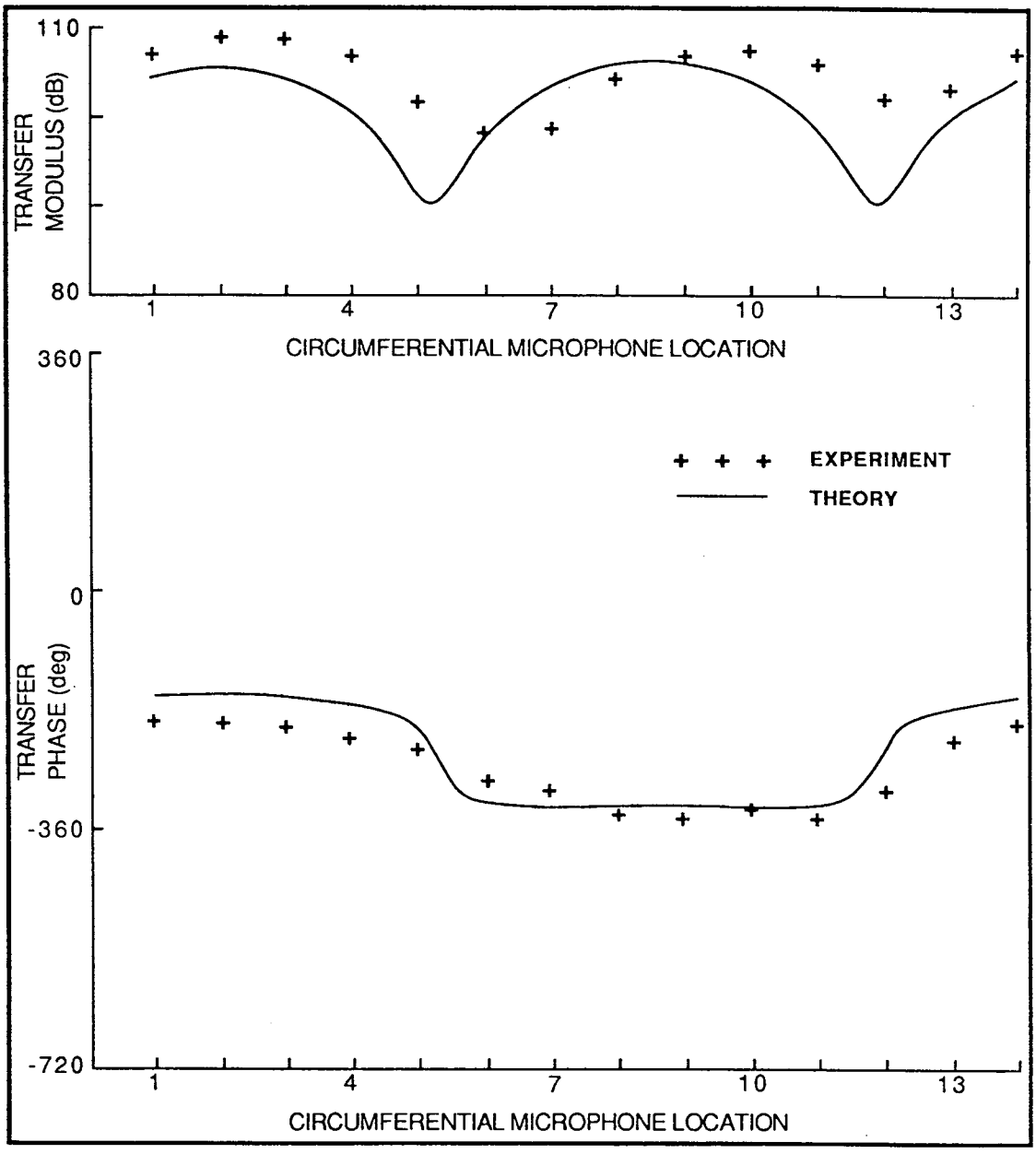

FIGURE 5.16(a). The pressure distribution around the cabin circumference at a frequency of 76.0Hz. The experimental distribution has been evaluated from the transfer impedance measurements made at each of the microphone locations shown in Figure 5.14.

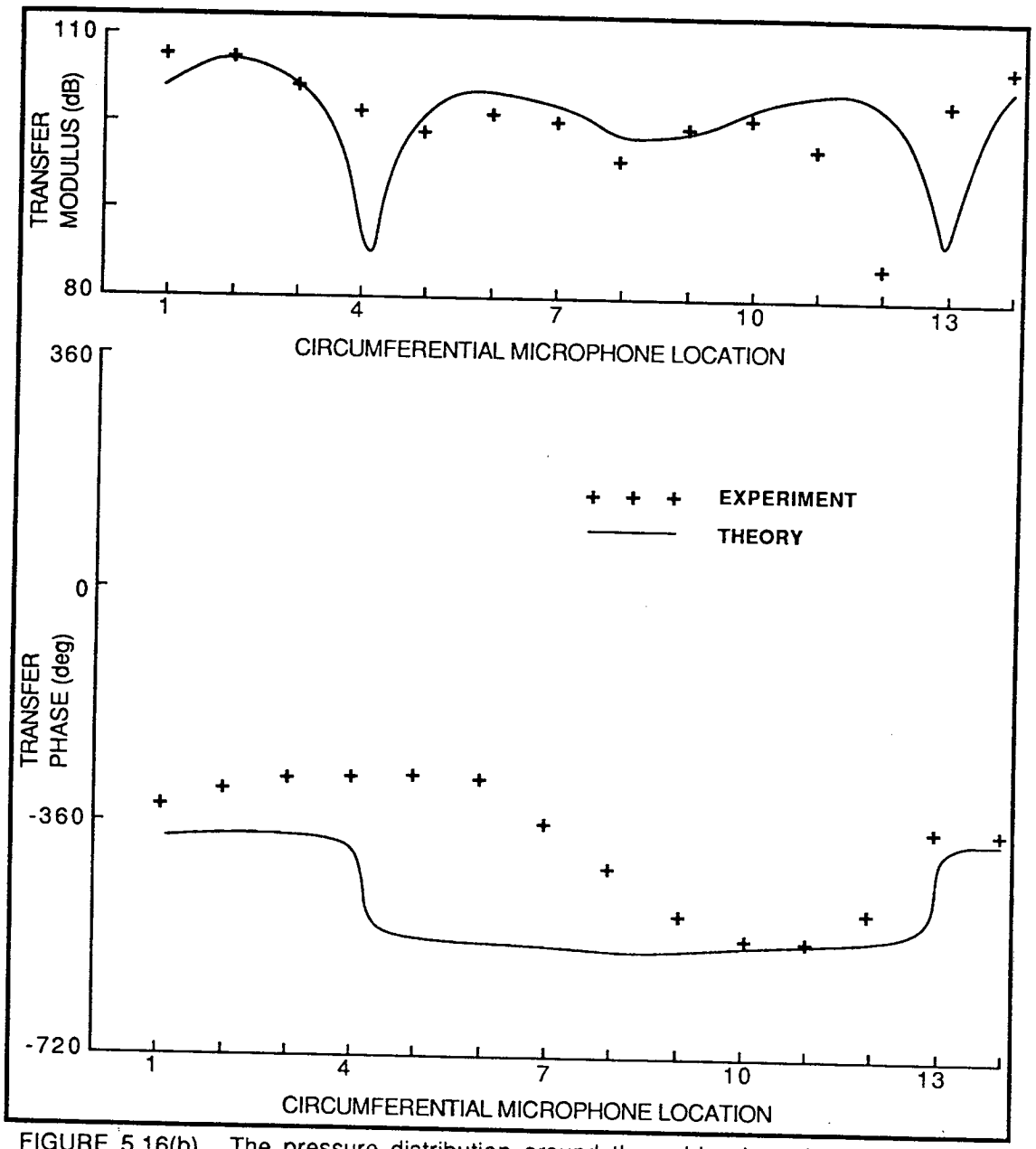

FIGURE 5.16(b). The pressure distribution around the cabin circumference at a frequency of 128.0Hz. The experimental distribution has been evaluated from the transfer impedance measurements made at each of the microphone locations shown in Figure 5.14.

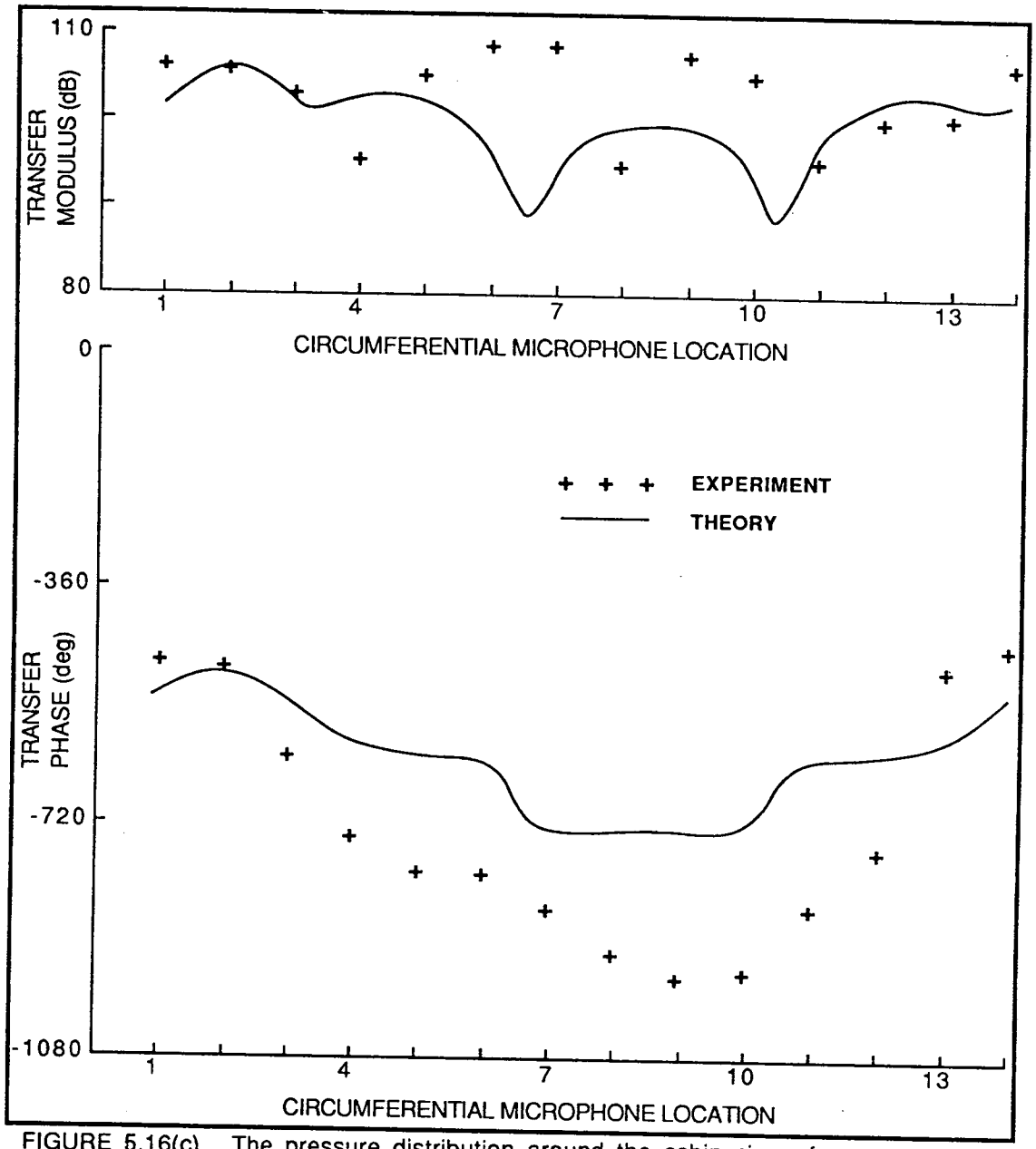

FIGURE 5.16(c). The pressure distribution around the cabin circumference at a frequency of 176.0Hz. The experimental distribution has been evaluated from the transfer impedance measurements made at each of the microphone locations shown in Figure 5.14.

CHAPTER 6

AN ANALYTICAL MODEL OF THE STRUCTURAL RESPONSE OF A B.Ae. 748 AIRCRAFT FUSELAGE

6.1 Introduction

The results of the previous chapter have demonstrated that, by using simple cylindrical room acoustics theory, it is possible to model the acoustic response of the B.Ae. 748 aircraft cabin reasonably well at frequencies encompassing the first two blade passage harmonics. It must, however, be re-emphasized that this approach can only be expected to predict general features of the cabin acoustics such as the overall effects of acoustic damping and the acoustic modal density. Both these properties of the sound field have been shown in Chapters 2, 3 and 4 to affect the performance of active noise control systems and it is therefore important that they should be modelled realistically. However, it has also been demonstrated in these chapters that the proximity of the secondary sources to the primary source is also a major factor in determining the levels of reductions which can be achieved using active noise control. In the examples of Chapters 2 and 3 all the sources, including the primary, were modelled as discrete piston sources whose diameters were much less than a wavelength of the sound being considered. In the case of an aircraft cabin it is not obvious what form the primary source distribution will adopt. It is conceivable that the cabin sidewall response will be dominated by a large vibration amplitude concentrated at the point of closest approach of the propeller. Equally possible, the propeller field could set up some structural wave which travels relatively unimpeded along the fuselage, thus exciting the interior acoustic field over the whole of the cabin surface. These two extreme examples demonstrate the importance of correctly specifying the primary source distribution if it is intended to design a practical system using the results of such a theoretical model. For example, if the former suggestion of a highly localized excitation were true, then very few secondary sources may need to be placed adjacent to the local areas of large vibrational amplitude. On the other hand, if the latter suggestion were true, then potentially many more secondary sources may need to be distributed throughout the cabin.

Perhaps the most obvious way to specify the primary source distribution correctly would be to measure it using an array of accelerometers placed over the interior surface of the cabin. However, this method has a number of drawbacks. Firstly, on an aircraft such as the B.Ae 748 under consideration the number of measurements required may become prohibitively large. Secondly, even if enough measurements could be taken they would then be required as input parameters to any computer model, another arduous task unless some simple analytic function could be fitted to them. Finally, these results would only apply to the aircraft on which they were measured.

An alternative method would be to predict the fuselage structural response from a knowledge of the external propeller pressure field, which could be determined either from a propeller noise prediction scheme or again by fitting some idealized analytic function to the measured distribution of external acoustic pressure data. This latter possibility may at first sight appear to be no better than the suggestion of measuring the fuselage vibration. However, published results [68,69,70] have shown typical external pressure fields to be much simpler than the fuselage vibration and concentrated in the plane of the propellers, the pressure falling off rapidly fore or aft of the propeller plane. Consequently, relatively few external pressure measurements should be required to adequately describe the propeller field. It is this approach which has been adopted for the current work, the chosen external pressure field being based on flight data collected by British Aerospace [71] on the trials B.Ae. 748 aircraft described in Chapter 5. It should be noted that this approach assumes that the airborne noise transmission path into the aircraft cabin is the dominant source of the internal noise.

The problem now is to choose a suitable theoretical model for the structural response of the aircraft fuselage. This structural response model is to be used in conjunction with the cabin acoustics model described in Chapter 5 which is itself only approximate. Consequently there is little point in developing a highly detailed and unnecessarily complex model of the fuselage structural response. What is important is that the model should adequately describe the dominant features of the

fuselage vibration which may affect the performance, and therefore the design, of an active control system.

The work in this chapter describes the choice and subsequent validation of a suitable model. The choice of a suitable model from the published literature on this topic was made difficult by the nature of most of these references as parametric studies, and the general lack of comparison between measured and predicted structural responses, most comparisons only being made between measured and predicted volume averaged interior acoustic responses. However, a brief review of some of these works is presented for completeness.

Koval *et al* [47,72,73] have published a series of papers. In the first two of these a theoretical model of a plane wave incident on an infinite, isotropic cylindrical shell has been used to study the effects of forward flight speed on sound transmission into the cylinder. In the third paper [73] the shell theory has been modified to include the effects of "smeared" out stringers and frames, thus allowing the effects of orthotropy to be evaluated. Fuller *et al* [49,74,75,8,76] have used the same basic structural model of an isotropic, infinite shell to study a number of parameters thought to affect sound transmission into aircraft cabins. The original model [49] used a dipole source to model the propeller field and was used to investigate the value of synchrophasing as a noise control measure. More recent publications have modified the propeller field to include circumferential convection around the fuselage by using a "virtually rotating dipole" source [74]. Also, the effects of a structurally integral floor have been presented [75], and the possibilities of applying both active noise control [8] and active vibration control [76] have been addressed. Bhat *et al* [77] have used a finite, orthotropic cylinder and a convected circumferential external pressure field to study the effects of the convection speed on the sound transmission through the cylinder. Junger *et al* [48] have modelled the sound transmission through the wing roots due to propeller wake excitation of the wing. In this work the wing has been modelled as a beam, rigidly attached to a finite, isotropic cylindrical shell model of the fuselage.

The above references are typical of most of the published work in that they set out to evaluate the effect a particular parameter has on the sound transmission qualities of aircraft fuselages, and the structural response models used have been chosen to exemplify the dependence on this parameter. This is quite understandable when one considers the complexity of a real aircraft, and the number of parameters which could affect the sound transmission. It is for this reason that the same type of approach is to be used in this work. However, before leaving this section, the work of Pope *et al* [70,78,79] should be mentioned. The work presented in their publications attempts to draw together many of the individual factors whose effects have been studied elsewhere and shown to be of some importance to the problem of fuselage sound transmission. For example, the model described in reference [70] uses a propeller radiation prediction scheme to determine the external pressure field, the fuselage structural response is modelled using a finite, frame and stringer stiffened shell having an integral, stringer stiffened floor. This structural response is then coupled to the interior cabin acoustics via a trim transfer function which describes the response of the cabin trim, and the internal acoustic field is modelled using finite difference techniques so, for example, the effects of the floor and luggage bins may be included.

As stated above, the work presented in this chapter follows the trend of the former referenced works, and therefore uses the simplest possible analytical theory which adequately models the effects which are thought to be of major importance when considering the application of active noise control, namely the extent and nature of the primary source (cabin wall) velocity distribution. The choice of a suitable, simple theory was, in practice, performed in a logical manner by starting with the simplest possible model of a point driven, finite, isotropic cylinder, and modifying it when it failed to adequately predict some significant feature of the measured structural response or internal cabin sound field.

This procedure led to the resulting choice of model consisting of a finite, isotropic cylinder having dimensions comparable to those of the test aircraft. The chosen external pressure forcing field decays exponentially away from the assumed plane of the propellers and is reflected circumferentially around the shell. The use of this model is

justified in the present work by comparison with in-flight measurements made on the test aircraft. However, its choice in preference to other, potentially simpler, models is not discussed here. This aspect of the modelling has been detailed separately in reference [87]*.

The work presented in this chapter is split into three parts. Firstly the general construction of the B.Ae.748 aircraft is described and the results of the available in-flight structural and acoustic measurements are presented. Using this information a suitable model for the propeller pressure forcing field and the fuselage structural response are suggested. Secondly, all the necessary analytical expressions relating to the chosen model are given and, lastly, results obtained using these expressions are compared with the in-flight structural and acoustic measurements.

6.2 The Choice of a Suitable Analytical Description of the Propeller Pressure Field and the Fuselage Structural Response

6.2.1 The B.Ae.748 test aircraft

A three view diagram of the B.Ae. 748 test aircraft has been presented in Figure 5.1, where the major physical dimensions of the aircraft are also listed. The fuselage is of conventional design being composed of a series of cylindrical frames which are spaced fairly evenly along the fuselage. These frames are connected together by longitudinal stringers and over this framework is wrapped a thin membrane ($\simeq$ 0.8 mm thick) which forms the outer surface of the fuselage. The basic material for all these components is aluminium. Inside the fuselage, a floor is attached across the fuselage at points corresponding approximately to $\theta = 60^{\circ}$ and $\theta = 300^{\circ}$ (see Figure 5.14), and the metal framework is finished using plastic trim panels. External to the fuselage are mounted two four-bladed propellers, one each side. These propellers both turn in

---

**Reference [87] contains a full comparison between the use of finite and infinite isotropic cylinder response theory. It also contains results that compare the use of various types of external forcing function. These results demonstrate the importance of the convection of the external pressure field around the shell and of representing this pressure field as a distributed, not concentrated, load.*

a clockwise sense as one looks aft along the fuselage. They are positioned above the low mounted wing such that the minimum fuselage/blade tip clearance is approximately 0.6 m and this occurs at approximately $\theta = 85^{\circ}$ (port) and $\theta = 275^{\circ}$ (starboard), where $\theta = 0^{\circ}$ corresponds to the keel of the aircraft.

6.2.2 A review of the available experimental data for use in model validation

Since active noise control is predicted to be most effective at low frequencies, and because the A-weighted internal cabin sound levels of the test aircraft tend to be dominated by the first two blade passage frequency components, this chapter will describe the choice of an appropriate analytical model on the basis of comparisons between theory and experiment at the first two blade passage harmonics only. The available experimental data for these two harmonics is shown in Figures 6.1 to 6.6 and has been taken from the British Aerospace research project reports of references [71,81,82,83,84]*. All the data has been collected from the same B.Ae. 748 series 2B aircraft under the same operating conditions (to within experimental limitations).

The data has been reproduced by the kind permission of British Aerospace and, at their request, no absolute levels of either sound pressure, or acceleration are given. Instead the results have all been scaled such that the peak external pressure on the fuselage due to the port propeller fundamental tone has been taken as being of unit amplitude ($1\ Nm^{-2} = 94$ dB), and all other values have been scaled relative to this (for example, the peak external pressure due to the port second harmonic tone has been taken as $0.76\ Nm^{-2}$ ($= 91.6$ dB)).

**Note that these reports were made accessible by B.Ae. for the purposes of this study and are not generally available.*

Figures 6.1 and 6.2 show the scaled external pressure measurements for the first and second blade passage harmonics respectively. Both are for the port propeller and both show a section of the port side of the fuselage which includes the propeller plane. The circumferential convection of the pressure in the direction of the blade rotation is discernible from the phase measurements shown. Note the phases have all been expressed relative to the pressure at microphone "M" for each harmonic.

Figures 6.3 and 6.4 show the scaled structural radial acceleration amplitudes for the first and second harmonics respectively. For each harmonic both axial and circumferential responses are shown. The axial responses were taken on a line along the fuselage which intersects the point of closest approach of the propeller and the results plotted include accelerations measured on frames, stringers and skin panels. The circumferential responses were all taken on the frame lying closest to the propeller plane.

Figures 6.5 and 6.6 show the scaled internal acoustic sound pressure levels for the two harmonics. The five measurements in each row correspond to one measurement at seated head height for each of the four seats, and an extra measurement in the centre aisle. It should be pointed out that the rear four outside starboard measurements have been estimated using data from a previous series of measurements as they were not available from the measured data of reference [84].

6.2.3 An analytical representation of the propeller pressure field

The external pressure measurements of Figure 6.1 and 6.2 are unfortunately too few to allow a precise specification of the propeller forcing field acting over the fuselage surface near the propeller plane. They do, however, provide three important pieces of information. Firstly they provide the absolute levels of the pressure amplitude (although the quoted levels have been scaled according to the procedure outlined in Section 6.2.2). Secondly they indicate a convection of the pressure field around the fuselage circumference in the direction of the propeller rotation, where the speed of this convection can be determined from the measured phase of the pressure. Lastly the results show that

the pressure amplitude is greatest at the measurement location, M, which lies nearest to the point of closest approach of the propeller tip. This last feature indicates that the pressure decays as one moves away from this point, although the nature of this decay is not clear. However, other reported results [68,70,77] have shown the decay of the pressure along the fuselage to be exponential, and for it to be convected in the direction of the decay. The exact nature of this decay and convection will in practice depend on the aircraft's air speed, but for the present it shall be assumed that the axial pressure distribution of the pressure amplitude can be represented by a function of the form (see Figure 6.7)

$$P_f(z) = \begin{cases} Pe^{-d(z_o - z)} & z < z_o \\ Pe^{-d(z - z_o)} & z > z_o \end{cases} \qquad (6.1)$$

where z_o is the propeller plane, d specifies the rate of decay of the force away from z_o (d is assumed to be purely real and positive) and where P is the maximum value of the applied pressure. Note that in using equation (6.1) the pressure is assumed to decay at an equal rate fore and aft of the propeller plane, and the axial convection of the pressure field is neglected. Similarly it shall be assumed that the circumferential pressure distribution can be represented by a function of the form (see Figure 6.7)

$$P_f(\theta) = \begin{cases} P\,\dfrac{\theta - \theta_1}{\theta_o - \theta_1} e^{jk_\theta \theta} & \theta < \theta_o \\ P\,\dfrac{\theta_2 - \theta}{\theta_2 - \theta_o} e^{jk_\theta \theta} & \theta > \theta_o \end{cases} \qquad (6.2)$$

where θ_1 and θ_2 are the circumferential locations where the pressure drops to zero (i.e., where $P_f(\theta) = 0$) and θ_o is the location of the peak pressure, P. The quantity k_θ is a circumferential propagation constant (purely real) which specifies the convection speed of the pressure field around the fuselage in terms of the phase change per unit angle travelled.

6.2.4 The fuselage structural response model

In the introduction to this chapter it was stressed that the aim of current work is to produce an analytical model which can adequately cribe the "important" features of the fuselage structural response. By portant" it is meant the gross features of the experimentally measured ponse, such as the average vibration amplitude and the extent of this ration over the fuselage surface.

The complex construction of the fuselage makes it likely that its uctural response will be equally complex. For example, it is not ious which of the structural elements, or indeed which combination of uctural elements, will dominantly support the wave motion in the quency range to be considered. It is common practice when studying the frequency response of such structures to ignore the local effects of me/skin, stringer/skin and frame/stringer interactions and to "smear " the effects of the frames and stringers [73,77]. However, whilst s is much simplified over a discrete frame/stringer model it still olves a large number of controlling structural parameters. It should in be remembered that the primary aim of this work is to assess the ectiveness of active noise control, and therefore any complicating fects in the peripheral elements of the model are best avoided if at possible. Consequently, if a simple isotropic shell theory can be equately fitted to the experimentally measured data, then this should used in preference to a more complicated model.

As a result of the above argument, it was decided to model the selage structural response as that of a finite, isotropic cylinder ose physical properties could be "matched" in some sense to the rcraft fuselage properties. The next sections outline the theory cessary to compute the vibration response of such a cylinder to an ternal pressure field of the form described in Section 6.2.3, and rther to compute the resulting internal acoustic pressure response due this vibration.

tructural Response of a Finite, Isotropic Cylinder

quations of motion for an isotropic cylindrical shell have been lsewhere [80] and so the derivation will not be repeated here. ions of motion according to the Goldenveizer-Novozhilov theory by

$$\frac{1-\nu}{2a^2}\frac{\partial^2 u}{\partial\phi^2} + \frac{1+\nu}{2a}\frac{\partial^2 v}{\partial z\partial\phi} + \frac{\nu}{a}\frac{\partial w}{\partial z} - \frac{\ddot{u}}{c_\ell^2} = 0 \qquad (6.3a)$$

$$\frac{\partial^2 u}{\partial z\partial\phi} + \frac{1-\nu}{2}(1+\beta^2)\frac{\partial^2 v}{\partial z^2} + \frac{1}{a^2}(1+\beta^2)\frac{\partial^2 v}{\partial\phi^2} + \frac{1}{a^2}\frac{\partial w}{\partial\phi} - \beta^2\left(\frac{\partial^3 w}{\partial z^2\partial\phi} + \frac{1}{a^2}\frac{\partial^3 w}{\partial\phi^3}\right) - \frac{\ddot{v}}{c_\ell^2} = 0 \qquad (6.3b)$$

$$\frac{u}{z} - \frac{1}{a^2}\frac{\partial v}{\partial\phi} + \beta^2\left(\frac{\partial^3 v}{\partial z^2\partial\phi} + \frac{1}{a^2}\frac{\partial^3 v}{\partial\phi^3}\right) - \frac{w}{a^2} - \beta^2\left(a^2\frac{\partial^4 w}{\partial z^4} + \frac{2\partial^4 w}{\partial z^2\partial\phi^2} + \frac{1}{a^2}\frac{\partial^4 w}{\partial\phi^4}\right) - \frac{\ddot{w}}{c_\ell^2} = -\frac{P_f(1-\nu^2)}{Eh} \qquad (6.3c)$$

ferring to Figure 6.8, u, v and w are the axial, tangential l displacements of the shell, respectively, a is the shell h the shell thickness; $\beta = (h/12a)^2$, ν is the Poisson's E the Young's modulus of the shell material, and c_ℓ is the al wavespeed in the shell material which is given by $))^{1/2}$, ρ_s being the density of the shell material. Damping is n the equations of motion by replacing E with a complex term,), where η_s is the hysteretic damping factor. The quantity right hand side of equation (6.3c) is the applied force, which to act radially to the shell and hence does not appear in (6.3a) or (6.3b). The choice of this particular set of was made using Leissa's [80] comprehensive survey of the ell equations of motion, and whilst these are not the simplest ll equations to implement it is felt that they are the most rward which are capable of accurate results over the range of meters considered in this work.

is assumed that the boundary conditions for the ends of the shear diaphragm/shear diaphragm, then

$$v = w = M_z = N_z = 0 \quad \text{at} \quad z = 0, L_z \tag{6.4}$$

and w are the tangential and radial displacements
ly, M_z is the bending moment, N_z is the longitudinal
orce and L_z is the length of the shell (see Figure 6.9). Thus,
d vibrational forms which satisfy these end conditions may be

$$\theta) = \sum_{r_1=0}^{\infty} \sum_{r_2=0}^{\infty} \sum_{r_3=0}^{1} U_r \cos\left[\frac{r_1 \pi z}{L_z}\right] \cos(r_2\theta - \frac{r_3\pi}{2}) e^{j\omega t} \tag{6.5a}$$

$$\theta) = \sum_{r_1=0}^{\infty} \sum_{r_2=0}^{\infty} \sum_{r_3=0}^{1} V_r \sin\left[\frac{r_1 \pi z}{L_z}\right] \sin(r_2\theta + \frac{r_3\pi}{2}) e^{j\omega t} \tag{6.5b}$$

$$z,\theta) = \sum_{r_1=0}^{\infty} \sum_{r_2=0}^{\infty} \sum_{r_3=0}^{1} W_r \sin\left[\frac{r_1 \pi z}{L_z}\right] \cos(r_2\theta - \frac{r_3\pi}{2}) e^{j\omega t} \tag{6.5c}$$

and r_2 are the axial and circumferential mode numbers
ly, U_r, V_r and W_r are the displacement amplitudes of the
gential and radial components respectively (the subscript r
imply a combination of the trio of integers r_1, r_2 and r_3 and
not be confused with the radial coordinate, r). and where
ime dependence has been assumed. The presence of both
al and sinusoidal circumferential modes indicates the
nature of the circumferential modes and, in general, both
be included to yield a full solution. Substituting equations
the equations of motion (6.3) and factoring out the terms
z,θ and t yields [80]

$$\begin{bmatrix} K_{11} & K_{12} & K_{13} \\ K_{21} & K_{22} & K_{23} \\ K_{31} & K_{32} & K_{33} \end{bmatrix} \begin{Bmatrix} U_r \cos(\frac{r_1\pi z}{L_z})\cos(r_2\theta - \frac{r_3\pi}{2}) \\ V_r \sin(\frac{r_1\pi z}{L_z})\sin(r_2\theta + \frac{r_3\pi}{2}) \\ W_r \sin(\frac{r_1\pi z}{L_z})\cos(r_3\theta - \frac{r_3\pi}{2}) \end{Bmatrix} = \begin{bmatrix} 0 \\ 0 \\ -\frac{P_f a^2(1-\nu^2)}{Eh} \end{bmatrix} \tag{6.6}$$

where

$$K_{11} = \Omega^2 - k_z^2a^2 - (\frac{1 - \nu}{2})r_2^2$$

$$K_{12} = (\frac{1 + \nu}{2})r_2k_za = K_{21}$$

$$K_{13} = \nu k_za = K_{31}$$

$$K_{22} = \Omega^2 - (\frac{1 - \nu}{2})(1 + \beta^2)k_z^2a^2 - (1 + \beta^2)r_2^2$$

$$K_{23} = -n - \beta^2(k_z^2a^2r_2 + r_2^3) = K_{32}$$

$$K_{33} = \Omega^2 - 1 - \beta^2(k_z^4a^4 + 2k_z^2a^2r_2^2 + r_2^4)$$

where $k_z = (r_1\pi/L_z)$ and where $\Omega = (\rho_s a^2(1 - \nu^2)\omega^2/E)^{1/2}$ is the non-dimensional frequency which has been normalized to equal unity at the shell ring frequency, ω_r, so $\Omega = \omega/\omega_r = \omega a/c_\ell$. Now multiplying both sides of equation (6.6) by $\sin(r_1'\pi z/L_z)\cos(r_2'\theta - r_3'\pi/2)$ and integrating over the curved surface of the shell, it is seen that all the terms for which $r_1 \neq r_1'$, $r_2 \neq r_2'$ and $r_3 \neq r_3'$ are zero, so equation (6.6) becomes

$$\begin{bmatrix} K_{11} & K_{12} & K_{13} \\ K_{21} & K_{22} & K_{23} \\ K_{31} & K_{32} & K_{33} \end{bmatrix} \begin{bmatrix} U_{r_1r_2} \\ V_{r_1r_2} \\ W_{r_1r_2} \end{bmatrix}$$

$$= \begin{bmatrix} 0 \\ 0 \\ -\frac{\epsilon_{r_2}a(1-\nu^2)}{L_z\pi Eh}\int_0^{2\pi}\int_0^{L_z} P_f(z,\theta)\sin(\frac{r_1\pi z}{L_z})\cos(r_2\theta - \frac{r_3\pi}{2})\,a\,dz\,d\theta \end{bmatrix} \qquad (6.7)$$

where $\epsilon_{r_2} = 1$, $r_2 = 0$ or $\epsilon_{r_2} = 2$, $r_2 > 0$. Note, too, that the applied pressure $P_f(z,\theta)$ is assumed to be a function of its position over the shell surface, and that it is assumed that this pressure varies harmonically with time. Thus, provided the applied pressure distribution is known, it is possible to evaluate the r'th mode's radial

tude from equation (6.7) as

$$W_r = - \frac{\epsilon_{r_2} a(1 - \nu^2)}{L_z \pi E h} \cdot I_{33} . I_r^s \qquad (6.8)$$

I_{33} indicates the (3,3) element of the inverse of matrix [K], or

$$I_{33} = \frac{K_{11}K_{22} - K_{12}K_{21}}{|K|} \qquad (6.9)$$

eing the determinant of matrix [K], and where I_r^s specifies the to which the applied force $p_f(z,\theta)$ couples spatially to the r'th ural mode. This is given by

$$= \int_0^{2\pi} \int_0^{L_z} p_f(z,\theta) \sin(\frac{r_1 \pi z}{L_z}) \cos(r_2\theta - \frac{r_3\pi}{2}) a dz d\theta \qquad (6.10)$$

us the radial shell displacement can be found by substituting on (6.8) into equation (6.5c) and by performing the modal ion to give

$$w(z,\theta) = - \sum_r \frac{\epsilon_{r_2} a(1 - \nu^2) I_{33}}{\pi L_z E h} . I_r^s \sin(\frac{r_1 \pi z}{L_z}) \cos(r_2\theta - \frac{r_3\pi}{2}) e^{j\omega t} \qquad (6.11)$$

Internal Acoustic Response of a Finite Cylindrical Room Excited the Normal Vibrations of a Finite Shell which Forms the Curved nding Surface

acoustic response of the cylindrical volume enclosed by the shell can be evaluated using the Green function technique [55] ed in the previous chapter. Despite the assumption of shear gm-shear diaphragm end conditions used for the shell structural it will be assumed that acoustically the end caps of the shell d and immobile and thus do not contribute any volume velocity

input to the enclosed sound field. Therefore, only the curved wall of the shell acts as an acoustic source, whose radial velocity component is given by the derivative with respect to time of equation (6.11). The internal acoustic pressure field can therefore be obtained from equations (6.11) and (5.1) as

$$p(z,\theta,r) = \sum_{n_1=0}^{\infty}\sum_{n_2=0}^{\infty}\sum_{n_3=0}^{\infty}\sum_{n_4=0}^{1} \frac{\omega\rho c^2}{V} \cdot \frac{\psi_n(z,\theta,r)}{2C_n\omega_n - j(\omega_n^2 - \omega^2)} \cdot I_n{}^a \cdot e^{j\omega t} \qquad (6.12)$$

where $I_n{}^a$ specifies the extent to which the cylinder sidewall normal velocity distribution couples spatially to the n'th acoustic mode, or

$$I_n{}^a = -\int_0^{2\pi}\int_0^{L_z}\sum_{r} \frac{\epsilon_{r_2} j\omega a(1-\nu^2) I_{33}}{\pi L_z E h} \cdot I_r{}^S \cdot \psi_n(z,\theta,a)$$

$$\times \sin\left(\frac{r_1\pi z}{L_z}\right)\cos\left(r_2\theta - \frac{r_3\pi}{2}\right) a\,dz\,d\theta \qquad (6.13)$$

and where $\psi_n(z,\theta,r)$ is the normalised mode shape function of the n'th acoustic mode which for the assumed cylindrical cabin is given by (see Chapter 5)

$$\psi_n(z,\theta,r) = \frac{\cos\left(\frac{n_1\pi z}{L_z}\right)\cos\left(n_2\theta - \frac{n_4\pi}{2}\right) J_{n_2}(k_{n_2 n_3} r)}{\Lambda_n{}^{1/2}} \qquad (6.14)$$

where Λ_n is a normalisation constant given by equation (5.3).

6.5 The Structural and Internal Acoustic Response of the Finite, Isotropic Shell to the Assumed Propeller Pressure Field

6.5.1 The shell structural response

The assumed propeller pressure field is given from equations (6.1) and (6.2) as

$$P_f(z,\theta) = Pe^{-d(z_o-z)}\frac{(\theta-\theta_1)}{(\theta_o-\theta_1)}e^{jk\theta} \qquad z < z_o,\ \theta < \theta_o$$

$$Pe^{-d(z-z_o)}\frac{(\theta-\theta_1)}{(\theta_o-\theta_1)}e^{jk_\theta\theta} \qquad z > z_o,\ \theta < \theta_o$$

$$Pe^{-d(z_o-z)}\frac{(\theta_2-\theta)}{(\theta_2-\theta_o)}e^{jk_\theta\theta} \qquad z < z_o,\ \theta > \theta_o$$

$$Pe^{-d(z-z_o)}\frac{(\theta_2-\theta)}{(\theta_2-\theta_o)}e^{jk_\theta\theta} \qquad z > z_o,\ \theta > \theta_o \qquad (6.15)$$

The shell radial displacement amplitude can be evaluated from ation (6.11) with I_r^s being evaluated by substituting each of the ve expressions in turn into equation (6.10) and then by summing the r separate contributions, or

$$s = P\Bigg\{\int_{\theta_1}^{\theta_o}\int_{o}^{z_o} e^{-d(z_o-z)}\frac{(\theta-\theta_1)}{(\theta_o-\theta_1)}e^{jk_\theta\theta}\sin(\frac{r_1\pi z}{L_z})\cos(r_2\theta-\frac{r_2\pi}{2})adzd\theta$$

$$+\int_{\theta_1}^{\theta_o}\int_{z_o}^{L_z} e^{-d(z-z_o)}\frac{(\theta-\theta_1)}{(\theta_o-\theta_1)}e^{jk_\theta\theta}\sin(\frac{r_1\pi z}{L_z})\cos(r_2\theta-\frac{r_2\pi}{2})adzd\theta$$

$$+\int_{\theta_o}^{\theta_2}\int_{o}^{z_o} e^{-d(z_o-z)}\frac{(\theta_2-\theta)}{(\theta_2-\theta_o)}e^{jk_\theta\theta}\sin(\frac{r_1\pi z}{L_z})\cos(r_2\theta-\frac{r_2\pi}{2})adzd\theta$$

$$+\int_{\theta_o}^{\theta_2}\int_{z_o}^{L_z} e^{-d(z-z_o)}\frac{(\theta_2-\theta)}{(\theta_2-\theta_o)}e^{jk_\theta\theta}\sin(\frac{r_1\pi z}{L_z})\cos(r_2\theta-\frac{r_2\pi}{2})adzd\theta\Bigg\}$$

(6.16)

Each of these integrals has been evaluated and the results are ented in Appendix 6.1.

The shell internal acoustic response

oustic response is found by substituting equation (6.10) into
(6.12) and (6.13) and integrating over the curved shell
Thus the integral term which specifies the coupling of the n'th
ode to the shell velocity distribution may be written from
6.13) as

$$\sum_{r} \frac{\epsilon_{r_2} a(1-\nu^2) I_{33}}{\pi L_z E h \Lambda_n^{1/2}} \cdot I_r^s \cdot J_{n_2}(k_{n_2 n_3} a)$$

$$\int_0^{L_z} \sin\left(\frac{r_1 \pi z}{L_z}\right)\cos\left(r_2\theta - \frac{r_3\pi}{2}\right)\left(\cos\left(\frac{n_1 \pi z}{L_z}\right)\cos\left(n_2\theta - \frac{n_4\pi}{2}\right)\right) a\,dz\,d\theta \qquad (6.17)$$

ntegral has been evaluated in Appendix 6.2 to yield

$$-\sum_{r} \frac{\epsilon_{r_2} j\omega a(1-\nu^2) I_{33} . I_r^s}{\pi L_z E h \Lambda n^{1/2}} \cdot \frac{a L_z 2}{\epsilon_{r_2}} \cdot \frac{r_1}{r_1^2 - n_1^2} J_{n_2}(k_n\ n\ a)$$

$(r_1 + n_1$ odd and $r_2 = n_2$ and $r_3 = n_4)$

$I_n^a = 0$ $(r_1 + n_1$ even or $r_2 \neq n_2$ or $r_3 \neq n_4)$

$\epsilon_{r_2} = 1$ $r_2 = 0$

$= 2$ $r_2 > 0$ (6.18)

that in performing the integrals of equation (6.13) it has
pparent that not every acoustic mode can be excited by every
al mode. This selective excitation of only a few acoustic modes
structural mode has been discussed in Appendix 6.2 and shown to
o the orthogonal properties of the sinusoidal and cosinusoidal
pe functions when their products are integrated over distances
rrespond to an integer number of half wavelengths. It is also
Appendix 6.2 that if the integration limits in equation (6.13)
red so the acoustic excitation does not occur over the entire
rface, then the selectivity of the acoustic mode excitation
s. This feature will be of considerable use in later sections.

6.6 Model Validation by Comparison with In-flight Experimental Measurements

6.6.1 Choosing the model parameters

Before any comparisons can be made between the theoretical and experimental results it is necessary to set the physical parameters in the equations governing the responses. For the external pressure field (equations (6.1) and (6.2)) these parameters are P, the peak pressure, d, the axial decay rate of the pressure, θ_1 and θ_2 the lower and upper circumferential limits of the pressure field, z_o and θ_o, the axial and circumferential coordinates of the point of maximum pressure, and k_θ the circumferential convection constant. From the experimental data (Figures (6.1) and (6.2)), the parameters listed in Table 6.1 have been chosen. These result in the pressure distributions shown in Figure 6.10. Note that the pressure has fallen by 20 dB within about 1 m of the point of closest approach of the propeller.

The physical parameters chosen for the shell have been selected to resemble those of the B.Ae. 748 aircraft shown in Figure 5.1 and the material properties have similarly been chosen as those of aluminium. A schematic diagram of this shell is shown in Figure 6.11. The length of the shell, 16.0 m, corresponds to a region in the test aircraft which extends from z = 0.0 m at the front of the flight deck to z = 16.0 m at the rear of the rear exit. This results in the propeller plane being located at z = 3.5 m (as per Table 6.1) and the standard configuration passenger cabin consisting of 12 rows of seats, each four abreast with a centre aisle, extending from z = 3.5 m to z = 12.5 m. The radius of the shell has been taken as 1.3 m, whilst the origin of the circumferential coordinates corresponds to the keel of the aircraft. The chosen shell parameters are listed in Table 6.2, although the hysteretic damping factor, η_s, and the shell thickness, h, remain to be estimated.

The chosen parameters for the acoustic response equations have already been presented in Chapter 5, but they are listed again in Table 6.3 for ease of reference.

There now remain just two parameters which have not been specified. These are the structural damping factor, η_s, and the shell thickness, h. Neither of these can be estimated in the same manner as the other shell

structural parameters have been estimated, that is by inspection of Figure 5.1. (Note that whilst the skin thickness, h, could be measured, the effects of the stringers and frames would also have to be explicitly accounted for in the shell thickness, and without progressing to an orthotropic shell model such as that used in reference [77] this is not possible.) Instead they are to be estimated by matching the shell structural response due to the assumed propeller pressure field with the experimentally measured structural response. It has been shown in Reference [87] that the shell thickness is the dominant parameter controlling the magnitude of the response close to the force, and the damping controls the decay of this response away from the force location. Bearing this in mind the shell structural responses due to the assumed pressure field have been evaluated, and the shell thickness and damping have been adjusted to give an acceptable match between the resulting responses and the measured responses of Figures 6.3 and 6.4. This resulted in the plots of Figures 6.12 and 6.13, where a shell thickness of 1.2 mm (compared to a measured skin thickness of 0.8 mm) and a damping factor of 0.3 have been chosen. The experimental responses of Figures 6.3 and 6.4 have been replotted on Figures 6.12 and 6.13 for direct comparison. (Notice that because all the experimental results (i.e., the external pressure fields, the acceleration responses and the internal pressure fields) have been scaled by the same constant, and the external pressure field model has also been scaled by this same constant, all the theoretical results presented are directly comparable with the measured results presented).

For the results of Figures 6.12 and 6.13, and for all subsequent results, all structural circumferential modes having orders from zero to twenty nine and all structural axial modes having orders from one to forty have been included. Checks showed that using this number of modes the response will converge at the frequencies considered, except in the immediate vicinity of a point force.

6.6.2 A comparison of the structural response results

From the manner in which the experimental and theoretical responses have been matched most emphasis has been placed on producing comparable absolute amplitudes between the responses evaluated around the

circumference (by adjusting the theoretical shell thickness) and on producing comparable decay rates on the responses evaluated along the fuselage (by adjusting the theoretical shell damping). The most prominent feature that the simple shell theory is not able to model correctly is the location of the peak vibrational response amplitude around the fuselage, particularly for the fundamental frequency results of Figure 6.12(c). In this case the theory predicts the maximum vibration amplitude to be under the point of maximum applied pressure ($\theta = 85°$), whereas the measured peak vibration amplitude occurs at approximately $\theta = 180°$. For the second harmonic frequency results of Figure 6.13(c) the situation is somewhat better, although the measured peak vibration amplitude is still rotated around the fuselage to occur at $\theta = 112°$ compared to a predicted peak at $\theta = 85°$. The reason for this behaviour is not clear, but it is possibly due to the constraints imposed on the fuselage vibration by the floor. However, the effect does explain the apparent overprediction of the acceleration responses as a function of location along the shell (Figures 6.12(a) and 6.13(a)), as these were all evaluated along the shell at $\theta = 85°$, where the theory predicts the maximum response.

Figures 6.14 and 6.15 show the theoretical structural acceleration responses corresponding to Figures 6.12 and 6.13, but these now show the entire shell surface presented in an "unwrapped" configuration. Both amplitude and phase information is presented on these plots which help to demonstrate more clearly the predicted extent of the cabin wall vibration away from the propeller plane.

6.6.3 A comparison of the internal acoustic response results

The final part of this model choice and validation is the comparison of the internal pressure fields which result from the structural responses of Figures 6.14 and 6.15. These are shown in Figures 6.16 and 6.17. All the plots show the sound pressure levels evaluated over the same head height plane as was used for the experimental measurements (see Figures 6.5 and 6.6) but a grid of 30 by 20 equispaced points has now been used to increase the spatial resolution of the isometric plots. Again it should be noted that, due to the constant scaling factor used,

the experimental and theoretical internal pressure fields are directly comparable.

Figure 6.16 shows the internal pressure field at the fundamental frequency due to the structural response of Figure 6.14. Comparing Figure 6.16 with Figure 6.5, the experimentally measured pressure field at the fundamental frequency, there appears to be reasonable agreement between the two, both in absolute level and in the general form of the pressure fields. However, when the same comparison is made between the theoretical and experimental pressure fields at the second harmonic frequency, Figures 6.17 and 6.6 respectively, the agreement is not so good. Although the theory does predict a general decrease in sound pressure level as one moves towards the rear of the cabin, it also shows a region of low pressure running along the centre of the head height plane, a feature not seen on the measured pressure field.

At this point it should be remembered that the predicted internal pressure fields have been evaluated without any account being taken of the response of the trim panels (although their effects on the acoustic damping have been included). Any attempt to include the trim in the model would be far too involved to warrant its inclusion in the current research. The internal sound field predictions are, therefore, liable to considerable uncertainty, and this could partly explain the differences seen in the measured and predicted fields at 176 Hz. It could also conceivably help to explain the <u>similarities</u> between the measured and predicted fields at 88 Hz which agree very well despite the measured structural vibration pattern being rotated around the fuselage by some 90° compared to the predicted vibration amplitude, as discussed in Section 6.6.2.

However, having accepted this as being a possible limitation of the model, it will now be attempted to improve on the predictions of the internal pressure fields by making simple, physically justifiable alterations to the simple theory used.

The presence of the low pressure region in the theoretical plots implies that the axisymmetric ($n_z = 0$) circumferential acoustic modes are contributing negligibly to the acoustic field, whereas from the

ponding experimental pressure field the axisymmetric
ferential modes appear to be contributing significantly. (This
sion is based on the fact that all acoustic non-axisymmetric modes
ave pressure minima along the centreline of the cylinder, and it is
he axisymmetric modes which will not demonstrate this feature. As
ane over which the pressure has been evaluated and measured for the
t examples is only 0.2 m above the cylinder centreline, the
ce of a low pressure region running along the centre of the plane
tes that no axisymmetric modes are being excited to a level
able with the levels of non-axisymmetric mode excitation.)

s discrepancy between theory and experiment is believed to occur
of the highly idealized nature of the theoretical model used, and
ner in which the structural response excites the enclosed acoustic
In the theory of Section 6.5.2 and Appendix 6.2 it has been
rated that, because the structural vibration of the shell is
to excite the acoustic field over its entire circumference, then
ral modes having a circumferential mode order of r_z can only
acoustic modes which have an equal circumferential mode order
$n_z = r_z$). Also, in the case of the finite cylinder, the
ve structural/acoustic mode coupling is further enhanced by the
ve excitation of only a few axial acoustic modes by each axial
al mode. This is again a result of the acoustic excitation
g over the entire length of the shell, as discussed in
6.2. Consequently, the extent of excitation of the acoustic
not only a function of the proximity of the mode resonance
y to the excitation frequency, but it is also strongly dependent
odal composition of the shell structural response. That is, the
sponse must contain significant contributions from modes which
le efficiently in both a circumferential and axial spatial sense
acoustic modes if these acoustic modes are to be significantly
[50]. Thus, for example, if the shell structural response does
ain a contribution from an axisymmetric circumferential mode,
ther can the acoustic response contain any contribution from this
ode. Similarly, if the shell structural response does not
n axial wavenumber component of, say, k_z then the acoustic modes
ibit a similar axial wavenumber are not likely to be excited to
ficant degree.

6.6.4 Modifying the structural excitation

he inhomogeneities present in any practical aircraft structure are ely to decrease this structural/acoustic mode coupling selectivity and s at any given frequency a different combination of modes are likely be excited than is predicted by this simple theory. In order to roduce this effect into the model (albeit in a rather *ad hoc* manner) excitation of the enclosed volume by the vibration of the shell is ified to occur over only part of the interior shell surface (see endix 6.2). Since the fuselage floor is joined to the cylindrical elage at points corresponding approximately to $\theta = 60°$ and $\theta = 300°$, because there are fixed bulkheads in the test aircraft at roximately z = 1.5 m and z = 12.5 m, it has been decided to choose e as the limits of the "primary source". Notice that whilst neither areas of fuselage below the floor line nor forward or aft of the d bulkheads are assumed to contribute any volume velocity input to enclosed acoustic field, the structural response of the shell is in ay altered by using this method. Figure 6.18 shows the modified of the shell wall which is assumed to drive the internal acoustic d.

Figures 6.19 and 6.20 show the predicted pressure fields over the 600 point grid as was used for Figures 6.16 and 6.17 but now the sure has been evaluated using the truncated structural excitation l, as described above. Figure 6.19 shows the predicted pressure d due to the port propeller operating at 88 Hz. Comparing this sure field with that of Figure 6.16 reveals little change in the al spatial distribution of the two fields, and therefore both of the s appear to produce a pressure field equally representative of what easured in practice (Figure 6.5).

igure 6.20 shows the predicted pressure field obtained using the ated excitation model due to the port propeller operating at 176 Comparing this pressure field with that of Figure 6.17 (obtained the unmodified model for the same situation) reveals a significant e in the general form of the sound field, although the averaged ure only increases by 0.5 dB. This small change in the averaged ure is due to the majority of the changes in the sound pressure

eld occurring where the pressure was initially very low, that is along e cabin centre line. However, what is most important from the present int of view is that both the absolute levels and the general features the spatial distribution of the pressure field due to the modified eory appear to agree well with the experimentally measured pressure eld, with the pressure being fairly uniform across the cabin but creasing in amplitude by approximately 15 dB as one moves from the opeller plane to the rear of the cabin. This is to be contrasted with e pressure field predicted by the original model (Figure 6.16) with its ry low pressure ridge running along the centre line of the evaluation rface.

The reasons why truncating the structural excitation of the acoustic eld affects the second harmonic response much more than it affects the ndamental response are discussed in the next section.

6.6.5 A comment on the effects of modifying the extent of the structural excitation

The reasons for the changes in the sound fields as a result of uncating the extent of the structural excitation can be demonstrated by ference to the current example by decomposing the structural and oustic responses into their modal components.

Figures 6.21 and 6.22 show examples of the relative contributions of e first eleven structural circumferential modes to the shell responses r each of the harmonics considered. For each case the relative rcumferential mode contributions both in the propeller plane and also e shell diameter aft of the propeller plane are given. From these sults it is apparent that the circumferentially convected external essure field is forcing most strongly those shell modes whose rcumferential wavenumber matches the pressure field circumferential venumber. So the 88 Hz pressure field predominantly excites the $r_z = 2$ d $r_z = 3$ structural modes, and the 176 Hz pressure field predominantly cites the $r_z = 3$ and $r_z = 4$ structural modes. It can also be seen that e $r_z = 0$ structural mode level is always at least 25 dB down on the ghest mode level in the plane of the propeller, and at one shell ameter distance aft from the propeller plane this difference increases

to over 65 dB down. If the shell ring frequency is evaluated [80] (this corresponds to the cut-on frequency of the $r_2 = 0$ mode) then it turns out to be approximately 650 Hz. It is therefore not surprising that axisymmetric modes contribute so little to the shell responses, particularly at regions away from the external forcing field. However, because of the selective structural/acoustic mode coupling described in Section 6.5.2 this also means that none of the possible acoustic modes having a zero circumferential mode order ($n_2 = 0$) will be excited appreciably (see Appendix 6.3 for verification).

The change in the modal composition of the sound field due to the "truncation" of the excitation can be shown by reference to Figures 6.23 to 6.26 which show the relative contributions of the most dominant acoustic modes to the total acoustic potential energy of the enclosed sound field at both of the harmonics. The modal contributions have been plotted as a function of the mode natural frequencies, but it should be pointed out that only those modes whose relative contribution falls within the specified ranges have been included on the graphs. Figure 6.23 shows the acoustic mode contributions due to excitation over the entire internal surfaces of the shell when excited at 88 Hz. Perhaps most striking from this plot is the "spread" of the modes, with modes having natural frequencies lying up to 150 Hz above the driving frequency being excited in preference to modes whose natural frequencies lie closer to the driving frequency. (The fact that such modes exist has already been demonstrated in Table 5.4 of Chapter 5.) Figure 6.24 shows the acoustic mode contributions for the shell when excited at 88 Hz, but this time for the case when the structural excitation has been truncated to allow less selective structural/acoustic mode coupling to occur. Comparison of these results with the results of Figures 6.23 immediately reveals two major differences. Firstly, the absolute level of the most dominant mode contribution has increased, and secondly the dominantly excited modes tend to have natural frequencies lying closer to the driving frequency. However, the same two modes dominate the response in both cases (see Appendix 6.3) and therefore the general form of the sound fields before and after the modification of the excitation are quite similar (Figures 6.16 and 6.19).

Figures 6.25 and 6.26 show the equivalent results to those described
ve but for the second harmonic frequency (176 Hz). In view of the
reased acoustic modal density at this frequency the features described
the 88 Hz case are not so significant for this case. However, the
itive acoustic modal contributions are clearly altered significantly
he truncation of the structural excitation, with more modes being
ted to a higher degree following the truncation of the excitation.
articular an axisymmetric mode is excited to a significant level (see
ndix 6.3), and whilst the contribution of this mode to the total
gy of the sound field is some 8.9 dB less than the most dominant
's contribution, its presence does increase the pressure in the
ially very low pressure region along the cabin centre line, as
irmed by comparing Figures 6.17 and 6.20.

Conclusions

From the results of all the previous sections an appropriate model
been chosen to be used for the active noise control predictions.
consists of a finite aluminium cylinder, 16.0 m long, 1.3 m in
us and 0.0012 m thick and having a structural damping factor of 0.3.
s excited by the external pressure field shown in Figure 6.10. The
rnal acoustic field is modelled using a cylindrical room acoustics
l which is excited by the normal vibrations of the shell wall, but
over a region extending from z = 3.5 m to z = 12.5 m and from θ =
to θ = 300°. The size of the cylindrical room used is assumed to
the same length and radius as the structural cylinder model. The
stic damping has been chosen from the results of Chapter 5 to
espond to that given in Table 5.5.

These model parameters have been chosen by the matching up of the
ted number of available experimental results with the idealized
retical model results. As was stressed in the introduction to both
ters 5 and 6, the theory is only expected to describe the gross
ures of the experimental results, and the chosen model does this
ly successfully. How representative the chosen model is of the
all response of the B.Ae. 748 test aircraft is open to considerable
tion, as the validation has only been performed over an extremely
ted range of experimental results.

However, throughout the model development it has always been aimed to "err on the safe side" as far as active control is concerned. The acoustic response has been chosen according to the largest dimension, thereby ensuring as high a modal density as possible. Care has been taken to assess the acoustic damping as accurately as possible (see Chapter 5). Also it has been ensured that the structural response is at least as extended over the shell surface as the experimental results indicate. By choosing the model parameters in this manner it is hoped that any active noise control predictions should be conservative estimates of what might occur in practice.

However, it is believed that to take such a structural/acoustic model, to change its parameters according to the dimensions of another aircraft and to use it to estimate that aircraft's structural and acoustic responses could be potentially very misleading. The assumptions which have been made to match up experimental and theoretical results in the present case lead to some concern over the validity of this very simple theoretical approach. Consider, for example, the manner in which the structural/ acoustic mode coupling has been enhanced, the very large structural damping factor used and the choice of shell thickness comparable with the aircraft skin thickness.

These latter two structural parameters, the thin shell thickness yet heavy damping factor, do not appear to be compatible. The frames and stringers rivetted to the skin could be assumed to add a simple damping layer to the skin. However, almost certainly, the frames and stringers do play an important role in the overall fuselage response, and it is recommended that in any future work their effects should be included, even if only in the form of an orthotropic smeared frame, stringer, shell model. Also, the effects of the cabin trim, the cabin floor, the constraints imposed by the wing spars and the propeller wake impinging on the tailplane leading to an increased fuselage response at the rear of the cabin, could all affect the responses and should be considered if an adaptable model is to be successful. However, the work of Pope *et al* [70] has demonstrated the difficulties involved in modelling such factors and for the present work, whose aim is to assess the effectiveness of active noise control when applied specifically to the B.Ae.748 aircraft, this type of development would be superfluous.

Table 6.1: External propeller pressure field parameters

	Fundamental (88 Hz)	Second Harmonic (176 Hz)
P (Nm^{-2})	1.0	0.76
z_o (m)	3.5	3.5
d (m^{-1})	2.3	2.3
θ_1 (deg)	0	0
θ_o (deg)	85	85
θ_2 (deg)	150	150
k_θ (dimensionless)	−1.5	−3.0

Table 6.2: Structural parameters

L_z (m)	16.0
a (m)	1.3
h (m)	0.0012
η_s	0.3
ρ_s ($kg.m^{-3}$)	2700
E (Nm^{-2})	7.1×10^{10}
ν	0.31
End conditions	Shear diaphragm/shear diaphragm

Table 6.3: Acoustic Parameters

L_z (m)	16.0	
a (m)	1.3	
$\bar{\alpha}$	0.16	f < 20 Hz
	0.008f	20 < f < 200 Hz
	1.6	f > 200 Hz
c (ms^{-1})	343.0	
ρ ($kg\ m^{-3}$)	1.21	

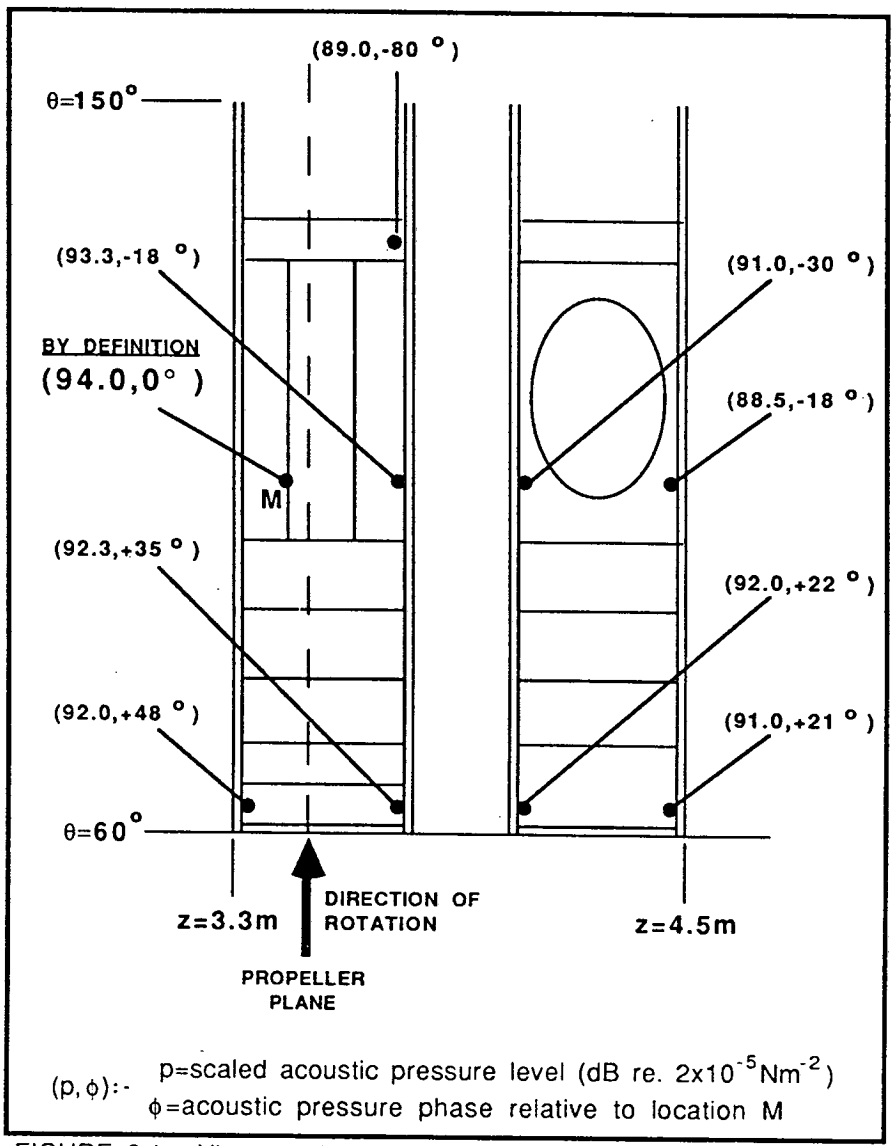

FIGURE 6.1. View on the port side of the aircraft looking inwards showing the external microphone locations and the scaled acoustic pressures measured during a 10000ft cruise with the port engine running at 14200r.p.m..The frequency is the blade passage fundamental of 88Hz.

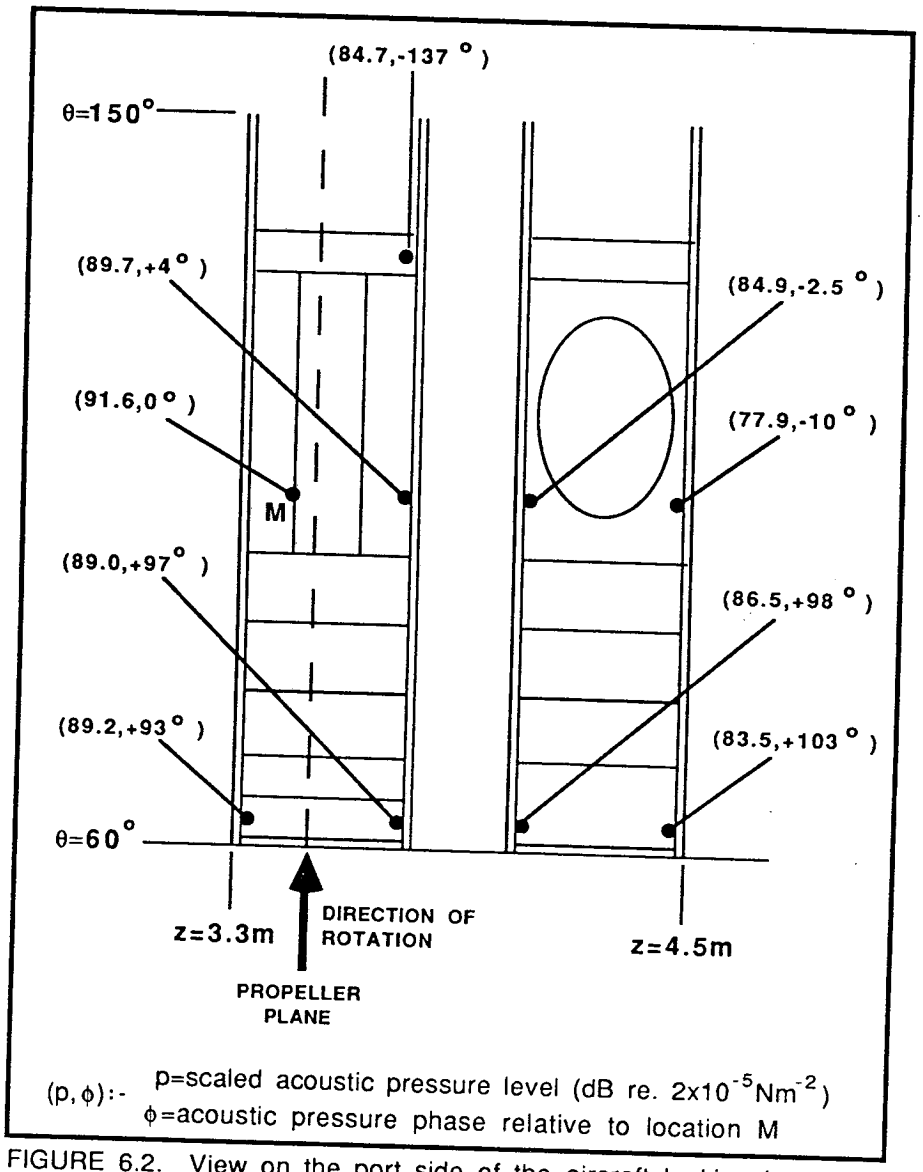

FIGURE 6.2. View on the port side of the aircraft looking inwards showing the external microphone locations and the scaled acoustic pressures measured during a 10000ft cruise with the port engine operating at 14200 r.p.m. The frequency is the blade passage second harmonic of 176Hz.

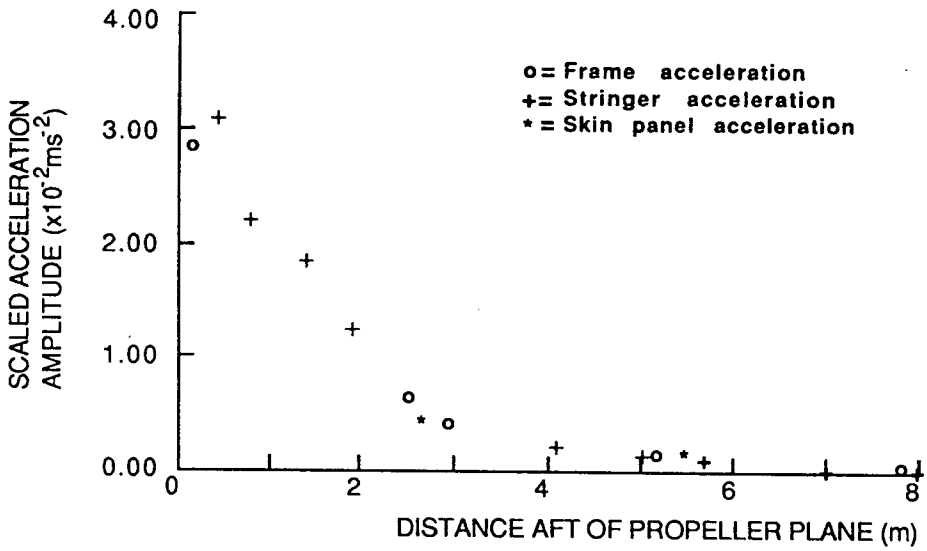

a) The scaled radial acceleration amplitude along the fuselage on a line corresponding to θ=85°.

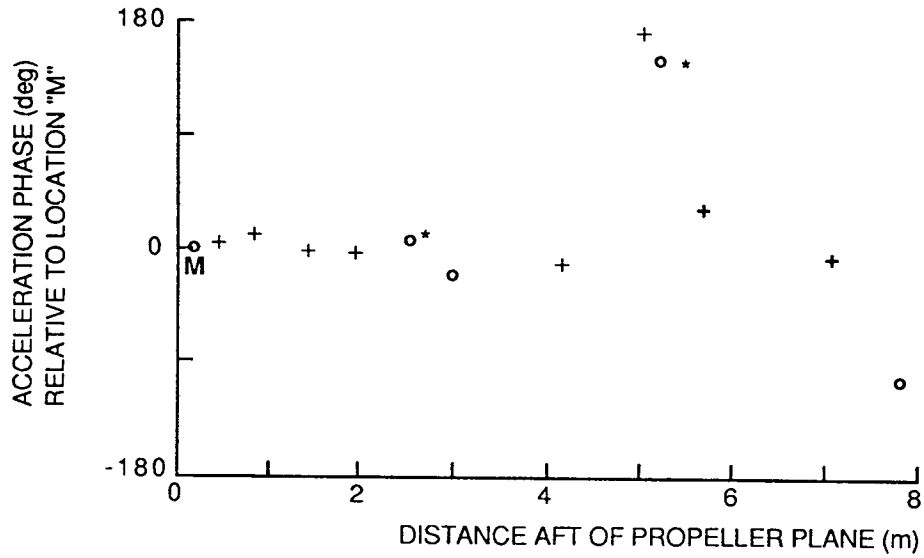

b) The radial acceleration phase along the fuselage on a line corresponding to θ=85°.

FIGURE 6.3. The measured radial acceleration response of the aircraft fuselage due to the port propeller only as a function of distance down the fuselage. Measurements were made during a 10000ft cruise with the port engine operating at 14200 r.p.m.. The frequency is the blade passage fundamental of 88Hz.

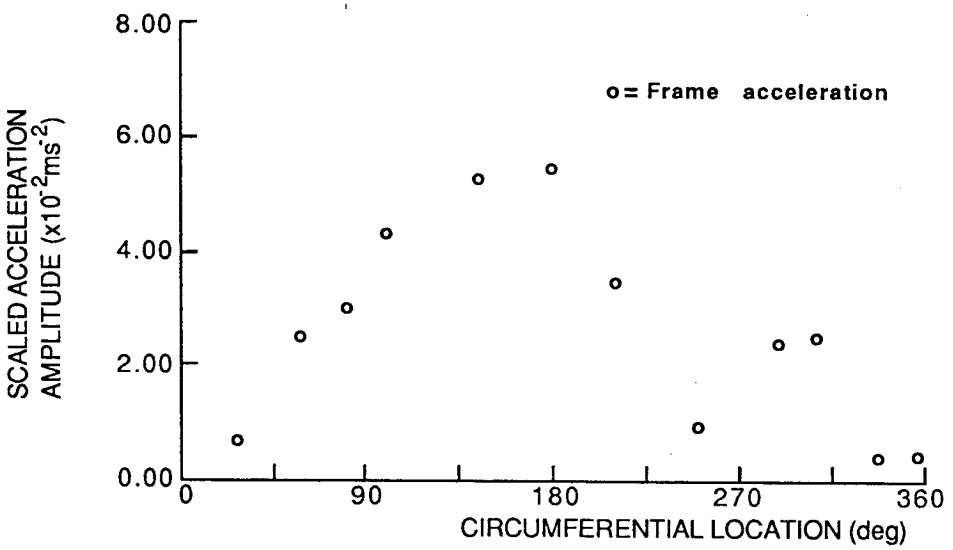

c) The scaled radial acceleration amplitude around the fuselage in the propeller plane.

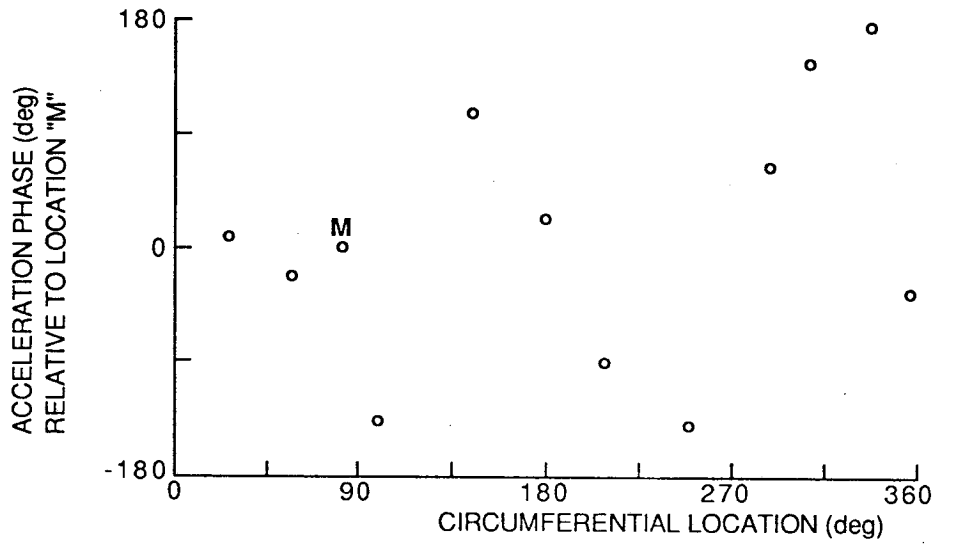

d) The radial acceleration phase around the fuselage in the propeller plane.

FIGURE 6.3(cont). The measured radial acceleration response of the aircraft fuselage due to the port propeller only as a function of angle around the fuselage. Measurements were made during a 1000ft. cruise with the port engine operating at 14200 r.p.m.. The frequency is the blade passage fundamental of 88Hz.

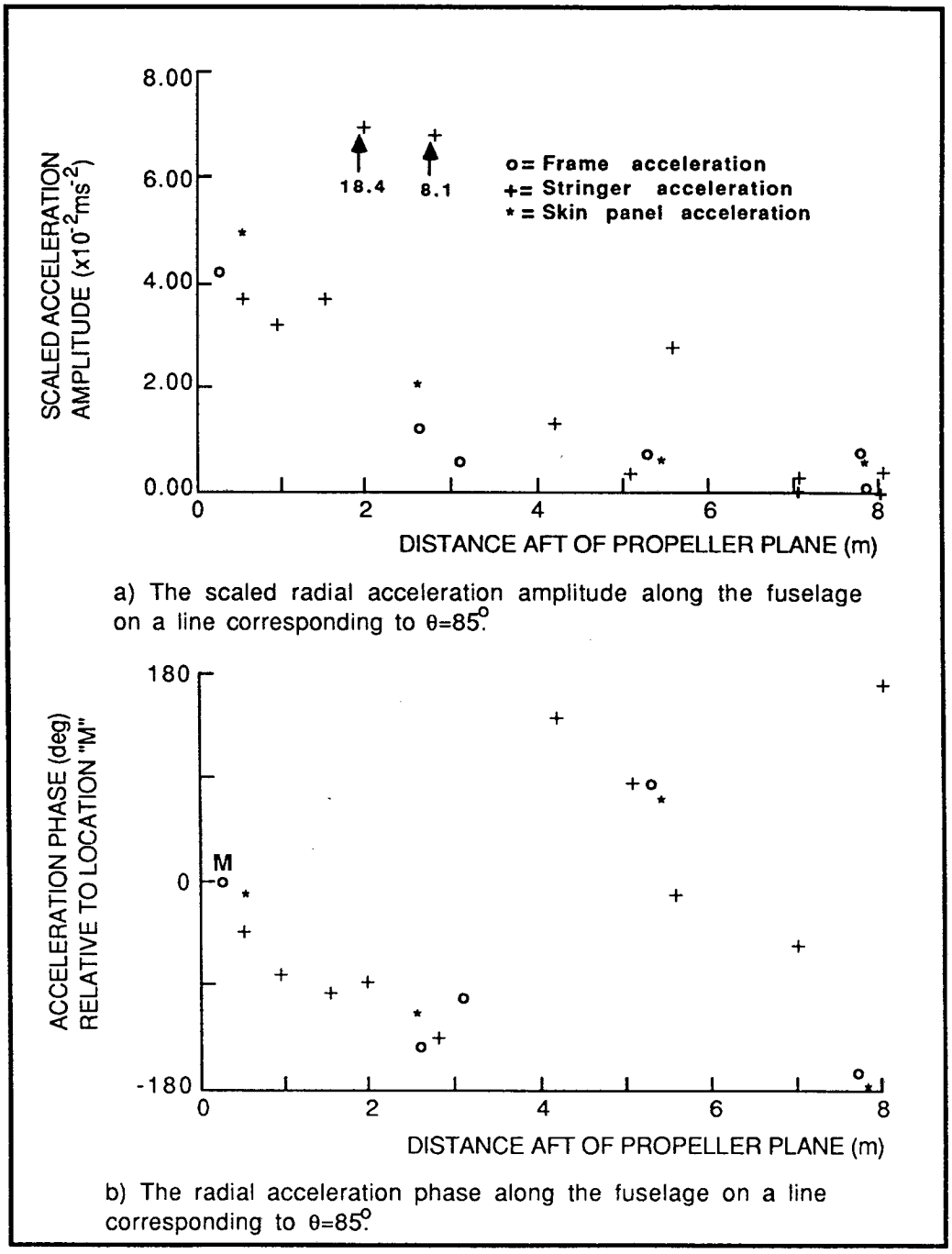

FIGURE 6.4. The measured radial acceleration response of the aircraft fuselage due to the port propeller only as a function of distance down the fuselage. Measurements were made during a 10000ft cruise with the port engine operating at 14200 r.p.m.. The frequency is the blade passage second harmonic of 176Hz.

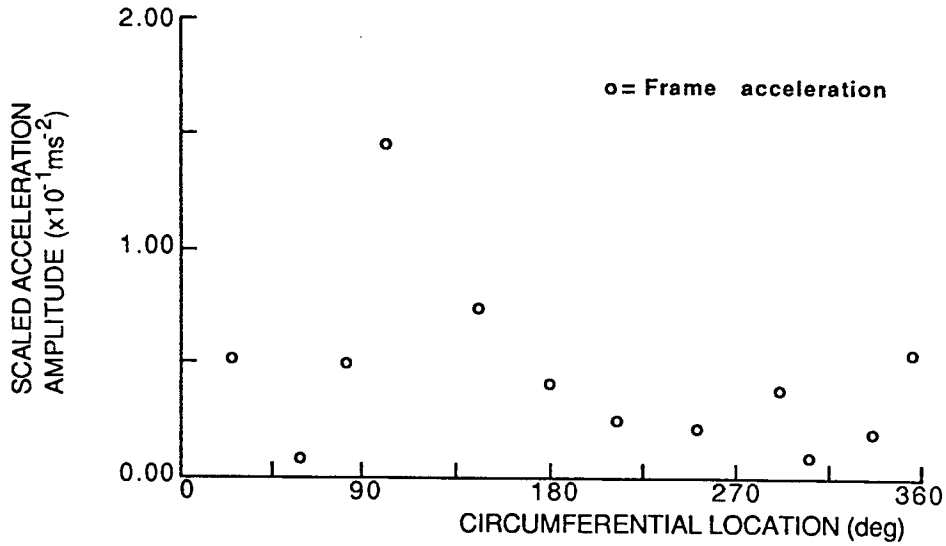

c) The scaled radial acceleration amplitude around the fuselage in the propeller plane.

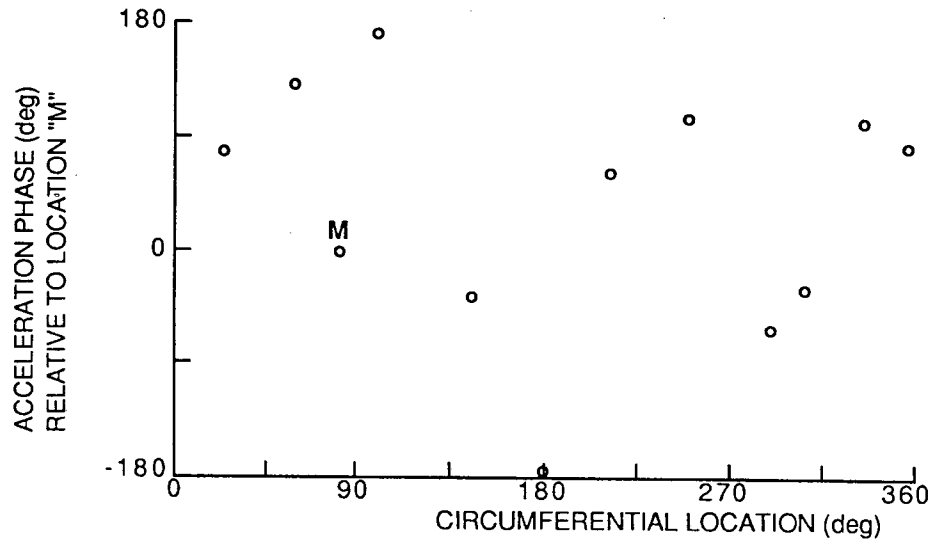

d) The radial acceleration phase around the fuselage in the propeller plane.

FIGURE 6.4(cont). The measured radial acceleration response of the aircraft fuselage due to the port propeller only as a function of angle around the fuselage. Measurements were made during a 1000ft. cruise with the port engine operating at 14200 r.p.m.. The frequency is the blade passage second harmonic of 176Hz.

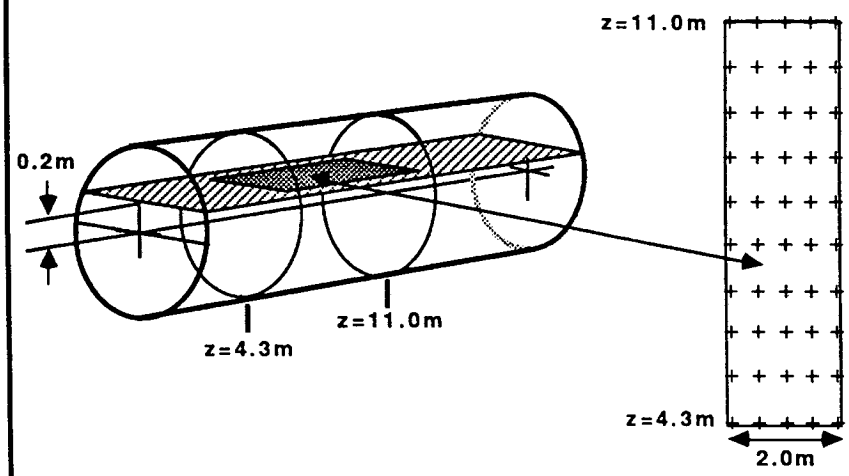

a)Schematic diagram showing the head height plane (0.2m above the fuselage centreline) and the measurement locations on the plane

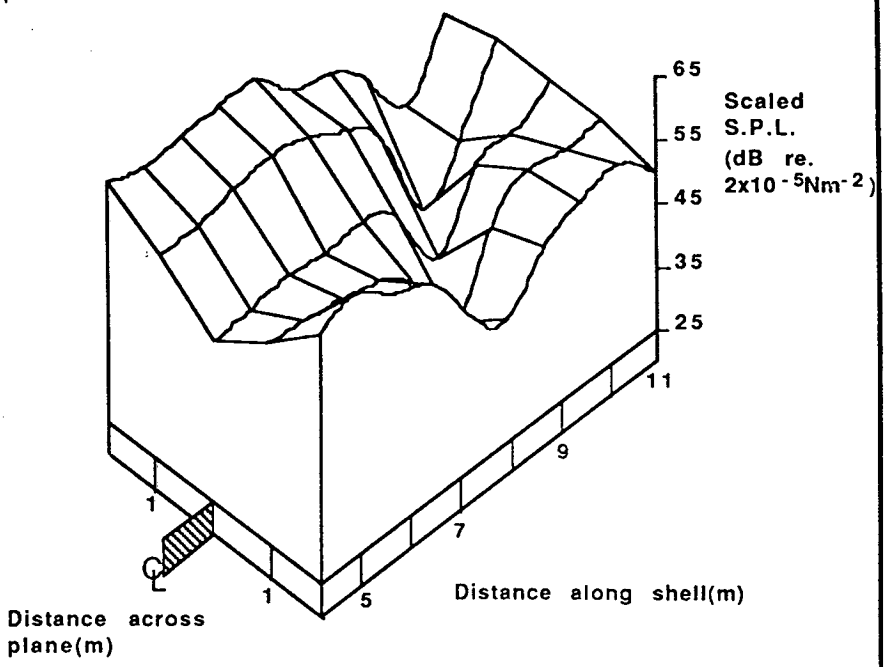

b)The scaled internal sound pressure levels measured over the head height plane

FIGURE 6.5. The scaled internal sound pressure level distribution at 88Hz due to the port propeller only measured over a 10 by 5 grid of points at seated head height. Measurements were made during a 10000ft cruise with the port engine operating at 14200 r.p.m..

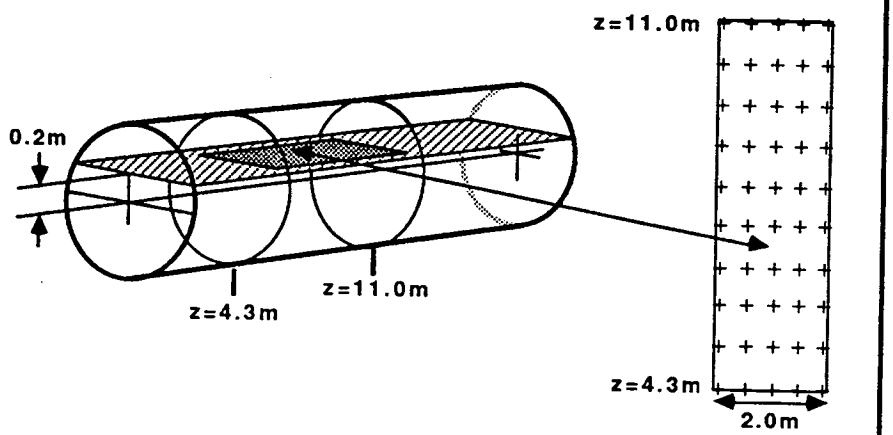

a)Schematic diagram showing the head height plane (0.2m above the fuselage centreline) and the measurement locations on the plane

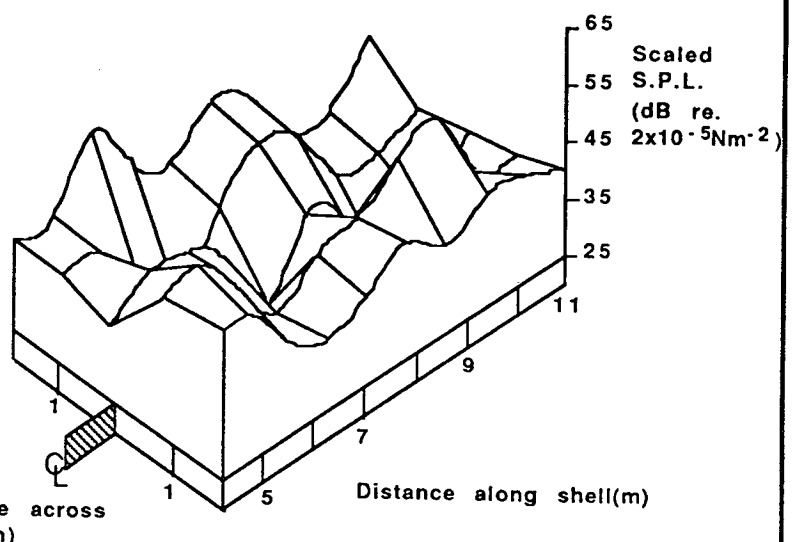

b)The scaled internal sound pressure levels measured over the head height plane

FIGURE 6.6. The scaled internal sound pressure level distribution at 176Hz due to the port propeller only measured over a 10 by 5 grid of points at seated head height. Measurements were made during a 10000ft cruise with the port engine operating at 14200 r.p.m..

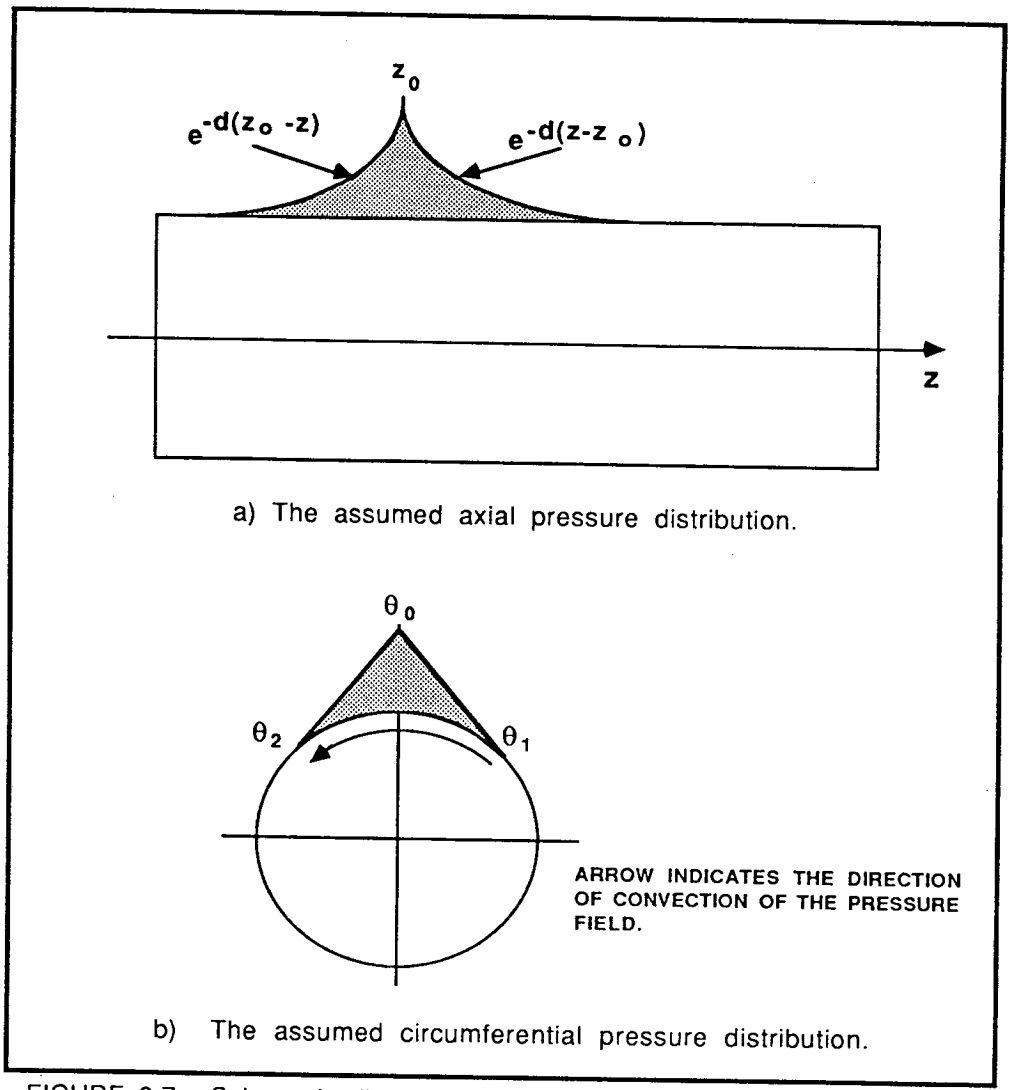

FIGURE 6.7. Schematic diagram showing the pressure distributions used to represent the external pressure field due to a single propeller.

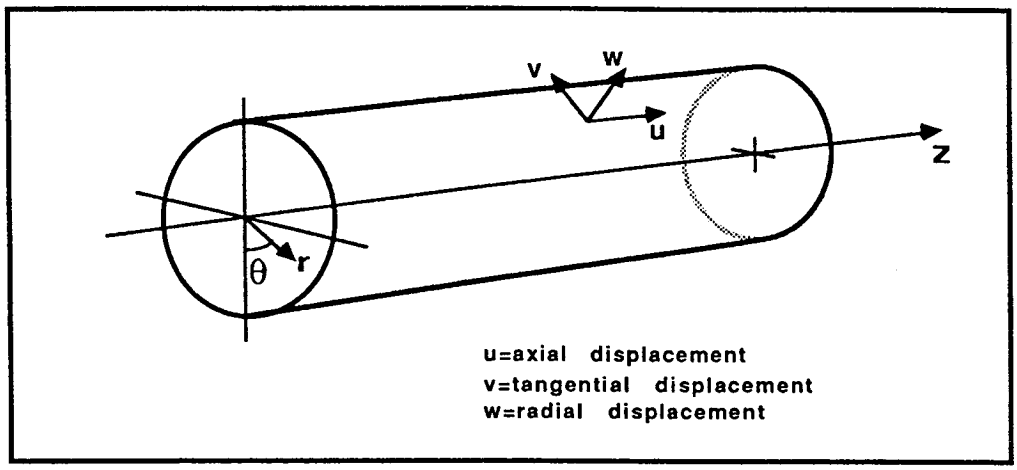

Figure 6.8. Schematic diagram of the shell coordinate system used.

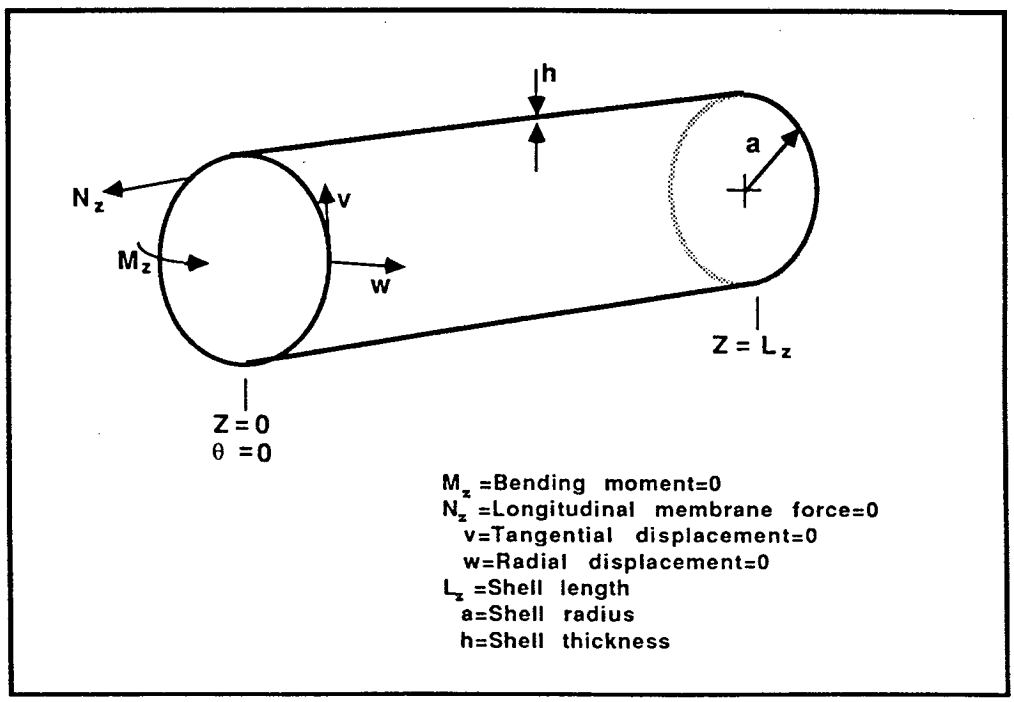

Figure 6.9. Schematic diagram of a finite shell having shear diaphragm-shear diaphragm end conditions.

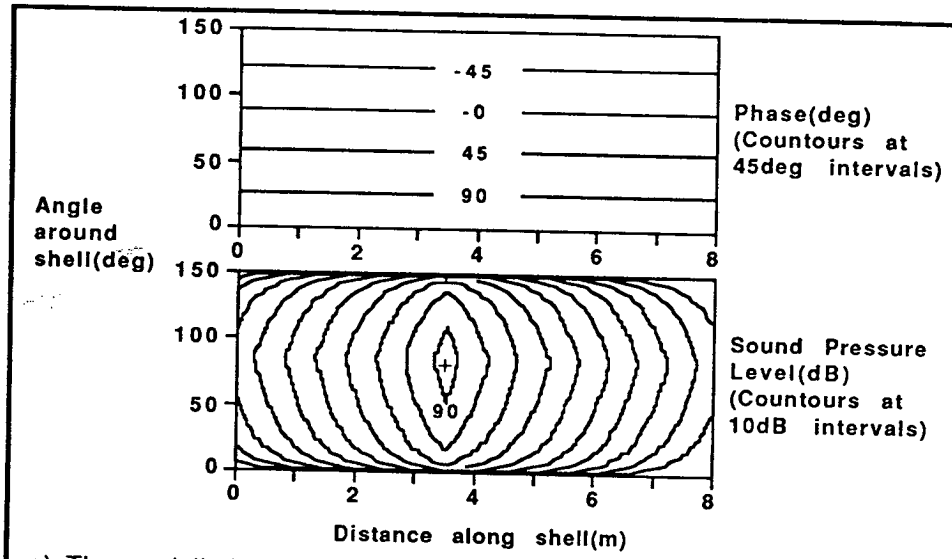

a) The modelled external port pressure field at the blade passage fundamental frequency (88Hz). The peak sound pressure level is 94dB at "+".

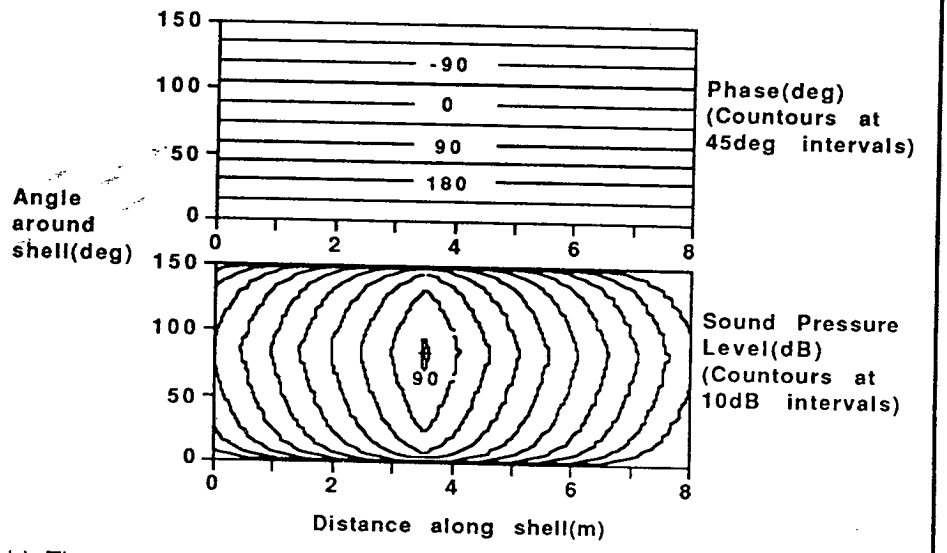

b) The modelled external port pressure field at the blade passage second harmonic (176Hz). The peak sound pressure level is 91.4dB at "+".

FIGURE 6.10. The external pressure fields used to model the port propeller pressure field acting on the fuselage at the blade passage first and second harmonics. The diagrams show the distribution over a section of "unwrapped" shell.

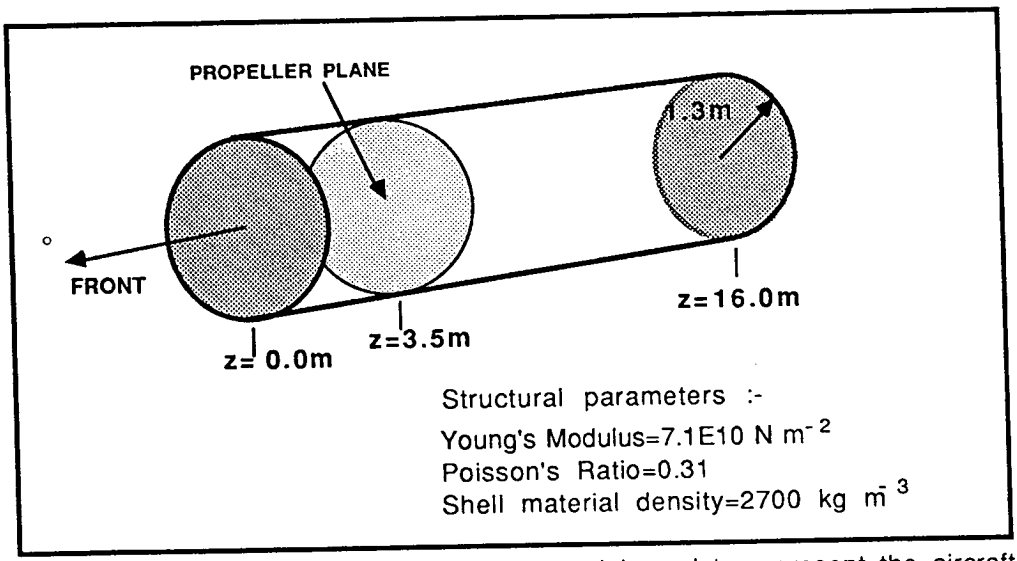

Figure 6.11. Schematic diagram of the model used to represent the aircraft fuselage structural response and the internal cabin acoustic response.

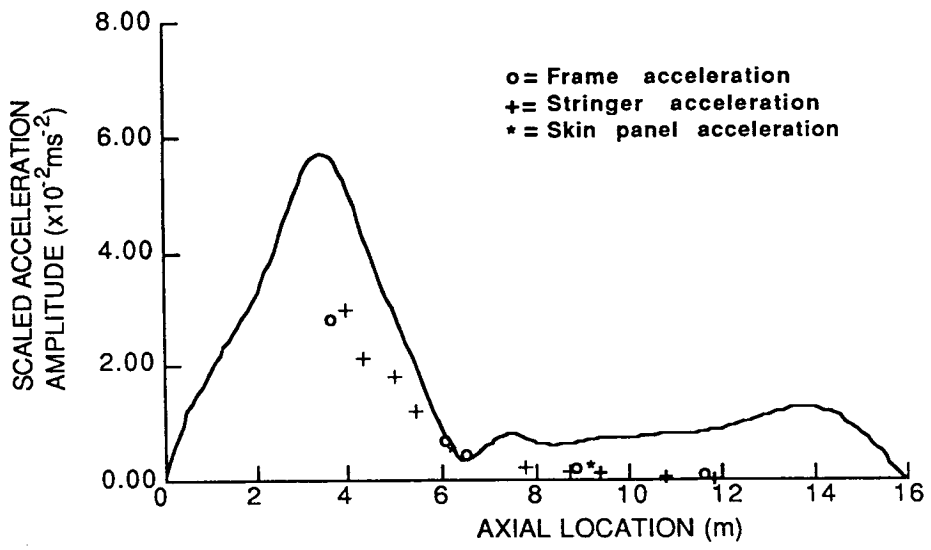

a) The predicted and measured radial acceleration amplitude along the shell/fuselage on a line corresponding to θ=85°.

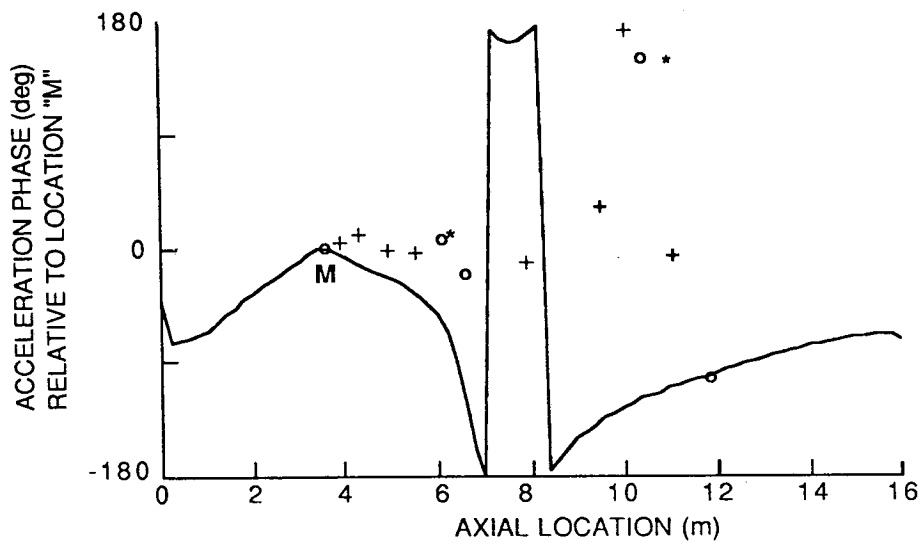

b) The predicted and measured radial acceleration phase along the shell/fuselage on a line corresponding to θ=85°.

FIGURE 6.12. The predicted radial acceleration response of the finite shell as a function of distance along the shell when it is excited by the 88Hz pressure distribution shown in Figure 6.10(a). The corresponding experimental measurements of Figure 6.3 are also shown for comparison.

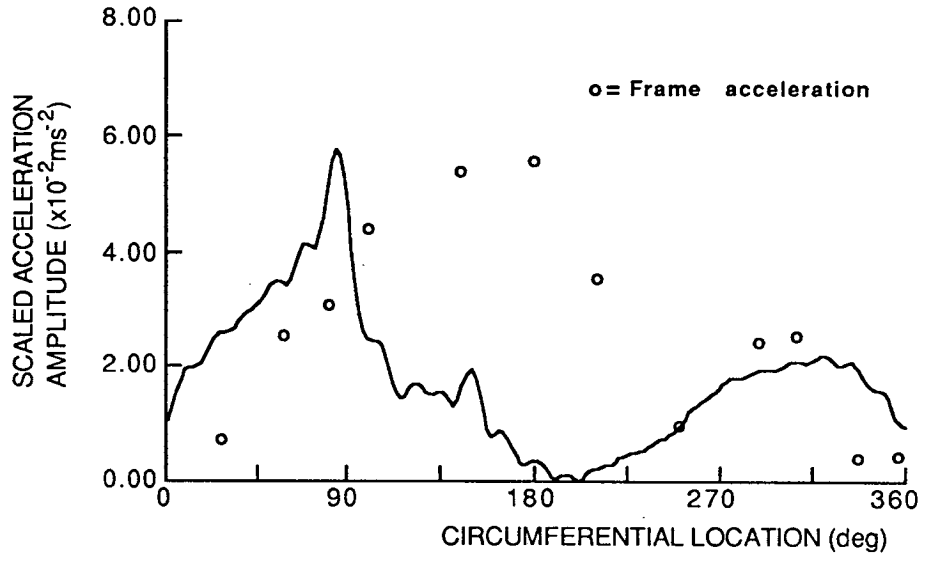

c) The predicted and measured radial acceleration amplitude around the shell/fuselage in the plane corresponding to z=3.5m.

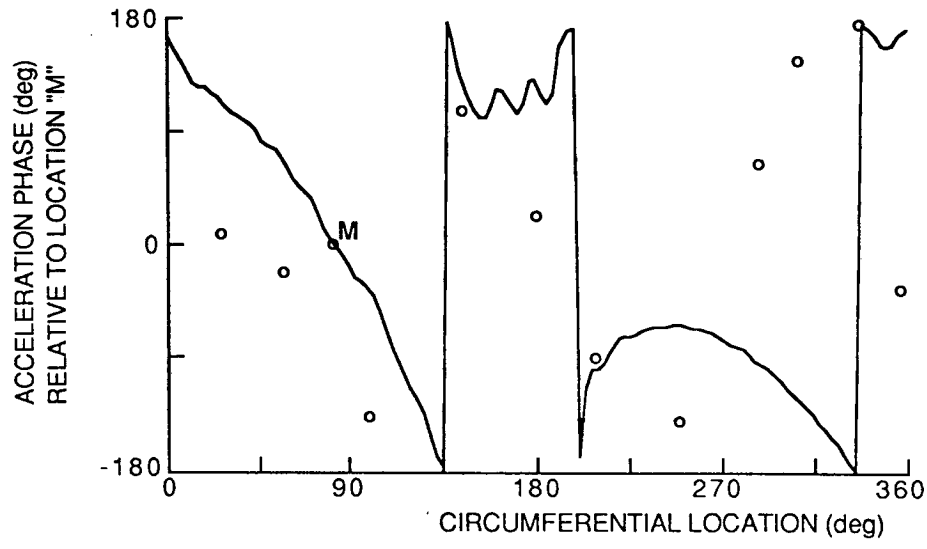

d) The predicted and measured radial acceleration phase around the shell/fuselage in the plane corresponding to z=3.5m.

FIGURE 6.12(cont). The predicted radial acceleration response of the finite shell as a function of angle around the shell when it is excited by the 88Hz pressure distribution shown in Figure 6.10(a). The corresponding experimental measurements of Figure 6.3 are also shown for comparison.

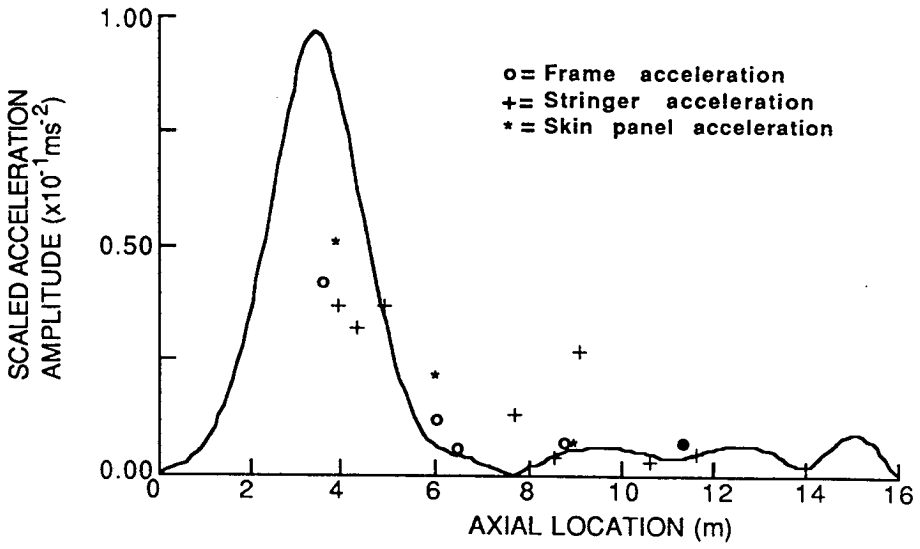

a) The predicted and measured radial acceleration amplitude along the shell/fuselage on a line corresponding to θ=85°.

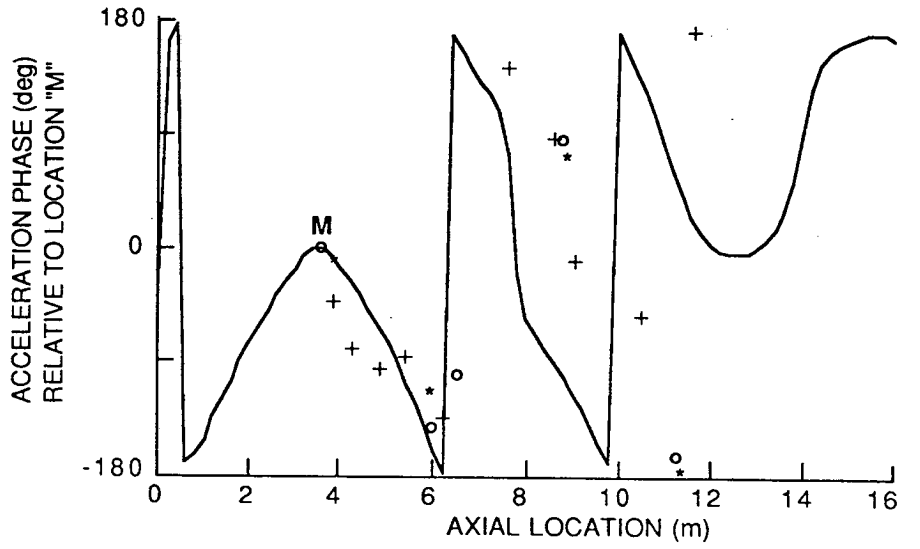

b) The predicted and measured radial acceleration phase along the shell/fuselage on a line corresponding to θ=85°.

FIGURE 6.13. The predicted radial acceleration response of the finite shell as a function of distance along the shell when it is excited by the 176Hz pressure distribution shown in Figure 6.10(b). The corresponding experimental measurements of Figure 6.4 are also shown for comparison.

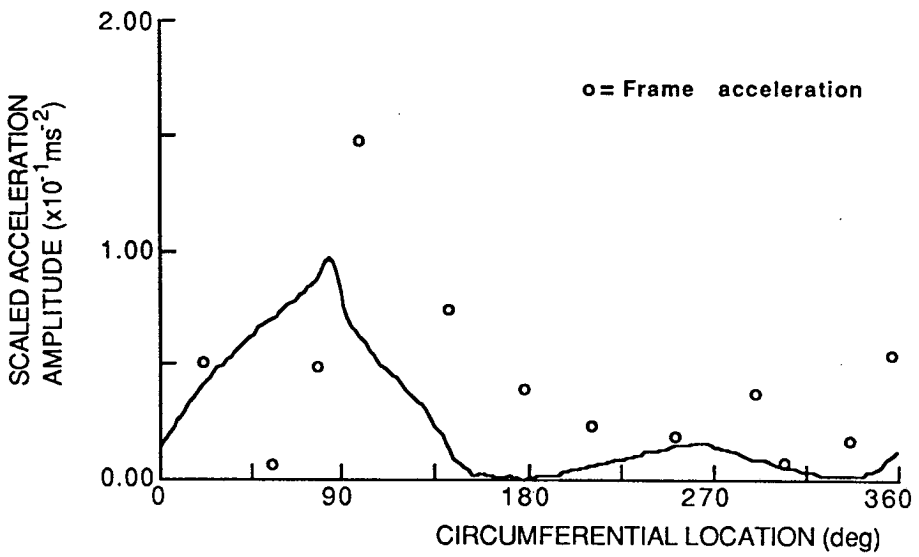

c) The predicted and measured radial acceleration amplitude around the shell/fuselage in the plane corresponding to z=3.5m.

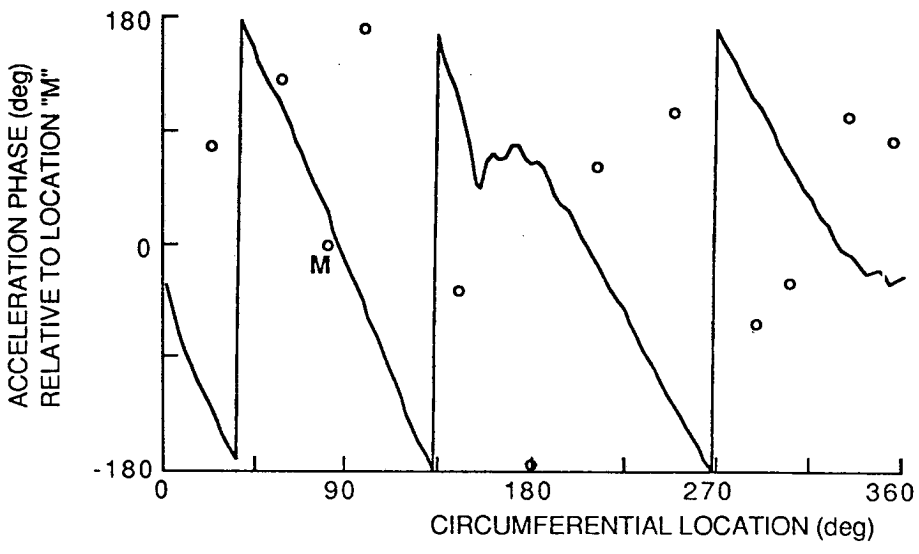

d) The predicted and measured radial acceleration phase around the shell/fuselage in the plane corresponding to z=3.5m.

FIGURE 6.13(cont). The predicted radial acceleration response of the finite shell as a function of angle around the shell when it is excited by the 176Hz pressure distribution shown in Figure 6.10(b). The corresponding experimental measurements of Figure 6.4 are also shown for comparison.

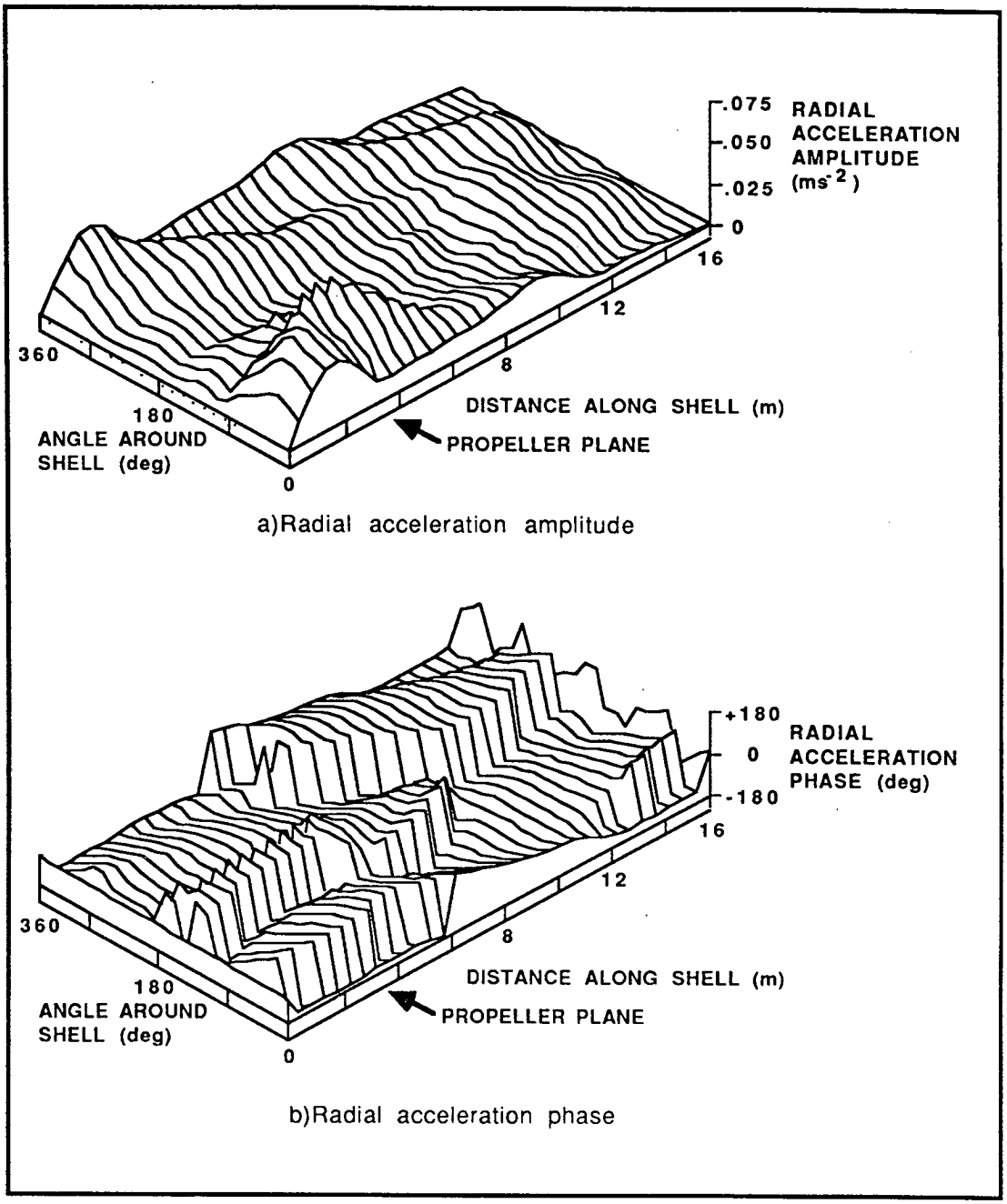

FIGURE 6.14. The predicted radial acceleration response of the shell when it is excited at 88Hz by the pressure distribution shown in Figure 6.10(a). Both amplitude and phase data are presented over the entire "unwrapped" shell surface.

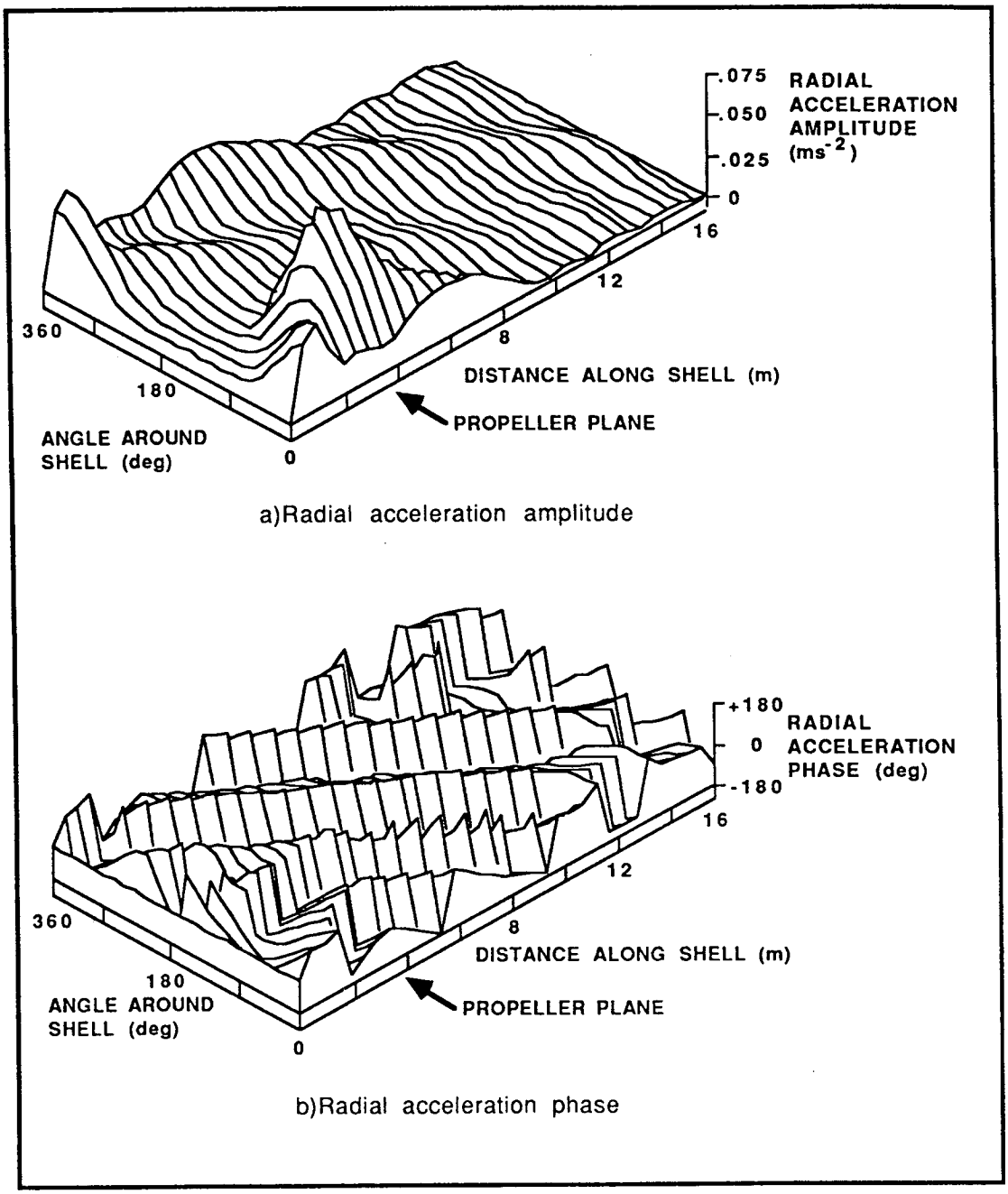

FIGURE 6.15. The predicted radial acceleration response of the shell when it is excited at 176Hz by the pressure distribution shown in Figure 6.10(b). Both amplitude and phase data are presented over the entire "unwrapped" shell surface.

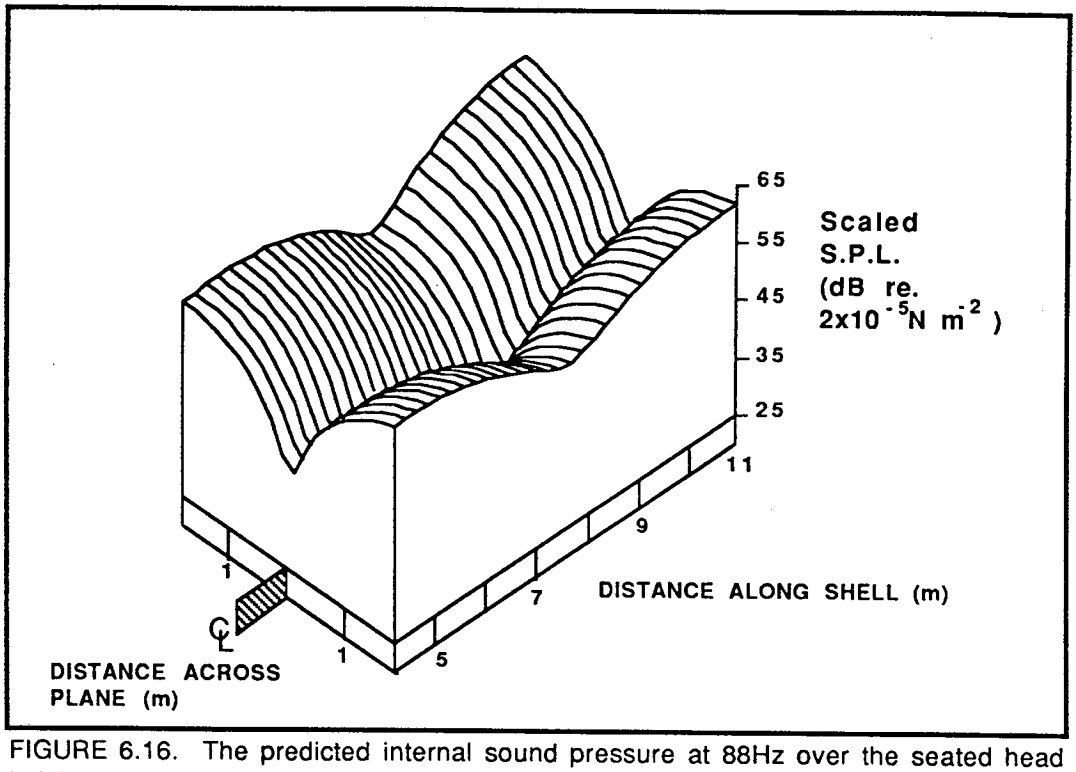

FIGURE 6.16. The predicted internal sound pressure at 88Hz over the seated head height plane due to the shell structural response shown in Figure 6.14. This corresponds to the experimentally measured pressure field shown in Figure 6.5.

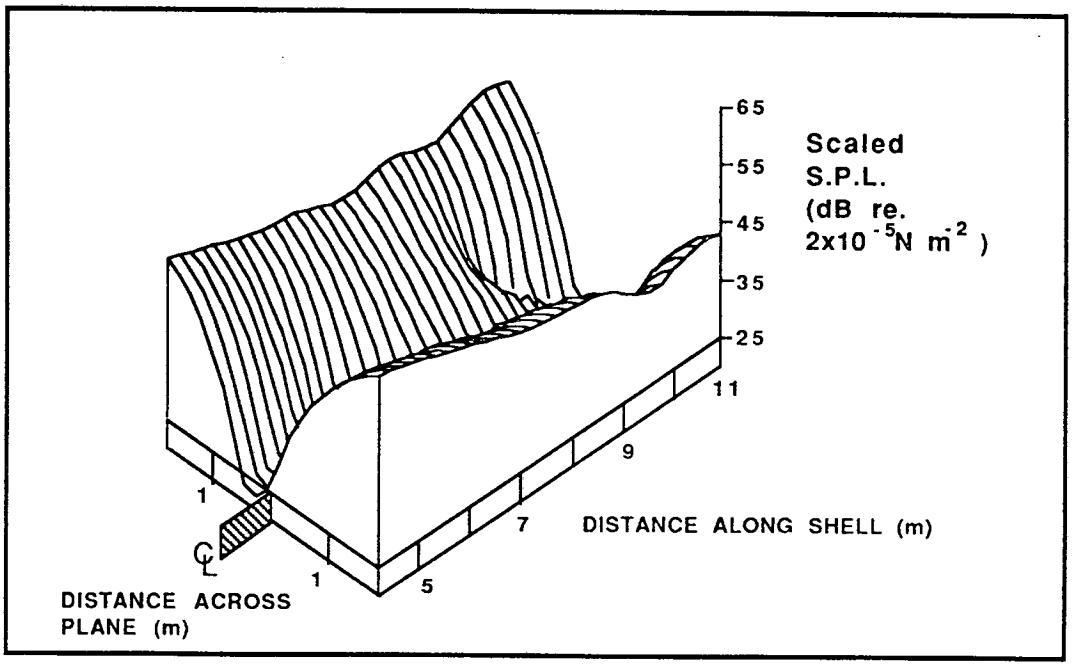

FIGURE 6.17. The predicted internal sound pressure at 176Hz over the seated head height plane due to the shell structural response shown in Figure 6.15. This corresponds to the experimentally measured pressure field shown in Figure 6.6.

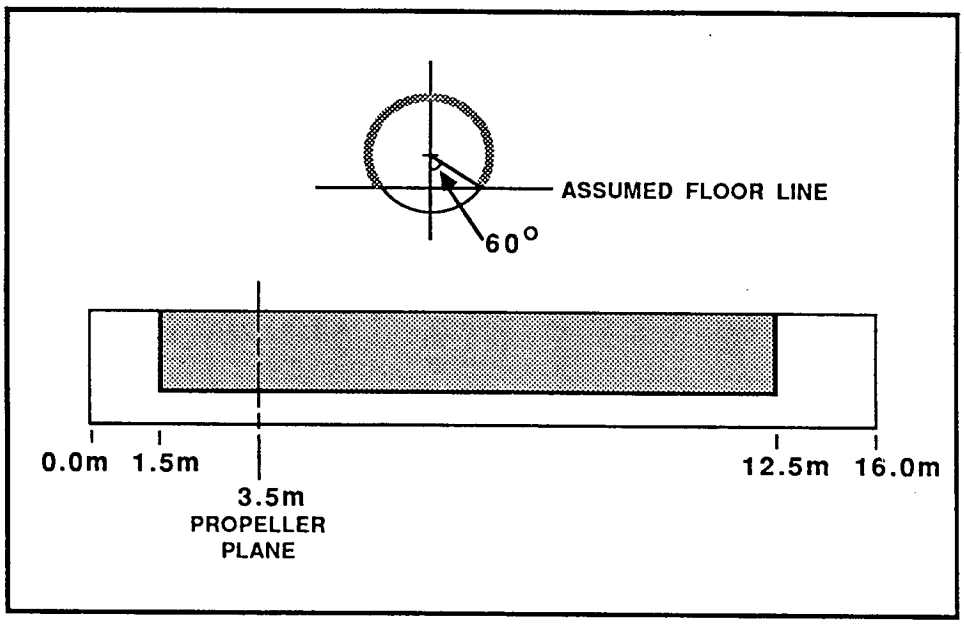

FIGURE 6.18. Schematic diagram showing the modified region of the shell wall (shaded) which is allowed to excite the internal acoustic field.

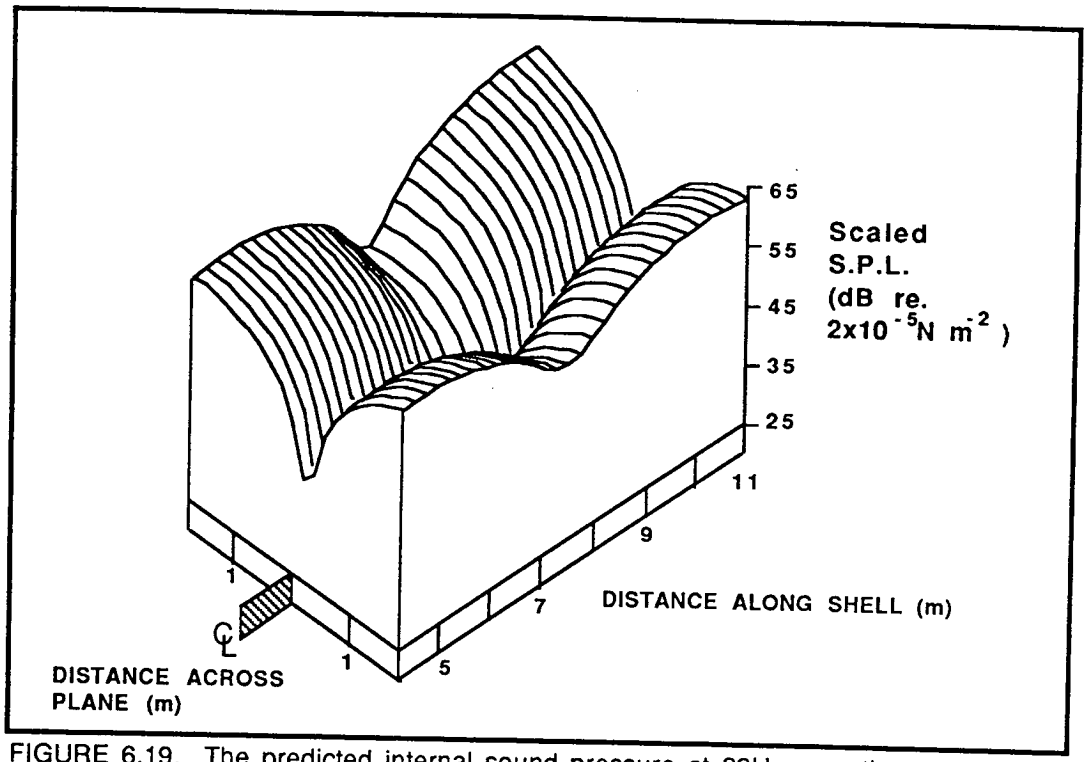

FIGURE 6.19. The predicted internal sound pressure at 88Hz over the seated head height plane due to the shell structural response shown in Figure 6.14. but "truncated" as shown in Figure 6.18. This corresponds to the experimentally measured pressure field shown in Figure 6.5.

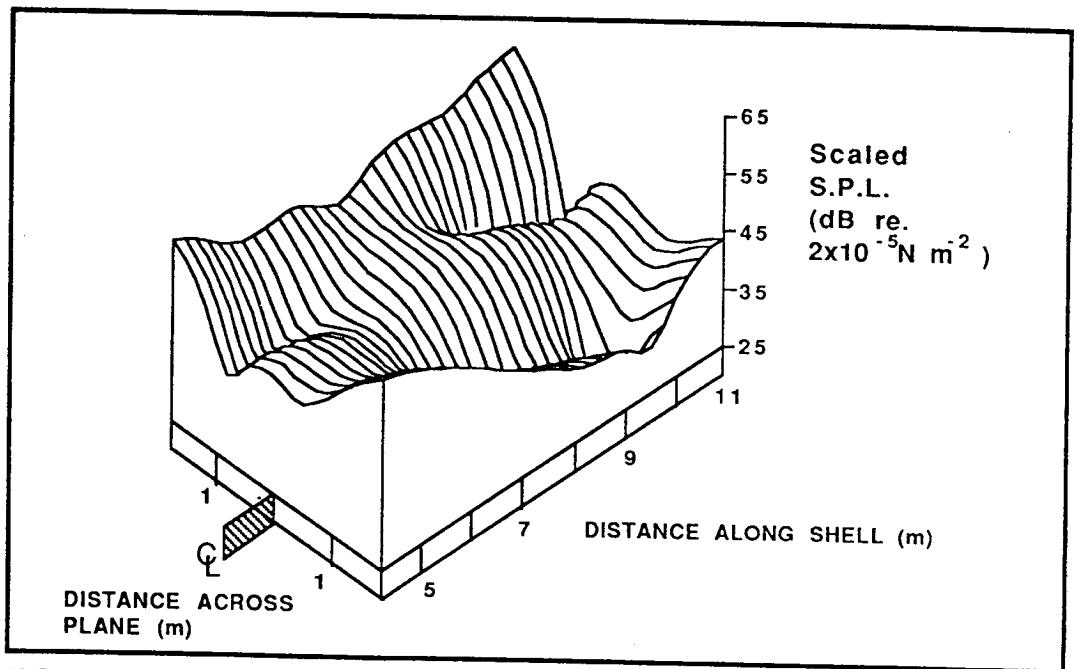

FIGURE 6.20. The predicted internal sound pressure at 176Hz over the seated head height plane due to the shell structural response shown in Figure 6.15. but "truncated" as shown in Figure 6.18. This corresponds to the experimentally measured pressure field shown in Figure 6.6.

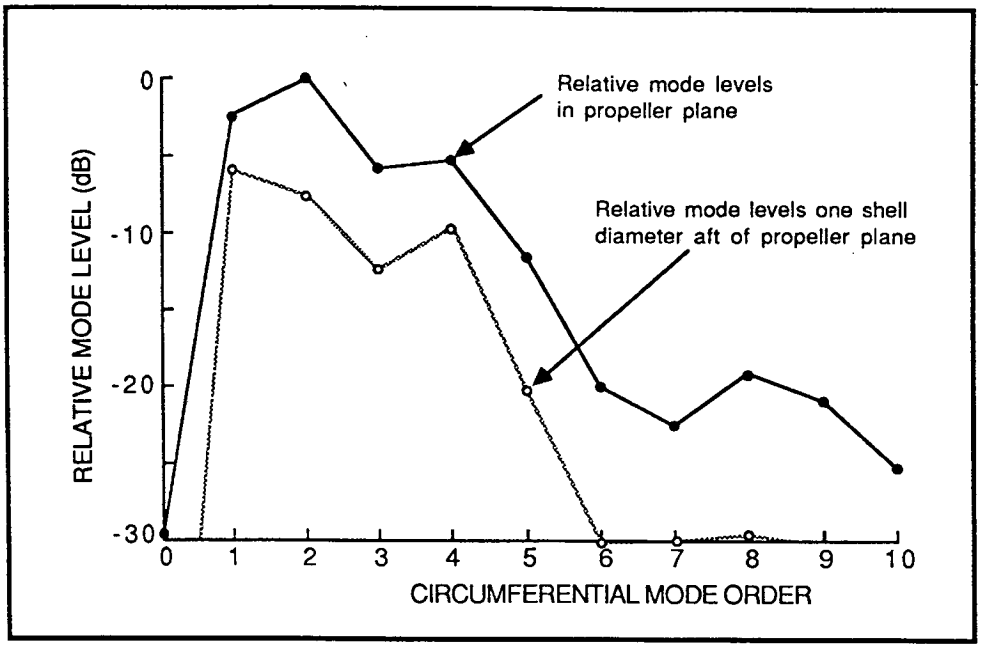

FIGURE 6.21. The relative contributions of the first ten circumferential structural modes to the shell response shown in Figure 6.14. The mode levels are expressed relative to the amplitude of the most dominant mode. The frequency is 88Hz.

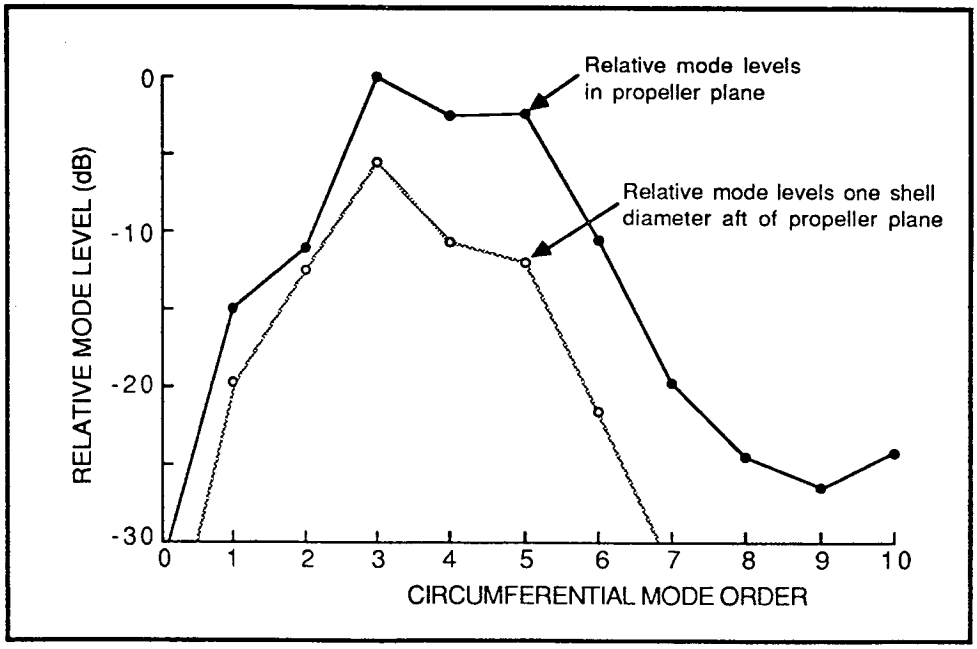

FIGURE 6.22. The relative contributions of the first ten circumferential structural modes to the shell response shown in Figure 6.15. The mode levels are expressed relative to the amplitude of the most dominant mode. The frequency is 176Hz.

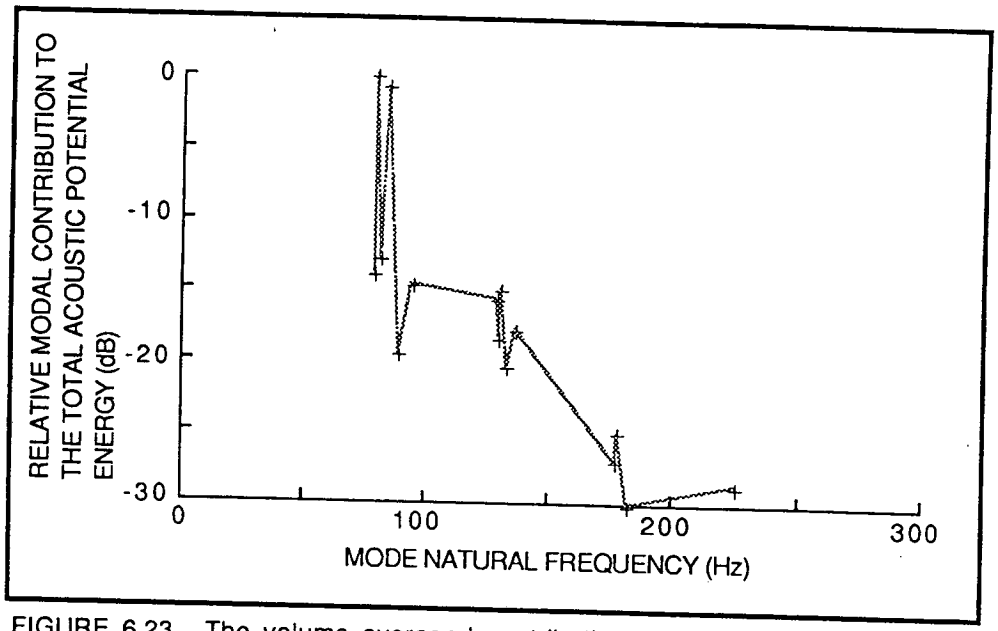

FIGURE 6.23. The volume averaged contributions of the most dominant acoustic modes inside the shell when it is excited at 88Hz by the shell structural response shown in Figure 6.14. The mode levels are expressed relative to the contribution of the most dominant mode.

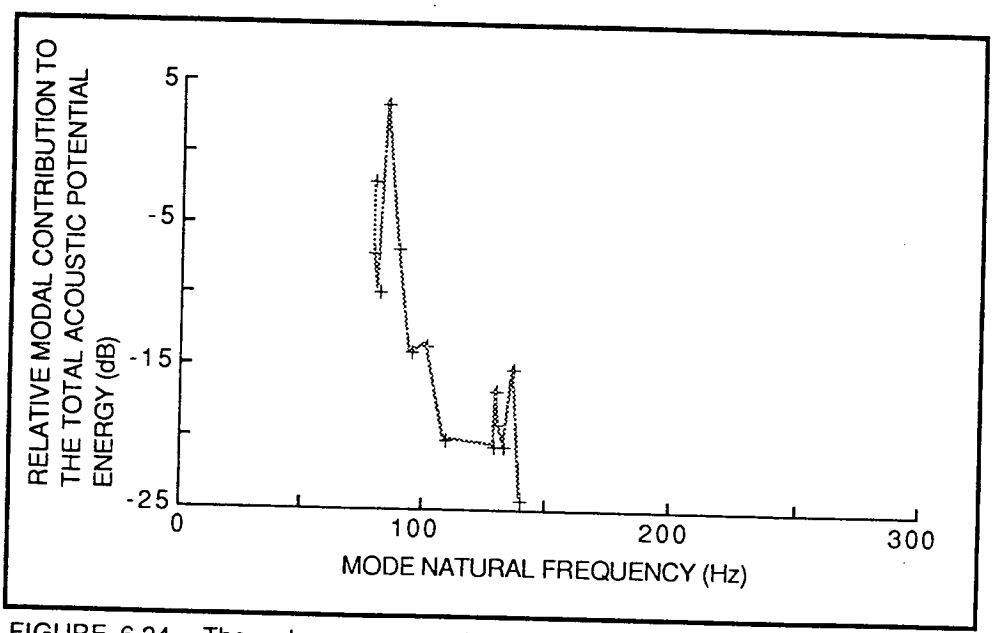

FIGURE 6.24. The volume averaged contributions of the most dominant acoustic modes inside the finite cylinder when it is excited at 88Hz by the shell structural response shown in Figure 6.14 but with the excitation only occurring over the region 1.5m<z<12.5m , $60^{o}< \theta <300^{o}$. The mode levels are expressed relative to the contribution of the most dominant mode of Figure 6.23.

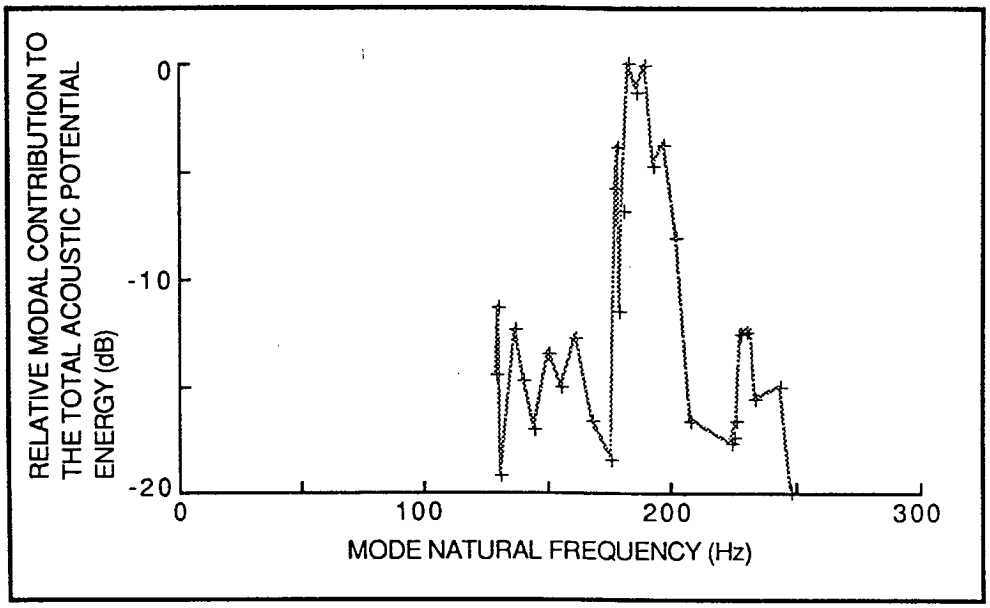

FIGURE 6.25. The volume averaged contributions of the most dominant acoustic modes inside the shell when it is excited at 176Hz by the shell structural response shown in Figure 6.15. The mode levels are expressed relative to the contribution of the most dominant mode.

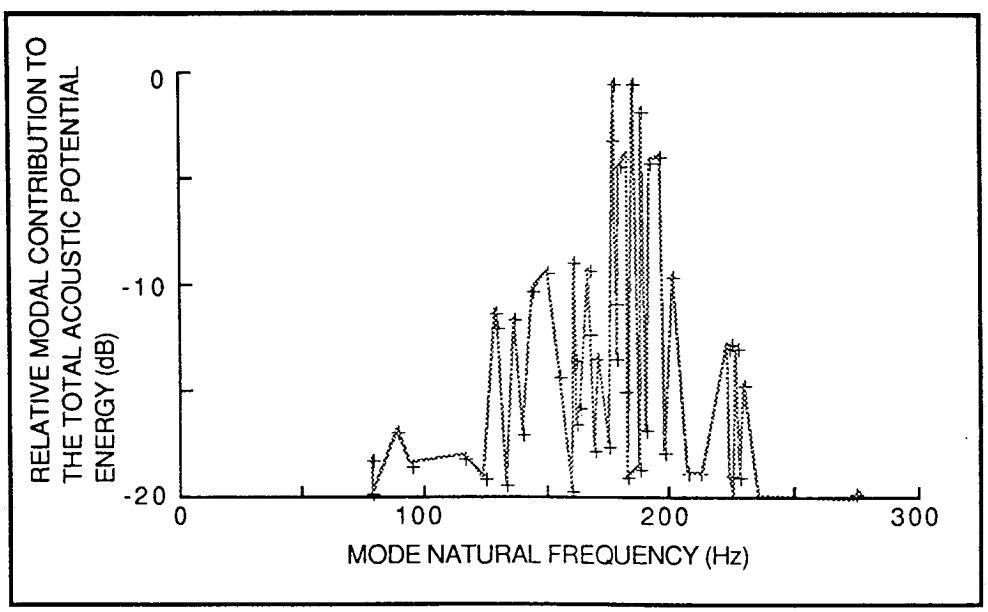

FIGURE 6.26. The volume averaged contributions of the most dominant acoustic modes inside the finite cylinder when it is excited at 176Hz by the shell structural response shown in Figure 6.15 but with the excitation only occurring over the region $1.5m<z<12.5m$, $60^{\circ}< \theta <300^{\circ}$. The mode levels are expressed relative to the contribution of the most dominant mode of Figure 6.25.

CHAPTER 7

IE APPLICATION OF ACTIVE CONTROL TO THE REDUCTION OF PROPELLER INDUCED CABIN NOISE

Introduction

Having developed in Chapters 5 and 6 a suitable analytical model for cribing the internal acoustic response within the B.Ae.748 test craft, the work presented in this chapter will now concentrate on ng this model, combined with the quadratic minimisation theory of pter 2, to predict the effectiveness of applying active noise control reduce the cabin internal sound levels. In particular the effect of numbers of secondary sources and sensors will be investigated, ether with the importance of the locations of these sources and sors. In general the results will concentrate on minimising the tribution due to the port propeller only to avoid any complicating ects produced by relative phase differences between the two pellers. However, the possibility of using "propeller synchrophasing" complement an active noise control system will be addressed in the ter part of the chapter.

The maximum size of active noise control system which shall be sidered will be a 24 source, 48 sensor system, where the sources will modelled as 0.25 m by 0.25 m pistons mounted flush with the cylinder l. With a system of this magnitude the number of possible rce/sensor combinations is obviously far too large to allow the luation of each different case in order to determine the optimal ations. Furthermore, it has not as yet been defined how the formance of the system is to be assessed. In Chapters 2, 3 and 4, re a very low modal density sound field was being studied it was the al time averaged acoustic potential energy which was chosen to judge effectiveness of the active control. In the present case, however, modal density can potentially be much higher and this, coupled with results of Chapter 6 which suggest that the primary source tribution is not highly localized, imply that global reductions are

less likely to be feasible with the size of control system chosen. Indeed, it may not even be desirable to produce global reductions. It may be more sensible to concentrate effort on reducing the sound levels around the passengers' head locations, thus reducing the problem to one of monitoring the pressure in a seated head height plane throughout the passenger cabin, and ensuring that the sound pressure levels in this region are reduced to an acceptable limit. What occurs elsewhere is, to a large extent, immaterial, although unacceptably high levels must of course be avoided in all regions of the cabin. It is this simplified strategy which has been chosen to be adopted for this work. Consequently, for most results a single figure, $J_{p_{sOO}}$, is quoted as being representative of the success of the active noise control system. The quoted reduction in $J_{p_{sOO}}$ represents the reduction in the average sound pressure level over a rectangular grid of 30 by 20 points evenly spaced over a seated head height plane 0.2 m above the cylinder centre line. The plane extends from z = 3.5 m to z = 12.5 m, and thus covers the entire twelve rows of seats in the passenger cabin of the test aircraft. A schematic diagram of this plane is shown in Figure 7.1. Later on in the chapter a modified average level, $J_{p_{sEO}}$, will also be introduced.

It should be noted that, despite the decision to only attempt "local" cancellation of the cabin sound field, the global effect on the total acoustic potential energy, E_p, of performing this local control is also often quoted throughout this chapter. This quantity is not intended as being indicative of the success of the particular control system under study, nor could it be used as a practical measure of control system effectiveness. Rather it is provided for completeness, to help demonstrate the differences between applying active noise control to sound fields of low modal density (Chapters 2, 3 and 4) and to the current sound fields of higher modal density.

Having chosen the strategy of reducing the pressure in the head height plane it would seem sensible to place the error sensors somewhere on this plane. The maximum number of sensors to be considered, 48, corresponds to the number of seat locations. As the seats are evenly

distributed throughout the cabin, and because it is an attractive practical proposition, the sensors will be constrained to be placed in the seat headrests. The location of the sensors and the grid system used to identify each one's location is shown on Figure 7.2a. Similarly, the secondary sources will be constrained to certain practically attractive locations. The maximum number of secondary sources which shall be used simultaneously in the following predictions is 24. However, these 24 may be chosen from any of the 48 possible secondary sources shown on Figure 7.2b. These sources are located such that their positions correspond approximately to the areas where the cabin floor joins the fuselage wall, and to the areas where the luggage bins are sited on the fuselage wall. The choice of possible source and sensor locations will be kept identical for both the fundamental and the second harmonic frequencies with the exception of one set of results for which the modified source/sensor distributions will be described when the need arises.

.2 The Application of Active Noise Control at the Propeller Blade Passage Fundamental Frequency

7.2.1 Results obtained using a 24 source/48 sensor system

The primary sound pressure field predicted by the computer model escribed above at the propeller blade passage fundamental frequency (88 z) due to the port propeller is shown in Figure 7.3. Note that it ppears slightly different to the primary field of Figure 6.19 because it as been evaluated over the larger area shown in Figure 7.1. Figure 7.4 hows the relative acoustic mode contributions to the total acoustic otential energy of the primary field. Taking the criterion that dominant modes" have contributions up to 20 dB lower than the peak modal ontribution, it is seen that ten modes dominate the acoustic field xcited by the shell structural vibration. This suggests that, at this requency in the cabin, the acoustic modal density is still fairly low nd therefore, if desired, global reductions should still be possible sing a practically sized and sensibly placed control system.

The investigation will commence by considering the "largest" system, i.e., 48 sensors and 24 sources. The 48 sensors are fixed at the locations shown on Figure 7.2(a). The 24 sources used are spaced in pairs evenly along the cabin and are shown as sources A1, A3, B2, B4, C1, C3, D2, D4, E1, E3, F2, F4, G1, G3, H2, H4, I1, I3, J2, J4, K1, K3, L2, L4 on Figure 7.2(b) and also on Figure 7.5(a). On minimising J_{p48} (i.e., the sum of the squared pressures at the 48 sensors) the results shown in Figures 7.5 are obtained. These results have been presented as four isometric plots for clarity. The "areas of pressure reduction" plot shows the levels of reduction in sound pressure level relative to the primary field which have been obtained over the grid of 30 by 20 points following the application of the active control. Areas where the sound pressure level has increased relative to the primary field are shown as zero. The plot "areas of pressure increase" shows the levels of increase in the sound pressure level relative to the primary field following the application of the active control. Areas where the sound pressure level has decreased are shown as zero. The reason for showing the primary field again, although it is identical to that of Figure 7.3, is that it is often important to judge visually how effective the active control has been by direct comparison of the four plots in each figure. This can be illustrated by reference to Figures 7.5. The reduction in J_{p600} over this plane following the application of the control is 16.3 dB and the "areas of pressure reduction" plot of Figure 7.5(d) confirms this large reduction. However, the "areas of pressure increase" plot of Figure 7.5(3) shows that some pressure increases of up to 8.5 dB do occur. This could be interpreted as an unsuccessful attempt to control the pressure over the plane, but if the primary field plot of Figure 7.5(b) is now referred to it becomes clear that the large pressure increases have only occurred where the pressure was initially very low. Consequently these pressure increases are of very little practical significance, thus demonstrating the importance of always considering the pressure reductions and pressure increases in relation to the primary pressure field.

The numerical results obtained from minimising J_{p48} using this 24 by 48 system are as follows: the reduction in J_{p600} is 16.3 dB, the reduction in J_{p48} (i.e., the reduction in J_p evaluated at the sensor locations) is 26.1 dB and the reduction in the total acoustic potential energy, E_p, is 1.0 dB. These and all subsequent results for the fundamental frequency active noise control predictions have been summarized in Table 7.2.

From these results it is evident that some very useful predicted reductions can be achieved. However, a 24 by 48 control system may be larger than is really needed and if either a smaller number of sources, or a smaller number of sensors, or a smaller number of both sources and sensors could be used to achieve similar reductions then this would be preferable. These possibilities will be addressed next.

7.2.2 The effect of the number of secondary sources

First the effect the number of secondary sources has on the reductions obtainable shall be investigated. For this the same 48 sensors as were used above are again used. Starting with a 4 source/48 sensor system, the number of secondary sources will be increased until reductions comparable with those obtained using the 24 source/48 sensors are obtained.

The choice of four secondary sources from the twenty four original sources shown in Figure 7.5(a) has been made by comparing their relative source strengths. Table 7.1 lists the strengths of each of the twenty four sources following the minimisation of J_{p48} using the 24-source system as described above. If one is limiting the number of secondary sources to four, it would seem sensible on the basis of the results of previous chapters to choose those sources which appear to be working hardest. Consequently, the four sources having the largest source strengths (A1, B2,D2 and K3) have been chosen. On minimising J_{p48} using these sources a reduction in J_{p48} of 5.8 dB and a reduction in J_{p600} of 5.0 dB is obtained. For comparison, if a second choice involving the

four sources having the smallest strengths (A3, E1, L2 and F2) is made and J_{p48} is again minimised, the reduction in J_{p48} is 2.8 dB and that in J_{pooo} is 2.5 dB. Neither of these cases show reductions comparable to those obtained using all 24 secondary sources. However, as expected the system using the four strongest secondary sources produces better results than that using the four weakest secondary sources, and it was therefore decided to add the secondary sources in order of decreasing strength according to Table 7.1. Table 7.2 lists the results of minimising J_{p48} by using 4, 6, 8, 12, 18 and 24 sources introduced according to this criterion. The resulting pressure fields for the 4, 6, 8, 12 and 18 source cases are shown in Figures 7.6 to 7.10 respectively.

The general indication from these results is that even with only 4 secondary sources, appreciable spatial regions of pressure reduction have been predicted, and in all cases the 48 error sensors used have ensured that no substantial regions of pressure increase have occurred. It is interesting to note that as the number of secondary sources is increased the reduction in both J_{p48} and J_{pooo} also generally increase. In particular there is a large (> 6 dB) improvement in both the J_{p48} and J_{pooo} reductions when the 8-source system is increased to a 12-source system. However, when the 12 sources are increased to 18, or even 24, sources then whilst the reductions in the average level over the error sensors (J_{p48}) continues to increase by up to 10.2 dB, the reductions over the 600 points of the head height plane increase by only up to 1.7 dB. Thus, as was suggested in Chapters 2 and 3, producing very large reductions at the error sensors (by allowing the number of secondary sources to tend towards the number of error sensors) is not always likely to be a practically attractive control strategy.

7.2.3 The use of secondary sources concentrated in the plane of the propeller

One further comment that can be made about these results is the general tendency for the secondary sources in the front half of the cabin (i.e., near the areas of maximum structural vibration amplitude) to have the largest source strength. However, the sources at the rear of the

cabin do also play their part and there is no firm evidence to suggest that concentrating all the loudspeakers at the front of the cabin would produce better results. This has been checked by choosing two sets of 12 secondary sources and minimising J_{p48}. The first set consisted of sources A1, A2, A3, A4, B1, B2, B3, B4, C1, C2, C3 and C4, the 12 sources closest to the propeller plane. Using these sources and minimising J_{p48} resulted in a reduction in J_{p48} of 3.7 dB, a reduction in J_{pSOO} of 2.6 dB and an increase in E_p of 12.0 dB. However, when 12 arbitrarily distributed sources were chosen, consisting of A1, B3, C2, D4, E1, F3, G2, H4, I1, J3, K2 and L4, and J_{p48} was again minimised, a reduction in J_{p48} or 19.7 dB, a reduction in J_{pSOO} of 17.7 dB and a reduction in E_p of 7.0 dB resulted. This is a clear indication that the secondary sources need to be distributed along the length of the cabin in order to be capable of producing large levels of reduction at the fundamental.

7.2.4 The effect of the number of error sensors

The second effect to be considered is the dependence of the reductions obtained on the number of error sensors used. Because the current aim is to determine the smallest system which will still give 'reasonable' reductions the same 8 sources A1, B2, D2, K3,B4, C1, H4 and F4, as were used for the results of Figure 7.8 will again be chosen. In that case, when J_p was minimised over 48 sensor locations, the average reduction in J_{pSOO} was 8.2 dB. The first reduced number of sensors to be tried is 12, evenly spaced along the head height plane, as shown in Figure 7.11a. When J_{p12} is minimised using this 8 source/12 sensor control system, the plots of Figures 7.11(b) to (e) result, with a reduction in J_{p12} of 11.8 dB and a reduction in J_{pSOO} of 6.7 dB, that is only 1.5 dB less than that obtained using 48 sensors. Looking at the residual pressure field of Figure 7.11(c) it appears that the feature preventing the J_{pSOO} reduction from being any greater are areas of higher pressure on the starboard side of the cabin. Increasing the number of sensors to 24, again evenly spaced over the plane, produces results as shown on Figures 7.12, with a reduction in J_{p24} of 8.9 dB and in J_{pSOO} of

7.9 dB. Thus 24 sensors produce a reduction over the plane of only 0.3 dB less than was obtained using 48 sensors, and the use of the 24 sensors has ensured that the areas of higher residual pressure which occurred when using 12 sensors has been attenuated. However, if such features as this do occur in practice it may be possible to overcome them with even fewer sensors. For example, by taking the 12 sensor system of Figure 7.11 and adding just 3 more sensors at locations F3, F4 and G3 (i.e., in an area of higher residual pressure), then when $J_{p_{1s}}$ is minimised the pressure fields of Figures 7.13 result. For this case the reduction in $J_{p_{1s}}$ is 10.7 dB, and the reduction in $J_{p_{800}}$ is 7.6 dB. Thus, by selectively choosing just a few extra sensors according to the results obtained using the smaller system, a substantially improved result has been achieved in which the sound pressure levels have been reduced at all points over the 600 point grid where they were initially high.

If this problem of an area of uncontrollable high pressure had still persisted when the sensors had been selectively chosen, then it may still have been possible to achieve an increased attenuation by weighting the error signals accordingly. This would allow more emphasis to be placed on minimising the pressure at those error sensors where problems were initially encountered in reducing the pressure. This strategy could be implemented practically by weighting (amplifying or attenuating) the error microphone signals as required. However, results concerning this effect are not reported in this thesis.

7.3 The Application of Active Noise Control at the Propeller Blade Passage Second Harmonic Frequency

7.3.1 Results obtained using a 24 source/48 sensor system

The primary sound pressure field predicted by the computer model at the propeller blade passage second harmonic frequency (176 Hz) due to the port propeller is shown in Figure 7.14. Figure 7.15 shows the relative acoustic mode contributions to the total acoustic potential energy of

e primary field, again plotted in decreasing order of the magnitude of eir contributions. Comparing Figure 7.15 with the equivalent plot for e fundamental frequency, Figure 7.4, shows a dramatic increase in the nber of "dominant" modes. For the second harmonic case there are 69 des which contribute "dominantly" to the total energy of the sound eld, compared to ten modes for the fundamental frequency (again the iterion is used that a "dominant" mode must contribute to the total oustic potential energy of the sound field by not less than 20 dB of e most dominant mode contribution). Thus, using a "single secondary urce per mode" argument [10], it is seen that even with 24 secondary urces large global reductions will not be ensured. Only if the primary urce distribution is compact, and the secondary sources can be placed jacent to it, will appreciable global reductions be feasible. Even in is latter case it must still be remembered that any practical system st have some measure of the modal contributions to the total acoustic tential energy if this is to be minimised. Therefore the number of ror sensors required may become impractically large to ensure that the cost function which has been chosen to be minimised as an proximation to E_p does indeed adequately mimic E_p.

As with the fundamental frequency, the investigations of this section ll commence by looking at the results obtained using the largest system nsisting of 24 secondary sources and 48 error sensors. The source and nsor locations are the same as those used for the system at the ndamental frequency and therefore correspond to those shown in Figure 2. Using this system the results of Figures 7.16 are obtained, with a duction in J_{p48} of 9.1 dB, a reduction in J_{p600} of 1.6 dB but an crease in E_p of 1.9 dB. (The results for the second harmonic equency active noise control predictions have been summarized in Table 4.) The relative strengths of the secondary sources are listed in ble 7.3. Using the same system to control the fundamental resulted in reduction in J_{p600} of 16.3 dB. Thus immediately the effects of the gher modal density are becoming apparent. However, whilst a reduction the average pressure level of 1.6 dB over the plane is still a rthwhile improvement, particularly as the second harmonic often

nates the fundamental frequency on an A-weighted basis, reference to re 7.16(d) indicates that the average reduction in sound pressure l over the plane is substantially larger than the J_{pSOO} figure ies. The reason for this is that the region of highest pressure in primary sound field (which is at the very front end of the plane) is act slightly increased following the minimisation of J_{p48}, despite other regions decreasing in pressure. This fact is not too imental to the performance of the active control as it has not been mpted to reduce the pressure in this region. This is because ough the passenger cabin forward bulkhead lies in a plane esponding to z = 3.5 m (which is where this high pressure region is rring), the most forward row of seat headrests lies at approximately 4.3 m. Consequently, as the strategy has been chosen to only place r sensors at the seat headrest locations, no error sensors have been ed forward of this front row of seat headrests. However, J_{pSOO} is uated as the linear average of the pressures over the head height e over the entire length of the passenger cabin, and this average is efore heavily weighted by this forward region of high pressure. If instead chooses to neglect the pressures over the first two rows of thirty rows over which the pressure has been evaluated (therefore ng the evaluation plane extend from z =4.1 m to z = 12.5 m, which l includes all the seated head locations) then a new figure, J_{pS6O}, be calculated. This is the average pressure over the modified grid by 20 points. When this is done for the present case then the ction in J_{pS6O} is 7.0 dB, compared to a reduction in J_{pSOO} of dB. Thus J_{pS6O} appears to be a better indication of the ctiveness of the active control system at the second harmonic ency. This point shall be reiterated throughout the results of section as the reductions in both J_{pSOO} and J_{pS6O} shall be quoted any of the cases considered. The substantial differences between and J_{pSOO} will help to indicate the much more localized nature of eductions around the error sensors for the second harmonic frequency for the fundamental frequency, where it was not found necessary to his modified J_{pS6O} measure of control system effectiveness.

7.3.2 The effect of the number of secondary sources

Now the 48 sensor locations used above will be kept identical and the same procedure as was followed in Section 7.2 will be adopted to determine how many secondary sources are required to produce a similar level of reduction to that obtained using 24 sources.

First introducing the 4 sources having the strongest strengths according to Table 7.3, i.e., sources A1, C1, B2, A3, a reduction in J_{p600} of 3.0 dB is obtained, although J_{p48} only reduces by 3.9 dB. The pressure fields resulting from this combination of sources and sensors are shown in Figures 7.17. By comparing the J_{p600} reductions obtained from the 24 source and 4 source system it would suggest that using 4 sources is better than using 24, but comparing the pressure fields does not support this conclusion. The reason is the previously mentioned region of high pressure in the propeller plane which the 4 source system in fact attenuates to a greater degree than the 24 source system. However, the reduction in J_{p560} for the 4 source case is only 3.1 dB, and therefore on this basis the 24 secondary source system is definitely a preferable choice over the 4 secondary source system.

Had the 4 weakest sources been chosen from Table 7.3, i.e., sources L4, I1, G1 and F2, then a reduction in both J_{p600} and J_{p48} of only 0.1 dB would have resulted. Therefore the strategy shall again be chosen to introduce the secondary sources in order of decreasing strength from Table 7.3.

Table 7.4 lists the results of minimising J_{p48} by using 4, 8, 12, 18 and 24 secondary sources introduced according to this criterion and the resulting pressure fields for the 8, 12 and 18 source cases are shown in Figures 7.18 to 7.20 respectively. The general conclusion to be drawn from these results is that, with these source arrangements, it appears to be slightly advantageous to use the larger numbers of secondary sources. For example, the system using twenty-four secondary sources does achieve a reduction in J_{p48} of 9.1 dB, and a reduction in J_{p560} of 7.0 dB. However, if the number of sources were to be increased still

further then whilst the J_{p48} reduction may continue to increase, it is likely that the corresponding J_{ps60} increase would be negligible, and that this value may even increase due to the reasons given in Section 7.2.2. Another observation which can be made from these results compared to the fundamental results is the relative importance of the forward secondary sources compared to those in the aft half of the cabin. Choosing the 12 secondary sources closest to the propeller plane (A1, A2, A3, A4, B1, B2, B3, B4, C1, C2, C3, C4) and minimising J_{p48} results in a reduction in J_{p48} of 5.9 dB, a reduction in J_{ps60} of 5.0 dB and an increase in E_p of 4.4 dB. However, choosing 12 sources arbitrarily distributed along the length of the cabin (A1, B3, C2, D4, E1, F3, G2, H4, I1, J3, K2, L4) and again minimising J_{p48} gives a reduction in J_{p48} of 3.7 dB, a reduction in J_{ps60} of 2.5 dB and a reduction in E_p of 0.1 dB. These results suggest that the shell structural response is exciting the acoustic field over a smaller area of the shell wall than at the fundamental frequency, the excitation being concentrated around the propeller plane.

7.3.3 The use of secondary sources concentrated in the plane of the propeller

If twelve 0.25 m square secondary sources are placed in a grid, centred on the point of maximum external applied pressure ($\theta = 85^{o}$, $z = 3.5$ m) as shown in Figure 7.21 [*N.B.* These sources were not included in the initial choice of 48 possible source locations.] then minimising J_{p48} results in a reduction in J_{p48} of 5.7 dB, a reduction in J_{ps60} of 5.2 dB and an increase in E_p of 4.2 dB. The pressure fields obtained for this situation are shown on Figure 7.22. If, as it appears to be, the primary source distribution can be considered as compact, then work quoted in reference [7] has indicated that placing both the secondary sources and the error sensors close to the primary source distribution can achieve appreciable global reductions. To check this the 12 sources of Figure 7.21 can again be used, and J_{p20} can be minimised using the 20 sensors shown on Figure 7.23 where each of the sensors is placed 0.03 m from the internal cylinder surface. The resulting reduction in J_{p20} is 33.3 dB, and the reduction in J_{ps00} is

4.1 dB with a reduction in E_p of 4.4 dB. Thus the method succeeds in producing a volume averaged reduction. However, Figures 7.24 show the resulting pressure field over the head height plane, and it is apparent that these reductions are due almost entirely to very large, but highly localised reductions close to the propeller excitation of the shell. This could be a useful feature in some instances, but in the present case reductions over most of the forward half of the 600 point grid are ideally required in order to sufficiently "even out" the sound field over the seated head height plane. Consequently, combinations of the original choice of sources and sensors shall be used for the remainder of these results.

7.3.4 The effect of the number of error sensors

The results presented above have demonstrated the effect the number of secondary sources has on the reductions which can be achieved at the second harmonic frequency. It is now required to investigate the effect of the number and locations of the error sensors. For all of these results the 8 secondary sources of Figure 7.18 will be used. Using these sources, a reduction in $J_{p_{2oo}}$ of 1.5 dB and a reduction in $J_{p_{2eo}}$ of 4.6 dB was achieved when all 48 sensors were used. As with the fundamental frequency, the first reduced number of sensors to be tried will be 12, the locations of which are shown on Figure 7.25(a). The pressure fields resulting from minimising $J_{p_{12}}$ over these sensors are shown in Figures 7.25(b) to (e). The reduction in $J_{p_{12}}$ is 8.3 dB, but $J_{p_{2oo}}$ increases by 10.7 dB, $J_{p_{2eo}}$ increases by 10.4 dB and E_p increases by 10.4 dB that is, the average pressure is substantially increased. From these plots the highly localized nature of the reductions around the sensors can be seen. This is to be compared with Figures 7.11(b) to (e) which show the results of minimising $J_{p_{12}}$ over the same 12 sensors but at the fundamental frequency. The comparison of these plots implies the need for many more sensors at the second harmonic frequency in order to produce such even reductions over the head height plane, although of course with a comparable number of sources the absolute levels of reduction at the second harmonic frequency are likely to be less than

those obtained at the fundamental frequency. If J_{p24} is minimised at the 24 sensor locations shown in Figure 7.26(a), again using the 8 secondary sources of Figure 7.16, then the pressure fields of Figures 7.26(b) to (e) result, with a reduction in J_{p24} of 7.2 dB, a reduction in J_{pSOO} of 1.5 dB, a reduction in J_{pS6O} of 3.4 dB and a reduction in E_p of 0.6 dB. The residual pressure field obtained using the 24 sensors is much more acceptable than that obtained using the 12 sensors. A reduction in J_{pS6O} of 3.4 dB has occurred in this case which can be compared with an <u>increase</u> in J_{pS6O} of 10.4 dB for the 12 sensor case.

However, looking at the pressure fields of Figures 7.26 it is seen that most of the reduction in J_{pS6O} is accounted for by reductions in the forward half of the head height plane, with the rear half being largely unaltered by the minimisation of J_{p24}. Were this a problem then the error sensors could be weighted, and more emphasis could be placed on reducing the pressure at these rear locations. However, looking at the primary field at the second harmonic it is apparent that the rear half of the cabin is of the order of 15 dB quieter than the forward half. It is therefore of less consequence that the active control is not appreciably reducing the pressures in this rear region. Indeed, use can be made of this fact by placing all 24 sensors in the forward half of the cabin, as shown in Figure 7.27(a). On minimising J_{p24} using these 24 sensors the pressure fields of Figures 7.27(b) to (e) result, with an associated reduction in J_{p24} of 12.7 dB, a reduction in J_{pSOO} of 0.7 dB, a reduction in J_{pS6O} of 4.3 dB, and an increase in E_p of 2.2 dB. Thus, using this arrangement has produced an average reduction over the 24 sensors 5 dB higher than with the previous case. Furthermore, these increased reductions are now concentrated in the forward half of the plane, where they are most needed, and this strategy has not substantially increased the levels in the rear of the cabin where there are no error sensors.

.4 <u>A Single Active Noise Control System for the Suppression of both the Propeller Blade Passage Fundamental and Second Harmonic Frequencies</u>

The results of Sections 7.2 and 7.3 have demonstrated the potential of applying active noise control at the propeller blade passage

damental and second harmonic frequencies respectively. However, the hod used to determine the source/sensor locations in each case was a ction of the system's performance at each of the harmonics ividually, leading to different combinations of sources and sensors each of the harmonics. The problem addressed in this section is: a single, practically sized, system be used to achieve useful uctions at both the fundamental and second harmonic frequencies?

Comparing the results of Sections 7.2 and 7.3 it is apparent that, at fundamental frequency, firstly fewer sources and sensors are required obtain substantially better average reductions over the head height he when compared to the second harmonic frequency, and secondly the ct placement of these sources and sensors is not so critical as for second harmonic system. This suggests that a system aimed at ucing both the fundamental and second harmonic pressure components uld be designed with the main aim of reducing the overall sound ssure levels at the second harmonic frequency as it is this objective ch is most difficult to achieve (and, on an A-weighted basis, it is o the sound pressure levels at the second harmonic frequency which d to dominate the experimentally measured seated head height sound lds). In other words, a system designed primarily to achieve large uctions at the second harmonic frequency is likely to also yield large uctions at the fundamental frequency, whereas a system designed marily to achieve large reductions at the fundamental frequency is not likely to yield similarly large reductions at the second harmonic quency.

Bearing this in mind, a 16 secondary source and 32 error sensor tem has been designed on the basis of the results given in Tables 7.1 7.3 for the previously considered 24 source/48 sensor fundamental and ond harmonic systems respectively. The method of choosing the sixteen ondary sources was as follows:- the first 12 secondary sources were sen as those sources whose amplitudes were greatest in the second monic 24 by 48 system (see Table 7.3), and the remaining 4 secondary rces were chosen as those sources whose amplitudes were greatest in fundamental 24 by 48 system (see Table 7.1) but which had not already n included in the initial twelve secondary sources. Thus, the sixteen sen secondary sources were A1, A3, B2, B4, C1, C3, D2, D4, E1, E3, F4,

, J2, J4, K3 and the locations of these sources on the shell
e are indicated in Figure 7.28(b). The 32 error sensor locations
hosen such that they were concentrated in the forward half of the
eight plane in order to ensure reduction over the whole of this
for the second harmonic frequency. Thus 24 of the error sensors
laced, one per headrest, at each of the seats in the front six rows
cabin. The remaining 8 error sensors were spaced fairly evenly
he rear six rows of seats to ensure that increases in sound
re level, particularly at the fundamental frequency, did not
The chosen 32 error sensor locations are shown on Figure 7.28(c).

though the error sensors described above have all been placed in
me head height plane as was used for the results of sections 7.2
3 (see Figure 7.1), and therefore no attempt has been made to
the regions of cancellation in a vertical sense, it will still be
to see how localized the reductions are in this vertical
ion. Consequently the results of this section present pressure
evaluated over three horizontal planes, spaced apart vertically by
with the central plane corresponding to the head height plane in
the error sensors have all been located. Also, whilst this active
l system has been chosen to assess the possibility of using a
system to simultaneously control both the fundamental and second
ic components of the pressure field, the results presented have
been decomposed into the individual frequency components for
y.

gures 7.29(a) to (d) show the effect of applying the 16 by 32
at the blade passage fundamental frequency. As might be expected
he results of Section 7.2, large reductions occur over virtually
e regions of the error sensor plane (plane "B" in the Figures), the
egions of pressure increase being those areas of initially very low
pressure level. Over this plane a reduction in $J_{p_{800}}$ of 14.1 dB
. This can be compared with an average reduction at the 32 error
s, $J_{p_{32}}$, of 19.2 dB and a reduction in the total acoustic potential
, E_p, of 2.4 dB. The results in the planes "A" and "C" show
r trends to those in plane "B" with reductions in $J_{p_{800}}$ of 11.0 dB
.3 dB respectively and with no unacceptable regions of pressure
se over either of the planes. The secondary source strengths

red to minimise $J_{p_{32}}$ for this fundamental frequency case are listed
ble 7.5.

igures 7.30(a) to (d) show the effect of applying the 16 by 32
m at the blade passage second harmonic. For this case a reduction
$_{32}$ of 11.6 dB occurs, but E_p <u>increases</u> by 2.2 dB. The secondary
e strengths which minimise $J_{p_{32}}$ at this second harmonic frequency
isted in Table 7.5. The reduction in $J_{p_{600}}$ over the error sensor
(plane "B") is 0.8 dB and the reduction in $J_{p_{560}}$ is 4.6 dB, with
largest reductions occurring over the forward half of the plane.
rence to Figure 7.30(b), the sound field following the application of
ve control, reveals a general "levelling off" of the sound field over
plane. The results in the planes "A" and "C" of Figures 7.30 are
quite so encouraging. Over plane "A" minimising $J_{p_{32}}$ results in a
ction in $J_{p_{600}}$ of 0.1 dB and a reduction in $J_{p_{560}}$ of 1.1 dB, and over
"C" an <u>increase</u> in $J_{p_{600}}$ of 1.0 dB and a decrease in $J_{p_{560}}$ of
dB result. Note that in plane "C" an increase in sound pressure
occurs not only in the rear half of the plane, but also along a
ow region in the forward half of the plane. However, reference to
re 7.30(a) shows that this increase occurs along a ridge of initially
pressure.

Propeller Synchrophasing and Active Noise Control

The previous two sections have demonstrated the potential of using
ve noise control to reduce propeller induced cabin noise. Another
ible method for reducing the interior noise levels is synchrophasing,
, the relative phasing of the two propellers. This has been the
ect of several recent investigations, e.g, [49,85]. Synchrophasing
been demonstrated to be a potentially powerful tool for reducing both
ctural vibration levels and internal noise levels, and it seems
ly that it will become an increasingly popular option on propeller
ven aircraft as it becomes possible to control the synchrophase angles
iner tolerances. This possibility could be used to advantage if an
ive noise control system is also incorporated, because a combined
ive noise control/synchrophasing system could be envisaged, whereby

propellers are considered as extra secondary sources whose phases, not amplitudes, are controlled together with the amplitudes and es of the loudspeaker secondary sources in order to minimise the en cost function. However, a coupled control system may not be ssary if the minimum value of the cost function occurs at the same hrophase angle when both active noise control and synchrophasing are ied simultaneously compared to when synchrophasing is applied e. If this is the case, then the cost function would be minimised lly well either by optimising the synchrophase angle, and then ing this constant whilst optimising the secondary source strengths of active noise control system, or, alternatively, by formulating the misation as the full coupled problem.

The results of this section will investigate these possibilities for the fundamental frequency and the second harmonic frequency. For harmonics a 6 source/24 sensor and a 12 source/24 sensor system have chosen. The sources and sensors used are listed in Figure 7.31. each case the port propeller excitation has been taken as that used he previous sections, and the starboard propeller excitation is lled as an identical pressure field, but shifted around the shell umference by 180° and with the appropriate phase difference. The s show the effects on the primary E_p and J_{p24} of varying the relative t angle phases in 5 degree steps. Also, at each of the 5 degree s, J_{p24} has been minimised using either 6 or 12 secondary sources, the plots show the residual values of E_p and J_{p24} following this misation.

Figures 7.32 and 7.33 show the results for the fundamental uency. Because of the relatively low modal density at this uency, and because of a rather fortuitous choice of source and sensor tions, the results for E_p and J_{p24} both show appreciable ctions. However, more importantly from the present point of view is result that, when 12 secondary sources are used, the residual value he cost function, J_{p24} varies by less than 2 dB over the entire range ynchrophase angles, even though the value of J_{p24} due to the primary d alone varies by up to 11 dB. This is believed to occur because, at fundamental frequency, less than 10 modes can be assumed to be nating the sound field. Varying the synchrophase angle merely varies

elative contributions of the various modes, but the number of antly contributing modes will still remain about the same. quently, the 12 secondary sources are sufficient to ensure that ver the relative modal contributions all the dominant modes can be iently driven by the secondary sources, and the level of the ual cost function is insensitive to the synchrophase angle. In ast, when only 6 secondary sources are used this situation is not ed, and the residual value of J_{p24} does vary with the synchrophase . This latter case also proves to be true for the second harmonic n, as shown in Figures 7.34 and 7.35, where for both the 6 source 2 source systems results the residual value of J_{p24} demonstrates a variation with the synchrophase angle. The reasons for this are me as those presented above, only at the second harmonic frequency imately 70 acoustic modes can be assumed to be dominantly buting and therefore even the 12 source system results show an iable variation with synchrophase angle. However, the main e of these results is the property that the minimum value of the unction when active noise control is applied occurs at imately the same synchrophase angle as that for which the cost on is minimised by the synchrophasing operating alone.

these results are subsequently shown to be representative of what in practice then the application of synchrophasing and active control together should be somewhat simplified. Firstly, the s have indicated the lack of need for a combined active noise l/synchrophasing system. From the data presented on Figures 7.32 5 it would prove just as effective to adapt to the optimum phase angle which minimises the cost function, and then to fix gle before turning the active noise control adaption on. y, provided enough secondary sources are used, the results d at the fundamental blade passage frequency are relatively tive to the synchrophase angle. Consequently, no account need be f the value of the cost function for this blade passage harmonic e optimum synchrophase angle is being set, and efforts can be rated on minimising the value of the cost function for the second c frequency only (assuming that it is only the first two blade harmonic frequencies which are of interest.) However, note that ng to Figures 7.32 to 7.35 the optimum synchrophase angle is

y the same for the two frequencies. This is not a feature which
en identified as being true for real aircraft, and this therefore
some doubt on the validity of the model when it is used to
igate the effects of synchrophasing.

nclusions

e results of this chapter have demonstrated the possible
ation of active noise control to the practical problem of reducing
ler induced cabin noise. It has been predicted that reductions in
erage pressure over a seated head height plane of at least 16 dB
achieved using a system containing 24 sources and 48 sensors and
ing at 88 Hz. However, the spatial extent of the reductions
the error sensors has been shown to decrease rapidly with
sing frequency. At the second harmonic frequency, 176 Hz, it has
redicted that the same 24 source/48 sensor system will only produce
ions in the average pressure over a similar head height plane of
der of 7 dB although it has also been shown that this system may
e localized reductions of up to 35 dB.

ese conclusions have been based on the work presented in Sections
d 7.3 of this chapter. However, it must be remembered that these
nclusions based on a rather limited set of results using a fixed
possible source and sensor locations. This approach has been
itated by the time involved in computing and analysing each set of
s. It is possible that with more time new source and sensor
ions could be found which provide larger attenuations whilst using
ources and/or sensors. The danger in performing this type of
and sensor location "optimisation" is that the improved reduction
epend on some idealization of the theoretical model which in
ice does not occur. By constraining the sources and sensors to
certain "physically reasonable" locations it is hoped that the
ilities for this type of error should be greatly reduced. The
lness of the theoretical model at this stage, therefore, has been to
t the approximate levels of attenuation which may be achieved at
of the propeller blade passage harmonics, to give an idea of how
ources and sensors are likely to be needed in order to achieve

se reductions, and to recommend whether global or local control of the
nd field should be implemented. There are still effects which remain
be investigated using this idealized model. One of the most
portant of these is the extent of the regions of reduction in the
tical plane, as all the results of Chapter 7 have involved the error
sors being set in one plane. Whilst this strategy appears to be
quate for the fundamental frequency, results obtained for the blade
sage second harmonic frequency have demonstrated its possible
rtfalls, even over vertical distances as short as 0.2 m. However, it
recommended that before this type of model is used to make more
cific recommendations about the exact nature of the active noise
trol system required, these initial results should be validated by
parison with the results of actual flight experiments.

1 The locations and source strengths of the 24 sources used for the fundamental frequency 24 source/48 sensor active control system. (All sources modelled as 0.25 m by 0.25 m pistons)

ce	rms displacement ($\times 10^{-5}$ m)	Order of decreasing source strength
	1.057	1
	0.085	24
	0.783	2
	0.340	5
	0.339	6
	0.198	11
	0.425	3
	0.208	10
	0.094	23
	0.179	13
	0.132	21
	0.208	8
	0.151	18
	0.160	16
	0.161	15
	0.274	7
	0.160	17
	0.151	19
	0.208	9
	0.198	12
	0.132	20
	0.377	4
	0.094	22
	0.170	14

TABLE 7.2 The effect of minimising the sum of the squared pressures at up to 48 error sensor locations (Figure 7.2(a)) using up to 24 secondary sources (Figure 7.2(b)). The frequency is the blade passage fundamental of 88 Hz.

(a) Predicted reductions using all 48 error sensors of Figure 7.2(a).

Number of sources	Source locations	Reduction in J_{p48} (dB)	Reduction in J_{p600} (dB)	Reduction in E_p (dB)
4	A1,B2,D2,K3	5.8	5.0	0.8
6	+B4,C1	6.5	5.9	-0.6
8	+H4,F4	9.0	8.2	0.1
12	+J2,D4,C3,J4	15.9	15.1	5.5
18	+E3,L4,H2,G3,I1,G1	23.3	16.8	1.0
24	+K1,I3,F2,L2,E1,A3	26.1	16.3	1.0
12	A1,A2,A3,A4,B1,B2, B3,B4,C1,C2,C3,C4	3.7	2.6	-12.0
12	A1,B3,C2,D4,E1,F3 G2,H4,I1,J3,K2,L4	19.7	17.7	7.0

(b) Predicted reductions using the eight secondary sources A1, B2, D2, K3, B4, C1, H4 and F4 of Figure 7.2(b).

Number of sensors (L)	Sensor locations	Reduction in J_{pL} (dB)	Reduction in J_{p600} (dB)	Reduction in E_p (dB)
12	B1,C4,D1,E4,F1, G4,H1,I4,J1,K4, L1,M4	11.8	6.7	-3.8
15	+F3,F4,G3	10.7	7.6	-1.6
24	B1,B4,C2,C3,D1, D4,E2,E3,F1,F4, G2,G3,H1,H4,I2, I3,J1,J4,K2,K3, L1,L4,M2,M3	8.9	7.9	-0.1

TABLE 7.3 The locations and source strengths of the 24 sources used for the second harmonic frequency 24 source/48 sensor active control system. (All sources modelled as 0.25 m by 0.25 m pistons)

Source	rms displacement ($\times 10^{-5}$ m)	Order of decreasing source strength
A1	1.783	1
A3	0.670	4
B2	0.858	3
B4	0.670	5
C1	0.868	2
C3	0.387	7
D2	0.113	14
D4	0.453	6
E1	0.255	8
E3	0.076	18
F2	0.076	19
F4	0.057	21
G1	0.038	22
G3	0.066	20
H2	0.217	9
H4	0.113	15
I1	0.019	24
I3	0.094	17
J2	0.151	12
J4	0.189	10
K1	0.142	13
K3	0.160	11
L2	0.104	16
L4	0.038	23

TABLE 7.4 The effect of minimising the sum of the squared pressures at up to 48 error sensor locations (Figure 7.2(a)) using up to 24 secondary sources (Figure 7.2(b)). The frequency is the blade passage second harmonic of 176 Hz.

(a) Predicted reductions using all 48 error sensors of Figure 7.2(a)

Number of sources	Source locations	Reduction in J_{p48} (dB)	J_{p600} (dB)	J_{p560} (dB)	E_p (dB)
4	A1,C1,B2,A3	3.9	3.0	3.1	1.0
8	+B4,D4,C3,E1	5.6	1.5	4.6	-1.3
12	+H2,J4,3,J2	7.3	1.8	5.8	-1.4
18	+K1,D2,H4,L2,I3,E3	8.6	1.3	6.6	-2.0
24	+G3,F2,F4,G1,L4,I1	9.1	1.6	7.0	-1.9
12	A1,A2,A3,A4 B1,B2,B3,B4 C1,C2,C3,C4	5.9	2.2	5.0	-4.4
12	A1,B3,C2,D4 E1,F3,G2,H4 I1,J3,K2,L4	3.7	2.0	2.5	0.1
12	Propeller plane	5.7	2.6	5.2	-4.2

(b) Predicted reductions using the eight secondary sources A1,C1,D2, A3,B4,D4,C3 and E1 of Figure 7.2(b).

Number of sensors (L)	Sensor locations	Reduction in J_{pL} (dB)	J_{p600} (dB)	J_{p560} (dB)	E_p (dB)
12	B1,C4,D1,E4, F1,G4,H1,I4, J1,K4,L1,M4	8.3	-10.7	-10.4	-10.4
24	B1,B4,C2,C3 D1,D4,E2,E3, F1,F4,G2,G3, H1,H4,I2,I3, J1,J4	7.2	1.5	3.4	-0.6
24	B1,B2,B3,B4 C1,C2,C3,C4, D1,D2,D3,D4, E1,E2,E3,E4, F1,F2,F3,F4 G1,G2,G3,G4	12.7	0.7	4.3	-2.2

TABLE 7.5 The locations and source strengths of the 16 sources used for the combined fundamental and second harmonic frequency 16 source/32 sensor active control system (all sources modelled as 0.25 m by 0.25 m pistons)

Source	rms displacement ($\times 10^{-6}$ m) required to control the fundamental	rms displacement ($\times 10^{-6}$ m) required to control the second harmonic
A1	8.319	1.834
A3	0.962	0.692
B2	6.066	0.900
B4	3.745	0.798
C1	2.864	0.890
C3	1.995	0.492
D2	3.644	0.108
D4	1.209	0.352
E1	1.825	0.252
E3	3.288	0.104
F4	1.695	0.125
H2	0.088	0.120
H4	2.261	0.032
J2	4.110	0.153
J4	4.675	0.173
K3	4.470	0.248

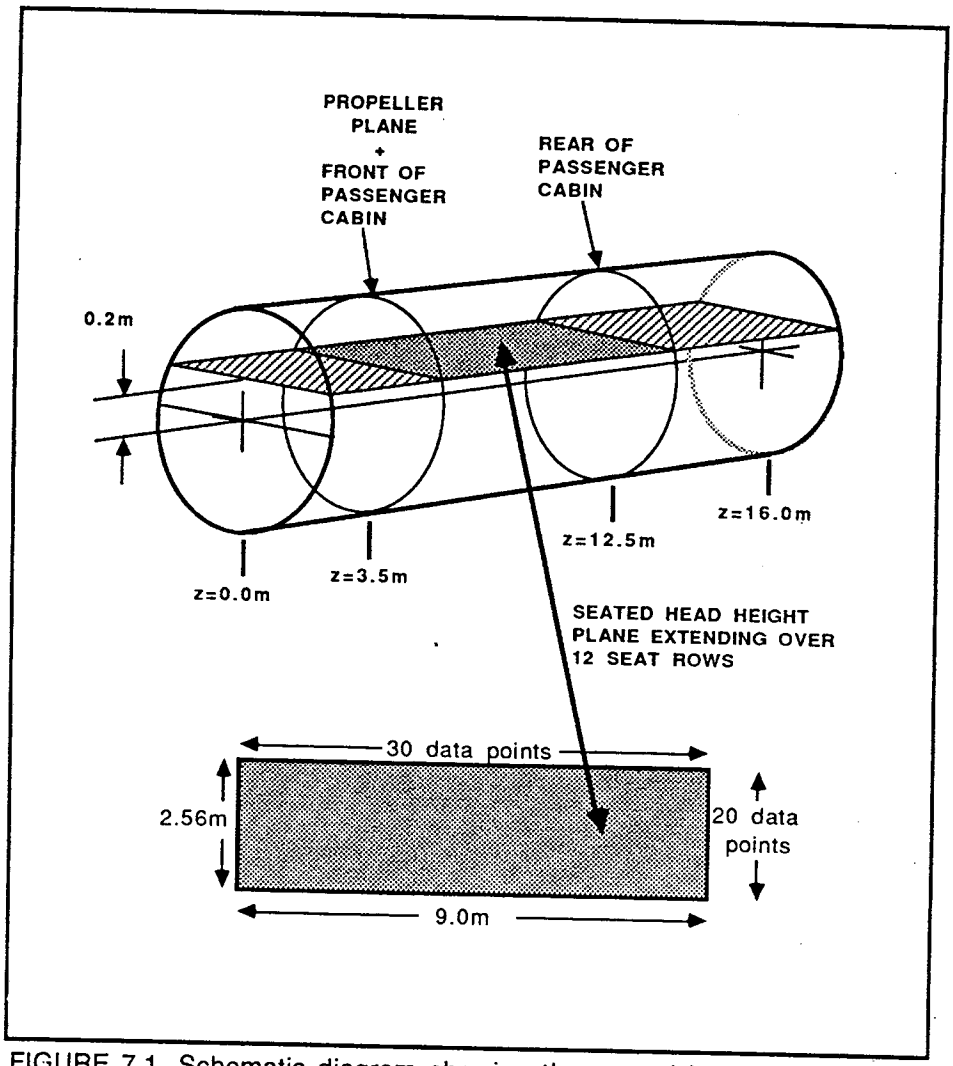

FIGURE 7.1. Schematic diagram showing the seated head height plane over which the pressure fields have been evaluated at 30 by 20 points for all the figures of Chapter 7.

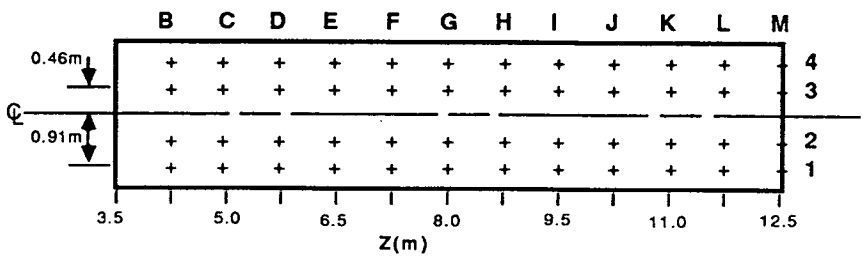

a) The choice of error sensor locations over the seated head height plane of Figure 7.1.

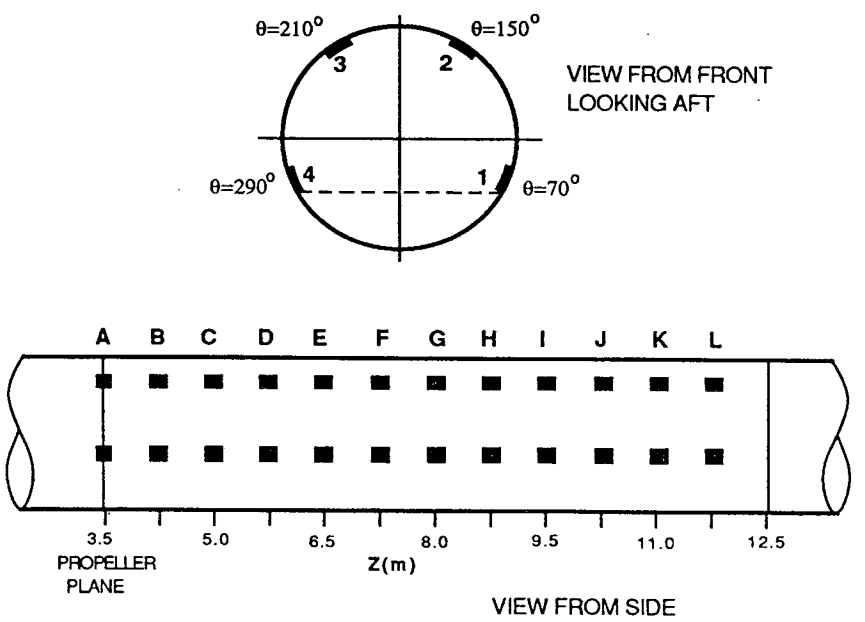

b) The choice of secondary source locations. All sources are modelled as 0.25m by 0.25m piston sources mounted flush with the shell wall.

FIGURE 7.2. Schematic diagram showing the possible locations of a) the error sensors and b) the secondary sources. Also shown are the identifying coordinates.

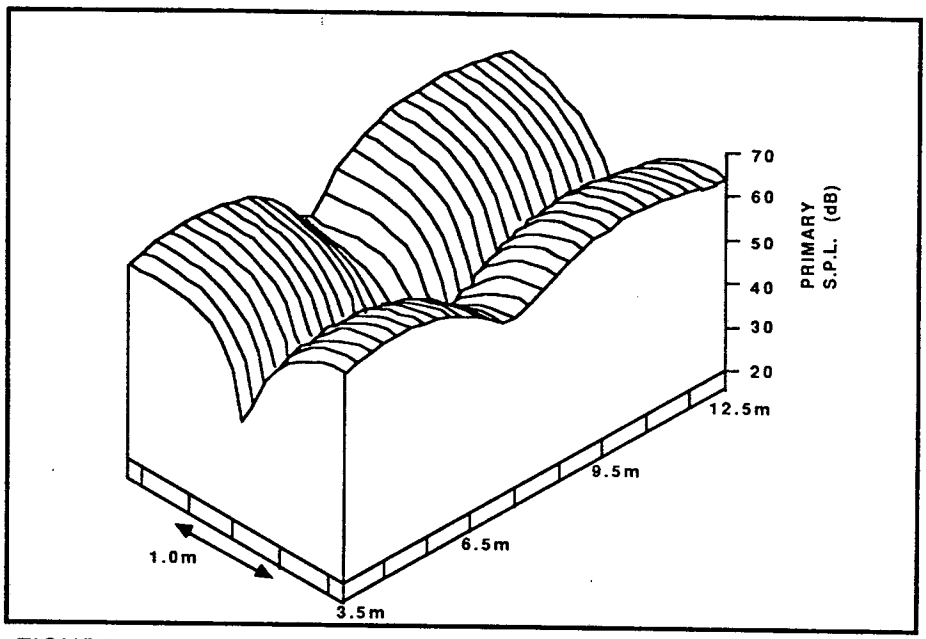

FIGURE 7.3. The pressure field in the head height plane of Figure 7.1 due to the shell structural response only. The frequency is 88Hz.

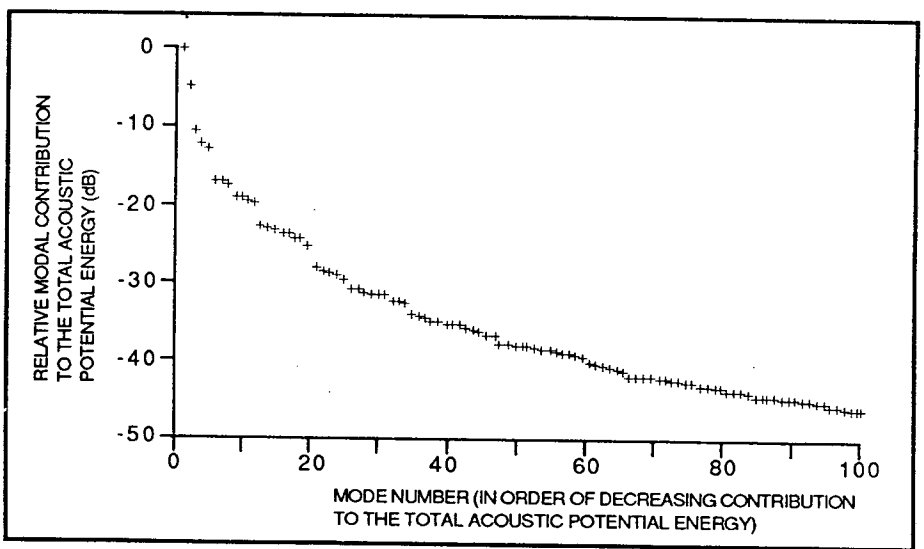

FIGURE 7.4. The relative contributions of the acoustic modes to the total acoustic potential energy when the modelled cabin sound field is excited by the shell structural response only. The frequency is 88Hz.

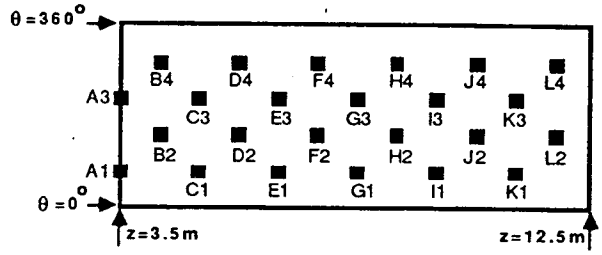

a) Diagram of the unwrapped shell showing the locations of the 24 sources used. Jp has been minimised using all 48 error sensors of Figure 7.2.

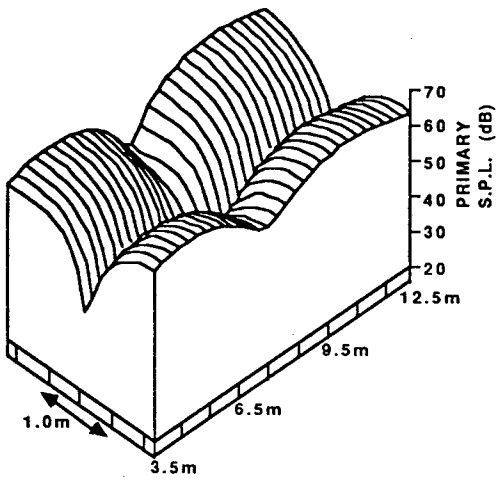

b) The pressure field over the head height plane due to the shell structural response only (primary field).

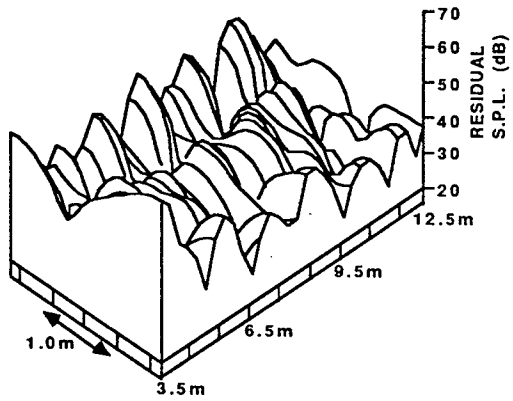

c) The pressure field over the head height plane after Jp has been minimised using the sources and sensors listed in Figure (a).

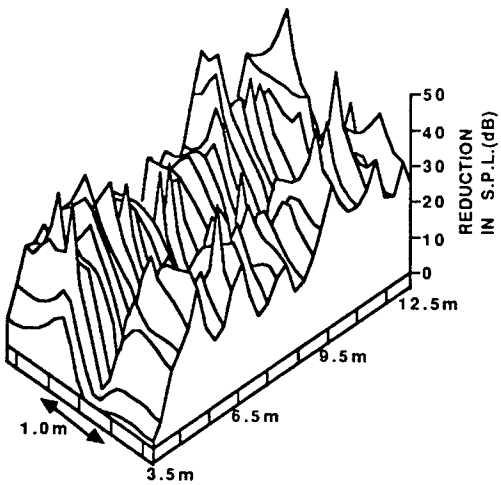

d) Areas of pressure decrease after Jp has been minimised.

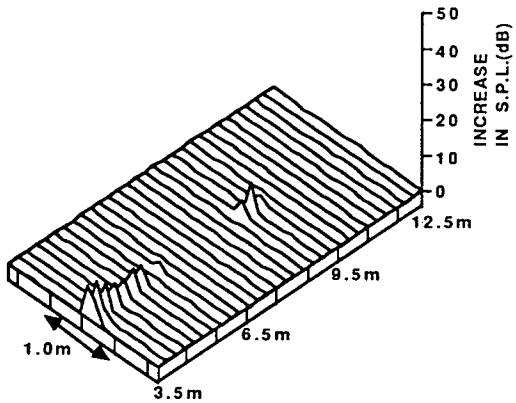

e) Areas of pressure increase after Jp has been minimised.

FIGURE 7.5. The sound pressure field in the head height plane of Figure 7.1 before and after Jp has been minimised using a 24 source/48 sensor active control system. The frequency is 88Hz.

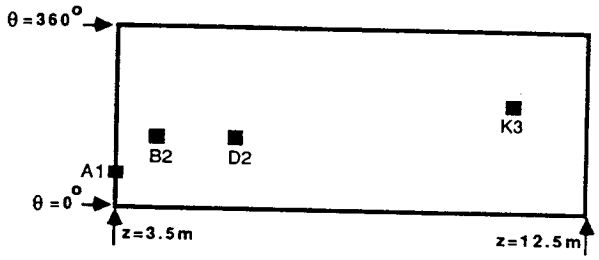

a) Diagram of the unwrapped shell showing the locations of the 4 sources used. Jp has been minimised using all 48 error sensors of Figure 7.2.

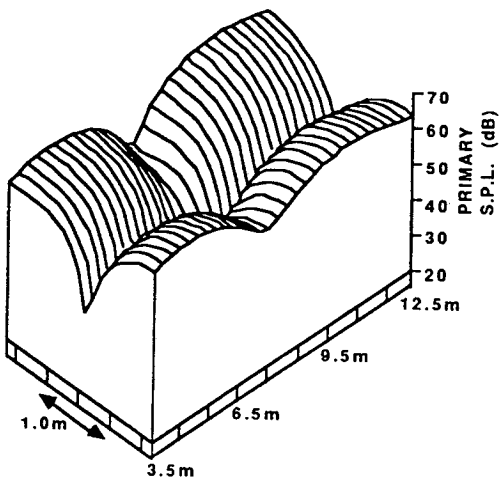

b) The pressure field over the head height plane due to the shell structural response only (primary field).

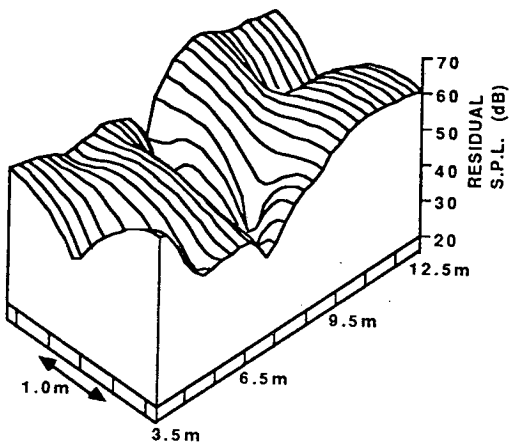

c) The pressure field over the head height plane after Jp has been minimised using the sources and sensors listed in Figure (a).

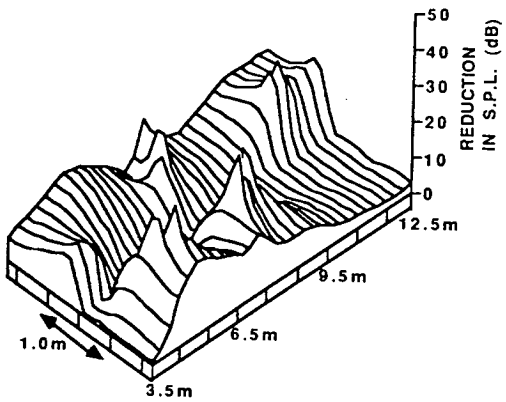

d) Areas of pressure decrease after Jp has been minimised.

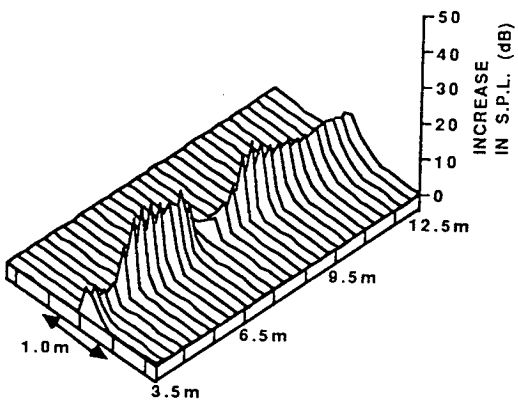

e) Areas of pressure increase after Jp has been minimised.

GURE 7.6. The sound pressure field in the head height plane of Figure 7.1. before and ter Jp has been minimised using a 4 source/48 sensor active control system. The equency is 88Hz.

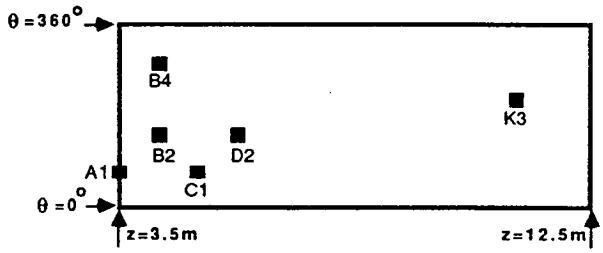

a) Diagram of the unwrapped shell showing the locations of the 6 sources used. Jp has been minimised using all 48 error sensors of Figure 7.2.

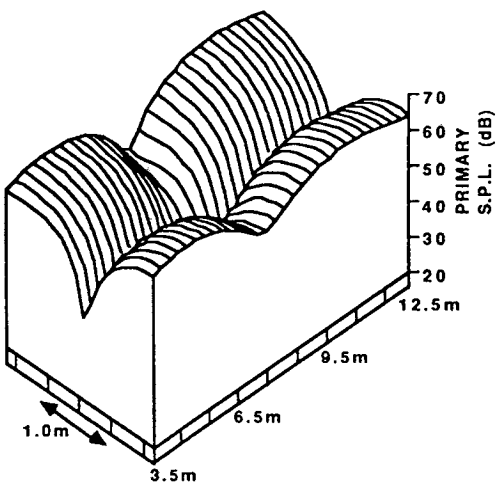

b) The pressure field over the head height plane due to the shell structural response only (primary field).

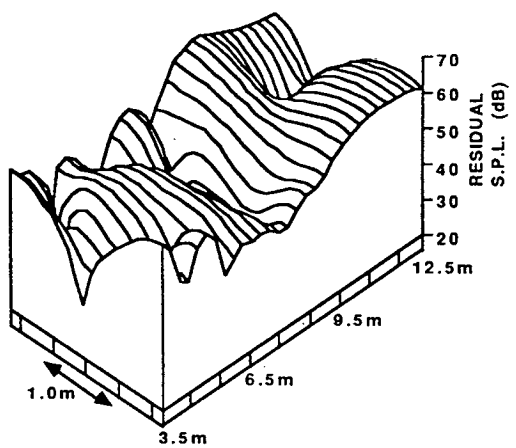

c) The pressure field over the head height plane after Jp has been minimised using the sources and sensors listed in Figure (a).

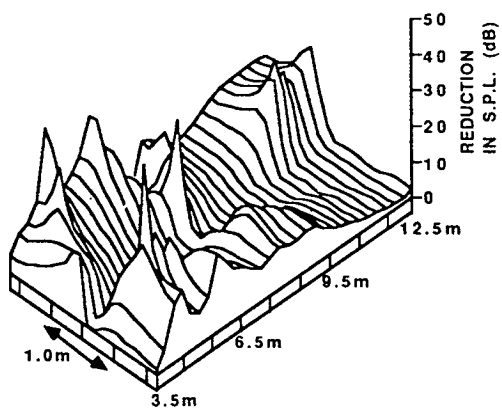

d) Areas of pressure decrease after Jp has been minimised.

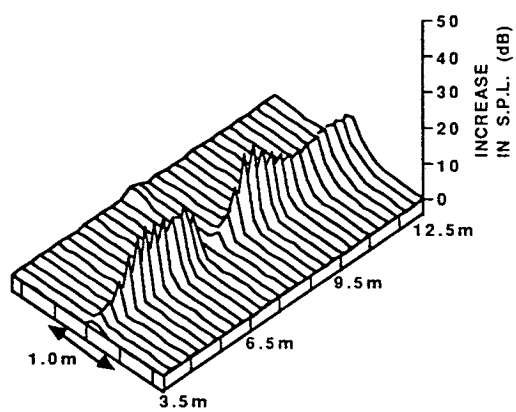

e) Areas of pressure increase after Jp has been minimised.

FIGURE 7.7. The sound pressure field in the head height plane of Figure 7.1 before and after Jp has been minimised using a 6 source/48 sensor active control system. The frequency is 88Hz.

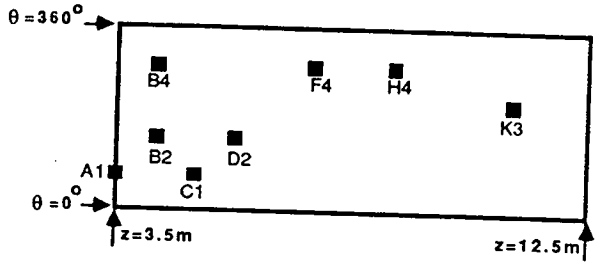

a) Diagram of the unwrapped shell showing the locations of the 8 sources used. Jp has been minimised using all 48 error sensors of Figure 7.2.

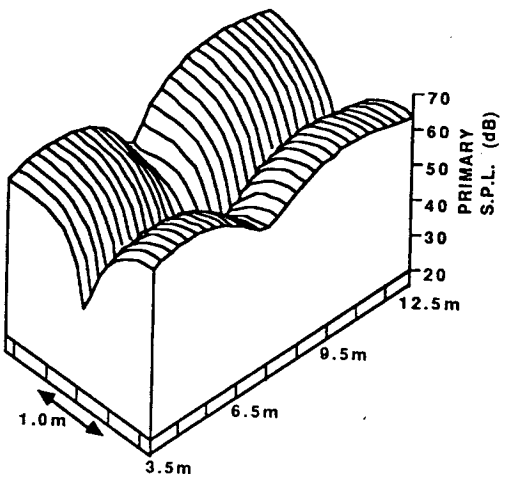

b) The pressure field over the head height plane due to the shell structural response only (primary field).

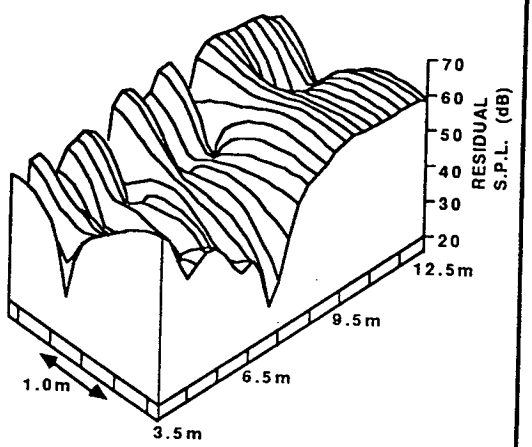

c) The pressure field over the head height plane after Jp has been minimised using the sources and sensors listed in Figure (a).

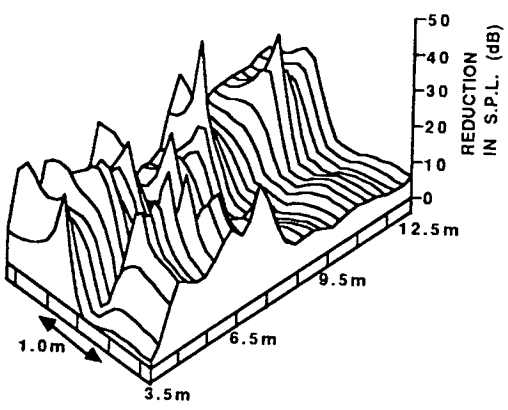

d) Areas of pressure decrease after Jp has been minimised.

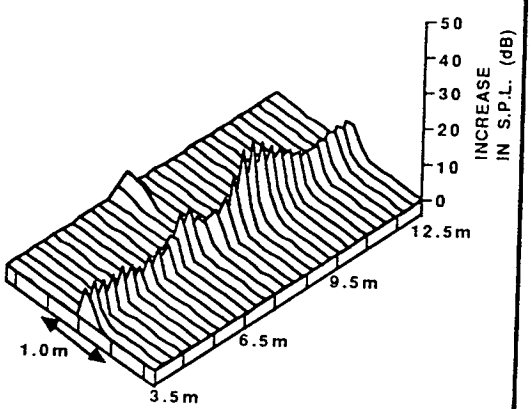

e) Areas of pressure increase after Jp has been minimised.

FIGURE 7.8. The sound pressure field in the head height plane of Figure 7.1 before and after Jp has been minimised using an 8 source/48 sensor active control system. The frequency is 88Hz.

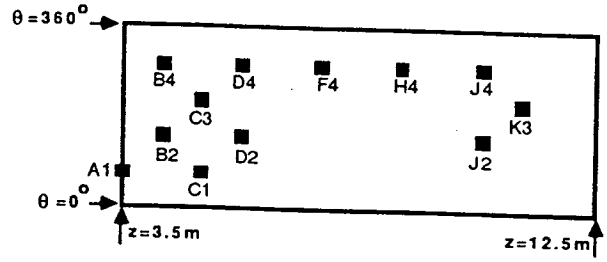

a) Diagram of the unwrapped shell showing the locations of the 12 sources used. Jp has been minimised using all 48 error sensors of Figure 7.2.

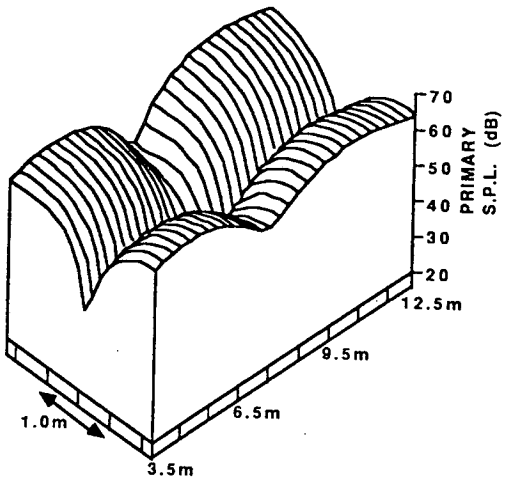

b) The pressure field over the head height plane due to the shell structural response only (primary field).

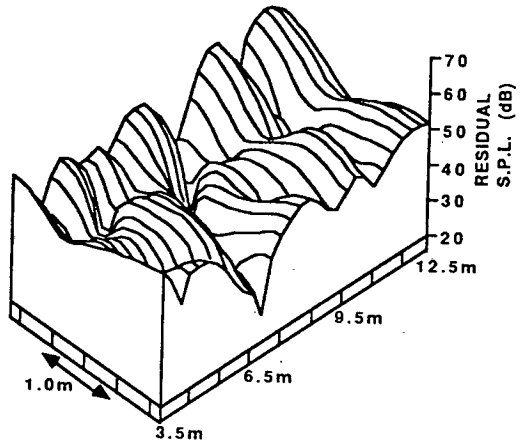

c) The pressure field over the head height plane after Jp has been minimised using the sources and sensors listed in Figure (a).

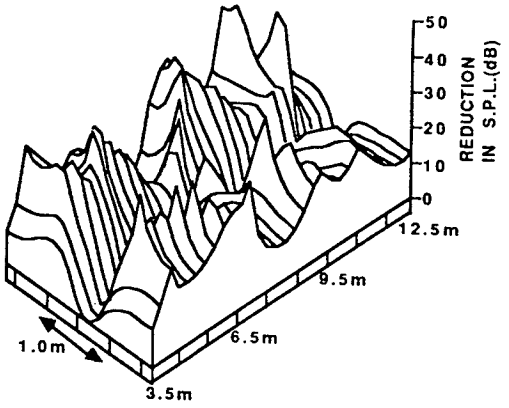

d) Areas of pressure decrease after Jp has been minimised.

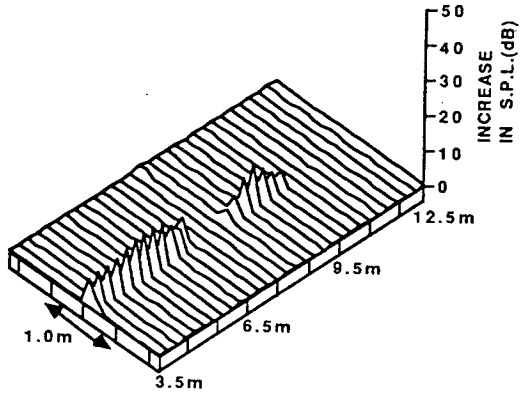

e) Areas of pressure increase after Jp has been minimised.

FIGURE 7.9. The sound pressure field in the head height plane of Figure 7.1 before and after Jp has been minimised using a 12 source/48 sensor active control system. The frequency is 88Hz.

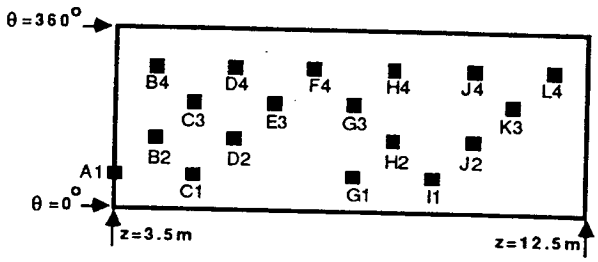

a) Diagram of the unwrapped shell showing the locations of the 18 sources used. Jp has been minimised using all 48 error sensors of Figure 7.2.

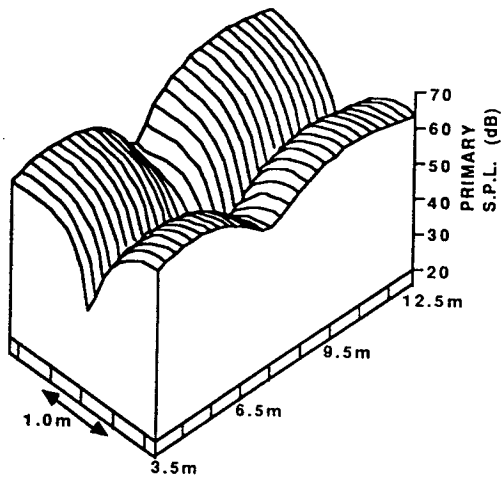

b) The pressure field over the head height plane due to the shell structural response only (primary field).

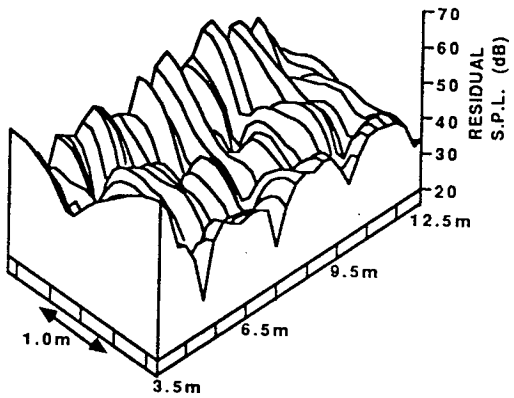

c) The pressure field over the head height plane after Jp has been minimised using the sources and sensors listed in Figure (a).

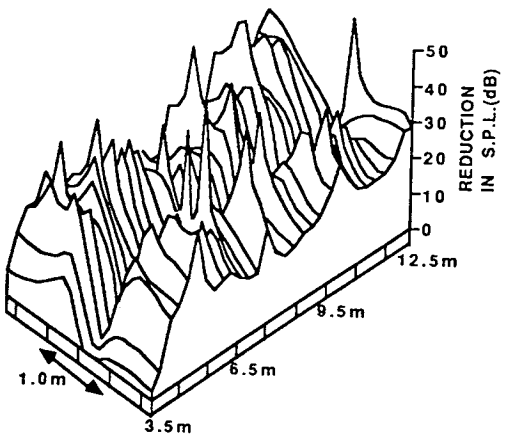

) Areas of pressure decrease after Jp has been minimised.

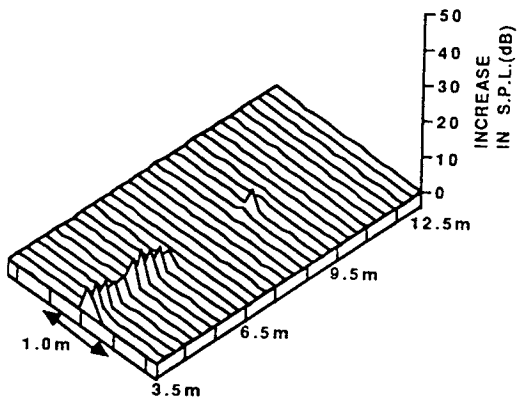

e) Areas of pressure increase after Jp has been minimised.

GURE 7.10. The sound pressure field in the head height plane of Figure 7.1 before d after Jp has been minimised using an 18 source/48 sensor active control system. e frequency is 88Hz.

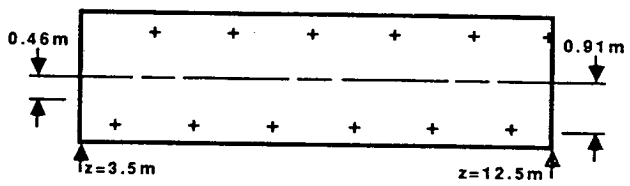

a) Diagram of the head height plane of Figure 7.1 showing the locations of the 12 sensors over which Jp has been minimised using the 8 secondary sources of Figure 7.8(a).

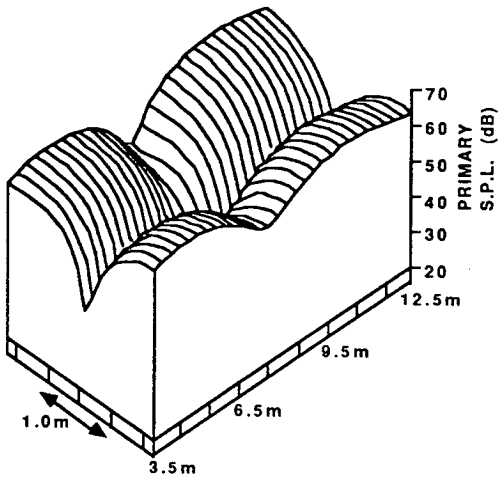

b) The pressure field over the head height plane due to the shell structural response only (primary field).

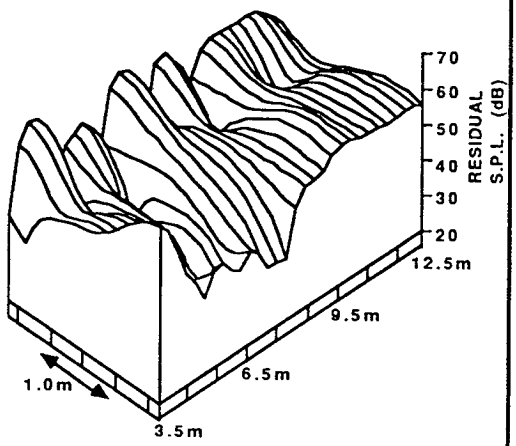

c) The pressure field over the head height plane after Jp has been minimised using the sources and sensors listed in Figure (a).

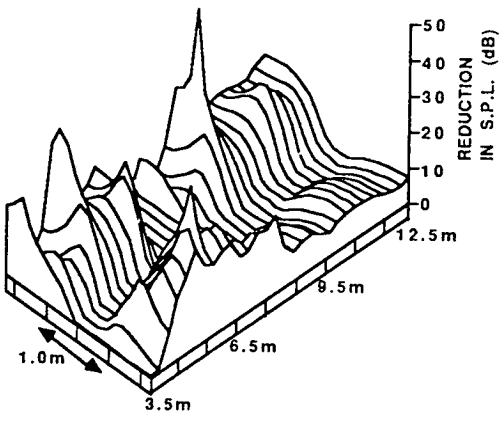

d) Areas of pressure decrease after Jp has been minimised.

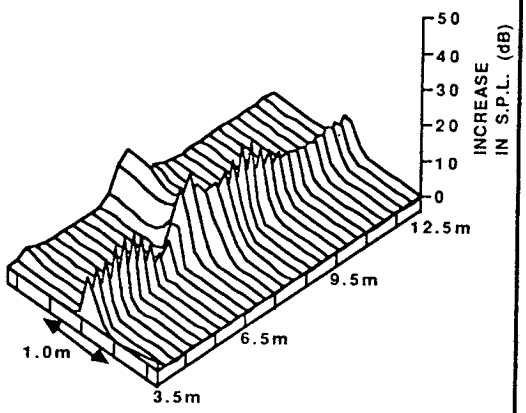

e) Areas of pressure increase after Jp has been minimised.

FIGURE 7.11. The sound pressure field in the head height plane of Figure 7.1 before and after Jp has been minimised using an 8 source/12 sensor active control system. The frequency is 88Hz.

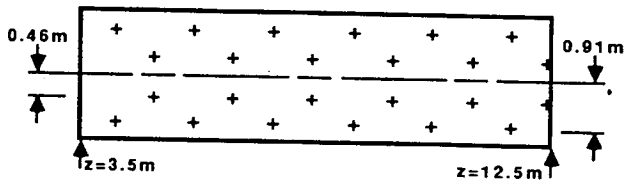

a) Diagram of the head height plane of Figure 7.1 showing the locations of the 24 sensors over which Jp has been minimised using the 8 secondary sources of Figure 7.8(a).

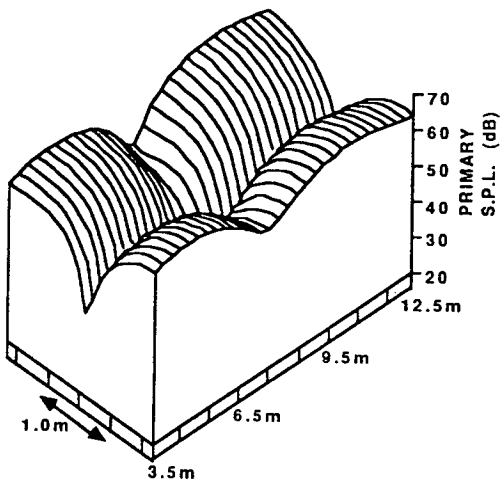

b) The pressure field over the head height plane due to the shell structural response only (primary field).

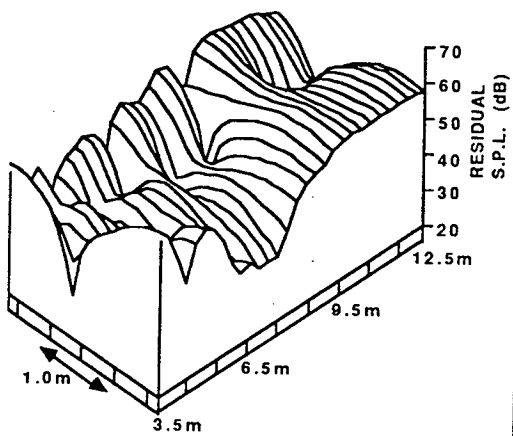

c) The pressure field over the head height plane after Jp has been minimised using the sources and sensors listed in Figure (a).

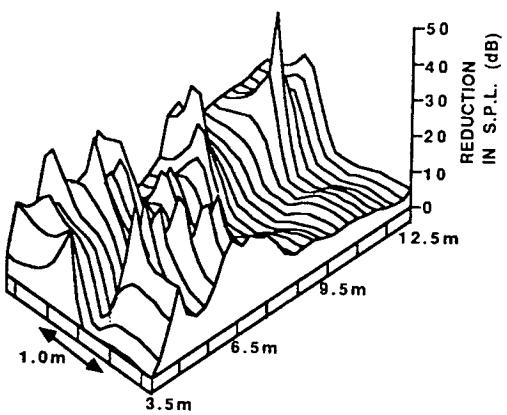

d) Areas of pressure decrease after Jp has been minimised.

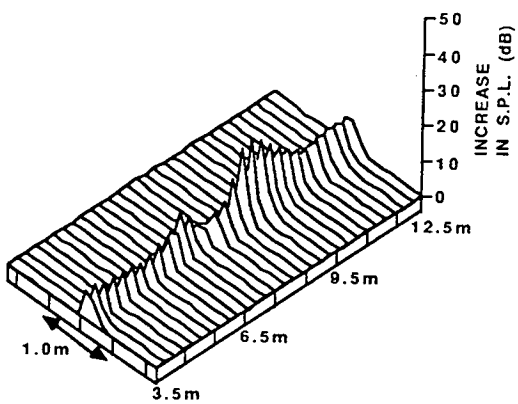

e) Areas of pressure increase after Jp has been minimised.

FIGURE 7.12. The sound pressure field in the head height plane of Figure 7.1 before and after Jp has been minimised using an 8 source/24 sensor active control system. The frequency is 88Hz

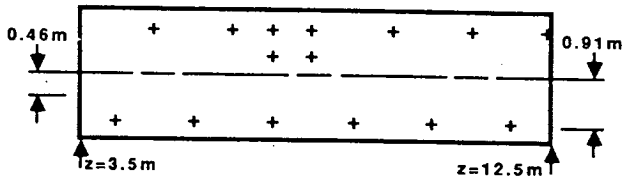

a) Diagram of the head height plane of Figure 7.1 showing the locations of the 15 sensors over which Jp has been minimised using the 8 secondary sources of Figure 7.8(a).

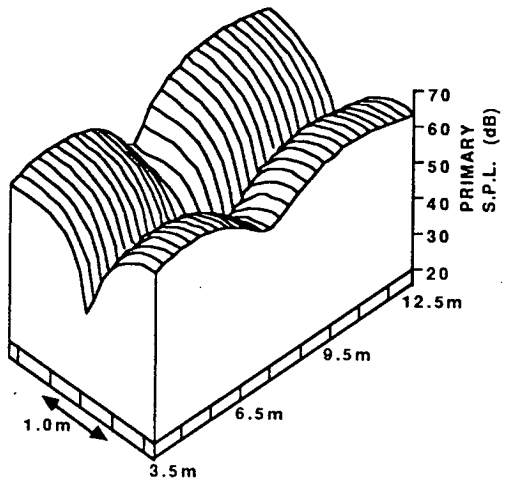

b) The pressure field over the head height plane due to the shell structural response only (primary field).

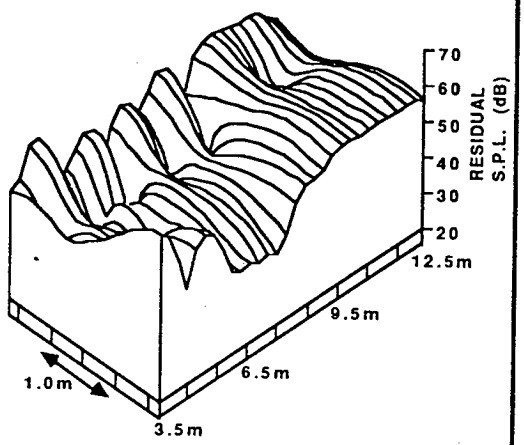

c) The pressure field over the head height plane after Jp has been minimised using the sources and sensors listed in Figure (a).

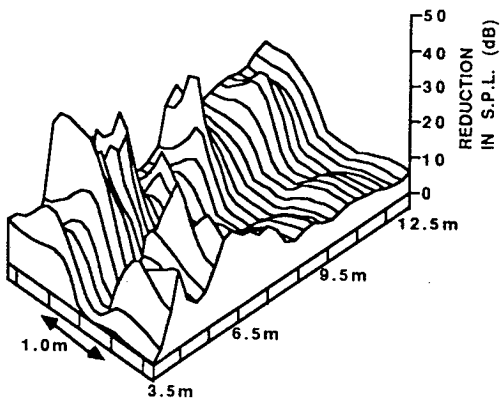

d) Areas of pressure decrease after Jp has been minimised.

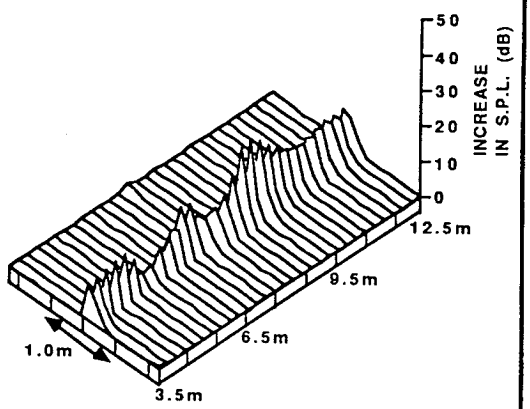

e) Areas of pressure increase after Jp has been minimised.

FIGURE 7.13. The sound pressure field in the head height plane of Figure 7.1 before and after Jp has been minimised using an 15 source/12 sensor active control system. The frequency is 88Hz

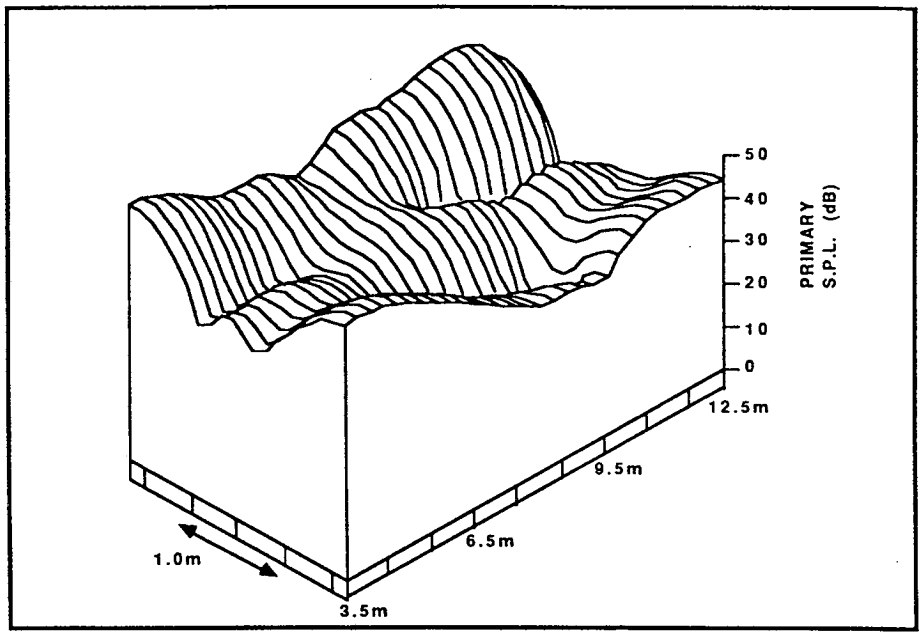

FIGURE 7.14. The pressure field in the head height plane of Figure 7.1 due to the shell structural response only. The frequency is 176Hz.

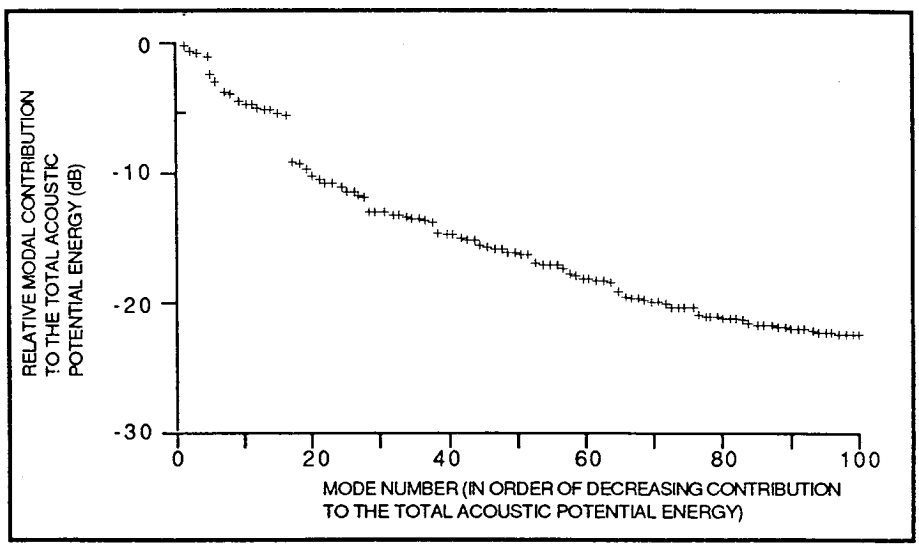

FIGURE 7.15. The relative contributions of the acoustic modes to the total acoustic potential energy when the modelled cabin sound field is excited by the shell structural response only. The frequency is 176Hz.

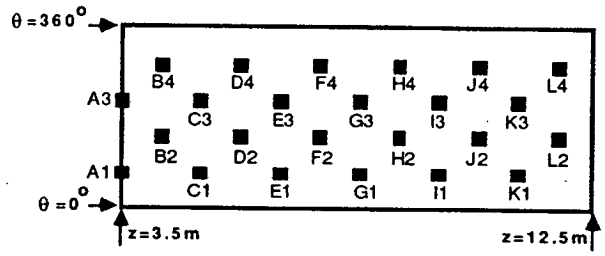

a) Diagram of the unwrapped shell showing the locations of the 24 sources used. Jp has been minimised using all 48 error sensors of Figure 7.2.

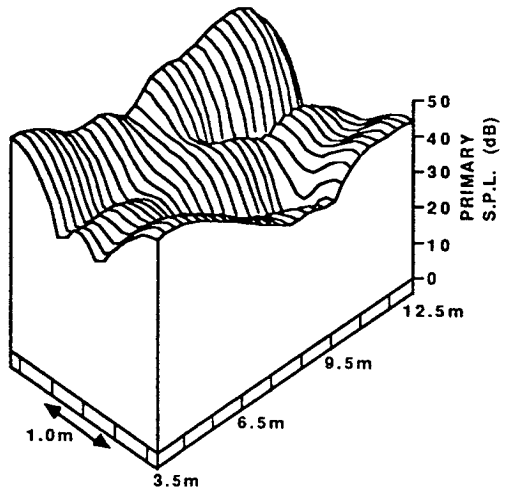

b) The pressure field over the head height plane due to the shell structural response only (primary field).

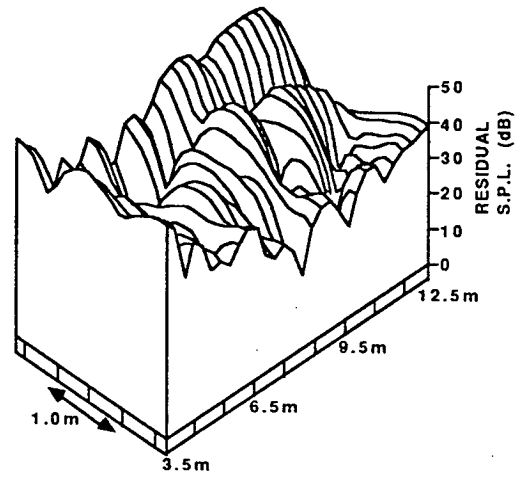

c) The pressure field over the head height plane after Jp has been minimised using the sources and sensors listed in Figure (a).

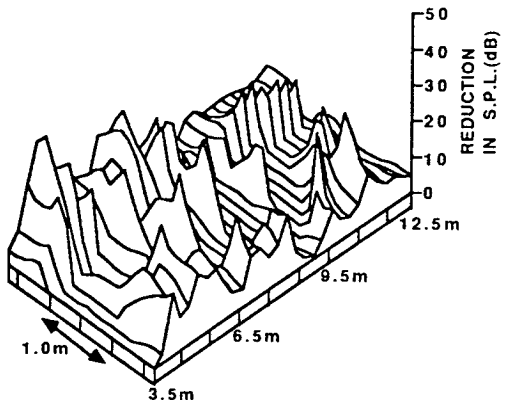

d) Areas of pressure decrease after Jp has been minimised.

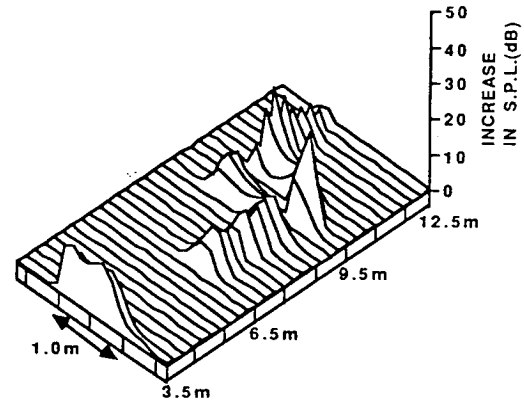

e) Areas of pressure increase after Jp has been minimised.

FIGURE 7.16. The sound pressure field in the head height plane of Figure 7.1 before and after Jp has been minimised using a 24 source/48 sensor active control system. The frequency is 176Hz.

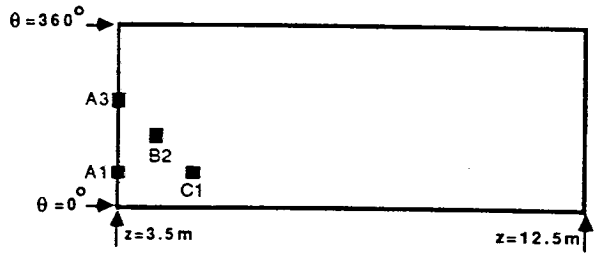

a) Diagram of the unwrapped shell showing the locations of the 4 sources used. Jp has been minimised using all 48 error sensors of Figure 7.2.

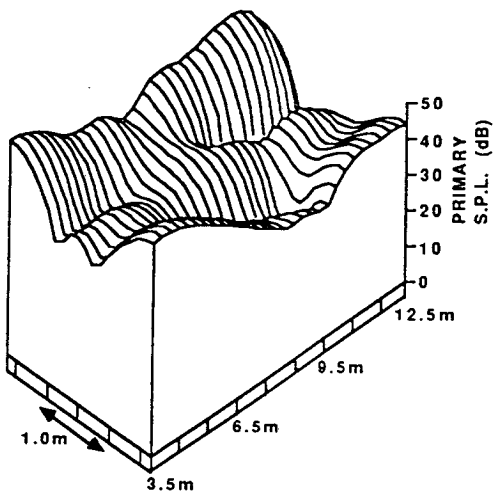

b) The pressure field over the head height plane due to the shell structural response only (primary field).

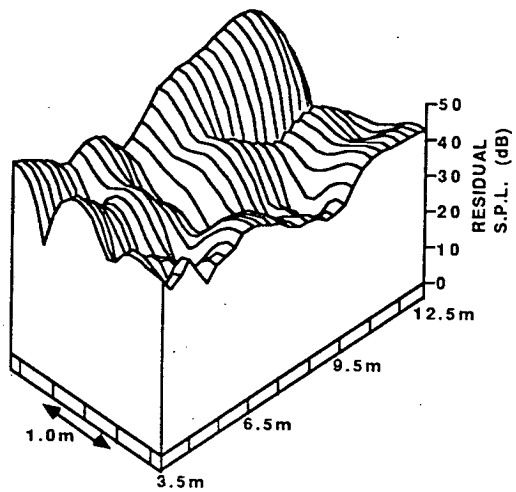

c) The pressure field over the head height plane after Jp has been minimised using the sources and sensors listed in Figure (a).

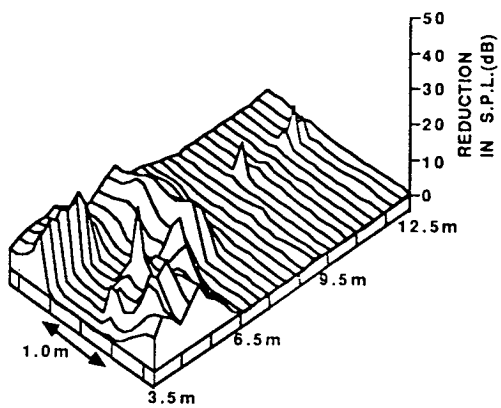

d) Areas of pressure decrease after Jp has been minimised.

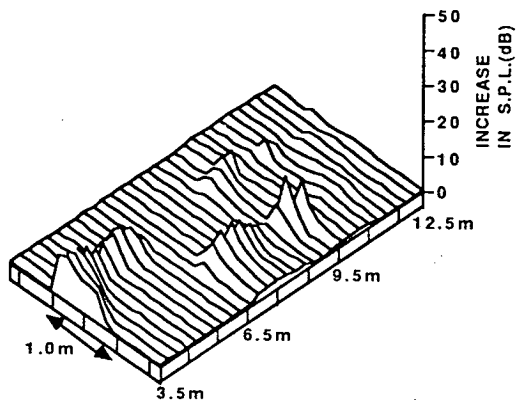

e) Areas of pressure increase after Jp has been minimised.

FIGURE 7.17. The sound pressure field in the head height plane of Figure 7.1 before and after Jp has been minimised using a 4 source/48 sensor active control system. The frequency is 176Hz.

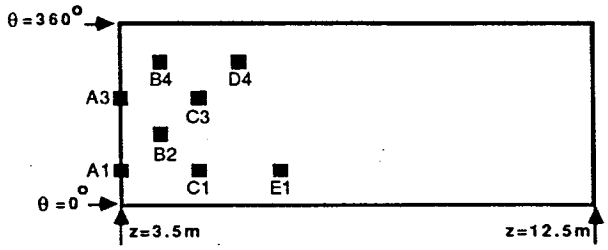

a) Diagram of the unwrapped shell showing the locations of the 8 sources used. Jp has been minimised using all 48 error sensors of Figure 7.2.

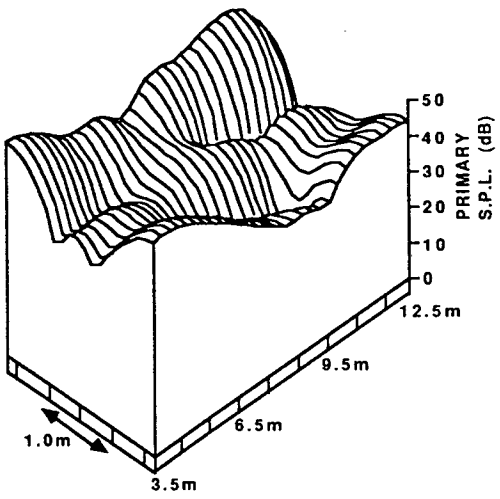

b) The pressure field over the head height plane due to the shell structural response only (primary field).

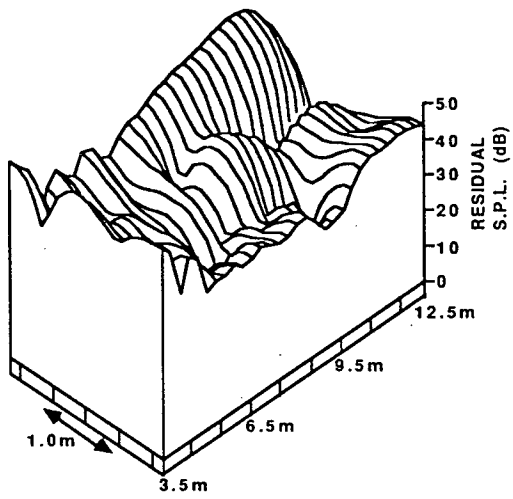

c) The pressure field over the head height plane after Jp has been minimised using the sources and sensors listed in Figure (a).

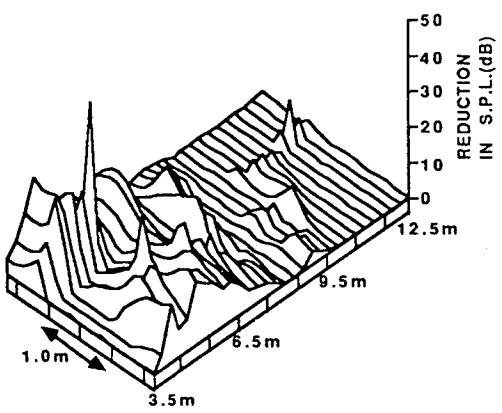

d) Areas of pressure decrease after Jp has been minimised.

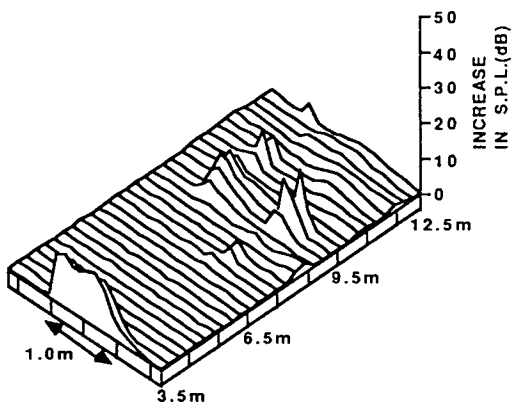

e) Areas of pressure increase after Jp has been minimised.

FIGURE 7.18. The sound pressure field in the head height plane of Figure 7.1 before and after Jp has been minimised using an 8 source/48 sensor active control system. The frequency is 176Hz.

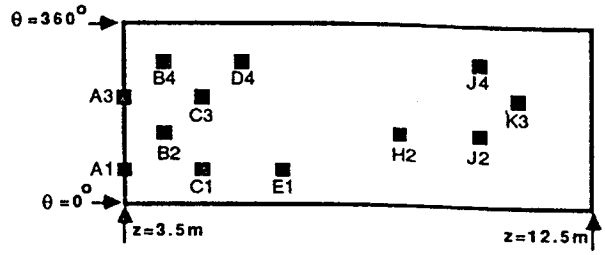

a) Diagram of the unwrapped shell showing the locations of the 12 sources used. Jp has been minimised using all 48 error sensors of Figure 7.2.

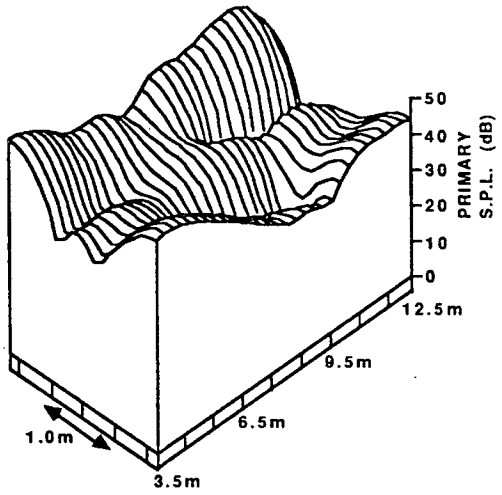

b) The pressure field over the head height plane due to the shell structural response only (primary field).

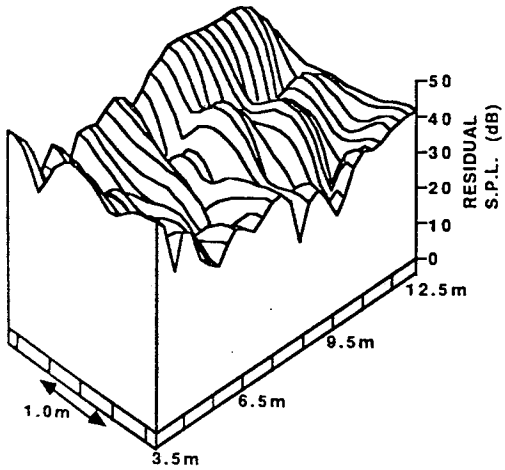

c) The pressure field over the head height plane after Jp has been minimised using the sources and sensors listed in Figure (a).

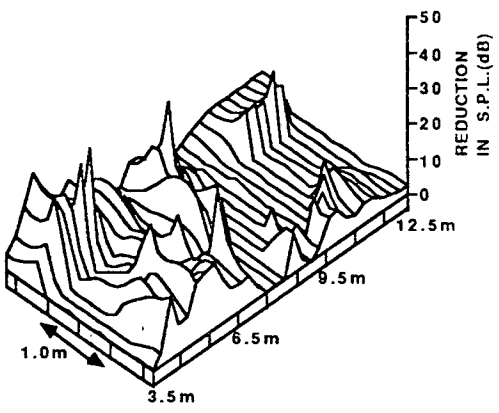

d) Areas of pressure decrease after Jp has been minimised.

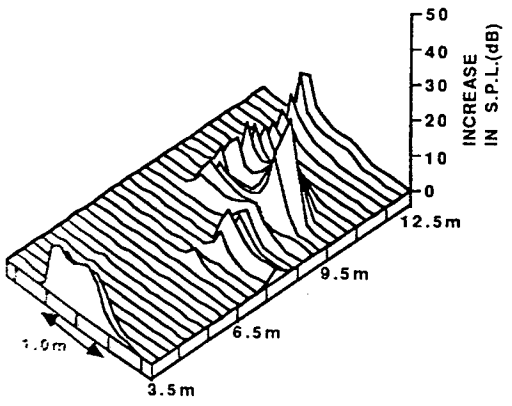

e) Areas of pressure increase after Jp has been minimised.

FIGURE 7.19. The sound pressure field in the head height plane of Figure 7.1 before and after Jp has been minimised using a 12 source/48 sensor active control system. The frequency is 176Hz.

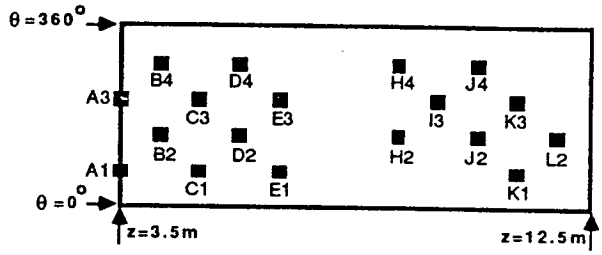

a) Diagram of the unwrapped shell showing the locations of the 18 sources used. Jp has been minimised using all 48 error sensors of Figure 7.2.

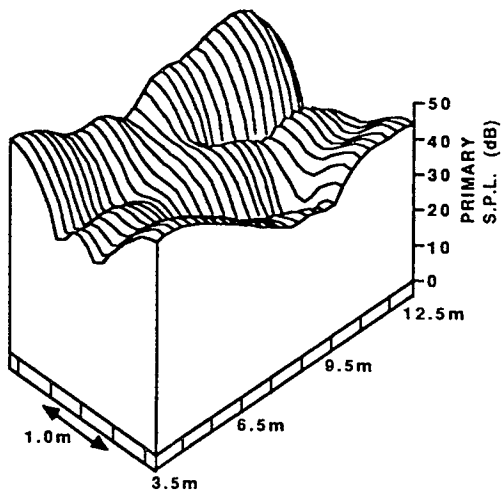

b) The pressure field over the head height plane due to the shell structural response only (primary field).

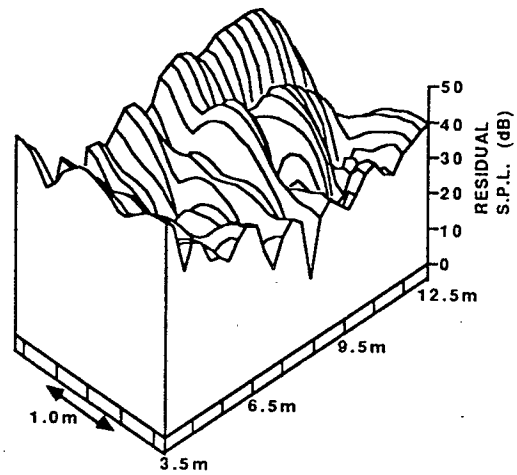

c) The pressure field over the head height plane after Jp has been minimised using the sources and sensors listed in Figure (a).

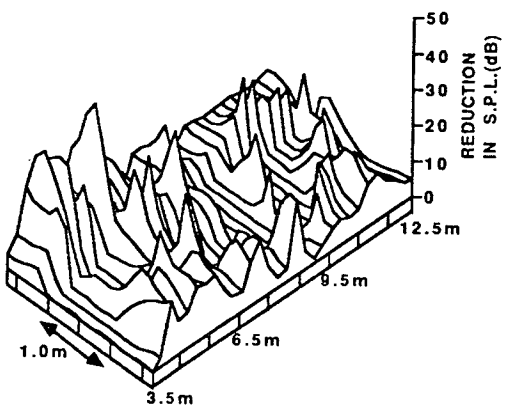

d) Areas of pressure decrease after Jp has been minimised.

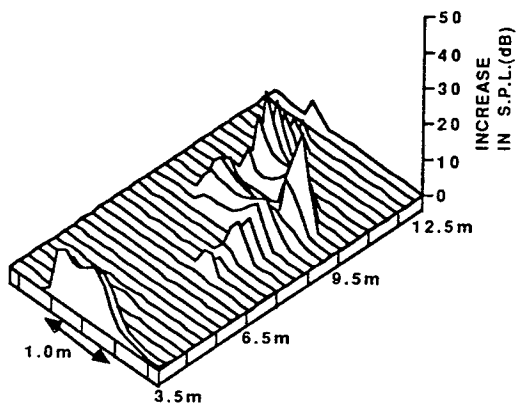

e) Areas of pressure increase after Jp has been minimised.

FIGURE 7.20. The sound pressure field in the head height plane of Figure 7.1 before and after Jp has been minimised using an 18 source/48 sensor active control system. The frequency is 176Hz.

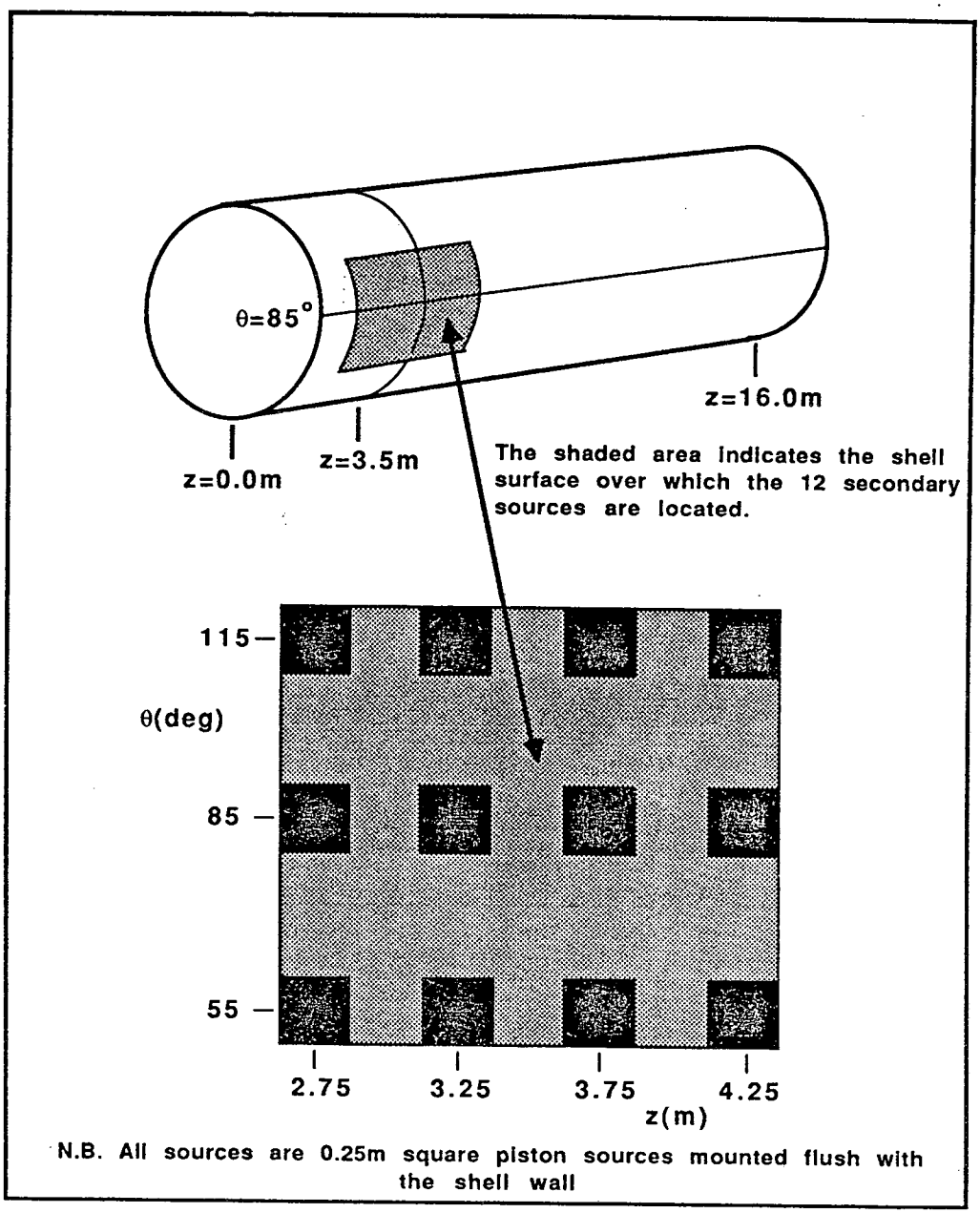

FIGURE 7.21. Schematic diagram showing the locations of the twelve secondary sources located in the propeller plane.

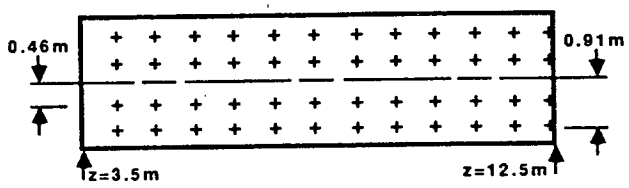

a) Diagram of the head height plane of Figure 7.1 showing the locations of the 48 sensors over which Jp has been minimised using the 12 secondary sources of Figure 7.21.

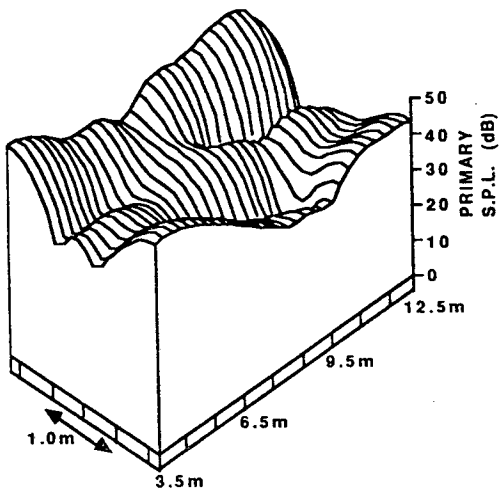

b) The pressure field over the head height plane due to the shell structural response only (primary field).

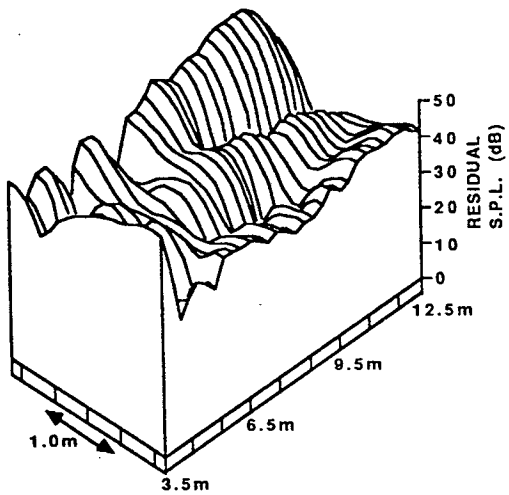

c) The pressure field over the head height plane after Jp has been minimised using the sources and sensors listed in Figure (a).

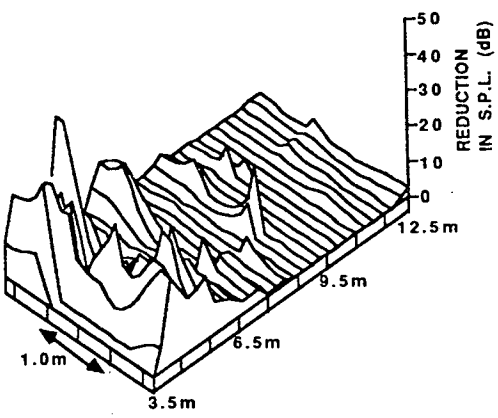

d) Areas of pressure decrease after Jp has been minimised.

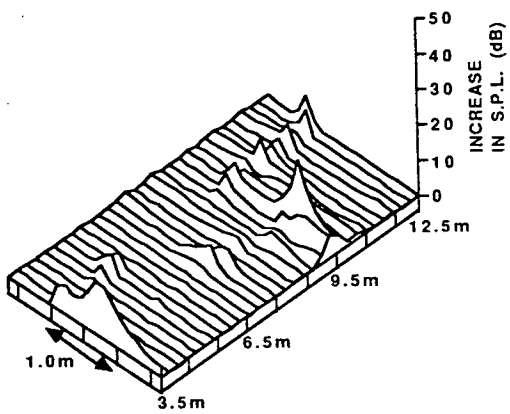

e) Areas of pressure increase after Jp has been minimised.

FIGURE 7.22. The sound pressure field in the head height plane of Figure 7.1 before and after Jp has been minimised using a 12 source/48 sensor active control system when the sources are mounted in the vicinity of the the propeller plane as shown in Figure 2.21. The frequency is 176Hz.

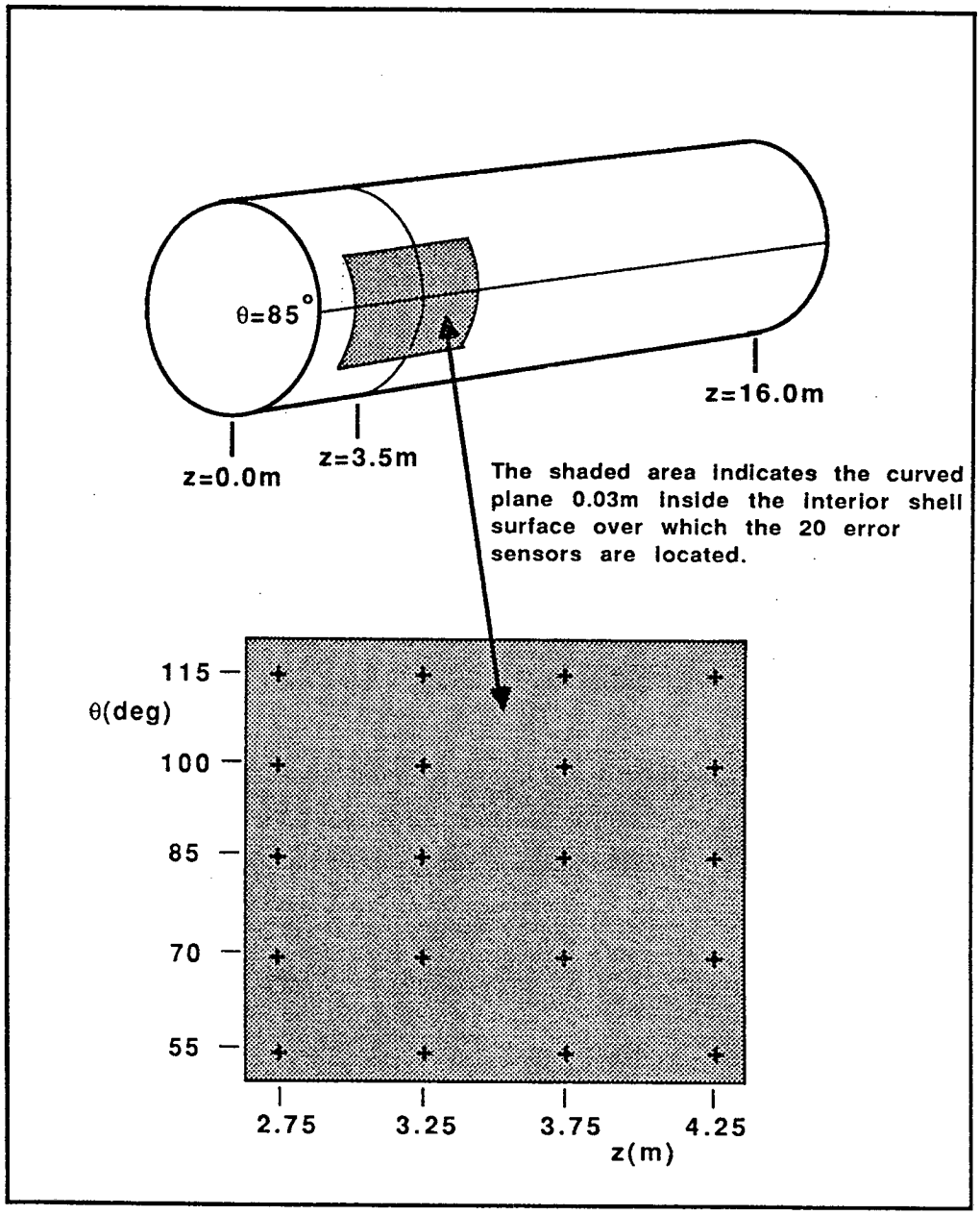

FIGURE 7.23. Schematic diagram showing the locations of the twenty error sensors located in the propeller plane.

FOR THE 12 SECONDARY SOURCE LOCATIONS SEE FIGURE 7.21
AND FOR THE 20 ERROR SENSOR LOCATIONS SEE FIGURE 7.23.

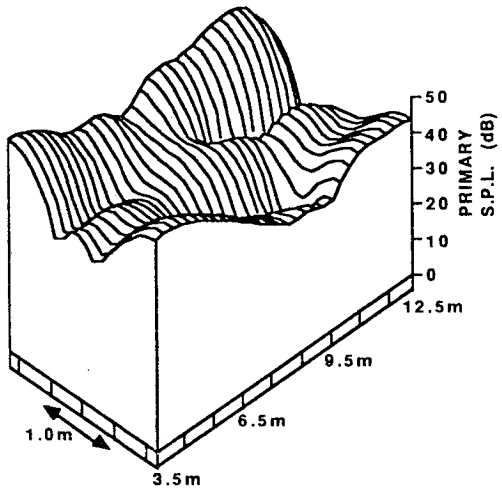

b) The pressure field over the head height plane due to the shell structural response only (primary field).

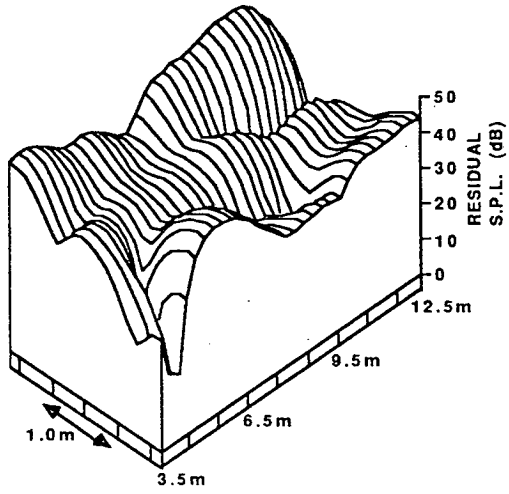

c) The pressure field over the head height plane after Jp has been minimised using the sources and sensors listed in Figure (a).

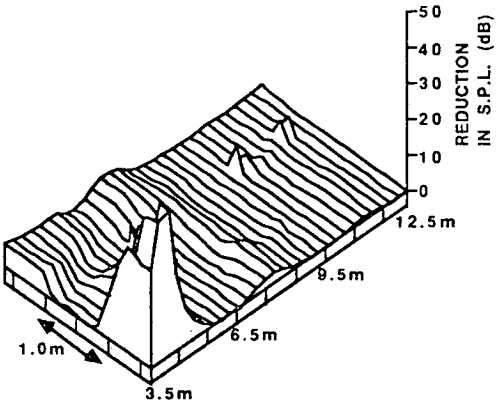

d) Areas of pressure decrease after Jp has been minimised.

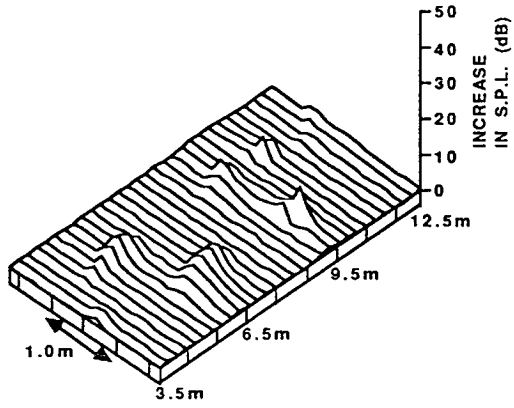

e) Areas of pressure increase after Jp has been minimised.

FIGURE 7.24. The sound pressure field in the head height plane of Figure 7.1 before and after Jp has been minimised using a 12 source/20 sensor active control system when the sources and sensors are all mounted in the vicinity of the propeller plane. The frequency is 176Hz.

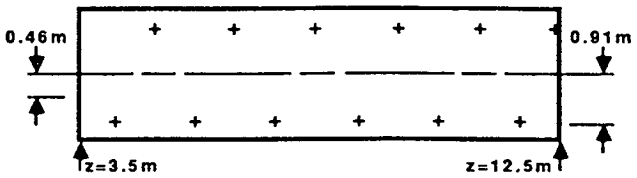

a) Diagram of the head height plane of Figure 7.1 showing the locations of the 12 sensors over which Jp has been minimised using the 8 secondary sources of Figure 7.18 (a).

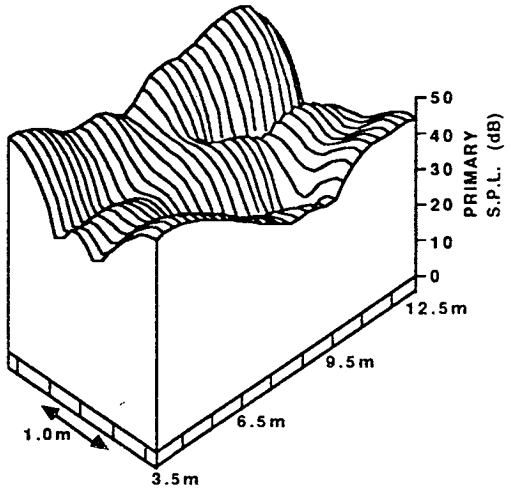

b) The pressure field over the head height plane due to the shell structural response only (primary field).

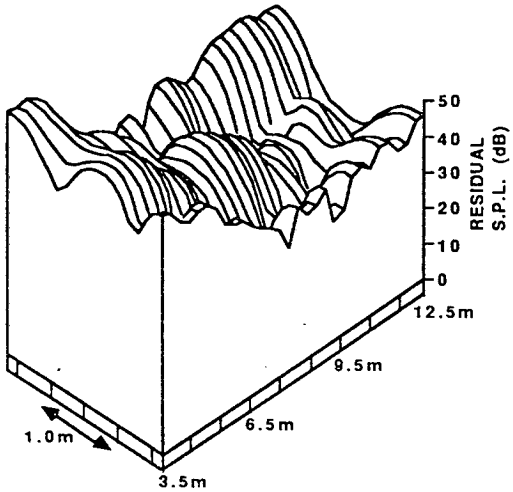

c) The pressure field over the head height plane after Jp has been minimised using the sources and sensors listed in Figure (a).

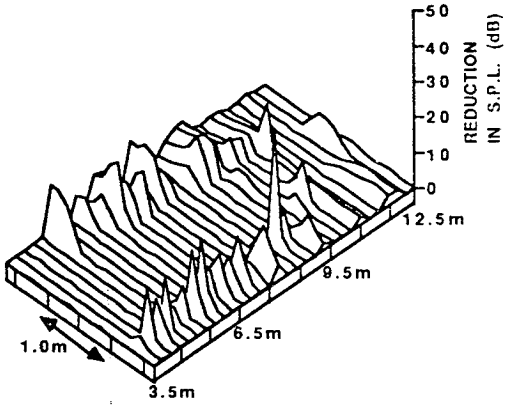

d) Areas of pressure decrease after Jp has been minimised.

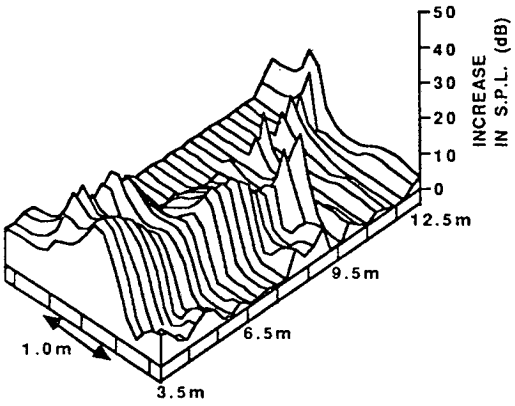

e) Areas of pressure increase after Jp has been minimised.

FIGURE 7.25. The sound pressure field in the head height plane of Figure 7.1 before and after Jp has been minimised using an 8 source/12 sensor active control system. The frequency is 176Hz

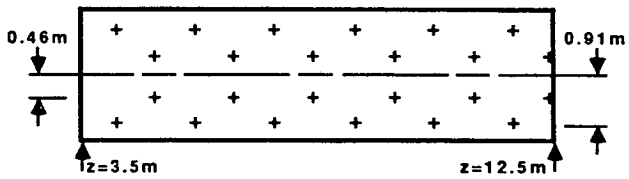

a) Diagram of the head height plane of Figure 7.1 showing the locations of the 24 sensors over which Jp has been minimised using the 8 secondary sources of Figure 7.18(a).

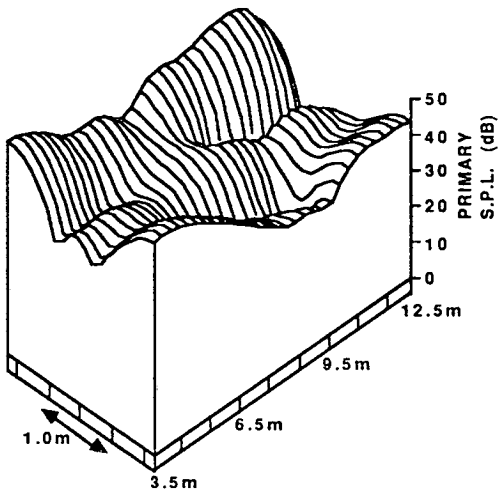

b) The pressure field over the head height plane due to the shell structural response only (primary field).

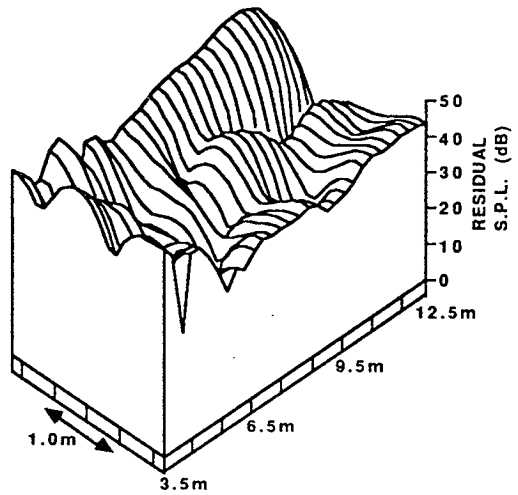

c) The pressure field over the head height plane after Jp has been minimised using the sources and sensors listed in Figure (a).

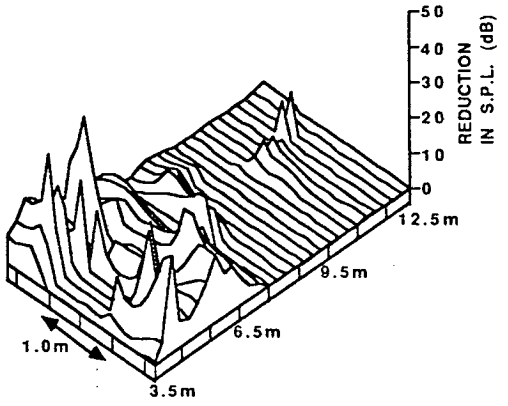

d) Areas of pressure decrease after Jp has been minimised.

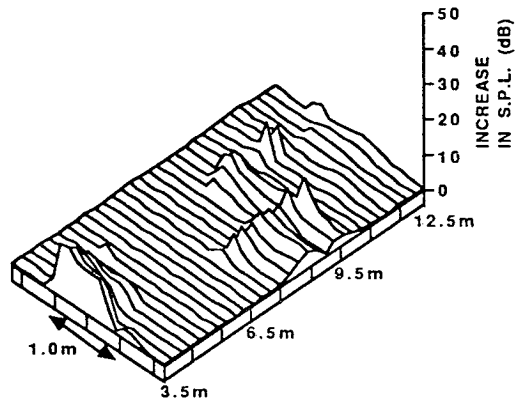

e) Areas of pressure increase after Jp has been minimised.

FIGURE 7.26. The sound pressure field in the head height plane of Figure 7.1 before and after Jp has been minimised using an 8 source/24 sensor active control system. The frequency is 176Hz

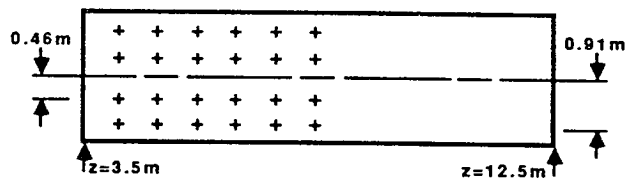

a) Diagram of the head height plane of Figure 7.1 showing the locations of the 24 sensors over which Jp has been minimised using the 8 secondary sources of Figure 7.18(a).

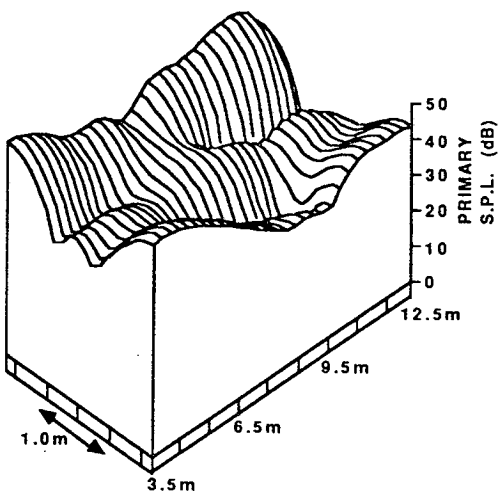

b) The pressure field over the head height plane due to the shell structural response only (primary field).

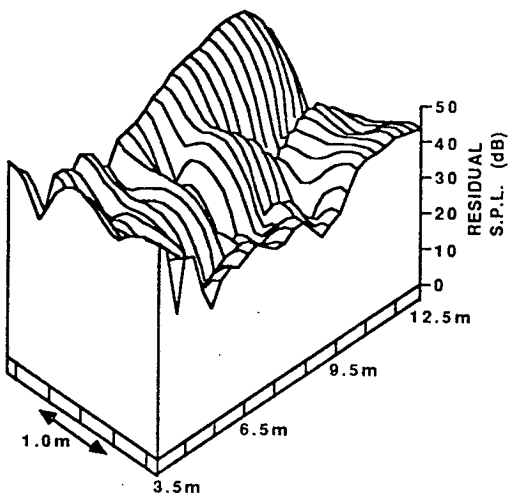

c) The pressure field over the head height plane after Jp has been minimised using the sources and sensors listed in Figure (a).

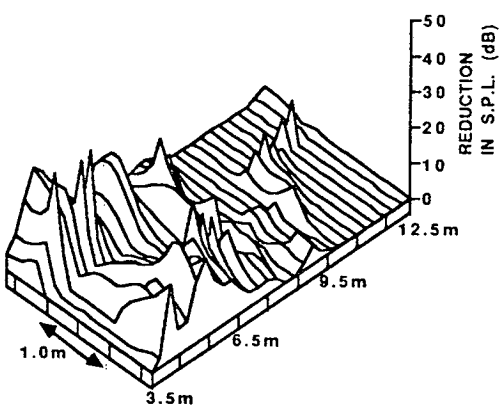

d) Areas of pressure decrease after Jp has been minimised.

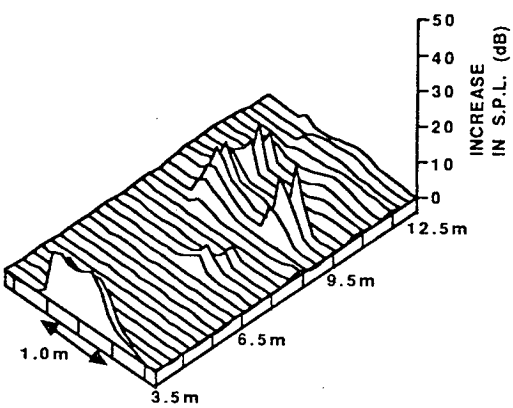

e) Areas of pressure increase after Jp has been minimised.

FIGURE 7.27. The sound pressure field in the head height plane of Figure 7.1 before and after Jp has been minimised using an 8 source/24 sensor active control system. The frequency is 176Hz.

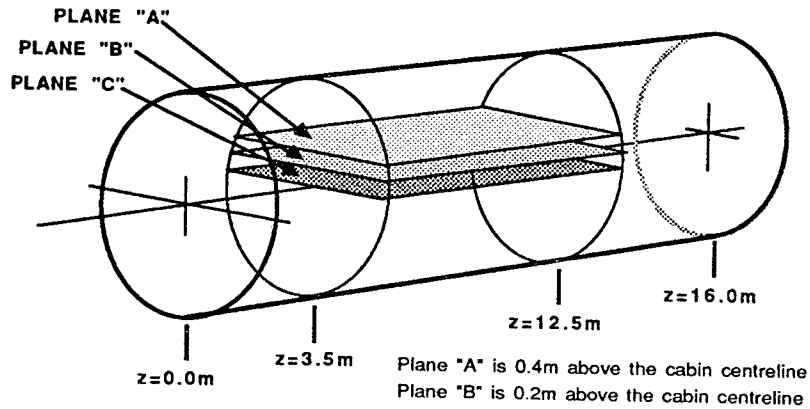

Plane "A" is 0.4m above the cabin centreline
Plane "B" is 0.2m above the cabin centreline
Plane "C" is 0.0m above the cabin centreline

a) Schematic diagram showing the three planes over which the pressure has been evaluated on a 30 by 20 point grid for Figures 7.29 and 7.30.

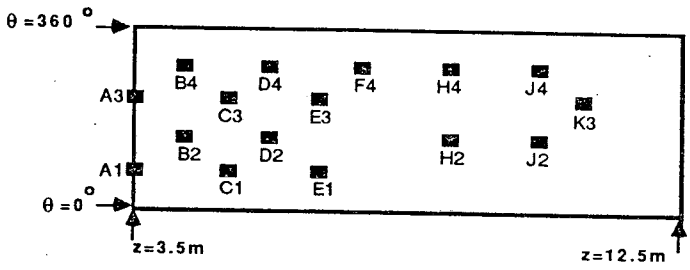

b) Diagram of the unwrapped shell showing the locations of the 16 sources used.

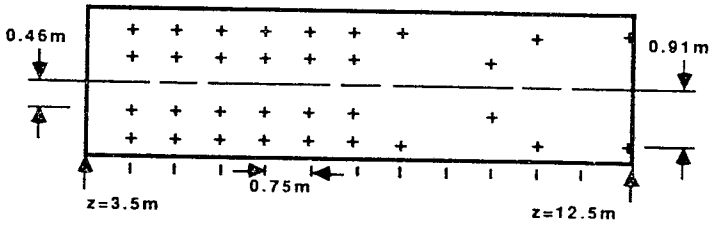

c) The 32 error sensor locations over plane "B" of Figure (a) (which corresponds to the head height plane of Figure 7.1.)

FIGURE 7.28. Schematic diagram showing the locations of the sources and sensors used for the 16 source/32 sensor results of Figures 7.29 and 7.30. Also shown are the three planes over which the pressure fields have been evaluated.

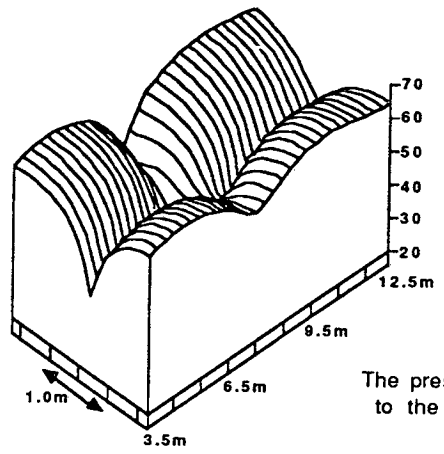

PRIMARY S.P.L.(dB)

The pressure field over the plane "A" of Figure 7.28 due to the shell structural response only (primary field).

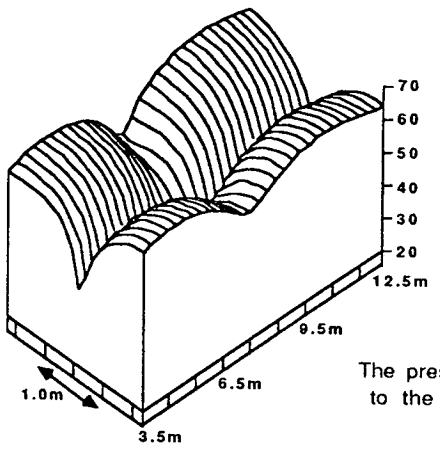

PRIMARY S.P.L.(dB)

The pressure field over the plane "B" of Figure 7.28 due to the shell structural response only (primary field).

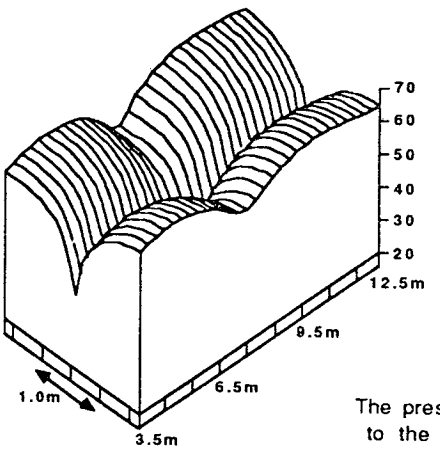

PRIMARY S.P.L.(dB)

The pressure field over the plane "C" of Figure 7.28 due to the shell structural response only (primary field).

FIGURE 7.29(a). The sound pressure fields over the three planes shown in Figure 7.28 due to the shell structural response only (primary field). The frequency is 88Hz.

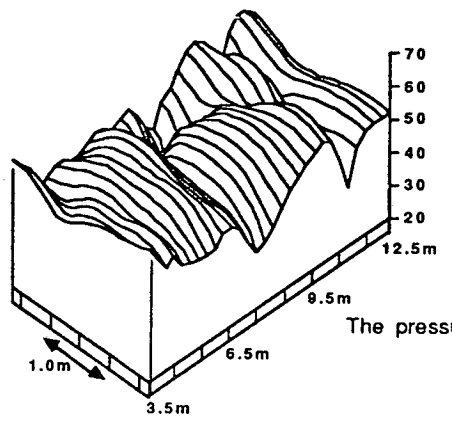

RESIDUAL S.P.L.(dB)

Reduction in Jp_{600} =11.0dB

The pressure field over the plane "A" of Figure 7.28 after Jp has been minimised.

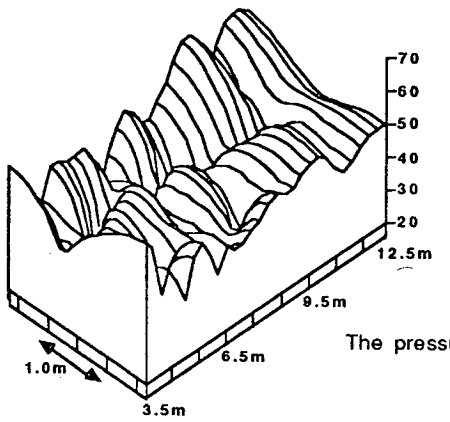

RESIDUAL S.P.L.(dB)

Reduction in Jp_{600} =14.1dB

The pressure field over the plane "B" of Figure 7.28 after Jp has been minimised.

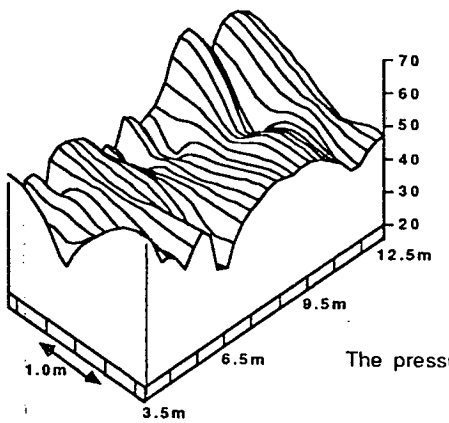

RESIDUAL S.P.L.(dB)

Reduction in Jp_{600} =10.3dB

The pressure field over the plane "C" of Figure 7.28 after Jp has been minimised.

FIGURE 7.29(b). The sound pressure fields over the three planes shown in Figure 7.28 after Jp has been minimised using the 16 source/32 sensor active control system which is also shown in Figure 7.28. The frequency is 88Hz.

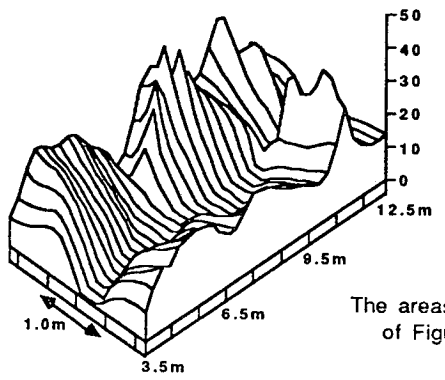

REDUCTION IN S.P.L.(dB)

The areas of pressure decrease over the plane "A" of Figure 7.28 after Jp has been minimised.

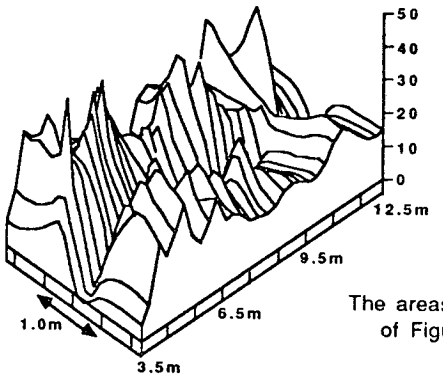

REDUCTION IN S.P.L.(dB)

The areas of pressure decrease over the plane "B" of Figure 7.28 after Jp has been minimised.

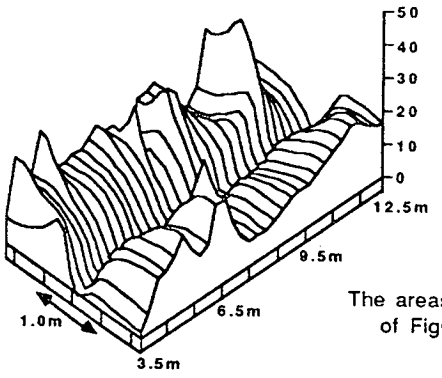

REDUCTION IN S.P.L.(dB)

The areas of pressure decrease over the plane "C" of Figure 7.28 after Jp has been minimised.

FIGURE 7.29(c). The regions of pressure reduction in the sound fields over the three planes shown in Figure 7.28 after Jp has been minimised using the 16 source/32 sensor active control system which is also shown in Figure 7.28. The frequency is 88Hz.

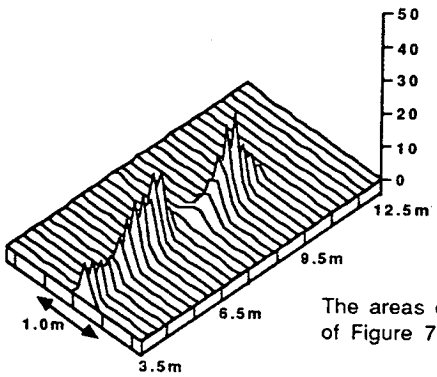

The areas of pressure increase over the plane "A" of Figure 7.28 after Jp has been minimised.

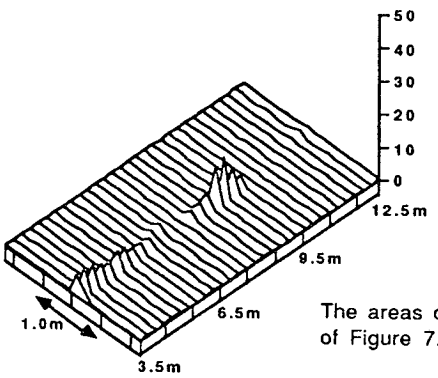

The areas of pressure increase over the plane "B" of Figure 7.28 after Jp has been minimised.

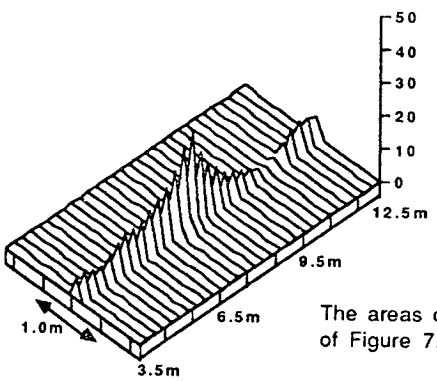

The areas of pressure increase over the plane "C" of Figure 7.28 after Jp has been minimised.

FIGURE 7.29(d). The regions of pressure increase in the sound fields over the three planes shown in Figure 7.28 after Jp has been minimised using the 16 source/32 sensor active control system which is also shown in Figure 7.28. The frequency is 88Hz.

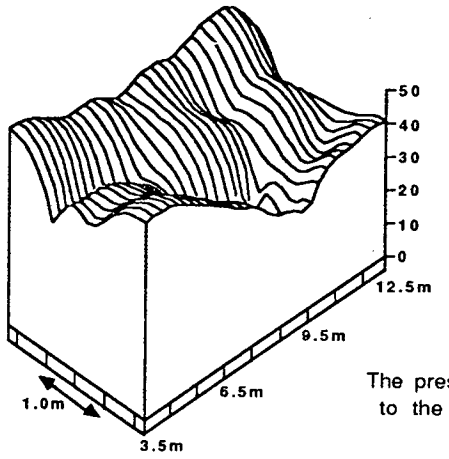

The pressure field over the plane "A" of Figure 7.28 due to the shell structural response only (primary field).

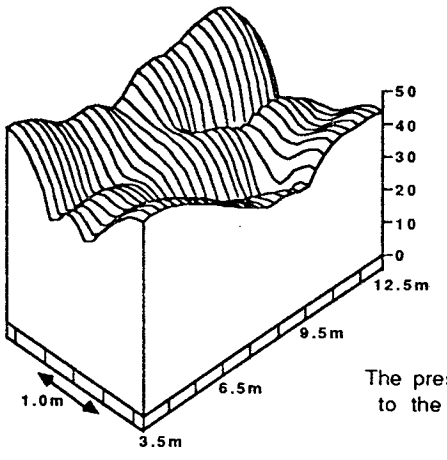

The pressure field over the plane "B" of Figure 7.28 due to the shell structural response only (primary field).

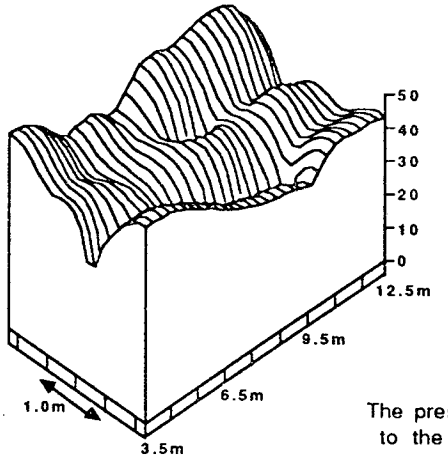

The pressure field over the plane "C" of Figure 7.28 due to the shell structural response only (primary field).

FIGURE 7.30(a). The sound pressure fields over the three planes shown in Figure 7.28 due to the shell structural response only (primary field). The frequency is 176Hz.

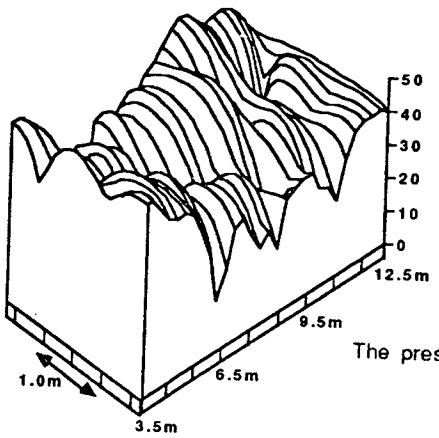

RESIDUAL S.P.L.(dB)

Reduction in Jp_{560}=1.1dB

The pressure field over the plane "A" of Figure 7.28 after Jp has been minimised.

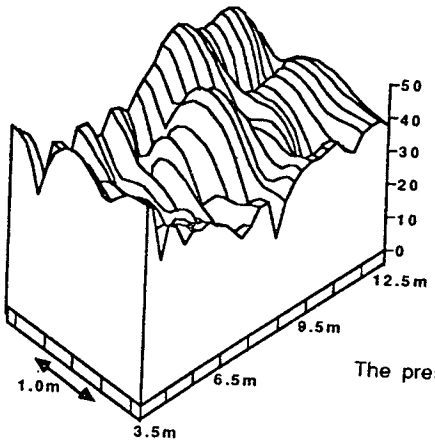

RESIDUAL S.P.L.(dB)

Reduction in Jp_{560}=4.6dB

The pressure field over the plane "B" of Figure 7.28 after Jp has been minimised.

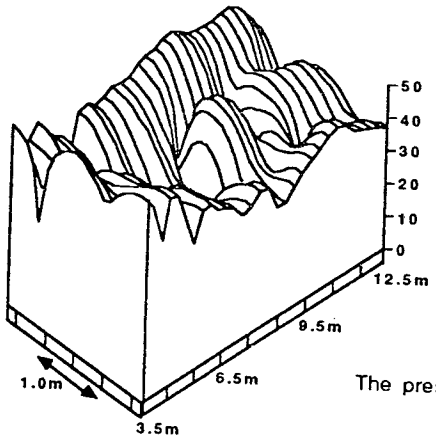

RESIDUAL S.P.L.(dB)

Reduction in Jp_{560}=0.7dB

The pressure field over the plane "C" of Figure 7.28 after Jp has been minimised.

IGURE 7.30(b). The sound pressure fields over the three planes shown in Figure 7.28 fter Jp has been minimised using the 16 source/32 sensor active control system which also shown in Figure 7.28. The frequency is 176Hz.

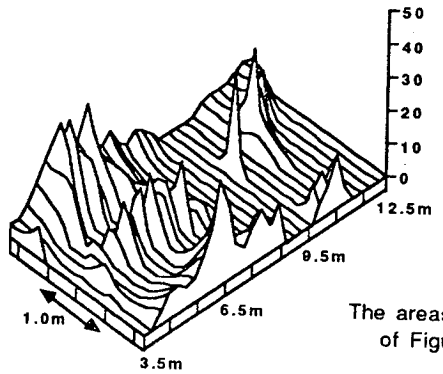

The areas of pressure decrease over the plane "A" of Figure 7.28 after Jp has been minimised.

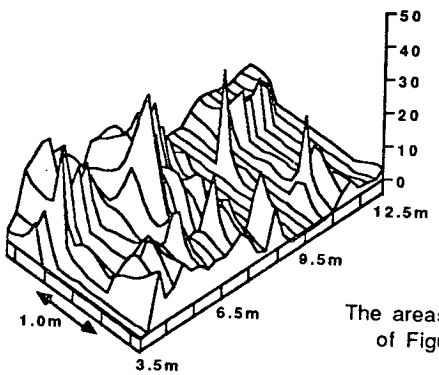

The areas of pressure decrease over the plane "B" of Figure 7.28 after Jp has been minimised.

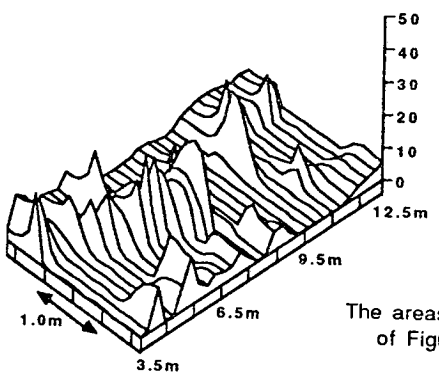

The areas of pressure decrease over the plane "C" of Figure 7.28 after Jp has been minimised.

FIGURE 7.30(c). The regions of pressure reduction in the sound fields over the three planes shown in Figure 7.28 after Jp has been minimised using the 16 source/32 sensor active control system which is also shown in Figure 7.28. The frequency is 176Hz.

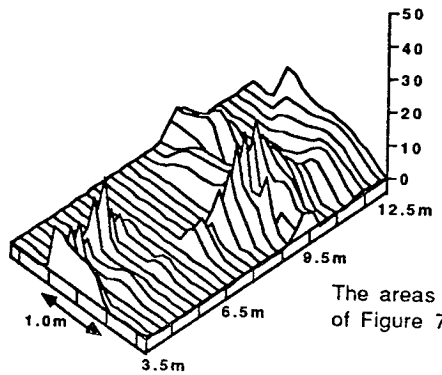

INCREASE IN S.P.L.(dB)

The areas of pressure increase over the plane "A" of Figure 7.28 after Jp has been minimised.

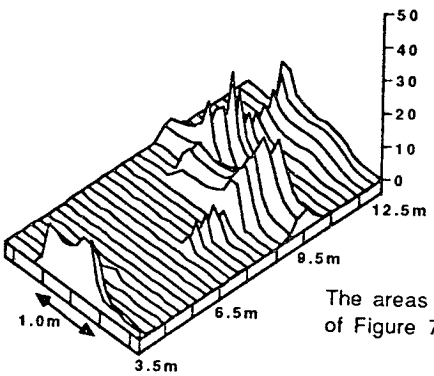

INCREASE IN S.P.L.(dB)

The areas of pressure increase over the plane "B" of Figure 7.28 after Jp has been minimised.

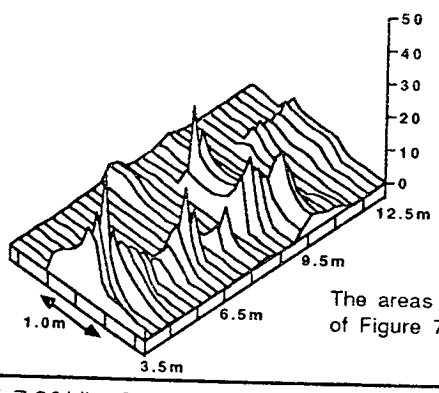

INCREASE IN S.P.L.(dB)

The areas of pressure increase over the plane "C" of Figure 7.28 after Jp has been minimised.

FIGURE 7.30(d). The regions of pressure increase in the sound fields over the three planes shown in Figure 7.28 after Jp has been minimised using the 16 source/32 sensor active control system which is also shown in Figure 7.28. The frequency is 176Hz.

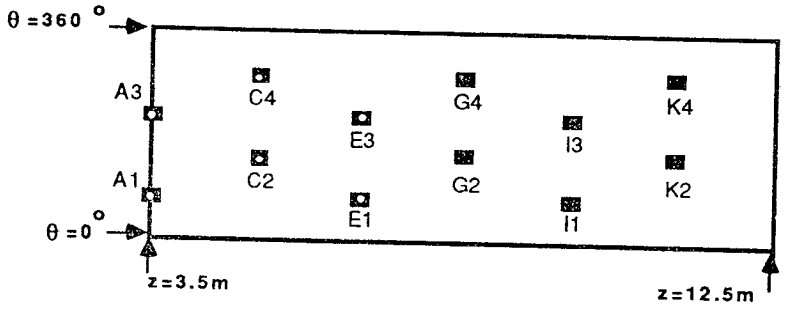

a) Diagram of the unwrapped shell showing the locations of the secondary sources used.

6 & 12 source systems

12 source system only

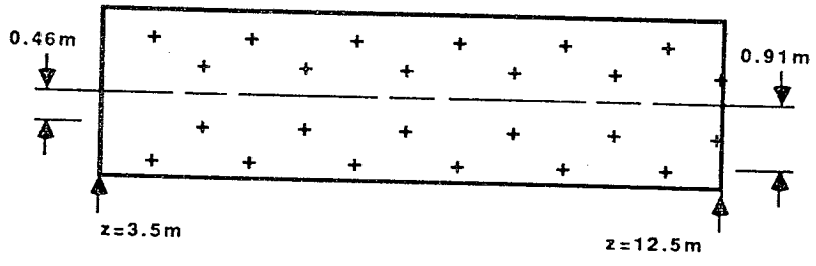

b)The sensor locations over the head height plane shown in Figure 7.1.

FIGURE 7.31. The source and sensor locations used to evaluate the performance of active noise control when propeller synchrophasing is also employed. For the results of Figures 7.32 and 7.33 the synchrophase angle has been set in 5 degree steps and then held constant while the active noise control has been applied.

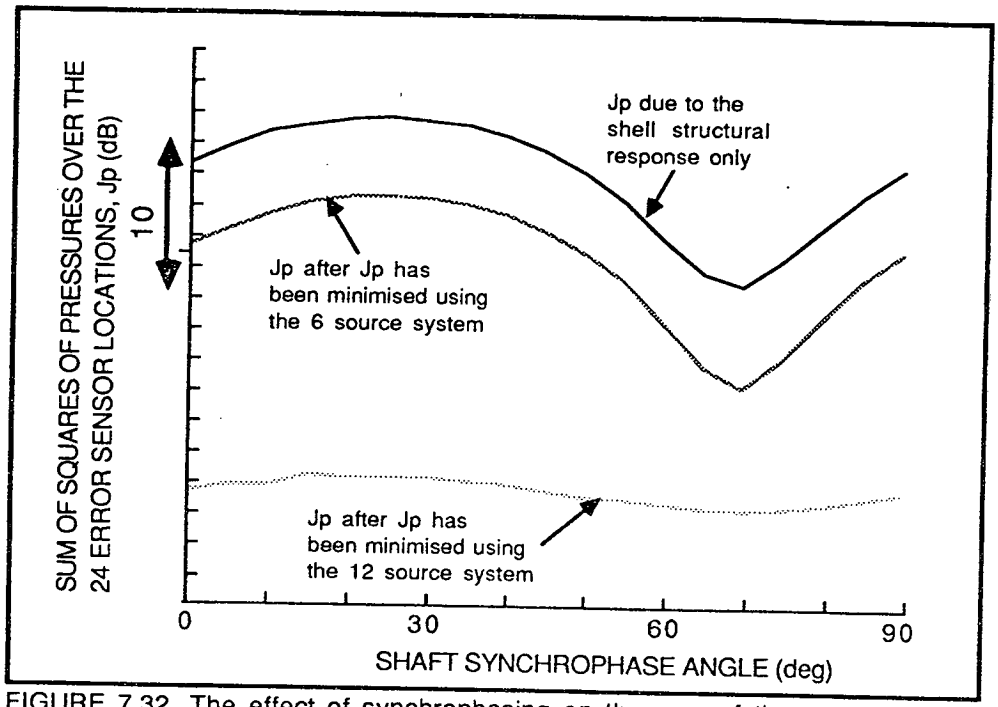

FIGURE 7.32. The effect of synchrophasing on the sum of the squared pressures at the 24 error sensor locations, Jp, both before and after Jp has been minimised using a) the 6 source/24 sensor and b) the 12 source/24 sensor active control systems shown in Figure 7.31. The frequency is 88Hz.

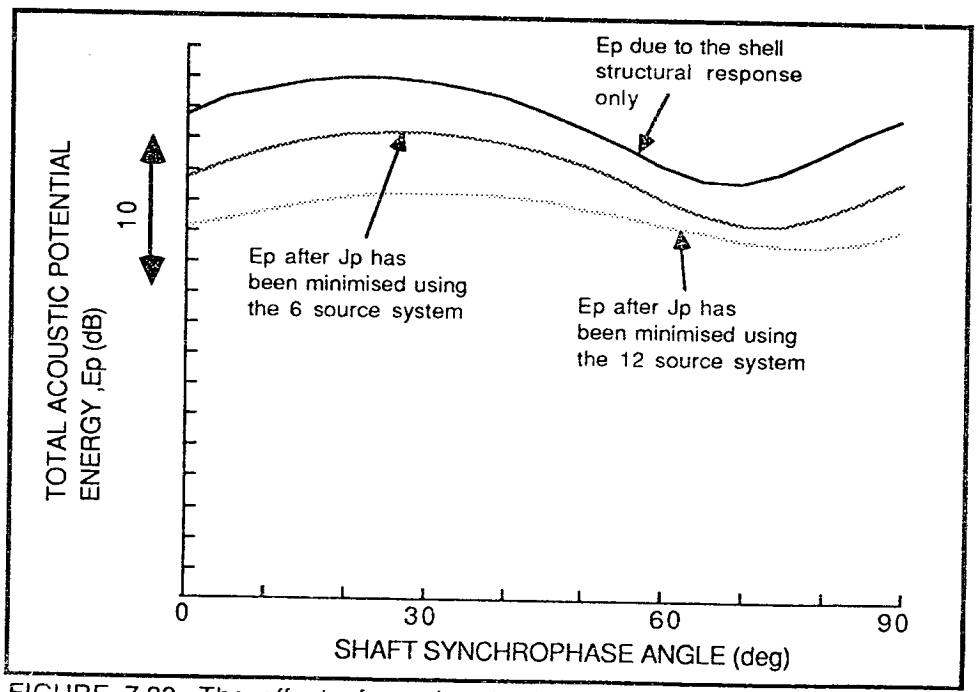

FIGURE 7.33. The effect of synchrophasing on the total acoustic potential energy, Ep, both before and after the sum of the squared pressures at the 24 error sensors, Jp, has been minimised using a) the 6 source/24 sensor and b) the 12 source/24 sensor active control systems shown in Figure 7.31. The frequency is 88Hz.

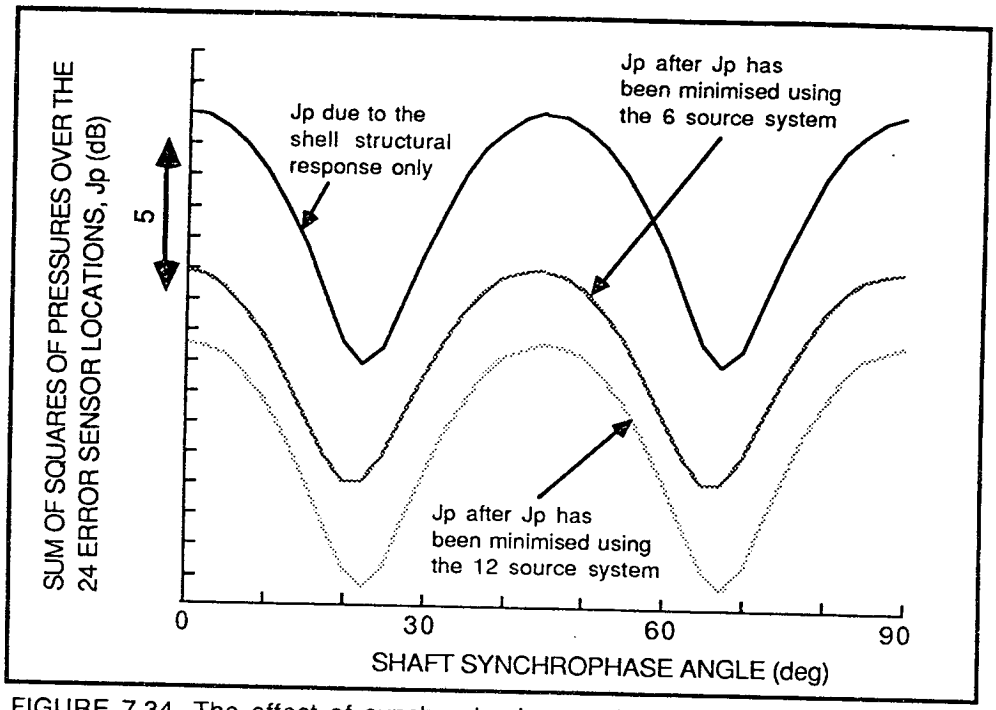

FIGURE 7.34. The effect of synchrophasing on the sum of the squared pressures at the 24 error sensor locations, Jp, both before and after Jp has been minimised using a) the 6 source/24 sensor and b) the 12 source/24 sensor active control systems shown in Figure 7.31. The frequency is 176Hz.

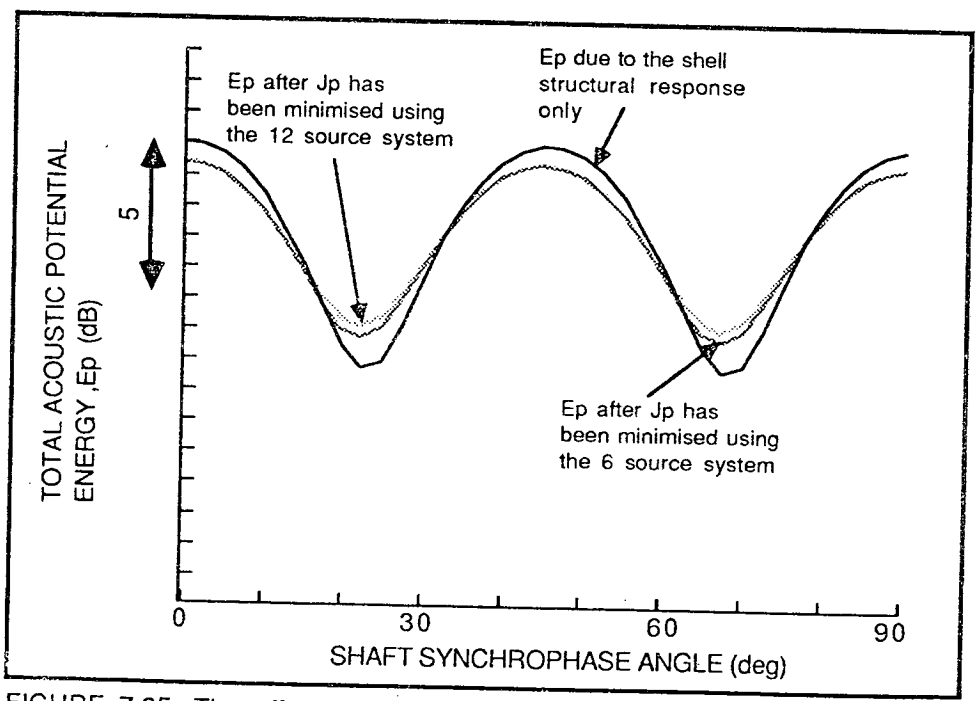

FIGURE 7.35. The effect of synchrophasing on the total acoustic potential energy, Ep, both before and after the sum of the squared pressures at the 24 error sensors, Jp, has been minimised using a) the 6 source/24 sensor and b) the 12 source/24 sensor active control systems shown in Figure 7.31. The frequency is 176Hz.

CHAPTER 8

CONCLUSIONS

8.1 The Application of Active Noise Control to Lightly Damped Enclosed Sound Fields of Low Modal Density

The work presented in this thesis has used the theory of quadratic optimisation as a basic theoretical framework for assessing the feasibility of applying active noise control to harmonic, enclosed sound fields. The basic requirement for using this theory is that the active noise control system must act so as to minimise some cost function which bears a quadratic relationship to the complex strengths of the secondary sources. This ensures the cost function has a unique global minimum and therefore there is a unique set of secondary source strengths which minimise the cost function.

In the first part of the thesis, the use of several different possible quadratic cost functions has been investigated theoretically by considering their application to the specific problem of controlling the sound field in a lightly damped, essentially two-dimensional rectangular enclosure at frequencies such that the modal density is very low. It has been demonstrated that, by choosing to minimise the total acoustic potential energy in the enclosure, large global reductions ($>$ 20 dB) in mean squared sound pressure level can be achieved by the introduction and control of only one or two secondary sources provided the system is operating at an acoustic resonance. However, it has also been demonstrated that in order to be effective these sources must be placed at antinodes of the dominant mode or modes and, for the best results, they should be placed as close to the primary source as is possible. Provided the secondary sources are placed at locations where they can efficiently drive the dominant acoustic modes the mechanism for the large ($>$ 20 dB) global reductions has been shown to be a mutual "unloading" effect such that the acoustic pressure over each of the source surfaces tends to decrease and to adopt a quadrature phase relationship with that source's velocity. This has been found to be true for all the sources involved, both primary and secondary, and thus the total power input to the enclosed sound field is reduced. The general property has been demonstrated that, in order to achieve large global reductions, each

dominant mode must have associated with it at least one control source which is positioned such that it can drive that mode efficiently. It has also been demonstrated that under certain conditions a single source can effectively attenuate the contributions of more than one dominant mode. However, the ability of a secondary source to couple efficiently with a dominant mode does not mean that by minimising the total acoustic potential energy this energy will decrease by an amount equal to removing that modal contribution. Rather, the energy will be decreased by a smaller amount, the magnitude of the reduction being governed by the increased excitation of any residual modes due to the action of the secondary source relative to the decreased excitation of the dominant mode. This increased excitation of residual modes following the application of active control has also been shown to result in the sound pressure level increasing in certain regions of the controlled sound field, even for cases when reductions in the total acoustic potential energy may exceed 20 dB. However, these regions of pressure increase are confined to regions where the sound pressure was initially very low. Therefore, the general effect of minimising the total acoustic potential energy is to "even out" the spatial pressure fluctuations whilst reducing the volume averaged amplitude of pressure fluctuations.

At frequencies not lying close to any of the lightly damped mode resonances global reductions in acoustic potential energy comparable with those achievable at mode resonances have been shown to require more secondary sources. This has again been shown to be due to the increased excitation of "residual" modes which, at non-resonant frequencies, may only contribute to the total acoustic potential energy by a few decibels less than the "dominant" modes. Indeed, the distinction between "dominant" and "residual" modes becomes somewhat blurred in these frequency ranges. The same effect can also occur at mode resonances if the acoustic damping is made large enough, and also at frequencies high enough such that the modal density becomes much higher.

The unsuitability of the total acoustic potential energy as a practical control system cost function has been discussed. As a practical alternative it has been suggested that the sum of the squared pressures at a number of error sensors, J_p, could be minimised. In the limit of an infinite number of evenly spaced error sensors it has been

shown that minimising J_p also results in the total acoustic potential energy being minimised. However, for the case of the lightly damped, low modal density, rectangular acoustic field considered, it has been shown that minimising J_p over just four sensors, one sensor being placed in each of the corners of the enclosure, can result in near optimal reductions in the total acoustic potential energy. The reason for this is that the four corner sensors ensure the detection of the most dominant modes, and thus their attenuation. In contrast, placing the error sensors at nodes of the dominant modes such that these modes are not detected has been shown to result in the total acoustic potential energy generally being increased following the minimisation of J_p, even though the sum of the squared pressures at the error sensors may be substantially reduced.

Another observation from minimising J_p has been that the spatial extent of the reductions in sound pressure level around the error sensor(s) can be substantially less than half a wavelength of the driving frequency. This can be particularly noticeable when the number of secondary sources equals the number of error sensors, and therefore the pressure is constrained to be zero at each of the sensor locations. This effect has been observed even for the very low modal density sound fields considered in Part I when error sensors were placed at nodes of the dominant modes. However, it has been shown to be very prevalent in the more heavily damped, much higher modal density sound fields within the aircraft cabin considered in Part II.

The theoretical possibility of maximising the power absorption of the secondary sources has also been investigated, and the global reductions achieved using this cost function have been shown to be less than those obtained if the same secondary source configuration is set to minimise the total acoustic potential energy. Furthermore, it has been found that, at frequencies lying between mode resonances, maximising the power absorption of the secondary sources can result in the total acoustic potential energy <u>increasing</u>. This is because the secondary sources can act so as to increase the radiation efficiency of the primary source by suitably modifying the pressure acting over the primary source's surface.

The work presented in Part I of the thesis has thus revealed some of the basic mechanisms by which the active control of harmonic enclosed sound fields can produce global reductions in the mean square pressure throughout an enclosed sound field, an effect often questioned. Whilst these conclusions have only been based on results obtained from very simple sound fields, they are equally applicable to much more complex sound fields. For example, if one wishes to reduce the sound levels in an enclosure which is much larger than the wavelength of the pure tone sound exciting it (i.e., the modal density will be high) and if the enclosed field is being excited over a large region of its bounding surface area, then an active noise control system consisting of only a few sources and error sensors (i.e., less than the number of dominantly contributing modes) will not be capable of producing appreciable global reductions. In such a case a strategy which produces localized zones of reduction must be adopted. Even if the primary excitation occurred over a highly localised region ($<< \lambda$) then whilst global reductions may in theory be achieved by locating the secondary sources adjacent to the primary source distribution, in practice the cost function to be minimised is still likely to be the sum of the squared pressures at the error sensors, and with only a few error sensors available it is unlikely that locations can be found which will ensure that global reductions are produced.

8.2 The Application of Active Noise Control to Propeller Induced Cabin Noise

The example cited above leads naturally into Part II of the thesis, in which the possible application of active noise control to a practical problem has been studied. The problem considered was the reduction of propeller induced noise in the passenger cabin of a 48 seat aircraft where the particular frequencies of interest were the propeller blade passage first (88 Hz) and second (176 Hz) harmonic frequencies. In this particular case, and in most other potential practical applications where extended regions of reduction in internal sound pressure level may be desirable (e.g., inside cars, tractor cabs, engine rooms, etc.) the enclosed sound field is neither likely to be of such a low modal density nor is it likely to be so extremely lightly damped as in the situation considered in Part I. Consequently, active noise control systems

consisting of relatively few secondary sources and error sensors are unlikely to be capable of producing appreciable, if any, global reduction (relative here implies the number of secondary sources and error sensors is smaller than the number of dominant acoustic modes). The aim of the work presented in Part II, therefore, has been to assess the effectiveness of applying practically sized control systems (up to 24 sources and 48 error sensors) to produce regions of pressure reduction of a useful spatial extent within the aircraft passenger cabin.

The results presented have all been theoretical predictions obtained using a much simplified analytical model of the structural and acoustic response of the aircraft fuselage and cabin to an assumed external pressure field. Using this analytical approach the fuselage structural response has been modelled as the response of a finite, isotropic shell to a circumferentially convected external pressure field, and the internal cabin acoustic response has been modelled as the response of a hard-walled cylindrical room. Whilst this is a highly idealized model of what is, in practice, a complex situation, theoretical results have been compared with experimentally measured data of the fuselage structural response and the cabin internal sound field. The model has been shown to be capable of producing results which match sufficiently well with experimentally measured data to justify the model's use as a preliminary method of estimating the effectiveness of applying active noise control to reduce propeller induced cabin noise over the frequency range considered.

Using the chosen analytical model results have been obtained which predict the effectiveness of applying active control at the first two propeller blade passage frequency harmonics. At both harmonics it has been attempted to produce a region of acceptably low sound pressure level which encompasses all 48 seated head locations. This has been done by placing up to 48 error sensors over a typical seated head height plane and then by minimising the sum of the squared pressures at these error sensors by the introduction and control of up to 24 secondary sources. The predicted reductions which can be obtained at each of the two harmonics have been found to differ appreciably.

At the fundamental frequency it has been predicted that an 8 source/15 error sensor system can achieve average reductions over the head height plane of 7.8 dB, but at the second harmonic frequency an 8 source/24 error sensor system is required to achieve a predicted average reduction of 4.3 dB evaluated over the same plane. It has also been demonstrated that whilst local reductions of over 35 dB are predicted at both frequencies, these high level reductions in sound pressure level are likely to be much more localized about the error sensor locations at the second harmonic frequency than at the fundamental frequency. The need to concentrate error sensors and secondary sources close to the propeller plane at the second harmonic frequency has also been predicted although the same did not appear to be true at the fundamental frequency where a fairly even spatial distribution of sources and sensors over the length of the cabin has been predicted to be most effective.

The chosen analytical model has been used further to investigate the design and performance of an active noise control system designed to simultaneously cancel the fundamental and second harmonic blade passage frequency components, and also to investigate the possibility of using active noise control in conjunction with propeller synchrophasing.

In general, the predictions suggest that active noise control may well be an effective method of reducing low frequency propeller induced cabin noise.

However, it is recommended that the results of these studies should be treated with caution until the model results can be validated by comparison with in-flight measurements obtained using an experimental active control system. Only when suitable validation studies have been performed can any confidence be placed in the model for it to be used as a possible design tool for specifying a practical active control system for reducing propeller induced cabin noise.

8.3 Suggestions for Further Work

The results presented in Part I of the thesis have demonstrated the basic properties of active noise control when it is applied to enclosed sound fields of low modal density. For the situations considered the effects of secondary source and error sensor locations have been studied, and by physical reasoning it has been possible to place these sources and sensors in effective locations. However, no formal attempt has been made to optimise the number or location of either the secondary sources or the error sensors. It is felt that the possible optimisation of these parameters should be investigated because, although it is not difficult in the low modal density sound fields considered, in situations such as those encountered in the aircraft cabin of Part II the specification of the "best" number and position of the secondary sources and error sensors is no longer clear merely by inspection of the problem.

In performing any source location optimisation, however, it is worth remembering that it will not necessarily be the best strategy to locate the secondary sources where they can produce the largest reduction in the chosen cost function. It may be that, in order to achieve this reduction, some of the source strengths will become impractically large as each secondary source acts to cancel out the fields due to the other secondary sources, as well as the field due to the primary source. In cases such as these it may be more sensible to optimise the secondary source locations with respect to both the reductions obtained and the source strengths necessary to achieve these reductions.

Another feature which arises from the work of Part II is the increasingly localized nature of reductions around the error sensors as the frequency is increased. The change over point from being able to produce global reductions to only being able to achieve local reductions appears to occur at frequencies such that individual modal contributions no longer dominate the acoustic response. This occurs either because the acoustic damping is large, or because the driving frequency is large enough to produce a high modal density sound field. The two frequency ranges are, therefore, separated by the Schroeder frequency. The fundamental work presented in Part I has only considered sound fields well below their Schroeder frequency. Work elsewhere has also shown

that in sound fields well above their Schroeder frequency the zones of reduction which can be achieved are very small and therefore, in order to be effective, any active noise control system must be mounted adjacent to the desired point of quiet (e.g., in headsets). However, in most practical situations (e.g., cars, aircraft) where active noise control might be applied to reduce internal noise levels, the most dominant frequencies to be attenuated are likely to occur somewhere in the transition region lying around the Schroeder frequency. It is therefore suggested that more attention should be focussed on this situation.

As far as the predictions of applying active noise control in the .Ae. 748 aircraft cabin are concerned it is felt that the current set of redicted results must be validated by flight tests before any further ecommendations can be made. However, some comments are felt worthwhile n the modelling of the structural and acoustic responses of the ircraft. Whilst the model used has generally provided results which gree well with the experimental measurements this agreement has been chieved by adjusting certain "unknown" model parameters. Furthermore, ven having performed this matching some features of the responses, and n particular the response of the fuselage around the circumference in he propeller plane, still do not agree very well. For these reasons it s recommended that such a simple model should not be used to represent ircraft other than the test aircraft, unless enough experimental esponse data are available from that aircraft to perform a similar atching procedure. If a more generally applicable model is required hen the effects of stringers and frames should be included (even if only the form of a "smeared" theory) and also the effect of the floor on e structural response should be considered. Also, no account has been ken in the present work of the effect of the cabin trim. This, too, rrants investigation, but not only into how it affects the cabin oustic response and the noise transmission into the cabin, but also as potential method of applying active noise control. For example, ther than using conventional discrete loudspeaker type secondary urces, secondary force actuators could drive the cabin wall trim thus oducing a truly "distributed" secondary source. Such a system could ther be configured to minimise the squared and summed internal essures or it could be configured to minimise some cost function lated to the vibrational amplitude of the trim itself. However, before

any such system could realistically be envisaged the effect of ordinary aircraft trim would first have to be better understood - a major work in itself.

REFERENCES

1. UDF runs at full throttle. 1985 *Flight International*, w.e. 12 October, 20-21.

2. WILBY, J.F., RENNISON, D.C. and WILBY, E.G. 1980 Noise control predictions for high speed, propeller-driven aircraft. *Proceedings of AIAA 6th Aeroacoustics Conference*, paper no. AIAA-80-0999.

3. SALIKUDDIN, M., TANNA, H.K., BURRIN, R.H. and CARTER, W.E. 1984 Application of active noise control to model propeller noise. *Proceedings of the AIAA/NASA 9th Aeroacoustics Conference*, paper no. AIAA-84-2344.

4. BSCHORR, O. 1984 Means for the reduction of noise of rotors. *UK Patent application no.* GB 213053 A.

5. WARNAKA, G.E., TICHY, J., ZALAS, J.M. and POOLE, L.A. 1983 Active control of noise in interior spaces. *Proceedings of Inter-Noise*, 415-418.

6. WARNAKA, G.E. and ZALAS, J.M. 1983 Active cancellation of noise in a closed structure. *UK Patent Application no.* GB 2132 053A.

7. NELSON, P.A. and ELLIOTT, S.J. 1987 Improvements in or relating to active noise reduction. *UK Patent No.* GB 2149 514B.

8. LESTER, H.C. and FULLER, C.R. 1986 Active control of propeller induced noise fields inside a flexible cylinder. *Proceedings of the AIAA 10th Aeroacoustics Conference*, Paper no. AIAA-86-1957.

9. BULLMORE, A.J., NELSON, P.A. and ELLIOTT, S.J. 1986 Active minimisation of acoustic potential energy in harmonically excited cylindrical enclosed sound fields. *Proceedings of the AIAA 10th Aeroacoustics Conference*, Paper no. AIAA-86-1958.

10. ROSS, C.F. 1986 Active noise control. Paper ICAS-86-5.8..3, 1186-1189. Proceedings of the 15th Congress of the International Council of Aeronautical Sciences.

11. OLSEN, H.F. and MAY, E.G. 1953 Electronic sound absorber. *Journal of the Acoustical Society of America* 25(6), 130-1137.

12. WARNAKA, G.E. 1982 Active attenuation of noise - the state of the art. *Noise Control Engineering*, 100-110.

13. FFOWCS-WILLIAMS, J.E. 1984 Anti-Sound. Review Lecture. *Proc. R. Soc. Lond.* A.395, 63-88.

14. LINDQVIST, E. 1983 Active sound reduction: a study of recent developments and some future possibilities. *Chalmers University of Technology*, Report no. F83-06, Gothenburg, Sweden.

15. BREWER, P.A. and LEVENTHALL, H.G. 1985 Active attenuation in small enclosures. *Proceedings of the Institute of Acoustics* 7, Pt.2, 111-114.

16. WHEELER, P.D. and HALLIDAY, S. 1981 An active noise reduction system for aircrew helmets. *NATO AGARD* cp.311.

17. CHAPLIN, G.B.B. and SMITH, R.A. 1983 Waveform synthesis - the Essex solution to repetitive noise and vibration. *Proceedings of Internoise*, 399-402.

18. BERGE, T. 1983 Active noise cancellation of low frequency sound inside vehicle cabs. *Proceedings of Internoise*, 457-460.

19. BERGE, T. 1984 Reduction of diesel engine noise inside passenger compartments using active, adaptive noise control. *Proceedings of Internoise*, 483-488.

20. NADIM, M. and SMITH, R.A. 1983 Synchronous adaptive cancellation in vehicle cabs. *Proceedings of Internoise*, 461-464.

21. CHAPLIN, G.B. 1980 The cancellation of repetitive noise and vibration. *Proceedings of Internoise*, 699-702.

22. SMITH, R.A. and CHAPLIN, G.B.B. 1983 The implications of synchronised cancellation for vibration. *Proceedings of Internoise*, 403-406.

23. OSWALD, L.J. 1984 Reduction of diesel engine noise inside passenger compartments using active, adaptive noise control. *Proceedings of Internoise*, 483-488.

24. CHAPLIN, G.B.B. Jan. 1983 Anti-noise - the Essex breakthrough. *Chartered Mechanical Engineer*, 41-47.

25. ZALAS, J.M. and TICHY, J. 1984 Active attenuation of propeller blade passage noise. *NASA CR*-172386.

26. SHORT, W.R. 1980 Global low frequency active noise attenuation. *Proceedings of Internoise*, 695-698.

27. GUICKING, D. and ROLLWAGE, M. 1984 Active systems in room acoustics - solved and unsolved problems. *Proceedings of Internoise*, 457-462.

. GUICKING, D., KARCHER, K. and ROLLWAGE, M. 1983 Active control of the acoustic reflection coefficient at low frequencies. *Proc. of Inter-Noise*, 419–422.

. ROSS, C.F. 1980 *Active Control of Sound*. Ph.D. Thesis, Cambridge University.

. EATWELL, G. 1986 The measurement of modes in a closed space. *Proceedings of the Euromech Colloquium 213*, Marseille.

. SWINBANKS, M. 1986 An overall perspective of active noise control: the balance between theoretical and practical research. *Proceedings of the Institute of Acoustics* 8 Pt. 1: Active Control of Noise and Vibration.

. PIRAUX, J. and NAYROLES, B. 1980 A theoretical model for active noise attenuation in three dimensional spaces. *Proceedings of Inter-Noise 80*, 703–706.

. MAZZANTI, S. and PIRAUX, J. 1983 An experiment of active noise attenuation in three dimensional space. *Proceedings of Inter-Noise 83*, 427–430.

. NELSON, P.A., CURTIS, A.R.D. and ELLIOTT, S.J. 1985. Quadratic optimisation problems in the active control of free and enclosed sound fields. *Proceedings of the Institute of Acoustics* 7, Pt. 2, 45–53.

. NELSON, P.A., CURTIS, A.R.D., ELLIOTT, S.J. and BULLMORE, A.J. 1987 The active minimisation of harmonic enclosed sound fields; Part I, Theory. *Journal of Sound and Vibration* 117(1),1–13.

. NELSON, P.A., CURTIS, A.R.D. and ELLIOTT, S.J. 1985 The active minimisation of harmonic enclosed sound fields. *Proceedings of the IUTAM Symposium*, Lyon.

. KUTRUFF, H. 1979 *Room Acoustics*. Applied Science Publishers Ltd., London.

. BULLMORE, A.J., NELSON, P.A., ELLIOTT, S.J. and CURTIS, A.R.D. 1987 The active minimisation of harmonic enclosed sound fields; Part II, A computer simulation. *Journal of Sound and Vibration* 117(1), 15–33.

. ELLIOTT, S.J., CURTIS, A.R.D., BULLMORE, A.J. and NELSON, P.A. 1987 The active minimisation of harmonic enclosed sound fields; Part III, An experimental investigation. *Journal of Sound and Vibration* 117(1), 35–58.

. BULLMORE, A.J., ELLIOTT, S.J. and NELSON, P.A. 1986 Mechanisms of the active suppression of harmonic enclosed sound fields. *Proceedings of the Euromech Colloquium 213*, Marseille.

. CURTIS, A.R.D., NELSON, P.A., ELLIOTT, S.J. and BULLMORE, A.J. 1987 Active suppression of acoustic resonance. *Journal of the Acoustical Society of America* 81(3), 624–631.

. CURTIS, A.R.D., NELSON, P.A. and ELLIOTT, S.J. 1985 Active control of one-dimensional enclosed sound fields. *Proceedings of Inter-Noise*, 579–582.

. NELSON, P.A., HAMMOND, J.K. and ELLIOTT, S.J. 1987 Causal constraints on the active control of sound. *Proceedings of the IEEE Conference on Acoustics, Speech and Signal Processing, Dallas*, 145–148.

. MORSE, P.M. 1948 *Vibration and Sound*. McGraw Hill Book Co. Inc. New York.

. MORSE, P.M. and BOLT, R.H. 1944 Sound waves in rooms. *Reviews of Modern Physics* 16(2).

. TAYLOR, J.W.R. (Editor) 1986 *Janes' all the World's Aircraft 1986-87*. Janes' Publishing Co. Ltd., London.

. KOVAL, L.R. 1976 On sound transmission into a thin cylindrical shell under flight conditions. *Journal of Sound and Vibration* 48(2), 265–275.

. JUNGER, M.C. 1987 Analytical model of the structure-borne interior noise induced by a propeller wake. *NASA-CR*-1172381.

. FULLER, C.R. 1984 Noise control characteristics of synchrophasing – an analytic investigation. *Proceedings of the 9th AIAA Aeroacoustics Conference*, Paper AIAA–84–2369.

. FAHY, F.J. 1987 *Sound and Structural Vibration*. Academic Press, London.

. GAUDEFROY, A. 1981 Examples d'attenuation actif de l'energie acoustique du moyen de sources monopolaires voisines drive source primaire ponctuelle. *Comptes Rendus Acad. Sci. Paris Serie B*, 291, 291–301.

. ROEBUCK, I. 1980 Optimisation and the relationship between adaptive signal processing and active noise control. Paper presented to *The Institute of Acoustics*.

. NOBLE, B. 1969 *Applied Linear Algebra*. Englewood Cliffs, New Jersey: Prentice Hall.

. ELLIOTT, S.J. and NELSON, P.A. 1986 The implications of causality in active control. *Proceedings of Inter-Noise*, 583–588.

55. MORSE, P.M. and INGARD, K.U. 1953 *Methods of Theoretical Acoustics*. McGraw Hill, New York.

56. LEWERS, T.H. 1984 The active control of steady single frequency sound in enclosures. *M.Sc. Dissertation*, University of Southampton.

57. NELSON, P.A., ELLIOTT, S.J., CURTIS, A.R.D. and BULLMORE, A.J. 1984 The active control of propeller induced cabin noise. *ISVR Contract Report* no. 84/8.

58. ELLIOTT, S.J. and STOTHERS, I.M. 1986 A multichannel adaptive algorithm for the active control of start-up transients. *Proceedings of Euromech Colloquium 213*, Marseille.

59. ELLIOTT, S.J. and NELSON, P.A. 1986 An adaptive algorithm for multichannel active control. *Proceedings of the Institute of Acoustics* 8, 135-147.

60. ELLIOTT, S.J., STOTHERS, I.M. and NELSON, P.A. 1987 (to appear) A multiple error LMS algorithm and its applications to the active control of sound and vibration. *IEEE Trans. on Acoustics, Speech and Signal Processing*.

61. ADBY, P.R. and DEMPSTER, M.A.H. 1974 *Introduction to Optimisation Methods*. Chapman and Hall, London.

62. SUNYACH, M. and COMTE-BELLOT, G. 1984 Acoustic pressure and intensity fields in active noise control systems. *Proceedings of the 9th AIAA/NASA Aeroacoustics Conference*, Paper no. AIAA-84-2271.

63. KINSLER, L.E., FRY, A.R. COPPENS, A.B. and SANDERS, J.V. 1982 *Fundamentals of Acoustics*, 3rd Edition. Wiley, New York.

64. BODLUND, K. 1980 Monotonic curvature of low frequency decay records in reverberation chambers. *Journal of Sound and Vibration* 73(1), 19-29.

65. DODDS, G. 1972 Assisted resonance and room acoustics in small auditoria. *Ph.D. Thesis*, Univesity of Southampton.

66. BODLUND, K. 1977 A normal mode analysis of the sound power injection in reverberation chambers at low frequencies and the effects of some response averaging methods. *Journal of Sound and Vibration* 55(4), 563-590.

67. WULFFTEN PATHE, D.W. van and VRIES, D. de 1979 Sound power radiated by a velocity monopole under reverberant and under freefield conditions. *Journal of the Acoustical Society of America* 65(2), 411-417.

68. MAGLIOZZI, B. 1980 Acoustic pressures on a prop-fan aircraft fuselage surface. *Proceedings of the 6th AIAA Aeroacoustics Conference*, Paper No. AIAA-80-1002.

69. MIXSON, J.S., BARTON, C.K., PIERSOL, A.G. and WILBY, J.F. 1979 Characteritics of propeller noise on an aircraft fuselage related to interior noise transmission. *Proceedings of the 5th AIAA Aeroacoustics Conference*, Paper NO. AIAA-79-0646.

70. POPE, L.D., WILBY, E.G. and WILBY, J.F. 1984 Propeller aircraft interior noise model. *NASA-CR-172381*.

71. EVERS, J.F. 1986 Private Communication.

72. KOVAL, L.R. 1978 Effects of cavity resonances on sound transmission into a thin cylindricl shell. *Journal of Sound and Vibration* 59(1), 23-33.

73. KOVAL, L.R. 1979 On sound transmission into an orthotropic shell. *Journal of Sound and Vibration* 63(1), 51-59.

74. MAHAN, J.R. and FULLER, C.R. An improved source model for aircraft interior noise studies. *Proceedings of the AIAA 26th SSDM Conference*.

75. FULLER, C.R. 1986 Structural influence of cabin floor on sound transmission into propeller aircraft - analytical investigation. *Proceedings of the AIAA 10th Aeroacoustics Conference*, Paper no. AIAA-86-1940.

76. JONES, J.D. and FULLER, C.R. 1987 Active control of sound fields in elastic cylinders by vibrational inputs. *Proceedings of Noise-Con 87*, 413-418.

77. BHAT, R.B. and MIXSON, J.S. 1978 A theoretical investigation of noise reduction through the cylindrical fuselage of a twin engine, propeller driven aircraft. *NASA-TP-1325*.

78. POPE, L.D., RENNISON, D.C., WILLIS, C.M. and MAYES, W.H. 1982 Development and validation of preliminary analytical models for aircraft interior noise prediction. *Journal of Sound and Vibration* 82(4), 541-575.

79. POPE, L.D., WILBY, E.G., WILLIS, C.M. and MAYES, W.H. 1983 Aircraft interior noise models: Sidewall trim, stiffened structures and cabin acoustics with floor partition. *Journal of Sound and Vibration* 89(3), 371-417.

80. LEISSA, A.W. 1973 Vibration of shells. *NASA-SP-288*.

81- EVERS, J.F. 1986 Private Communication.

85. MAGLIOZZI, B. 1983 Synchrophasing for cabin noise reduction of propeller driven aircraft. *Proceedings of the 8th AIAA Aeroacoustics Conference.* Paper no. AIAA-83-0717.

86. NELSON, P.A. and ELLIOTT, S.J. 1987 Active minimisation of acoustic fields. *ISVR Technical Report* 146.

87. BULLMORE, A.J. 1987 A comparison of simple analytical models for representing propeller aircraft fuselage structural and acoustic responses. *ISVR Technical Report* 153.

APPENDIX A4.1

DETERMINATION OF THE EIGENFUNCTIONS AND EIGENVALUES FOR THE SOUND FIELD IN A "SOFT" WALLED RECTANGULAR ENCLOSURE

The values of k_{n_i} and Φ_{n_i} of equation (4.16) of the main text can be evaluated by applying the boundary conditions of equations (4.12) and (4.13). Firstly, for the surface at $x_i = 0$, substituting equation (4.16) into equation (4.12) yields

$$\Phi_{n_i} = -\coth^{-1}\left(\frac{k_{n_i}}{k\beta^{o}_{x_i}}\right) \qquad \text{(A4.1.1)}$$

and for the surface at $x_i = L_i$, substituting equation (4.16) into equation (4.13) yields

$$\Phi_{n_i} = jk_{n_i}L_i + \coth^{-1}\left(\frac{k_{n_i}}{k\beta^{L}_{x_i}}\right) \qquad \text{(A4.1.2)}$$

Eliminating Φ_{n_i} from equations (1) and (2) gives

$$jk_{n_i}L_i + \coth^{-1}\left(\frac{k_{n_i}}{k\beta^{L}_{x_i}}\right) + \coth^{-1}\left(\frac{k_{n_i}}{k\beta^{o}_{x_i}}\right) = 0 \qquad \text{(A4.1.3)}$$

Equation (A4.1.3) has an infinity of roots. Provided both $\beta^{o}_{x_i}$ and $\beta^{L}_{x_i}$ are small, these roots can be evaluated by using the first terms of a power series expansion of equation (A4.1.3), so expanding $\coth^{-1}$ as $(1/x + 1/3x^2 \ldots)$ gives

$$k_{n_i} = \left(\frac{jk}{L_i}\right)^{1/2}\left(\beta^{o}_{x_i} + \beta^{L}_{x_i}\right)^{1/2}\left[1 - \frac{jkL_x}{6}\frac{\left(\left(\beta^{o}_{x_i}\right)^3 + \left(\beta^{L}_{x_i}\right)^3\right)}{\left(\beta^{o}_{x_i} + \beta^{L}_{x_i}\right)^2} + \ldots\ldots\right]$$

$$n_i = 0$$

$$k_{n_1} = \frac{n_1\pi}{L_x} + \frac{jk}{n_1\pi}(\beta^o_{x_1} + \beta^L_{x_1}) + \frac{k^2 L_x}{\pi^3 n_1^3}(\beta^o_{x_1} + \beta^L_{x_1})^2 + \ldots \qquad n_1 > 0$$

(A4.1.4)

Situations where one or both of the walls are quite soft will not be dealt with here. Appropriate solutions of equation (A4.1.3) for these cases have been presented by Morse and Bolt [45]. For the case where both walls are fairly hard, substituting equations (A4.1.1) and (A4.1.4) into equation (4.16), noting that $\coth^{-1}(k_{x_1}/k\beta^o_{n_1}) \simeq (k\beta^o/k_{x_1})$ as $k\beta^o_{x_1} << 1$, yields for the x_1 dependent eigenfunction

$$\psi_{n_1}(x_1) = \cosh\left\{\left[\frac{kL_1}{j(\beta^o_{x_1} + \beta^L_{x_1})}\right]^{1/2} \frac{1}{L_1}(\beta^o_{x_1} L_1 - \beta^o_{x_1} x_1 - \beta^L_{x_1} x_1)\right\} \qquad n_1 = 0$$

(A4.1.5)

$$\psi_{n_1}(x_1) = \cosh\left\{\left[\frac{jn_1\pi x_1}{L_1}\right] - \frac{k}{n_1\pi}\left[(\beta^o_{x_1} x_1 + \beta^L_{x_1} x_1) - \frac{\beta^o_{x_1} L}{1 + \frac{jk(\beta^o_{x_1} + \beta^L_{x_1})L_1}{n_1^2\pi^2}}\right]\right\} \qquad n_1 > 0$$

with similar expressions being obtained for the x_2 and x_3 components. The natural frequency (ω_n) and damping constant (C_n) of each mode may now be evaluated by inserting equations (A4.1.5) into the Helmholtz equation, which can be written from equation (4.9) as

$$\frac{\partial^2\psi_n(x_1)}{\partial x_1^2} + \frac{\partial^2\psi_n(x_2)}{\partial x_2^2} + \frac{\partial^2\psi_n(x_3)}{\partial x_3^2} + \frac{(\omega_n + jC_n)^2}{c^2} = 0 \qquad (A4.1.6)$$

Performing these substitutions and simplifying the resulting expression, discarding terms in which the admittance ratio is squared as being negligible ($\beta^2 << \beta$), yields

$$(\omega_n + jC_n)^2 = c^2\pi^2\left[\left\{\left(\frac{n_1}{L_1}\right)^2 - \frac{\epsilon_{n_1} k}{L_1\pi^2}(\sigma^o_{x_1} + \sigma^L_{x_1})\right\} + \right.$$

$$\left\{\left(\frac{n_1}{L_2}\right)^2 - \frac{\epsilon_{n_2} k}{L_2\pi}(\sigma^o_{x_2} + \sigma^L_{x_2})\right\} + \left\{\left(\frac{n_3}{L_3}\right)^2 - \frac{\epsilon_{n_3} k}{L_3\pi^2}(\sigma^o_{x_3} + \sigma^L_{x_3})\right\}\Big]$$

$$+ \frac{jc\omega}{4V}[4\epsilon_{n_1}(\kappa^o_{x_1} + \kappa^L_{x_1})S_1 + 4\epsilon_{n_2}(\kappa^o_{x_2} + \kappa^L_{x_2})S_2$$

$$+ 4\epsilon_{n_3}(\kappa^o_{x_3} + \kappa^L_{x_3})S_3] \qquad \text{(A4.1.7)}$$

where $\epsilon_n = 1$ if $n = 0$, or $\epsilon_n = 2$ if $n > 0$. Also $S_1 = L_2L_3$, $S_2 = L_1L_3$, $S_3 = L_1L_2$ and $\beta = \kappa + j\sigma$, where κ is the specific acoustic conductance and σ is the specific acoustic susceptance. Equating real and imaginary parts of equation (A4.1.7), neglecting C_n^2 as being negligibly small compared to ω_n^2, gives

$$\omega_n = c\pi\left[\left\{\left(\frac{n_1}{L_1}\right)^2 - \frac{\epsilon_{n_1} k}{L_1\pi^2}(\sigma^o_{x_1} + \sigma^L_{x_1})\right\}\right.$$

$$\left.\left\{\left(\frac{n_2}{L_2}\right)^2 - \frac{\epsilon_{n_2} k}{L_2\pi}(\sigma^o_{x_2} + \sigma^L_{x_2})\right\} + \left\{\left(\frac{n_3}{L_3}\right)^2 - \frac{\epsilon_{n_3} k}{L_3\pi^2}(\sigma^o_{x_3} + \sigma^L_{x_3})\right\}\right]^{1/2}$$

(A4.1.8)

$$2C_n\omega_n = \frac{c\omega}{4V}[4\epsilon_{n_1}(\kappa^o_{x_1} + \kappa^L_{x_1})S_1 + 4\epsilon_{n_2}(\kappa^o_{x_2} + \kappa^L_{x_2})S_2$$

$$+ 4\epsilon_{n_3}(\kappa^o_{x_3} + \kappa^L_{x_3})S_3] \qquad \text{(A4.1.9)}$$

However, from the form of equation (2.24) it is apparent that the damping term only affects the modal response appreciably when the driving frequency, ω, is close to the modal natural frequency, ω_n.

Consequently, ω on the right hand side of equation (A4.1.9) may be replaced by ω_n and the acoustic pressure response may be written as

$$p(\underline{x},\omega) = \frac{\omega\rho c^2}{V} \sum_{n=0}^{\infty} \frac{\psi_n(\underline{x}) \int_S v_n(\underline{x}_S,\omega)\psi_n(\underline{x}_S)ds}{2\omega_n C_n - j(\omega_n^2 - \omega^2)} \qquad \text{(A4.1.10)}$$

where the damping constant is given by

$$C_n = \frac{c}{8V} [4\epsilon_{n_1}(\kappa^o_{x_1} + \kappa^L_{x_1})S_1 + 4\epsilon_{n_2}(\kappa^o_{x_2} + \kappa^L_{x_2})S_2$$

$$+ 4\epsilon_{n_3}(\kappa^o_{x_3} + \kappa^L_{x_3})S_3] \qquad \text{(A4.1.11)}$$

and where the modal natural frequencies are given by equation (A4.1.8). Note that from the derivation of equation (A4.1.10) in Section 2.3, the eigenfunctions must be normalized according to

$$\int_V \psi_n^2(\underline{x})dV = V \qquad \text{(A4.1.12)}$$

Substituting equations (A4.1.5) into equation (A4.1.12) yields for the x_1 component of the normalised eigenfunctions

$$\psi_{n_1}(x_1) = \frac{\cosh\left\{\left(\frac{kL_1}{j(\beta^o_{x_1} + \beta^L_{x_1})}\right)^{1/2} \frac{1}{L_1}(\beta^o_{x_1} L - \beta^o_{x_1} x_1 - \beta^L_{x_1} x_1)\right\}}{\left\{1 - \frac{jkL_1}{3} \frac{((\beta^o_{x_1})^3 + (\beta^L_{x_1}))}{(\beta^o_{x_1} + \beta^L_{x_1})^2}\right\}} \qquad n_1 = 0$$

$$\psi_{n_1}(x_1) = \frac{\cosh\left\{\left(-\frac{jn_1\pi x_1}{L_1}\right) - \frac{k}{n_1\pi}\left(\beta^o_{x_1} x_1 + \beta^{L_1}_{x_1} x_1 - \frac{\beta^o_{x_1} L}{jk(\beta^o_{x_1} + \beta^L_{x_1})L_1}\right)\right\}}{1 + \frac{x_1}{n_1^2\pi^2}} \Big/ \left\{1 - \frac{jkL_1}{n^2\pi^2}(\beta^o_{x_1} + \beta^L_{x_1})\right\}^{1/2} \qquad n_1 > 0 \quad \text{(A4.1.13)}$$

with similar expressions being obtained for the x_2 and x_3 components of the eigenfunctions.

Thus, use of equations (A4.1.10), (A4.1.11), (A4.1.12) and (A4.1.13) enables the evaluation of the acoustic pressure response within a rectangular enclosure when the walls have a small, but non zero, admittance. The accuracy of these equations is governed primarily by the value of the admittance being considered, the greatest error being introduced by the truncation of the power series of equations (A4.1.4).

APPENDIX A5.1

A DISCUSSION ON THE USE OF REVERBERATION TIME AND STEADY STATE POWER BALANCE TECHNIQUES TO EVALUATE ACOUSTIC DAMPING AT LOW FREQUENCIES

The pressure at a point ($\underline{r}$) due to a point source at location ($\underline{r}_S$) having a harmonic volume velocity, $Q(\omega)$, is given from equation (5.1) of the main text as

$$p(\underline{r},\omega) = \frac{\omega\rho c^2}{V} \sum_N \frac{\psi_n(\underline{r})\psi_n(\underline{r}_S)Q(\omega)}{2\omega_n C_n - j(\omega_n - \omega^2)} \qquad \text{(A5.1.1)}$$

When dealing with reverberation time and steady state power measurements it is the mean squared pressure which is usually considered. This is obtained from equation (A5.1.1):

$$\tfrac{1}{2}|p(\underline{r}_S,\omega)|^2 = \tfrac{1}{2}p(\underline{r},\omega)p^*(\underline{r},\omega) = |Q(\omega)|^2 \frac{\omega^2\rho^2c^4}{2V^2} \sum_N \sum_{N'} \psi_n(\underline{r})\psi_{n'}(\underline{r}) \times$$

$$\psi_n(\underline{r}_S)\psi_{n'}(\underline{r}_S) \frac{2\omega_n C_n + j(\omega_n^2 - \omega^2)}{4\omega_n^2 C_n^2 + (\omega_n^2 - \omega^2)^2} \cdot \frac{2\omega_{n'} C_{n'} - j(\omega_{n'}^2 - \omega^2)}{4\omega_{n'}^2 C_{n'}^2 + (\omega_{n'}^2 - \omega^2)^2} \qquad \text{(A5.1.2)}$$

Thus the evaluation of the mean square pressure at a fixed point in a room due to a source at another fixed point in the room necessitates a double summation over the necessary number of room modes to ensure convergence of equation (A5.1.2). It also requires the exact form of the room eigenfunctions to be known, so that the extent to which each mode is both excited by the source and detected by the sensor can be predicted. In the present case of the sound field within an aircraft cabin it is hoped that using cylindrical room eigenfunctions may adequately model the true eigenfunctions such that gross features of the sound field may be predicted. It is not expected that these very simple functions will be able to predict the presure point for point. Consequently, in order to make equation (A5.1.2) useful in practice, it will be necessary to volume average both the source and sensor

locations. Thus, equation (A5.1.2) becomes

$$\langle |p(\omega)|^2 \rangle = \frac{\omega^2 \rho^2 c^4 |Q(\omega)|^2}{2V^2} \sum_N \frac{1}{4\omega_n^2 C_n^2 + (\omega_n^2 - \omega^2)^2} \qquad \text{(A5.1.3)}$$

where $\langle\ \rangle$ indicates a volume average, and where, due to the orthogonal properties of the modes, all the mode cross terms have reduced to zero. Equation (A5.1.3) represents the volume averaged mean squared pressure due to a harmonic driving signal. In practice when making either steady state power measurements or reverberation time measurements the excitation signal often used is white noise. This type of excitation can be accounted for in equation (A5.1.3) by replacing $|Q(\omega)|^2$ with the spectral density of the source volume velocity, $S_Q(\Delta\omega)$ (where this represents a filtered white noise signal having a bandwidth of $\Delta\omega$), and by integrating over the frequency range of the excitation, so the mean square volume averaged pressure is given by

$$\overline{\langle p^2(\Delta\omega) \rangle} = \frac{\rho^2 c^4}{2V^2} \int_{\omega_1}^{\omega_2} \sum_N \frac{S_Q(\Delta\omega).\omega^2}{4\omega_n^2 C_n^2 + (\omega_n^2 - \omega^2)^2} \, d\omega \qquad \text{(A5.1.4)}$$

where $\overline{\quad}$ indicates a time average.

Integral expressions similar to this have been derived by Bodlund [66] and Wulfften Pathe *et al* [67]. However it has been rederived here because of the confusion which can so easily arise from differing notation from text to text, particularly in the definition of the damping term. Solutions to this integral are presented in both of references [66] and [67]. In Reference [66] the integral is evaluated by substitution, although in order to do this some assumptions must be made. Firstly it must be assumed that only modes having natural frequencies within the source bandwidth are excited. Thus the integral limits may be extended from zero to infinity. Secondly, because the

integral term is largest when $\omega \simeq \omega_n$, it will make negligible difference substituting $\omega_n\omega$ for ω^2 in the numerator. Therefore the integral becomes

$$\overline{\langle p^2(\Delta\omega)\rangle} = \frac{\rho^2c^4}{2V^2} S_Q(\Delta\omega)\int_0^\infty \sum_{n\in\Delta\omega} \frac{\omega_n\omega}{4\omega_n^2C_n^2 + (\omega^2 - \omega_n^2)^2}\, d\omega \qquad \text{(A5.1.5)}$$

which, when evaluated and simplified, yields

$$\overline{\langle p^2(\Delta\omega)\rangle} = \frac{\rho^2c^4S_Q(\Delta\omega)\pi}{8V^2} \sum_{n\in\Delta\omega} \frac{1}{C_n} \qquad \text{(A5.1.6)}$$

Reference [67] evaluates the integral of equation (A5.1.4) by the method of residues. In order to make this possible, the assumption must again be made that only modes having natural frequencies within the source bandwidth are excited. Also it must be assumed that because the magnitude of the integrand is only significantly affected by the damping term when $\omega \simeq \omega_n$, then the $\omega_n^2C_n^2$ term in the denominator can be replaced by $\omega^2C_n^2$. Having made these assumptions, the integral may be evaluated to give the same result as in equation (A5.1.6).

Equation (A5.1.6) thus presents a means of estimating the volume averaged mean square pressure in the aircraft cabin provided the source volume velocity is known, and provided, too, that the damping constants for each of the modes can be determined. However, it is the inverse of this problem which we desire to solve; that is, if the mean square pressure in the room can be measured, either in the steady state or transient state, is it possible to estimate the damping constants from the measurements?

Consider first transient measurements. If an initially steady noise source is suddenly turned off at time $t = 0$ then, according to Morse and Ingard [55], the subsequent pressure wave is given by

$$p(t) = \sum_{n\in\Delta\omega} D_n e^{-C_n t} \cos(\omega_n t + \Phi_n) \qquad t > 0 \qquad \text{(A5.1.7)}$$

where D_n specifies the extent to which the n'th mode was excited just before the source was turned off, and Φ_n specifies the phase of the n'th mode. From equation (A5.1.7) the short time averaged mean square pressure can be written as [37]

$$\overline{p^2(t)} = \sum_{n\in\Delta\omega} \frac{D_n^2}{2} e^{-2C_n t} \qquad \text{(A5.1.8)}$$

and therefore, from equations (A5.1.6) and (A5.1.8), the volume average decay of the mean squared pressure can be expressed as

$$\langle\overline{p^2(\Delta\omega,t)}\rangle = \frac{\rho^2 c^4 S_Q(\Delta\omega)\pi}{8V^2} \sum_{n\in\Delta\omega} \frac{e^{-2C_n t}}{C_n} \qquad \text{(A5.1.9)}$$

where for the assumed cylindrical cabin the damping constants, C_n, can be substituted from equation (5.6) of the main text. Thus the sound pressure decay is seen to consist of a number of individual modal decays, with each mode potentially having a different rate of decay and different initial amplitude. If this is the case, then the measured decay curve will not be linear, as would be expected from diffuse field theory. Consequently it will not be possible to estimate the effective absorption unless the mode structure of the sound field is known exactly to allow the type of mode, or indeed the combination of modes, responsible for each region of decay to be determined. This type of approach could be used for very simple enclosures for which the modes can be determined with reasonable accuracy, but for the case of an irregularly shaped aircraft cabin it is concluded that this technique is not a feasible proposition.

An alternative method which can be used to estimate the absorption is

the steady state power balance method. Like the reverberation time technique this is widely used in situations where the frequency is high enough such that the sound field can be considered as diffuse. The basic principle is that, if a source of known power output is placed in a room and the mean square pressure in that room is measured, then these two can be related by the knowledge that in the steady state the power input to the room must equal the power lost. If the frequency is low enough, then it can be assumed that all the energy absorption occurs at the enclosure boundaries, and therefore a simple relationship can be determined between the wall absorption coefficients, the power input to the room and the mean squared pressure throughout the room. However, if the frequency is too low, then the sound field will no longer be diffuse and this simple relationship will no longer apply. In such instances the normal mode type of analysis used to derive equation (A5.1.6) is more appropriate, but the question must now be addressed as to whether there remains a simple relationship beween the source power output, the volume averaged mean square pressure, and the acoustic damping. Equation (A5.1.6) presents a relationship between the source volume velocity, the mean squared pressure and the damping. However, in practice it is the power output of the source which is usually used to characterize the source strength. Therefore a relationship is required between the source power output and the source volume velocity. The acoustic power output, W, of a high internal impedance source can be determined by integrating the total power absorbed at the enclosure walls [64]. So, from equation (4.25)

$$W = \int_S \frac{1}{16} \left(p^*(\underline{x}_S,\omega)p(\underline{x}_S,\omega)\right) \frac{\bar{\alpha}}{\rho c} \, ds \qquad \text{(A5.1.10))}$$

where the relationship $\bar{\alpha} \simeq 8\kappa$ has been used. Unfortunately, as pointed out by Bodlund [64], if equation (A5.1.10) is evaluated the relationship between the sound power output and the volume velocity of the source is not at all simple and therefore this method of estimating the acoustic damping is discarded.

An alternative possibility for using the power balance method has been presented by Wulfften Pathe *et al* [67]. Using this method the mean square pressure is expressed as a function of the free field power output of a source, $W_o(\Delta\omega)$, the modal damping constants, C_n, and the high frequency asymptotic value of the number of modes ($M_o = \omega^3 V/6\pi^2 c^3$) excited in the source bandwdith, to give

$$\langle\overline{p^2(\Delta\omega)}\rangle = W_o(\Delta\omega)\,\frac{4\rho c}{M_o}\sum_{n\in\Delta\omega}\frac{1}{C_n} \qquad \text{(A5.1.11)}$$

If C_n is substituted from equation (5.6) (or equation (4.21) as this formula holds equally well for rectangular shaped enclosures), then the similarity between equation (A5.1.11) and the equivalent diffuse field equation, given by [37]

$$\overline{p^2} = \frac{4\rho c W}{\bar{\alpha} S} \qquad \text{(A5.1.12)}$$

becomes evident, and in the high frequency limit (as N tends to M_o, W tends to W_o, $\overline{p^2}$ tends to $\langle\overline{p^2}\rangle$ and as oblique modes tend to dominate the response) the two become equal. Because the free field power output of a source is easily measured, and because M_o can be calculated provided a simple enough room geometry is chosen, equation (A5.1.11) appears to be practically attractive. However, because of the assumptions that have been made in order to derive this equation, its use in estimating the low frequency absorption in the aircraft cabin could lead to erroneous results. The main assumptions are now discussed.

ASSUMPTION 1. Only modes having natural frequencies within the bandwidth are excited:-

For a lightly damped room having either an extremely low modal density with respect to the source bandwidth, or alternatively a reasonably high modal density, it may be true that modes having natural

frequencies outside the source bandwidth will contribute negligibly to the sound field. However, in the intermediate modal density region, and in particular if the damping is increased, it is quite possible that modes lying outside the source bandwidth will contribute significantly.

ASSUMPTION 2. A true volume averaging of both source and sensor locations must be performed.

At the frequencies of interest in the aircraft cabin (i.e., below 200 Hz) the modal structure of the sound field is likely to be such that large spatial variations in the mean squared pressure can occur. Therefore very many averages would have to be taken to ensure true volume averaging.

ASSUMPTION 3. The modes in the cabin space correspond to those which can exist in a cylindrical room.

This assumption has to be made for a number of reasons. Firstly because the high frequency asymptotic limit of the number of modes in the bandwidth needs to be evaluated, and in order to do this the permissible modes must be known. Secondly, because it must be known which modes are excited in the bandwidth, and how the modal damping constant depends on each of these modes. However, in the present case, cylindrical room modes have been chosen to represent a space which consists of a cylinder with a longitudinal partition (a floor), several vertical partitions (the bulkheads) and with many other intrustions into the volume of the space (e.g., the luggage bins and seats).

When these assumptions have all been taken into account, it is seen that several potential sources of error will exist if equation (A5.1.11) is applied to the evaluation of the aircraft cabin acoustic damping at low frequencies, and whilst the relative importance of these errors have not been evaluated, it was decided that the extra computation involved would not justify the use of this method to estimate the low frequency

absorption in this situation. Instead, the standard diffuse field theory of equation (A5.1.12) was used as a quick and simple method of estimating the acoustic absorption in the cabin, even for the lowest frequency band measured (125 Hz). Whilst this method is obviously susceptible to considerable errors, the agreement obtained between the results obtained using this method and those obtained using the transfer impedance method of estimating the acoustic absorption showed reasonable agreement.

APPENDIX 6.1

EVALUATING THE INTEGRALS OF EQUATION (6.16) OF THE MAIN TEXT

It is simplest if each integral is split into two parts. Thus the z-dependent integrals are

$$I_{z1} = \int_{o}^{z_o} e^{-d(z_o-z)} \sin\left(\frac{r_1 \pi z}{L_z}\right) dz \qquad \text{(A6.1.1)}$$

and

$$I_{z2} = \int_{z_o}^{L_z} e^{-d(z-z_o)} \sin\left(\frac{r_1 \pi z}{L_z}\right) dz \qquad \text{(A6.1.2)}$$

which on integrating by parts yields for equation (A6.1.1)

$$I_{z1} = \left| e^{-d(z_o-z)} \; \frac{\{d \sin\left(\frac{r_1 \pi z}{L_z}\right) - \left(\frac{r_1 \pi}{L_z}\right)\cos\left(\frac{r_1 \pi z}{L_z}\right)\}}{(d^2) + \left(\frac{r_1 \pi}{L_z}\right)^2} \right|_{o}^{z_o} \qquad \text{(A6.1.3)}$$

and, similarly, for the second integral

$$I_{z2} = \left| e^{-d(z-z_o)} \; \frac{\{-d \sin\left(\frac{r_1 \pi z}{L_z}\right) - \left(\frac{r_1 \pi}{L_z}\right)\cos\left(\frac{r_1 \pi z}{L_z}\right)\}}{(d^2) + \left(\frac{r_1 \pi}{L_z}\right)^2} \right|_{z_o}^{L_z} \qquad \text{(A6.1.4)}$$

The θ-dependent integrals are

$$I_{\theta 1} = \int_{\theta_1}^{\theta_o} \left(\frac{\theta - \theta_1}{\theta_o - \theta_1}\right) e^{jk_\theta \theta} \cos\left(r_2\theta - \frac{r_3\pi}{2}\right) a\,d\theta \qquad \text{(A6.1.5)}$$

and

$$I_{\theta 2} = \int_{\theta_o}^{\theta_2} \left(\frac{\theta_2 - \theta}{\theta_2 - \theta_o}\right) e^{jk_\theta \theta} \cos\left(r_2\theta - \frac{r_3\pi}{2}\right) a\,d\theta \qquad \text{(A6.1.6)}$$

Expanding the first equation gives

$$I_{\theta 1} = \int_{\theta_1}^{\theta_o} \left(\frac{1}{\theta_o - \theta_1}\right)\left(\theta e^{jk_\theta \theta} \cos\left(r_2\theta - \frac{r_3\pi}{2}\right) - \theta_1 e^{jk_\theta \theta} \cos\left(r_2\theta - \frac{r_3\pi}{2}\right)\right) a\,d\theta \qquad \text{(A6.1.7)}$$

which, on integrating by parts yields

$$I_{\theta_1} = \left|\frac{-1}{(\theta_o - \theta_1)}\left\{\theta_1\left[e^{jk_\theta \theta} \frac{(jk_\theta \cos\left(r_2\theta - \frac{r_3\pi}{2}\right) + r_2 \sin\left(r_2\theta - \frac{r_3\pi}{2}\right))}{(jk_\theta)^2 + (r_2)^2}\right]\right.\right.$$

$$+ \left[\theta e^{jk_\theta \theta} \frac{(jk_\theta \cos\left(r_2\theta - \frac{r_3\pi}{2}\right) + r_2 \sin\left(r_2\theta - \frac{r_3\pi}{2}\right))}{(jk_\theta)^2 + (r_2)^2}\right.$$

$$\left.\left.\left. - e^{jk_\theta \theta} \frac{(((jk_\theta)^2 - (r_2)^2)\cos\left(r_2\theta - \frac{r_3\pi}{2}\right) + 2jk_\theta r_2 \sin\left(r_2\theta - \frac{r_3\pi}{2}\right))}{((jk_\theta)^2 + (r_2)^2)^2}\right]\right\}\right|_{\theta_1}^{\theta_o} \qquad \text{(A6.1.8)}$$

Similarly, the second integral can be expanded and integrated by parts to give

$$I_{\theta z} = \left|\frac{1}{(\theta_z - \theta_o)}\left\{\theta_z\left[e^{jk_\theta\theta}\,\frac{(jk_\theta\cos(r_z\theta - \frac{r_3\pi}{2}) + r_z\sin(r_z\theta - \frac{r_3\pi}{2}))}{(jk_\theta)^2 + (r_z)^2}\right]\right.\right.$$

$$- \left[\theta e^{jk_\theta\theta}\,\frac{(jk_\theta\cos(r_z\theta - \frac{r_3\pi}{2}) + r_z\sin(r_z\theta - \frac{r_3\pi}{2}))}{(jk_\theta)^2 + (r_z)^2}\right.$$

$$\left.\left. - e^{jk_\theta\theta}\,\frac{\{((jk_\theta)^2 - (r_z)^2)\cos(r_z\theta - \frac{r_3\pi}{2}) + 2jk_\theta r_z\sin(r_z\theta - \frac{r_3\pi}{2})\}}{((jk_\theta)^2 + (r_z)^2)^2}\right]\right\}\Bigg|_{\theta_o}^{\theta_z}$$

(A6.1.9)

APPENDIX 6.2

EVALUATING THE INTEGRAL OF EQUATION (6.17) OF THE MAIN TEXT

The integral to be evaluated is of the form

$$I = \int_{\theta_1}^{\theta_2}\int_{z_1}^{z_2} \sin\left(\frac{r_1\pi z}{L_z}\right)\cos\left(r_2\theta - \frac{r_3\pi}{2}\right)\cos\left(\frac{n_1\pi z}{L_z}\right)\cos\left(n_2\theta - \frac{n_4\pi}{2}\right)a\,dz\,d\theta \qquad (A6.2.1)$$

First evaluating the integral over the circumferential coordinate, θ, or

$$I_\theta = \int_{\theta_1}^{\theta_2} \cos\left(r_2\theta - \frac{r_3\pi}{2}\right)\cos\left(n_2\theta - \frac{n_4\pi}{2}\right)a\,d\theta \qquad (A6.2.2)$$

On integrating by parts, six possible solutions are obtained

(a) $r_2 = n_2, \quad r_3 = n_4 = 0$

$$I_\theta = a\left|\frac{\theta}{2} + \frac{\sin(2n_2\theta)}{4n_2}\right|_{\theta_1}^{\theta_2} \qquad (A6.2.3)$$

If $\theta_2 - \theta_1 = 360^\circ$ then this reduces to

$$I_\theta = a\pi\,\frac{2}{\epsilon_{n_2}} \qquad \text{where} \quad \epsilon_n = 1, \quad n_2 = 0$$
$$= 2, \quad n_2 > 0$$

(b) $r_2 = n_2, \quad r_3 = n_4 = 1$

$$I_\theta = a\left|\frac{\theta}{2} - \frac{(\sin 2n_2\theta)}{4n_2}\right|_{\theta_1}^{\theta_2} \qquad (A6.2.4)$$

If $\theta_2 - \theta_1 = 2\pi$ then this reduces to

$$I_\theta = 0, \qquad n_2 = 0$$

$$= a\pi, \qquad n_2 > 0$$

(c) $r_2 \neq n_2, \quad r_3 = n_4 = 0$

$$I_\theta = \left| \frac{\sin(r_2 - n_2)\theta}{2(r_2 - n_2)} + \frac{\sin(r_2 + n_2)\theta}{2(r_2 + n_2)} \right|_{\theta_1}^{\theta_2} \qquad \text{(A6.2.5)}$$

$$= 0 \quad \text{if} \quad \theta_2 - \theta_1 = 360^\circ$$

(d) $r_2 \neq n_2, \quad r_3 = n_4 = 1$

$$I_\theta = \left| \frac{\sin(r_2 - n_2)\theta}{2(r_2 - n_2)} - \frac{\sin(r_2 + n_2)\theta}{2(r_2 + n_2)} \right|_{\theta_1}^{\theta_2} \qquad \text{(A6.2.6)}$$

$$= 0 \quad \text{if } \theta_2 - \theta_1 = 360^\circ$$

(e) $r_2 = n_2, \quad r_3 \neq n_4$

$$I_\theta = \left| \frac{\sin^2 n_2\theta}{2n_2} \right|_{\theta_1}^{\theta_2} \qquad \text{(A6.2.7)}$$

$$= 0 \quad \text{if} \quad \theta_2 - \theta_1 = 360^\circ$$

(f) $r_2 \neq n_2, \quad r_3 \neq n_4$

$$I_\theta = \left| \frac{-\cos(r_2 - n_2)\theta}{2(r_2 - n_2)} - \frac{\cos(r_2 + n_2)\theta}{2(r_2 + n_2)} \right|_{\theta_1}^{\theta_2} \qquad \text{(A6.2.8)}$$

$$= 0 \quad \text{if} \quad \theta_2 - \theta_1 = 360^\circ.$$

Thus, if the shell structural response is allowed to excite the acoustic field over its entire circumference then, due to the orthogonal nature of the circumferential modes, only those structural and acoustic modes having the same mode order ($r_2 = n_2$, $r_3 = n_4$) can couple, and the

expression for the circumferential integral reduces to

$$I_\theta = a\pi \frac{2}{\epsilon_{n_z}} \qquad r_2 = n_2,\ r_3 = n_4 \qquad \text{(A6.2.9)}$$

However, this only occurs if the entire circumference of the shell is assumed to drive the acoustic modes (e.g., the coupling integrals are evaluated from 0 to 2π). If it is instead assumed that only part of the cabin wall vibration excites the acoustic modes, then the orthogonality of the structural and acoustic modes will no longer ensure that the $r_2 r_3$'th structural circumferential modes will only be able to excite the acoustic circumferential modes having the same order ($r_2 = n_2$, $r_3 = n_4$), although this is still likely to be the dominantly excited mode. If this situation exists, then all of equations (A6.2.3) to (A6.2.8) must be used to evaluate the total coupling of the structural vibration to each acoustic mode, with the appropriate upper and lower circumferential integration limits substituted for θ_1 and θ_2.

Now evaluating the axial integral

$$I_z = \int_{z_1}^{z_2} \sin\left(\frac{r_1 \pi z}{L_z}\right)\cos\left(\frac{n_1 \pi z}{L_z}\right)dz \qquad \text{(A6.2.10)}$$

Integrating by parts yields two possible solutions

(a) $r_1 \neq n_1$

$$I_z = \left| -\frac{\cos(r_1 - n_1)\frac{\pi z}{L_z}}{\left(\frac{2(r_1 - n_1)\pi}{L_z}\right)} - \frac{\cos(r_1 + n_1)\frac{\pi z}{L_z}}{\left(\frac{2(r_1 + n_1)\pi}{L_z}\right)} \right|_{z_1}^{z_2} \qquad \text{(A6.2.11)}$$

If $z_1 = 0$ and $z_2 = L_z$ this reduces to

$$= \frac{L_z}{2\pi}\left\{-\frac{\cos(r_1 - n_1)\pi}{(r_1 - n_1)} - \frac{\cos(r_1 + n_1)\pi}{(r_1 + n_1)} + \frac{1}{(r_1 - n_1)} + \frac{1}{(r_1 + n_1)}\right\}$$

$$= \frac{L_z}{\pi}\left\{\frac{r_1}{r_1^2 - n_1^2}\right\} \qquad r_1 + n_1 \text{ odd}$$

$$= 0 \qquad r_1 + n_1 \text{ even} \qquad \text{(A6.2.12)}$$

(b) $r_1 = n_1$

$$I_z = \left|\frac{\sin^2(\frac{n_1\pi z}{L_z})}{\frac{2n_1\pi}{L_z}}\right|_{z_1}^{z_2} \qquad \text{(A6.2.13)}$$

$= 0$ if $z_1 = 0$ and $z_2 = L_z$

Notice again that, due to the integral properties of the products of the cosine and sine functions, if the shell structural response is allowed to excite the acoustic field over the entire shell length, then each structural mode can only selectively excite a few acoustic modes. However, if the structural excitation of the acoustic field is truncated short of the shell ends (i.e., $z_1 \neq 0$ and $z_2 \neq L_z$) then many more acoustic modes can be excited.

From the above results the integral contained in equation (6.17) of the main text is given by

$$I = a\,\frac{2}{\epsilon n_z}\,L_z\left\{\frac{r_1}{r_1^2 - n_1^2}\right\} \qquad \text{(A6.2.14)}$$

APPENDIX 6.3

THE RELATIVE ACOUSTIC MODAL CONTRIBUTIONS TO THE TOTAL ACOUSTIC POTENTIAL ENERGY WITHIN THE SHELL

Table A6.3.1 lists the relative acoustic mode contributions to the total acoustic potential energy within the shell when it is excited by the unmodified 88 Hz shell structural response of Figure 6.14. The first twenty modes have been listed in order of decreasing level, where the specified levels have been expressed in decibels relative to the contribution of the most dominant mode in each case. Table A6.3.2 lists the relative acoustic mode contributions within the shell when it is excited by the 176 Hz shell structural response of Figure 6.15. From Tables A6.3.1 and A6.3.2 it is seen that no axisymmetric acoustic modes are present in either of the lists, thereby supporting the assumption made in Section 6.6.3 that the low pressure region running along the centre of the predicted pressure fields may be due to a dominance of non-axisymmetric ($n_2 > 0$) acoustic modes. Tables A6.3.3 and A6.3.4 list the relative volume averaged acoustic mode contributions to the internal sound fields corresponding to the internal pressure fields of Figures 6.19 and 6.20, i.e., after the shell velocity distribution has been "truncated". Notice now that in Table A6.3.4, the modes due to the "truncated" excitation of the shell at 176 Hz, the (4,0,1) mode contribution is only 8.9 dB less than the contribution of the most dominant mode.

It is also interesting to note the lack of higher order axial modes in the acoustic responses, even after the modification of the structural excitation. For example, the resonant frequency of the (8,0,0) acoustic mode is 86 Hz, and the resonant frequency of the (16,0,0) acoustic mode is 172 Hz, yet neither of these modes are excited to any degree by either the 88 Hz or 176 Hz shell excitation. The reason for this is that at both 88 Hz and 176 Hz the axial structural wavenumbers are lower than the acoustic axial wavenumbers corresponding to these modes. Therefore the structural responses do not couple efficiently with the higher order axial acoustic modes. Truncating the structural excitation at z = 1.5 m and z = 12.5 m does not appreciably increase the excitation of these higher order axial modes as the structural vibration amplitude for

$z < 1.5$ m and $z > 12.5$ m is seen from Figures 6.12 to 6.15 to be relatively small compared to the structural vibration amplitude in the region of shell lying between $z = 1.5$ m and $z = 12.5$ m. However, the lack of these higher order axial modes in the acoustic responses does not appear to detract from the generally good comparisons between the measured and predicted sound fields, and it is therefore a feature which may occur in practice.

TABLE A6.3.1 The relative contributions of the twenty most dominant acoustic modes to the total acoustic potential energy inside the finite cylinder when it is excited at 88 Hz by the shell structural response shown in Figure 6.14. The mode levels are expressed relative to the most dominant mode (see also Figure 6.23).

Axial mode order n	Circumferential mode order, n_2	Radial mode order, n_3	Mode natural frequency (Hz)	Relative mode level (dB)
1	1	0	78.1	0.0
3	1	0	83.7	-0.7
2	1	0	80.2	-12.6
0	1	0	77.3	-13.8
5	1	0	94.1	-14.5
2	2	0	130.0	-14.7
0	2	0	128.3	-15.5
4	2	0	135.2	-17.6
1	2	0	128.8	-18.1
4	1	0	88.4	-19.2
3	2	0	132.2	-20.1
1	3	0	176.7	-24.9
0	3	0	176.4	-26.8
1	1	0	224.1	-28.4
4	3	0	181.6	-29.7
7	1	0	107.7	-30.4
2	3	0	177.8	-30.6
6	2	0	143.5	-30.6
5	4	0	229.6	-32.2
5	2	0	139.0	-32.4

TABLE A6.3.2 The relative contributions of the twenty most dominant acoustic modes to the total acoustic potential energy inside the finite cylinder when it is excited at 176 Hz by the shell structural response shown in Figure 6.15. The mode levels are expressed relative to the most dominant mode (see also Figure 6.25).

Axial mode order n	Circumferential mode order, n_2	Radial mode order, n_3	Mode natural frequency (Hz)	Relative mode level (dB)
4	3	0	181.6	0.0
6	3	0	187.8	-0.1
5	3	0	184.4	-1.3
8	3	0	196.2	-3.7
1	3	0	176.7	-3.8
7	3	0	191.7	-4.8
0	3	0	176.4	-5.7
3	3	0	179.3	-6.7
9	3	0	201.1	-8.0
1	2	0	128.7	-11.3
2	3	0	177.7	-11.4
4	2	0	135.2	-12.3
5	4	0	229.6	-12.4
4	4	0	227.4	-12.5
9	2	0	160.5	-12.6
7	2	0	148.6	-13.4
0	2	0	128.3	-14.4
5	2	0	139.0	-14.6
8	2	0	154.3	-14.9
9	4	0	243.2	-15.0

TABLE A6.3.3 The relative contributions of the twenty most dominant acoustic modes to the total acoustic potential energy inside the finite cylinder when it is excited at 88 Hz by the shell structural response shown in Figure 6.14, but with the excitation only occurring for $1.5 < z$ 12.5 m and $60^\circ < \theta < 300^\circ$. The mode levels are expressed relative to the most dominant mode (see also Figure 6.24).

Axial mode order n	Circumferential mode order, n_2	Radial mode order, n_3	Mode natural frequency (Hz)	Relative mode level (dB)
3	1	0	83.7	0.0
1	1	0	78.1	-5.6
4	1	0	88.4	-10.0
0	1	0	77.3	-10.3
2	1	0	80.2	-13.1
6	1	0	100.6	-16.9
5	1	0	94.1	-17.4
4	2	0	135.2	-18.5
1	2	0	128.7	-20.0
2	2	0	130.0	-22.2
7	1	0	107.7	-23.4
0	2	0	128.3	-23.8
3	2	0	132.2	-23.9
5	2	0	139.0	-27.6
1	3	0	176.7	-29.7
0	3	0	176.4	-30.0
4	3	0	181.6	-30.4
3	3	0	179.3	-31.1
10	1	0	132.2	-32.4
1	0	1	161.3	-33.1

ABLE A6.3.4 The relative contributions of the twenty most dominant coustic modes to the total acoustic potential energy inside the finite ylinder when it is excited at 176 Hz by the shell structural response hown in Figure 6.15, but with the excitation only occurring for .5 < z 12.5 m and 60° < θ < 300°. The mode levels are expressed relative to the most dominant mode (see also Figure 6.26).

Axial mode order n	Circumferential mode order, n_2	Radial mode order, n_3	Mode natural frequency (Hz)	Relative mode level (dB)
1	3	0	176.7	0.0
5	3	0	184.4	-0.0
6	3	0	187.8	-1.3
0	3	0	176.4	-2.7
8	3	0	196.2	-3.4
4	3	0	181.6	-3.6
7	3	0	191.7	-3.7
3	3	0	179.3	-3.9
9	2	0	160.5	-8.5
4	0	1	166.5	-8.9
7	2	0	148.6	-8.9
9	3	0	201.1	-9.1
6	2	0	143.5	-9.8
2	3	0	177.7	-10.4
0	2	0	128.3	-10.8
4	2	0	135.2	-11.1
1	2	0	128.7	-11.5
10	2	0	167.1	-11.7
1	4	0	223.6	-12.3
4	4	0	227.4	-12.4